Project Title: An Integrated Approach to Characterizing Bypassed Oil in Heterogeneous and Fractured Reservoirs Using Partitioning Tracers

FINAL REPORT
Reporting Period Start Date: June 2002
Reporting Period End Date: December 2006

Principal Author: Akhil Datta-Gupta
March, 2007

DOE Contract No. DE-FC26-02NT15345

Submitting Organization:
Texas Engineering Experiment Station
Texas A&M University, College Station, TX

Subcontractor: Gary A. Pope
Petroleum and Geosystems Engineering
University of Texas, Austin, TX

DISCLAIMER

ABSTRACT

We explore the use of efficient streamline-based simulation approaches for modeling partitioning interwell tracer tests in hydrocarbon reservoirs. Specifically, we utilize the unique features of streamline models to develop an efficient approach for interpretation and history matching of field tracer response. A critical aspect here is the underdetermined and highly ill-posed nature of the associated inverse problems. We have investigated the relative merits of the traditional history matching ('amplitude inversion') and a novel travel time inversion in terms of robustness of the method and convergence behavior of the solution. We show that the traditional amplitude inversion is orders of magnitude more non-linear and the solution here is likely to get trapped in local minimum, leading to inadequate history match. The proposed travel time inversion is shown to be extremely efficient and robust for practical field applications.

The streamline approach is generalized to model water injection in naturally fractured reservoirs through the use of a dual media approach. The fractures and matrix are treated as separate continua that are connected through a transfer function, as in conventional finite difference simulators for modeling fractured systems. A detailed comparison with a commercial finite difference simulator shows very good agreement. Furthermore, an examination of the scaling behavior of the computation time indicates that the streamline approach is likely to result in significant savings for large-scale field applications. We also propose a novel approach to history matching finite-difference models that combines the advantage of the streamline models with the versatility of finite-difference simulation. In our approach, we utilize the streamline-derived sensitivities to facilitate history matching during finite-difference simulation. The use of finite-difference model allows us to account for detailed process physics and compressibility effects. The approach is very fast and avoids much of the subjective judgments and time-consuming trial-and-errors associated with manual history matching. We demonstrate the power and utility of our approach using a synthetic example and two field examples.

We have also explored the use of a finite difference reservoir simulator, UTCHEM, for field-scale design and optimization of partitioning interwell tracer tests. The finite-difference model allows us to include detailed physics associated with reactive tracer transport, particularly those related with transverse and cross-streamline mechanisms. We have investigated the potential use of downhole tracer samplers and also the use of natural tracers for the design of partitioning tracer tests. Finally, we discuss several alternative ways of using partitioning interwell tracer tests (PITTs) in oil fields for the calculation of oil saturation, swept pore volume and sweep efficiency, and assess the accuracy of such tests under a variety of reservoir conditions.

TABLE OF CONTENTS

EXECUTIVE SUMMARY

In this project we have explored the use of efficient streamline-based simulation approaches for modeling partitioning interwell tracer tests in hydrocarbon reservoirs. We utilized the unique features of streamline models to develop an efficient approach for interpretation and history matching of field tracer response. A critical aspect here is the underdetermined and highly ill-posed nature of the associated inverse problems. As a result, the interpretation of the tests can be highly ambiguous and non-unique. To circumvent the problem, we have adopted an integrated approach whereby we integrate data from multiple sources to minimize the uncertainty and non-uniqueness in the interpreted results. For partitioning interwell tracer tests, these are primarily the distribution of reservoir permeability and oil saturation distribution. We have also explored the use of a finite difference reservoir simulator, UTCHEM, for field-scale design and optimization of partitioning interwell tracer tests. The finite-difference model allows us to include detailed physics associated with reactive tracer transport, particularly those related with transverse and cross-streamline mechanisms. We have investigated the potential use of downhole tracer samplers and also the use of natural tracers for the design of partitioning tracer tests.

We have generalized streamline-based simulation to describe fluid transport in naturally fractured reservoirs through a dual-media approach. Describing fluid transport in naturally fractured reservoirs entails additional challenge because of the complicated physics arising from matrix-fracture interactions. The fractures and matrix are treated as separate continua that are connected through a transfer function, as in conventional finite difference simulators for modeling fractured systems. The transfer functions that describe fluid exchange between the fracture and matrix system can be implemented easily within the framework of the current single-porosity streamline models. In particular, the streamline time of flight concept is utilized to develop a general dual porosity dual permeability system of equations for water injection in naturally fractured reservoirs. We compare our results with a commercial finite-difference simulator for waterflooding in five spot and nine-spot patterns. For both dual porosity and dual permeability formulation, the streamline approach shows close agreement in terms of recovery histories and saturation profiles with a marked reduction in numerical dispersion and grid orientation effects. An examination of the scaling behavior of the computation time indicates that the streamline approach is likely to result in significant savings for large-scale field applications.

We have also proposed a novel approach to history matching finite-difference models that combines the advantage of the streamline models with the versatility of finite-difference simulation. In our approach, we utilize the streamline-derived sensitivities to facilitate history matching during finite-difference simulation. First, the velocity field from the finite-difference model is used to compute streamline trajectories, time of flight and parameter sensitivities. The sensitivities are then utilized in an inversion algorithm to update the reservoir model during finite-difference simulation. The use of finite-difference model allows us to account for detailed process physics and compressibility effects. Although the streamline-derived sensitivities are only approximate, they do not seem to noticeably impact the quality of the match or efficiency of the approach. For history matching, we use ‘a generalized travel-time inversion’ that is shown to be extremely robust because of its quasi-linear properties and converges in only a few iterations. The approach is very fast and avoids much of the subjective judgments and time-consuming

trial-and-errors associated with manual history matching. We demonstrate the power and utility of our approach using a synthetic example and two field examples.

We enhanced the widely used assisted history matching in two important aspects that can significantly improve its efficiency and effectiveness. First, we utilize streamline-derived analytic sensitivities to relate the changes in reservoir properties to the production response. These sensitivities can be computed analytically and contain much more information than that used in the assisted history matching. Second, we utilize the sensitivities in an optimization procedure to determine the spatial distribution and magnitude of the changes in reservoir parameters needed to improve the history-match. By intervening at each iteration during the optimization process, we can retain control over the history matching process as in assisted history matching. This allows us to accept, reject, or modify changes during the automatic history matching process. We demonstrate the power of our method using two field examples with model sizes ranging from 10^5 to 10^6 grid blocks and with over one hundred wells. The reservoir models include faults, aquifer support and several horizontal/high angle wells. History matching was performed using both assisted history matching and our previously proposed generalized travel time inversion, (GTTI). Whereas the general trends in permeability changes were similar for both the methods, the GTTI seemed to significantly improve the water cut history matching on a well-by-well basis within a few iterations. Our experience indicates that the GTTI can also be used very effectively to improve the quality of history match derived from the assisted history matching. The changes to the reservoir model from GTTI were found reasonable with no artificial discontinuities or apparent loss of geologic realism. Most importantly, history matching using GTTI took only few hours as compared to weeks or months by assisted history matching.

We have also extended the streamline-based production data integration technique to naturally fractured reservoirs using the dual porosity approach. The principal features of our method are the extension of streamline-derived analytic sensitivities to account for matrix-fracture interactions and the use of our previously proposed generalized travel time inversion for history matching. Our proposed workflow has been demonstrated by using both a dual porosity streamline simulator and a commercial finite difference simulator. Our approach is computationally efficient and well suited for large scale field applications in naturally fractured reservoirs with changing field conditions. The use of the generalized travel time concept enabled us to match both the breakthrough and amplitude of the reference response in one step.

This final report is divided into four major parts that describes the major results and accomplishments from this project. Additional details can be found in the annual reports that have been submitted to the Department of Energy at the end of every year of the project. The following papers were published based on the work from this research project.

- He, Zhong, Datta-Gupta, A., and Vasco, D. W., "Rapid Inverse Modeling of Pressure Interference Tests Using Trajectory-based Travel Time and Amplitude Matching" Water Resources Research, 42, W03419, doi:10.1029/2004WR003783, March 2006.
- Al-Harbi, M., Cheng, H., He, Zhong and Datta-Gupta, A., "Streamline-based Production Data Integration in Naturally Fractured Reservoirs," SPE Journal, 10(4), December 2005, 426-439.

- Cheng, H, Khargoria, A., He, Z. and Datta-Gupta, A., "Fast History Matching of Finite-difference Models Using Streamline-derived Sensitivities," SPE Reservoir Evaluation and Engineering, 8 (5), October 2005, p426-436.
- Cheng, H., Datta-Gupta, A. and He, Zhong., "A Comparison of Travel Time and Amplitude Inversion for Production Data Integration into Geologic Models: Sensitivity, Non-linearity and Practical Implications," SPE Journal, 10(1), March 2005, p75-90.
- Cheng, H., Wen, X, Milliken, W. and Datta-Gupta, A., "Field Experiences with Assisted and Automatic History Matching Using Streamline Models," SPE 89857 presented at the SPE Annual Technical Conference and Exhibition, Houston, TX, September 26-29, 2004.
- Al-Huthali, A. and Datta-Gupta, A., "Streamline Simulation of Counter-Current Imbibition in Naturally Fractured Reservoirs," Journal of Petroleum Science and Engineering , 43 (2004), 271-300.
- Malallah, A., Perez, H., Datta-Gupta, A. and Alamody, W., "Multiscale Data Integration Using Markov Random Fields and Markov Chain Monte Carlo: A Field Application in the Middle East," SPE Reservoir Engineering and Evaluation, 8(6), December 2004.

INTRODUCTION

Streamline Modeling of Partitioning Interwell Tracer Tests

Streamline models approximate 3D fluid flow calculations by a sum of 1D solutions along streamlines. The choice of streamline directions for the 1D calculations makes the approach extremely effective for modeling convection-dominated flows in the presence of strong heterogeneity. Briefly, in this approach we first compute the pressure distribution using a finite difference solution to the conservation equations. The velocity field is then obtained using Darcy's law. A key step is streamline simulation is the decoupling of flow and transport by a coordinate transformation from the physical space to one following flow directions. This is accomplished by defining a streamline 'time of flight' as follows:

$$\tau(\psi) = \int_{\psi} \frac{1}{|\mathbf{v}(\mathbf{x})|} dr \tag{1}$$

Thus, the time of flight is simply the travel time of a neutral tracer along a streamline. In Eq.(1), r is the distance along the streamline and $\mathbf{x}$ refers to the spatial coordinates. We will exploit an analogy between streamlines and seismic ray tracing to utilize efficient techniques from geophysical inverse theory for analysis of field tracer tests. To facilitate this analogy, we will rewrite the time of flight in terms of a 'slowness' commonly used in ray theory in seismology. The 'slowness' is defined as the reciprocal of velocity as follows

$$s(\mathbf{x}) = \frac{1}{|\mathbf{v}(\mathbf{x})|} = \frac{\mu \phi(\mathbf{x})}{k(\mathbf{x})|\nabla P(\mathbf{x})|} \tag{2}$$

where we have used Darcy's law for the interstitial velocity v and ϕ is the porosity, k is permeability, and P is the pressure. The streamline time of flight can now be written as

$$\tau(\psi) = \int_{\psi} s(\mathbf{x}) dr \tag{3}$$

Consider the convective transport of a neutral tracer. The conservation equation is given by

$$\frac{\partial C(\mathbf{x},t)}{\partial t} + \mathbf{v} \cdot \nabla C(\mathbf{x},t) = 0 \tag{4}$$

where C represents the tracer concentration. We can rewrite (4) in the streamline time of flight coordinates using the operator identity

$$\mathbf{v} \cdot \nabla = \frac{\partial}{\partial \tau}. \tag{5}$$

Physically, we have now moved to a coordinate system where all streamlines are straightlines and the distance is measured in units of τ. The coordinate transformation reduces the multidimensional transport equation into a series of one-dimensional equations along streamlines,

$$\frac{\partial C(\tau,t)}{\partial t} + \frac{\partial C(\tau,t)}{\partial \tau} = 0. \tag{6}$$

The tracer response at a producing well can be obtained by simply integrating the contributions of individual streamlines reaching the producer,

$$C(t) = \int C_0\left(t - \tau(\psi)\right) d\psi = \int C_0\left(t - \int_{\psi} s(\mathbf{x}) dr\right) d\psi \tag{7}$$

where C_0 is the tracer concentration at the injection well. If we include longitudinal dispersion along streamlines, then the tracer concentration at the producing well will be given by

$$C(t) = \int \frac{\exp[-(t-\tau(\psi))^2/(4\alpha\omega)]}{\sqrt{4\alpha\omega}} d\psi \tag{8}$$

where α is longitudinal dispersivity and $\omega = \int_{\psi} \frac{dr}{\left|\mathbf{v}(\mathbf{x})\right|^2}$.

During partitioning interwell tracer tests the retardation of partitioning tracers in the presence of oil saturation can simply be expressed as an increase in travel time along streamlines. This in turn results in an increased slowness as follows

$$s(\mathbf{x}) = \frac{1}{\left|\mathbf{v}(\mathbf{x})\right|}(S_w + K_N S_N) = \frac{\mu\,\phi(\mathbf{x})}{k(\mathbf{x})\left|\nabla P(\mathbf{x})\right|}(S_w + K_N S_N) \tag{9}$$

where S_w and S_N denote water and oil saturation and K_N is the partitioning coefficient of tracer defined as the ratio of tracer concentration in the oil phase to that in the water phase. Notice that when the tracer has equal affinity towards water and oil ($K_N = 1$), the tracer response will be insensitive to oil saturation as one would expect and Eq.(8) reverts back to Eq.(2) for single phase tracer transport. If the oil is mobile, the impact of oil saturation on the hydraulic conductivity can be accounted for through the use of appropriate relative permeability functions.

Fast and Robust History Matching of Field Tracer Tests: A Comparison of Travel Time vs. Amplitude Inversion

Traditional approach to reconciling geologic models to field tracer data involves an "amplitude matching", that is matching the tracer history directly. It is well-known that such amplitude matching results in a highly non-linear inverse problem and difficulties in convergence, often leading to an inadequate history match. The non-linearity can also aggravate the problem of non-uniqueness and instability of the solution. Recently, dynamic data integration via 'travel-time matching' has shown great promise for practical field applications. In this approach the observed data and model predictions are lined up at some reference time such as the breakthrough or 'first arrival' time. Further extensions have included amplitude information via a 'generalized travel-time' inversion. Although the travel-time inversion has been shown to be more robust compared to amplitude matching, no systematic study has been done to examine the relative merits of the methods in terms of the non-linearities and convergence properties, particularly for field-scale applications. In this work we quantitatively investigate the non-linearities in the inverse problems related to travel-time, generalized travel-time and amplitude matching during production data integration. Our results show that the commonly used amplitude inversion can be orders of magnitude more non-linear compared to the travel-time inversion. The travel-time matching is extremely robust and the minimization proceeds rapidly even if the prior geologic model is not close to the solution. The travel-time sensitivities are more uniform between the wells compared to the amplitude sensitivities that tend to be localized near the wells. This prevents over-correction near the wells. Also, for field data characterized by multiple peaks, the travel-time inversion can prevent the solution from converging to secondary peaks, resulting in a better fit to the production response. We have demonstrated our results using a field application involving a multiwell, multitracer interwell tracer injection study in the McCleskey sandstone of

the Ranger field, Texas. Starting with a prior geologic model, the traditional amplitude matching could not reproduce the field tracer response which was characterized by multiple peaks. Both travel time and generalized travel time exhibited better convergence properties and could match the tracer response at the wells with realistic changes to the geologic model. Our results appear to confirm the power and robustness of the travel-time matching for field scale production data integration.

Streamline Simulation of Water Injection in Naturally Fractured Reservoirs

Until recently streamline simulators were limited to single-porosity systems and not suitable for modeling fluid flow and transport in naturally fractured reservoirs. Describing fluid transport in naturally fractured reservoirs entails additional challenge because of the complicated physics arising from matrix-fracture interactions. In this paper the streamline-based simulation is generalized to describe fluid transport in naturally fractured reservoirs through a dual-media approach. The fractures and matrix are treated as separate continua that are connected through a transfer function, as in conventional finite difference simulators for modeling fractured systems. The transfer functions that describe fluid exchange between the fracture and matrix system can be implemented easily within the framework of the current single-porosity streamline models. In particular, the streamline time of flight concept is utilized to develop a general dual porosity dual permeability system of equations for water injection in naturally fractured reservoirs. We solve the saturations equations using an operator splitting approach that involves 'convection' along streamline followed 'matrix-fracture' exchange calculations on the grid. Our formulation reduces to the commonly used dual porosity model when the flow in the matrix is considered negligible.

We have accounted for the matrix-fracture interactions using two different transfer functions: the conventional transfer function (CTF) and an empirical transfer function (ETF). The ETF allows for analytical solution of the saturation equation for dual porosity systems and is used to validate the numerical implementation. We also compare our results with a commercial finite-difference simulator for waterflooding in five spot and nine-spot patterns. For both dual porosity and dual permeability formulation, the streamline approach shows close agreement in terms of recovery histories and saturation profiles with a marked reduction in numerical dispersion and grid orientation effects. An examination of the scaling behavior of the computation time indicates that the streamline approach is likely to result in significant savings for large-scale field applications.

Streamline-Based Production Data Integration in Naturally Fractured Reservoirs

Streamline-based models have shown great potential in reconciling high resolution geologic models to production data. In this work we extend the streamline-based production data integration technique to naturally fractured reservoirs. Describing fluid transport in fractured reservoirs poses additional challenge arising from the matrix-fracture interactions. We use a dual-porosity streamline model for fracture flow simulation by treating the fracture and matrix as separate continua that are connected through a transfer function. Next, we analytically compute the sensitivities that define the relationship between the reservoir properties and the production response in fractured reservoirs. The sensitivities are an integral part of our approach and can be evaluated very efficiently as 1-D integrals along streamlines. Finally, the production data integration is carried out via a generalized travel time inversion which has been shown to be

robust because of its quasi-linear properties and utilizes established techniques from geophysical inverse theory.

We also apply the streamline-derived sensitivities in conjunction with a dual porosity finite difference simulator to combine the efficiency of the streamline approach with the versatility of the finite difference approach. This significantly broadens the applicability of the streamline-based approach in terms of incorporating compressibility effects and complex physics. We demonstrate the power and utility of our approach using 2-D and 3-D synthetic examples designed after actual field conditions. The reference fracture patterns are generated using a discrete fracture network (DFN) model that allows us to include statistical properties of fracture swarms, fracture densities and network geometries. The DFN is then converted to a continuum model with equivalent grid block permeabilities. Starting with prior models with varying degrees of fracture information, we match the water-cut history from the reference model. Both dual porosity streamline and finite difference simulators are used to model fluid flow in the fractured media. Our results indicate the effectiveness of our approach and the role of prior information and production data in reproducing fracture connectivities and preferential flow paths.

Field-Scale Design Optimization via Numerical Simulation

To complement the streamline-based studies carried out at Texas A&M, a parallel effort has been ongoing using a finite difference model, UTCHEM for field-scale design and optimization of tracer tests. This work is carried out under the supervision of Dr. Gary A. Pope at the University of Texas, a subcontractor to the project.

The past several years have seen a great increase in the development, deployment and application of permanent in-well fiber optic monitoring systems. In-well fiber optic sensors are either currently available or under active development for measuring pressure, temperature, flow rate, phase fraction, strain, acoustics, and sand production. Potential future sensor developments include measurement of density and fluid chemistry. This study is a preliminary investigation of the use of downhole sensors to enhance the value of Partitioning Interwell Tracer Tests (PITTs). The idea being investigated is to measure the tracer concentrations in real time at multiple depths using downhole sensors. These tracer concentration data could be used to estimate oil saturations at the corresponding depths using the method of moments and/or inverse modeling.

Crude oil is a mixture of organic components of varying water solubility. A novel idea being investigated in this research is to use some of the more water-soluble components of crude oil as natural partitioning tracers to estimate oil saturations and swept pore volumes, and hence as a substitute for injected tracers. The rate at which these components will dissolve into water will depend upon their partition coefficients under reservoir conditions. In this study we have identified some of the common components of crude oils that might be used as natural partitioning tracers. Equations have been derived to estimate pore volumes and average oil saturations in a reservoir for both single-phase and multiphase flow and two simulations used to illustrate their validity under the assumed conditions.

EXPERIMENTAL

No experiments were performed at Texas A&M during the project.

RESULTS AND DISCUSSION: PART I

Fast and Robust History Matching of Field Tracer Tests: A Comparison of Travel Time vs. Amplitude Inversion

Introduction

Geological models derived from static data alone often fail to reproduce the production history of a reservoir. Reconciling geologic models to the dynamic response of the reservoir is critical to building reliable reservoir models. In recent years several techniques have been developed for integrating production data into reservoir models.[1-14] The theoretical basis of these techniques is generally rooted in the least-squares inversion theory that attempts to minimize the difference between the observed production data and the model predictions. This can be referred to as 'amplitude' matching. The production data can be water-cut observations, tracer response or pressure history at the wells. It is well known that such inverse problems are typically ill-posed and can result in non-unique and unstable solutions. Proper incorporation of static data in the form of a prior model can partially alleviate the problem. However, there are additional outstanding challenges that have deterred the routine integration of production data into reservoir models. The relationship between the production response and reservoir properties can be highly non-linear. The non-linearity can result in multiple local minima in the misfit function. This can cause the solution to converge to a local minimum, leading to an inadequate history match. All these can make it difficult to obtain a meaningful estimate of the parameter field, particularly if the initial model is far from the solution.

Recently streamline-based methods have shown significant potential for incorporating dynamic data into high resolution reservoir models.[1-14] A unique feature of the streamline-based production data integration has been the concept of a 'travel-time match' that is analogous to seismic tomography. Instead of matching the production data directly, the observed data and model predictions are first 'line-up' at the breakthrough time. This is typically followed by a conventional 'amplitude match' whereby the difference between the observed and calculated production response is minimized. A major part of the production data misfit reduction occurs during the travel-time inversion and most of the large-scale features of heterogeneity are resolved at this stage.[2,4-5]

The concept of travel-time inversion is not limited to streamline models. Recently, it has been extended for application to finite-difference models via a 'generalized travel-time' inversion.[9] The 'generalized travel-time' inversion ensures matching of the entire production response rather than just the breakthrough times and at the same time retains most of the desirable properties of the travel-time inversion. The concept follows from wave-equation travel-time tomography and is very general, robust and computationally efficient.[12,15] The generalized travel-time inversion has been utilized to extend the streamline-based production data integration methods to changing field conditions involving rate changes and infill drilling.

The advantages of the travel-time inversion compared to amplitude inversion mainly stems from its quasilinear properties. Unlike conventional 'amplitude' matching which can be highly non-linear, it has been shown that the travel-time misfit function is quasilinear with respect to changes in reservoir properties.[2,4-5] As a result, the minimization proceeds rapidly even if the initial model is not close to the solution. These advantages of travel-time inversion are

well-documented in the context of seismic inversion.[15] However, no systematic study has been done to examine the benefits of travel-time inversion for production data integration in terms of non-linearity and convergence properties. Characterizing the degree of nonlinearity can be as important as finding the solutions to the inverse problem itself. However, quantitative measures of nonlinearity for the inverse problems related to production data integration haven't been adequately addressed.

We discuss the mathematical foundation for the measure of nonlinearity and its implications on the production data integration. We quantitative investigate the extent of nonlinearity in travel-time inversion and amplitude inversion. In particular, we show that the nonlinearity in travel-time inversion is orders of magnitude smaller than that of the amplitude inversion. This leads to better convergence properties and a robust method for production data integration. We illustrate our results using both synthetic and field applications. The field application is from the McCleskey sandstone, the Ranger field, Texas and involves a multiwell, multitracer interwell tracer injection study. The results clearly demonstrate the benefits of travel-time inversion for field-scale production data integration. In particular, the generalized travel-time inversion appears to outperform both travel-time and amplitude inversion in reconciling the geologic model to the field tracer response.

Background and Approach

Travel-Time Inversion, Amplitude Inversion and Generalized Travel-Time Inversion. Travel-time inversion attempts to match the observed data and model predictions at some reference time, for example the breakthrough time or the peak arrival time. Thus, we are lining-up the production response along the time axis. Fig.1a illustrates the travel-time inversion. On the other hand, the amplitude inversion attempts to match the production response directly. This is illustrated in Fig.1b whereby we match the observed tracer concentration and model predictions at the producing well. Creatively, we can combine the travel-time inversion and amplitude inversion into one step while retaining most of the desirable features of a travel-time inversion. This is the 'generalized travel-time inversion' and follows from the work of Luo and Schuster[15] in the context of wave equation travel-time tomography.

A generalized travel-time or travel-time shift is computed by systematically shifting the computed production response towards the observed data until the cross-correlation between the two is maximized. The approach is illustrated in Figs. 1c and 1d. It preserves the robustness of a travel-time inversion and improves computational efficiency by representing the production data misfit at a well in terms of a single travel-time shift. It can be shown to reduce to the more traditional least-squared misfit functional as we approach the solution.[12]

The advantages of travel-time inversion are well documented in the geophysics literature. For example, Luo and Schuster[15] pointed out that travel-time inversion is quasi-linear as opposed to amplitude inversion which can be highly non-linear. Amplitude inversion typically works well when the prior model is close to the solution. This was the rationale behind our previously proposed two-step approach to production data integration: travel-time match followed by amplitude match.[2,4] In this paper, we will quantitatively investigate the relative merits of the different methods in terms of non-linearity and convergence properties.

Measures of Nonlinearity. Characterizing and assessing the nonlinearity in the parameter estimation problem is critical to designing efficient and robust approaches to production data

integration. There are several methods for quantifying the degree of non-linearity in inverse problems. We will use the measure proposed by Bates and Watts[16] to examine the non-linearities in travel-time and amplitude inversion. Grimsted and Mannseth[17-18] applied this measure to examine the relationship between non-linearity, scale and sensitivity in parameter estimation problems. If F represents an outcome, for example, the tracer response, then the nonlinearity measure is defined as $\kappa=||Fkk||/||Fk||2$, where F_k is the vector of the first-order derivatives with respect to the parameter vector k, that is, the sensitivity vector, and F_{kk} is the vector of second-order derivatives. This measure is based on the geometric concept of curvature and κ represents the inverse of a radius of the circle that best approximates the outcome locus F in the direction of F_k at k. Smoother and more linear outcome will have smaller curvature (larger radius) and thus smaller measure of non-linearity as illustrated in Fig. 2.

In our application, we evaluate $\kappa=||Fkk||/||Fk||2$ for every iteration during inversion. In addition, for amplitude inversion, we compute the measure for different observations and choose the maximum. The details of the computations, including the derivative calculations for travel-time, amplitude, and generalized travel-time will be discussed later. In the following section, we first illustrate the approach using a synthetic example.

Non-linearity Measure in Production Data Integration: A Simple Illustration. This example involves integration of tracer response in a heterogeneous 9-spot pattern as shown in Fig. 3. The mesh size is 21×21. The reference permeability distribution consists of a low-permeability trend towards north and a high-permeability trend towards south. The tracer responses from the eight producers in the 9-spot pattern are shown in Fig. 4a. Also superimposed in Fig. 4a are the tracer responses corresponding to our initial model, a homogeneous permeability field that is conditioned at the well locations.

We compare the relative performance of travel-time, amplitude, and generalized travel-time inversion and also the non-linearities inherent in these approaches. Fig. 4b shows the tracer concentration matches after travel-time inversion. All the peak times are now in agreement although there are some discrepancies in the details of the tracer responses. Fig. 4c shows the tracer concentration matches after generalized travel-time inversion. Not only the peak arrival-times but also the amplitudes are matched much better compared to the travel-time inversion. Fig. 4d shows the tracer-responses match after the amplitude inversion. Although the matches are quite good for most wells, they are unsatisfactory for wells 2 and 7. Incidentally, these are the two wells that exhibited maximum discrepancy based on the initial model.

Fig. 5 shows the convergence behavior for the three methods. Both travel-time and generalized travel-time inversion reproduce the arrival times perfectly. The generalized travel-time further reduces the tracer concentration misfit. In contrast, direct amplitude match shows high arrival time misfit and is unable to reproduce the tracer response at two wells. Fig. 6a is the estimated permeability field after travel-time match. On comparing with Fig. 3, we can identify the low-permeability areas and some of the moderate-to-high permeability areas, although the high permeability area is not well reproduced. Fig. 6b shows the permeability field derived by generalized travel-time inversion. It reproduces not only the low-permeability area but also the high-permeability regions. Fig. 6c shows the estimated permeability field after the amplitude inversion. Clearly, the results show signs of instability because of the high non-linearity as discussed below.

Fig. 7 shows the measure of nonlinearity for the three approaches. We can see that both the travel-time and the generalized travel-time exhibit the same degrees of non-linearity. In

contrast, the amplitude inversion is three to four orders of magnitudes more nonlinear than the travel-time inversion. This is partly the reason for the failure of the amplitude inversion when the initial model is far from the solution. The generalized travel-time inversion appears to retain most of the desirable features of a travel-time inversion while obtaining an adequate amplitude match.

Mathematical Formulation: Sensitivity Computations and Measures of Nonlinearity

We now discuss the mathematical details related to sensitivity computation and measure of non-linearity for travel-time, generalized travel-time and amplitude inversion. Although the approach is generally applicable, we will use a streamline simulator here because of the advantages in sensitivity computations. The sensitivities quantify change in production response because of a small change in reservoir properties. They are an integral part of most inverse modeling methods. We also need the sensitivities to quantify non-linearities in the various inverse methods examined in this study. Several approaches can be used to compute sensitivity coefficients of model parameters. Most of these methods fall into one of the three categories: perturbation method, direct method, and adjoint state method[19-21] and can be computationally demanding, particularly for large-scale field applications. However, for streamline models, it is possible to analytically derive a relationship between perturbations in reservoir properties, such as permeability or porosity, and changes in observations such as watercut and tracer response. Streamline-based sensitivity computation is very fast and involves quantities computed by a single streamline simulation. Hence, we will limit our discussion to streamline models only.

We use the theory of Bates and Watts[16] to measure the nonlinearity in production data integration. Bates and Watts[16] separate the nonlinearity measures into parameter-effect curvature and intrinsic curvature; thus they decompose the second-order derivative F_{kk} into one component parallel to the tangent plane defined by F_k for all directions and another component normal to that plane. Here we do not separate the intrinsic curvature and parameter effect curvature; neither do we consider the direction in the parameter space since it is not practical to do so for our problem. However, the theory we applied is essentially the same as that of Bates and Watts.[16]

Sensitivity and Nonlinearity of Travel-time. Streamline methods decouple flow and transport by a coordinate transformation from the physical space to the time-of-flight along streamlines.[22] The time-of-flight is defined as

$$\tau = \int_{\psi} s(x)dr \quad , \tag{1}$$

where the integral is along the streamline trajectory, Ψ, and s is the slowness defined as the reciprocal of the interstitial velocity,

$$s = \frac{1}{|v|} = \frac{\phi}{k\lambda_{rt}|\nabla P|} \quad . \tag{2}$$

The first-order derivative of slowness with respect to permeability is

$$\frac{\partial s}{\partial k} = -\frac{s}{k} \quad . \tag{3}$$

and the second-order derivative of slowness is

$$\frac{\partial^2 s}{\partial k^2} = \frac{s}{k^2} \quad . \tag{4}$$

If we assume that the streamlines do not shift because of small perturbations in reservoir properties, we can then relate the change in travel time δτ to the change in slowness by

$$\delta\tau = \int_{\Psi} \delta s(x) dr$$
$$= \int_{\Psi} \left[-\frac{s(x)}{k(x)} \delta k(x) + \frac{s(x)}{\phi(x)} \delta\phi(x) \right] dr \quad . \tag{5}$$

The travel-time sensitivity along a single streamline at a producer with respect to permeability for a grid block at location x is given by integrating Eq. 3 from the inlet to the outlet of the streamline Ψ within the grid block:

$$\frac{\partial \tau(\psi)}{\partial k(x)} = \int_{inlet}^{outlet} \left[-\frac{s(x)}{k(x)} \right] dr(\psi) \quad . \tag{6}$$

The overall travel-time sensitivity is then obtained by summing the sensitivities over all streamlines contributing to the arrival time of a particular concentration (for example, the peak concentration):

$$\frac{\partial \tau}{\partial k(x)} = \sum_{all\ \psi} \frac{\partial \tau(\psi)}{\partial k(x)} \quad . \tag{7}$$

The second-order derivative of travel-time along a single streamline is obtained by integrating Eq. 4,

$$\frac{\partial^2 \tau(\psi)}{\partial k^2(x)} = \int_{inlet}^{outlet} \frac{s(x)}{k^2(x)} dr(\psi) \quad , \tag{8}$$

and then integrating over all streamlines contributing to a producer,

$$\frac{\partial^2 \tau}{\partial k^2(x)} = \sum_{\Psi} \frac{\partial^2 \tau(\psi)}{\partial k^2(x)} \quad . \tag{9}$$

The components of the tangent vector Fk and acceleration vector Fkk can now be obtained from Eqs. 7 and 9:

$$\text{Fk} = \left(\frac{\partial \tau}{\partial k_1}, \frac{\partial \tau}{\partial k_2}, \cdots, \frac{\partial \tau}{\partial k_{n_b}} \right)^T \quad ; \tag{10}$$

$$\text{Fkk} = \left(\frac{\partial^2 \tau}{\partial k_1^2}, \frac{\partial^2 \tau}{\partial k_2^2}, \cdots, \frac{\partial^2 \tau}{\partial k_{n_b}^2} \right)^T \quad . \tag{11}$$

The 2-norms are used to calculate the vector norms,

$$||\text{Fk}|| = \left(\sum_{j=1}^{n_b} \left(\frac{\partial \tau}{\partial k_j} \right)^2 \right)^{1/2} \quad , \tag{12}$$

$$||\text{Fkk}|| = \left(\sum_{j=1}^{n_b} \left(\frac{\partial^2 \tau}{\partial k_j^2} \right)^2 \right)^{1/2} \quad . \tag{13}$$

Now we can calculate the nonlinearity measure of travel-time inversion κtt according to the theory of Bates and Watts16 by

$$\kappa tt = ||\text{Fkk}|| / ||\text{Fk}||2 \tag{14}$$

Sensitivity and Nonlinearity of Amplitude. Tracer transport can be described by the following convection-diffusion equation,

$$\phi\frac{\partial C(x,t)}{\partial t}=\nabla\cdot\left[D(x)\cdot\nabla C(x,t)\right]-u\cdot\nabla C(x,t) \quad (15)$$

Ignoring the dispersion term, Eq. 15 can be rewritten as

$$\phi\frac{\partial C(x,t)}{\partial t}+u\cdot\nabla C(x,t)=0 \quad (16)$$

Applying a transformation to the time-of-flight coordinate, the tracer transport equation along a streamline can be expressed as22

$$\frac{\partial C(\tau,t)}{\partial t}+\frac{\partial C(\tau,t)}{\partial \tau}=0 \quad (17)$$

For a unit-impulse concentration at (τ, t)=(0,0), the solution is22

$$C(x,t)=\delta\left(t-\tau(x)\right), \quad (18)$$

where δ is the Dirac-delta function. If the input is C0, then

$$C(x,t)=C_0(t-\tau) \quad (19)$$

Summing the contributions of all streamlines reaching a producer, we get the tracer response at a producer as

$$C(t)=\int_{all\ \psi} C_0(t-\tau)d\psi \quad (20)$$

From Eq. 19, tracer response at the producer along a single streamline is

$$C(t)=C_0\left(t-\int_{\Psi} s(x)dr)\right) \quad (21)$$

where we have used the definition of time of flight from Eq.1.

Now, consider a small perturbation in reservoir properties, say permeability. The resulting changes in slowness and concentrations can be written as

$$s(x)=s^0(x)+\delta s(x), \quad (22)$$

$$C(t)=C^0(t)+\delta C(t), \quad (23)$$

where s0 and C0 are initial slowness distribution in the reservoir and the associated tracer response respectively. Applying Eqs. 21 and 22, the change in concentration response can be expressed as

$$\begin{aligned}\delta C(t)&=C(t)-C^0(t)\\&=C_0\left(t-\int_{\Psi}\left[s^0(x)+\delta s(x)\right]dr\right)-C_0\left(t-\int_{\Psi_0} s^0(x)dr)\right)\end{aligned} \quad (24)$$

Using a Taylor series expansion and assuming $\Psi=\Psi_0$ (stationary streamlines), we get

$$\begin{aligned}&C_0\left(t-\int_{\Psi}\left[s^0(x)+\delta s(x)\right]dr\right)\\&=C_0\left(t-\int_{\Psi_0} s^0(x)dr-\int_{\Psi_0}\delta s(x)dr\right)\end{aligned}$$

$$\approx C_0\left(t-\int_{\Psi_0} s^0(x)dr\right)+\left[\left(t-\int_{\Psi_0} s^0(x)dr-\int_{\Psi_0}\delta s(x)dr\right)\right.$$
$$\left.-\left(t-\int_{\Psi_0} s^0(x)dr\right)\right]C_0'\left(t-\int_{\Psi_0} s^0(x)dr\right)$$
$$=C_0\left(t-\int_{\Psi_0} s^0(x)dr\right)-\int_{\Psi_0}\delta s(x)dr\cdot C_0'\left(t-\int_{\Psi_0} s^0(x)dr\right). \quad (25)$$

Hence the perturbation in C(t) and s(x) are related by

$$\delta C(t)=-C_0'\left(t-\int_{\Psi_0} s^0(x)dr\right)\int_{\Psi_0}\delta s(x)dr. \quad (26)$$

The tracer-concentration sensitivity along a single streamline Ψ is then

$$\frac{\partial C(t)}{\partial k(x)}=-C_0'\left(t-\int_{\Psi} s^0(x)dr\right)\int_{\Psi}\frac{\partial s(x)}{\partial k(x)}dr$$
$$=-C_0'\left(t-\int_{\Psi} s^0(x)dr\right)\int_{\Psi}[-\frac{s(x)}{k(x)}]dr$$
$$=-C_0'\left(t-\int_{\Psi} s^0(x)dr\right)\frac{\partial\tau(\Psi)}{\partial k(x)}. \quad (27)$$

The second-order derivative of the tracer concentration with respect to permeability is

$$\frac{\partial^2 C(t)}{\partial k^2(x)}=-C_0'\left(t-\int_{\Psi} s^0(x)dr\right)\int_{\Psi}\frac{\partial^2 s(x)}{\partial k^2(x)}dr$$
$$=-C_0'\left(t-\int_{\Psi} s^0(x)dr\right)\int_{\Psi}\frac{s(x)}{k^2(x)}dr$$
$$=-C_0'\left(t-\int_{\Psi} s^0(x)dr\right)\frac{\partial^2\tau(\Psi)}{\partial k^2(x)}. \quad (28)$$

As before, we need to sum over all streamlines reaching a producer to get the final first-order and second-order derivatives of the concentration response at the producer.

Now we need to evaluate the tangent vector Fk, the acceleration vector Fkk, and measure of nonlinearity κ at different observation times. The vectors and norms are expressed as follows

$$\text{Fk(ti)}=\left(\frac{\partial C(t_i)}{\partial k_1},\frac{\partial C(t_i)}{\partial k_2},\cdots,\frac{\partial C(t_i)}{\partial k_{n_b}}\right)^T, \quad (29)$$

$$\text{Fkk(ti)}=\left(\frac{\partial^2 C(t_i)}{\partial k_1^2},\frac{\partial^2 C(t_i)}{\partial k_2^2},\cdots,\frac{\partial^2 C(t_i)}{\partial k_{n_b}^2}\right)^T; \quad (30)$$

$$\text{||Fk(ti)||}=\left(\sum_{j=1}^{n_b}(\frac{\partial C(t_i)}{\partial k_j})^2\right)^{1/2}, \quad (31)$$

$$\text{||Fkk(ti)||}=\left(\sum_{j=1}^{n_b}(\frac{\partial^2 C(t_i)}{\partial k_j^2})^2\right)^{1/2}. \quad (32)$$

By definition, the measure of nonlinearity at observation time ti is

$$\kappa(ti)=||Fkk(ti)||/||Fk(ti)||2. \quad (33)$$

The final measure of nonlinearity for amplitude inversion κam is given by the maximum over all observed data,

$$\kappa_{am} = \max\left(\kappa(t_1), \kappa(t_2), \cdots, \kappa(t_{n_o})\right). \tag{34}$$

Sensitivity and Nonlinearity of Generalized Travel Time. In generalized travel-time inversion we define the misfit between the calculated and observed tracer concentrations in terms of the following correlation function:[12,15]

$$f(x,\tau) = \int dt \frac{C(x,t+\tau)_o}{A_o} C(x,t)_c, \tag{35}$$

where A is the maximum amplitude of tracer concentration and τ is the shift time between calculated and observed tracer concentrations. We seek a τ that shifts the calculated tracer response so that it best matches the observed tracer response.

The criterion for the "best" match is defined as the travel-time residual Δτ that maximizes the correlation function above, that is,

$$f(x,\Delta\tau) = \max\{f(x,\tau) \mid \tau \in [-T,T]\}, \tag{36}$$

where T is the estimated maximum travel-time difference between the observed and calculated tracer responses. So the derivative of $f(x,\tau)$ with respect to τ should be zero at Δτ unless the maximum is at an end point T or –T,

$$\begin{aligned} \dot{f}_{\Delta\tau} &= \left[\frac{\partial f(x,\tau)}{\partial\tau}\right]_{\tau=\Delta\tau} \\ &= \frac{1}{A}\int dt \frac{\partial C(t+\Delta\tau)_o}{\partial t} C(t)_c \frac{\partial t}{\partial\tau} \\ &= \frac{1}{A}\int dt \frac{\partial C(t+\Delta\tau)_o}{\partial t} C(t)_c = 0 \end{aligned}. \tag{37}$$

Note that $\partial t/\partial\tau = 1$ in this derivation. Eq. 37 is the function that is used to compute the sensitivity of the generalized travel time.

Using Eq. 37 and the rule for the derivative of an implicit function, we get

$$\frac{\partial\Delta\tau}{\partial k(x)} = -\frac{\frac{\partial(\dot{f}_{\Delta\tau})}{\partial k(x)}}{\frac{\partial(\dot{f}_{\Delta\tau})}{\partial\Delta\tau}}. \tag{38}$$

Taking the derivatives of $\dot{f}_{\Delta\tau}$ with respect to k(x) and Δτ, we have

$$\begin{aligned} \frac{\partial(\dot{f}_{\Delta\tau})}{\partial k(x)} &= \frac{1}{A}\int dt \frac{\partial C(t+\Delta\tau)_o}{\partial t}\frac{\partial C(t)_c}{\partial k(x)} \\ &= \frac{1}{A}\int dt \frac{\partial C(t+\Delta\tau)_o}{\partial t}\frac{\partial C(t)_c}{\partial t}\frac{\partial t}{\partial\tau}\frac{\partial\tau}{\partial k(x)} \\ &= \frac{1}{A}\int dt \frac{\partial C(t+\Delta\tau)_o}{\partial t}\frac{\partial C(t)_c}{\partial t}\frac{\partial\tau}{\partial k(x)} \end{aligned}. \tag{39}$$

and

$$\frac{\partial\dot{f}_{\Delta\tau}}{\partial\Delta\tau} = \frac{\int dt \cdot E}{A}, \tag{40}$$

where

$$E = \frac{\partial C(t+\Delta\tau)_o}{\partial t}\frac{\partial C(t)_c}{\partial \Delta\tau} + C(t)_c \frac{\partial[\frac{\partial C(t+\Delta\tau)_o}{\partial t}]}{\partial \Delta\tau}$$
$$= \frac{\partial C(t+\Delta\tau)_o}{\partial t}\frac{\partial C(t)_c}{\partial t}\frac{\partial t}{\partial \Delta\tau} + C(t)_c \frac{\partial^2 C(t+\Delta\tau)_o}{\partial t^2}\frac{\partial t}{\partial \Delta\tau}$$
$$= \frac{\partial C(t+\Delta\tau)_o}{\partial t}\frac{\partial C(t)_c}{\partial t} + C(t)_c \frac{\partial^2 C(t+\Delta\tau)_o}{\partial t^2} \quad . \tag{41}$$

In the derivation above, we have applied the relationship $\frac{\partial t}{\partial \Delta\tau} = \frac{\partial t}{\partial \tau} = 1$ at $\tau = \Delta\tau$.

Substitution of Eqs. 39 through 41 into Eq. 38 gives

$$\frac{\partial \Delta\tau}{\partial k(x)} = \frac{\int dt[\frac{\partial C(t+\Delta\tau)_o}{\partial t}\frac{\partial C(t)_c}{\partial t}\frac{\partial \tau}{\partial k(x)}]}{\int dt[\frac{\partial C(t+\Delta\tau)_o}{\partial t}\frac{\partial C(t)_c}{\partial t} + C(t)_c \frac{\partial^2 C(t+\Delta\tau)_o}{\partial t^2}]} \quad . \tag{42}$$

The second-order derivative of generalized travel-time with respect to permeability is then

$$\frac{\partial^2 \Delta\tau}{\partial k^2(x)} = \frac{\int dt[\frac{\partial C(t+\Delta\tau)_o}{\partial t}\frac{\partial C(t)_c}{\partial t}\frac{\partial^2 \tau}{\partial k^2(x)}]}{\int dt[\frac{\partial C(t+\Delta\tau)_o}{\partial t}\frac{\partial C(t)_c}{\partial t} + C(t)_c \frac{\partial^2 C(t+\Delta\tau)_o}{\partial t^2}]} , \tag{43}$$

where $\frac{\partial^2 \tau}{\partial k^2}$ is calculated by Eq. 8.

Finally, to calculate measures of nonlinearity, the components of the tangent vector Fk and acceleration vector Fkk are obtained from Eqs. 42 and 43 as follows

$$\text{Fk} = \left(\frac{\partial \Delta\tau}{\partial k_1}, \frac{\partial \Delta\tau}{\partial k_2}, \cdots, \frac{\partial \Delta\tau}{\partial k_{n_b}}\right)^T ; \tag{44}$$

$$\text{Fkk} = \left(\frac{\partial^2 \Delta\tau}{\partial k_1^2}, \frac{\partial^2 \Delta\tau}{\partial k_2^2}, \cdots, \frac{\partial^2 \Delta\tau}{\partial k_{n_b}^2}\right)^T . \tag{45}$$

The 2-norms of the vectors are calculated by

$$||\text{Fk}|| = \left(\sum_{j=1}^{n_b} (\frac{\partial \Delta\tau}{\partial k_j})^2\right)^{1/2} ; \tag{46}$$

$$||\text{Fkk}|| = \left(\sum_{j=1}^{n_b} (\frac{\partial^2 \Delta\tau}{\partial k_j^2})^2\right)^{1/2} . \tag{47}$$

The measure of nonlinearity for the generalized travel-time inversion is evaluated using Eqs. 46 and 47

$$\kappa gt = ||\text{Fkk}||/||\text{Fk}||2, \tag{48}$$

Sensitivity Computations: A ¼ Five-spot Example. We illustrate sensitivity computations for the three methods using the tracer response in a heterogeneous quarter 5-spot pattern (**Fig. 8**). **Fig. 9a** is the sensitivity distribution for the peak travel-time, and **Fig. 9b** is the sensitivity distribution for the generalized travel-time. **Figs. 10a**, **10b**, and **10c** show the sensitivity

distribution for the amplitude before, at, and after peak time respectively. From **Figs. 9** and **10**, we can see that the sensitivity distribution between the wells for travel-time inversion is more uniform than that for amplitude inversion. Also, the magnitude of the amplitude sensitivity is much smaller than that of the travel-time sensitivity. This smaller sensitivity contributes to the high nonlinearity of amplitude inversion because the nonlinearity is evaluated by $||\boldsymbol{F}_{kk}||/||\boldsymbol{F}_k||^2$, where $\boldsymbol{F}_k$ is the sensitivity vector. Such relationship between non-linearity and sensitivity for inverse modeling has also been observed by Grimstad and Mannseth.[17-18]

Data Inversion

Our goal is to reconcile high-resolution geologic models to field production history, for example tracer response. This typically involves the solution of an underdetermined inverse problem. The mathematical formulation behind such streamline-based inverse problems has been discussed elsewhere.[2,4-5] Briefly, in our approach we start with a prior static model that already incorporates geologic, well log, and seismic data. We then minimize a penalized misfit function consisting of the following three terms,

$$\|\delta d - S\delta R\| + \beta_1\|\delta R\| + \beta_2\|L\delta R\| \quad \text{.....} \quad (49)$$

In **Eq. 49**, $\delta\boldsymbol{d}$ is the vector of data residuals at the wells, S is the sensitivity matrix containing the sensitivities of the observed data with respect to the reservoir parameters. Also, δR corresponds to the change in the reservoir property and L is a second-spatial-difference operator. The first term ensures that the difference between the observed and calculated production response is minimized. The second term, called a norm constraint, penalizes deviations from the initial model. This helps preserve geologic realism because our initial or prior model already incorporates available geologic and static information related to the reservoir. Finally, the third term, a roughness penalty, simply recognizes the fact that production data are an integrated response and are thus, best suited to resolve large-scale structures rather than small-scale property variations.

The minimum in Eq. 49 can be obtained by an iterative least-squares solution to the augmented linear system

$$\begin{pmatrix} S \\ \beta_1 I \\ \beta_2 L \end{pmatrix} \delta R = \begin{pmatrix} \delta d \\ 0 \\ 0 \end{pmatrix}. \quad \text{.....} \quad (50)$$

The weights β_1 and β_2 determine the relative strengths of the prior model and the roughness term. The selection of these weights can be somewhat subjective although there are guidelines in the literature.[23] In general, the inversion results will be sensitive to the choice of these weights.

In **Eq. 50**, $\delta\boldsymbol{d}$ is replaced by $\delta\boldsymbol{\tau}$ for travel-time inversion, $\delta\boldsymbol{C}$ for amplitude inversion, and $\delta\Delta\boldsymbol{\tau}$ for generalized travel-time inversion. The sensitivity matrix S is also replaced by the corresponding expression.

Note that one of the major advantages of travel-time and the generalized travel-time approach is that the size of the sensitivity matrix S is dependent only on the number of wells regardless of the number of data points. This leads to considerable savings in computation time. We use an iterative sparse matrix solver, LSQR, for solving this augmented linear system efficiently.[24] The LSQR algorithm is well suited for highly ill-conditioned systems and has been widely used for large-scale tomographic problems in seismology.[25]

Field Application: The Ranger Field, Texas

Dataset Description. A multiwell, mulitracer, interwell tracer injection study was carried out in the McCleskey sandstone of the Ranger field, Texas. The first description of this data set was published by Lichtenberger.[26] The dataset was also described later by Allison *et al*.[27] The 320-acre area of interest includes 13 producers and 4 injectors, injecting 7 different tracers. The seven tracers injected included 5 conservative tracers consisting of four decaying (Tritium, Cobalt-57, Cobalt-58, and Cobalt-60), one chemical (sodium thiocyanate, NaSCN), and two partitioning tracers (tertiary butyl alcohol, TBA, and isopropyl alcohol, IPA).

All tracers were injected in small slugs on the same day except for TBA, which was injected in a small slug 20 days later. Tracer sampling continued for 826 days after injection of the first set of tracers. The tracer injection pattern is shown in **Fig. 11**. Detailed information for injection locations and the amounts of each tracer injected can be found elsewhere.[28] We use averaged well-production and injection rates over the life of the project for our work. The average production and injection rates for all wells are summarized in **Fig. 12**.

We can use the conservative tracers (Tritium and NaSCN) to obtain permeability distribution in the study area. However, the Tritium response may be affected by a chromatographic delay because of tritium exchange with immobile hydrogen.[26] We selected NaSCN as the conservative tracer for permeability inversion. Totally 5,655 lbs of NaSCN was injected into Well 38. The observed tracer responses are shown in **Fig. 13**.

Choice of an Initial Model. During inverse modeling, a proper selection of the initial model can be critical to ensure a plausible solution. Such an initial model should incorporate all available prior information. For our simulation studies, we use a 31×45×6 grid which corresponds to 100×100 ft gridblocks areally and 2 to 4 ft vertically. A total of 141 core samples were available for analysis. We did not have well- and depth-specific data but rather a summary of the core data for all wells. A histogram and cumulative distribution of the core permeabilities are shown in **Fig. 14**. The core data indicated a fair degree of permeability heterogeneity in the reservoir but only slight variation in porosity. For the initial model, we used a uniform value of porosity and a heterogeneous permeability field generated using Sequential Gaussian Simulation[29] based on well data (**Fig. 15)**.

Estimating permeability. We matched the NaSCN data to obtain the permeability distribution in the study area using the three different approaches: travel-time inversion, generalized travel-time inversion, and amplitude inversion. **Fig. 13** shows the NaSCN responses from a streamline simulator using the initial permeability field. Also, superimposed are the observed NaSCN concentrations. Clearly, there is a large difference between the calculated and observed NaSCN response. **Fig. 16** shows the NaSCN concentration match after travel-time inversion. The peak arrival times are now in agreement with the observed data. The tracer concentration amplitudes show improvement but the overall match is still not satisfactory. **Fig. 17** is the NaSCN concentration match after the generalized travel-time inversion. From Fig. 17 we can see that not only are the peak-arrival times well matched, but the calculated concentration amplitudes are also in close agreement with the observed data. This shows that generalized travel-time inversion is an effective one-step inversion process. **Fig. 18** displays the NaSCN concentration match after direct amplitude inversion. Clearly the calculated responses have changed very little from the initial responses. The results indicate that amplitude inversion may not be as effective as the travel-time inversion, particularly when the initial model is far from the solution. Generalized

travel-time inversion stands out as the best among the three inversion methods. This is also demonstrated by **Fig. 19**, which shows the convergence behavior for travel-time inversion, generalized travel-time inversion, and amplitude inversion for the field case.

Fig. 20 summarizes nonlinearity for the three inversion methods. The measure of nonlinearity for the field example is given by the maximum amongst the three producers. Amplitude inversion displays the highest measure of nonlinearity, about 200 to 250, while travel-time inversion is quasi-linear with a nonlinearity of around 0.2 to 0.4. The generalized travel-time inversion is between these two cases in terms of non-linearity measure. However, it is one order of magnitude larger than the travel-time inversion while two orders of magnitude smaller than that of the amplitude inversion. Generalized travel-time inversion keeps most of the favorable features of travel-time inversion and has a much better tracer-concentration amplitude match than travel-time inversion. The severe nonlinearity of the amplitude inversion is partly responsible for its poor performance for the field case.

Fig. 21 shows the permeability fields derived by travel-time inversion and generalized travel-time inversion. **Fig. 22** shows the permeability change after travel-time inversion and generalized travel-time inversion. Comparing these with the permeability distribution obtained by Allison *et al.*[27] by a manual matching of the tracer data using a finite-difference simulator reveals a general agreement between the location of the permeability multipliers and the areas with higher and lower permeability values. For example, we see that the high-permeability multipliers in the upper-right and central-left areas and the low-permeability multipliers in the lower-left areas in **Fig. 23** agree with the positive and negative changes shown in Fig. 22.

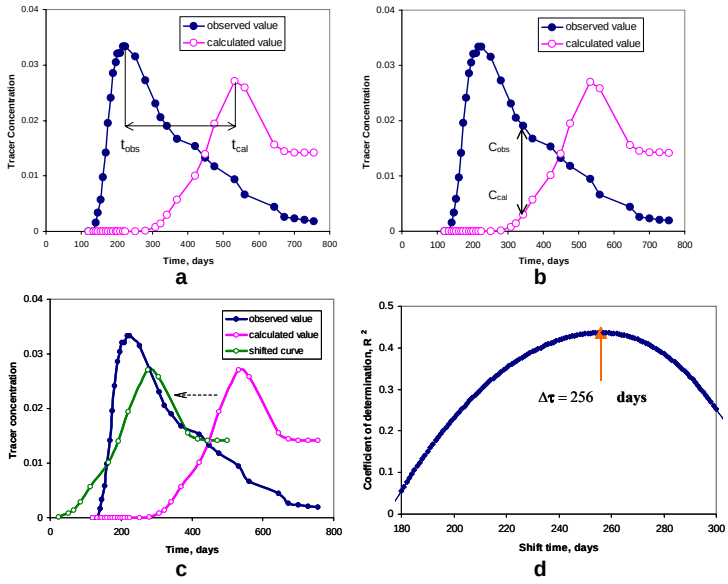

Fig. 1—Illustration of (a) travel-time inversion, (b) amplitude inversion, (c) generalized travel-time inversion, and (d) best time shift.

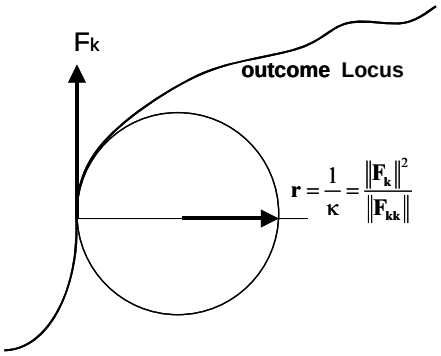

Fig. 2— Geometric meaning of the measure of nonlinearity.

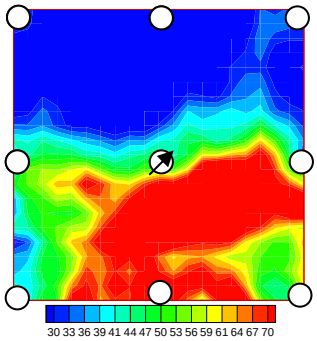

Fig. 3—Synthetic permeability distribution for the 9-spot case.

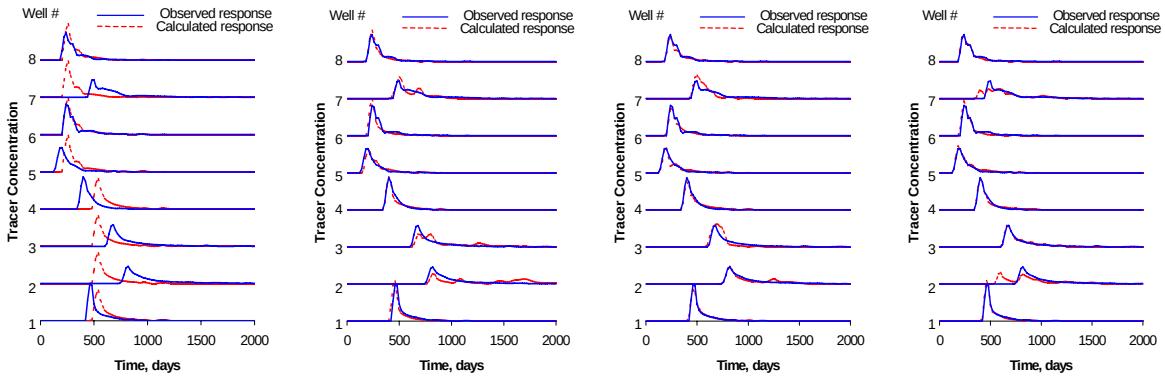

Fig. 4—Tracer response (a) for uniform initial permeability, (b) after peak arrival-time inversion, (c) after generalized travel-time inversion, and (d) after direct amplitude inversion.

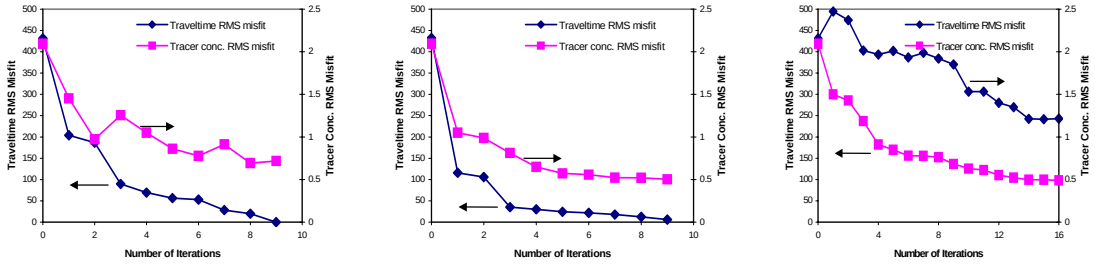

a b c

Fig. 5—Travel-time and tracer concentration misfit for (a) travel-time, (b) generalized travel-time, and (c) amplitude inversion.

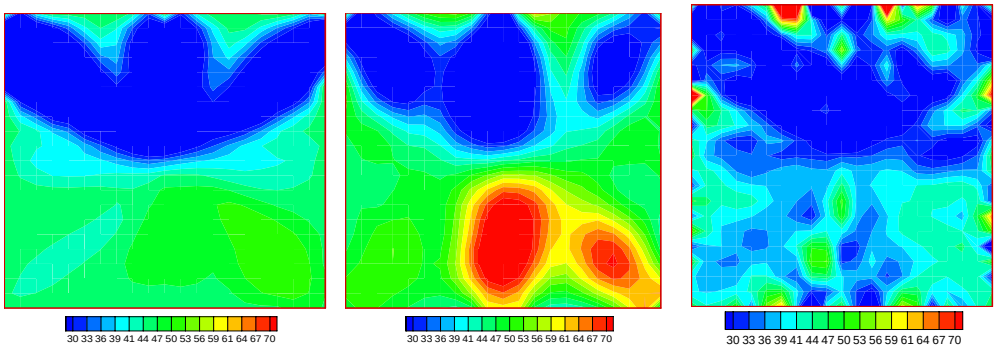

a b c

Fig. 6—Estimated permeability distribution for the 9-spot case (a) after travel-time inversion, (b) after generalized travel-time inversion, and (c) after amplitude inversion.

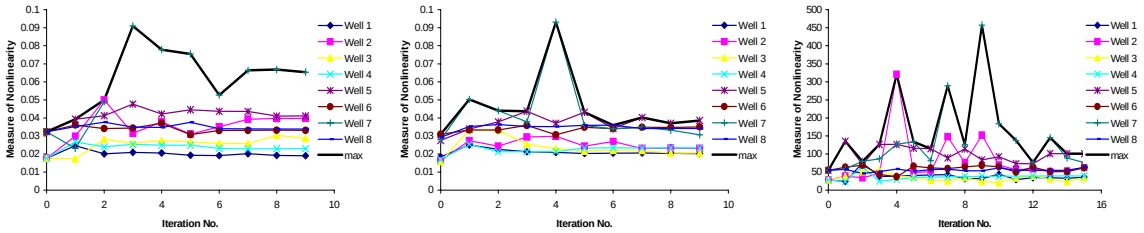

a b c

Fig. 7—Measure of nonlinearity for (a) travel-time inversion, (b) generalized travel-time inversion, and (c) amplitude inversion.

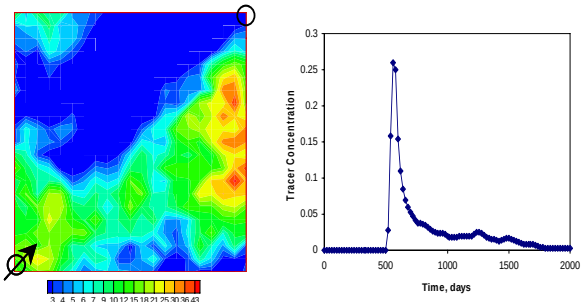

a b

Fig. 8—Tracer response for a ¼ five-spot heterogeneous case.

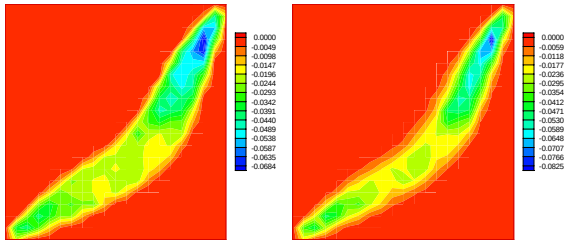

a b

Fig. 9—Sensitivity for (a) travel-time and (b) generalized travel- time inversion.

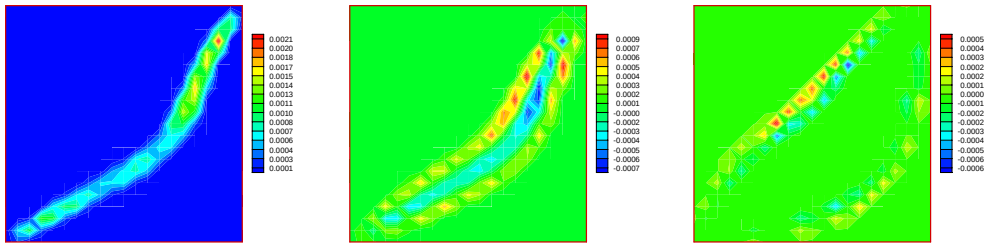

a b c

Fig. 10—Sensitivity distribution for amplitude inversion (a) before peak time, (b) at peak time, and (c) after peak time.

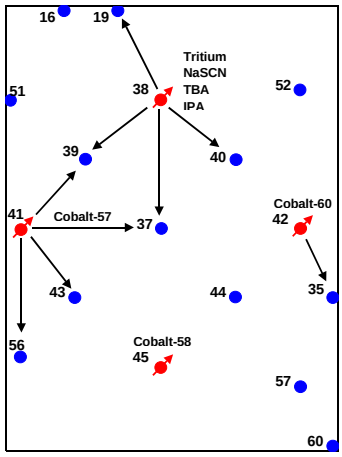

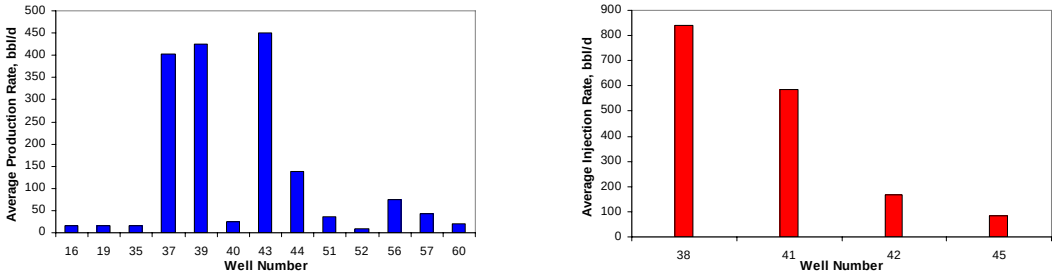

a b

Fig. 12— (a) Well production rates and (b) well injection rates.

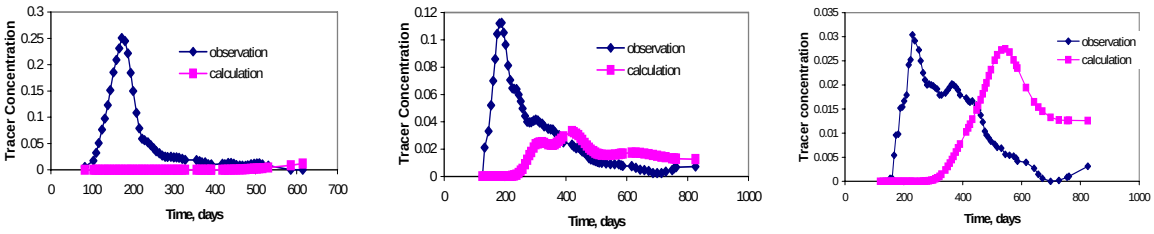

a b c

Fig. 13—NaSCN tracer response for the initial permeability field at (a) Well 40, (b) Well 37, and (c) Well 39.

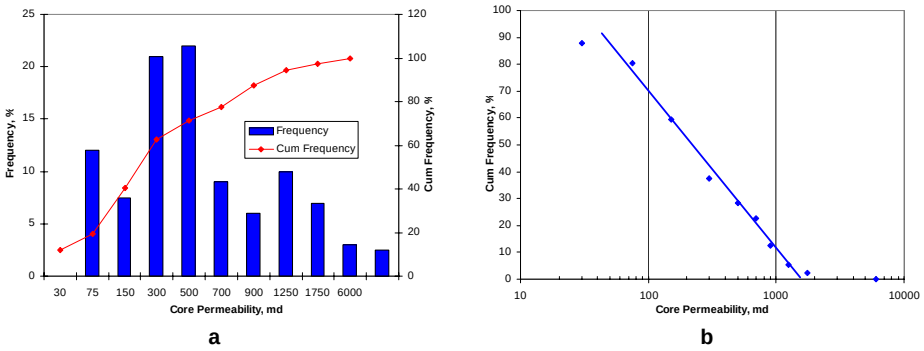

Fig. 14—Core permeability (a) histogram and (b) cumulative distribution.

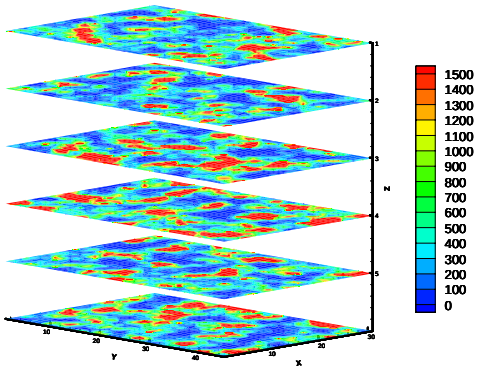

Fig. 15—Initial permeability distribution for the Ranger field case.

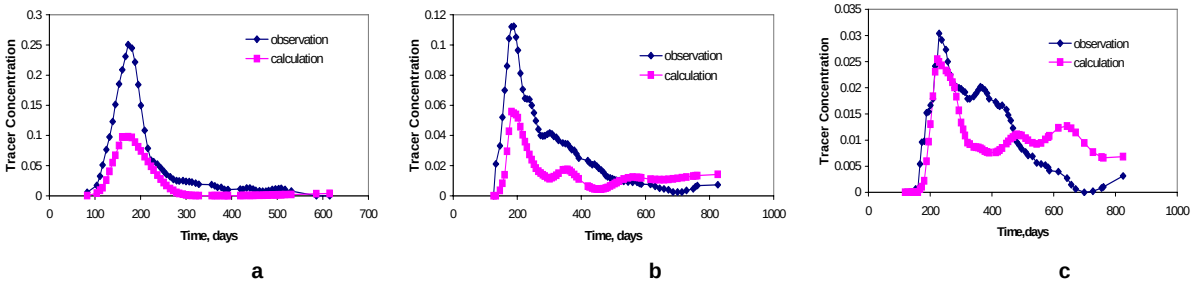

Fig. 16—NaSCN tracer response after travel-time inversion at (a) Well 40, (b) Well 37, and (c) Well 39.

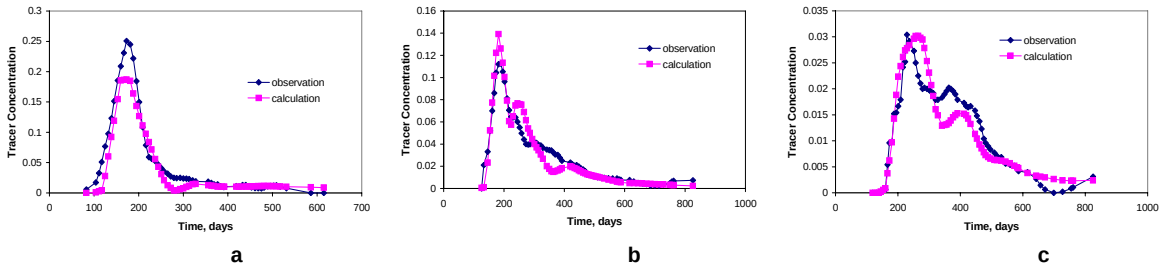

Fig. 17—NaSCN tracer response after generalized travel-time inversion at (a) Well 40, (b) Well 37, and (c) Well 39.

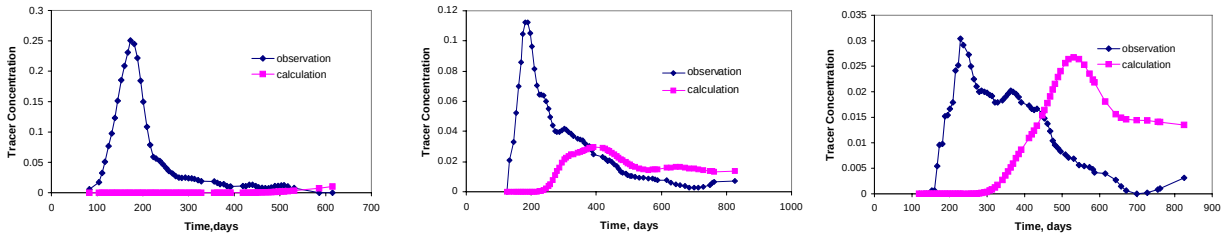

Fig. 18—NaSCN tracer response after direct amplitude inversion at (a) Well 40, (b) Well 37, and (c) Well 39.

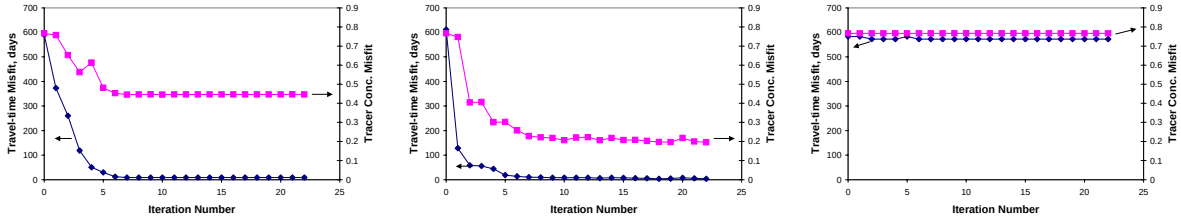

Fig. 19—Travel-time and tracer concentration misfit for (a) travel-time inversion, (b) generalized travel-time inversion, and (c) amplitude inversion.

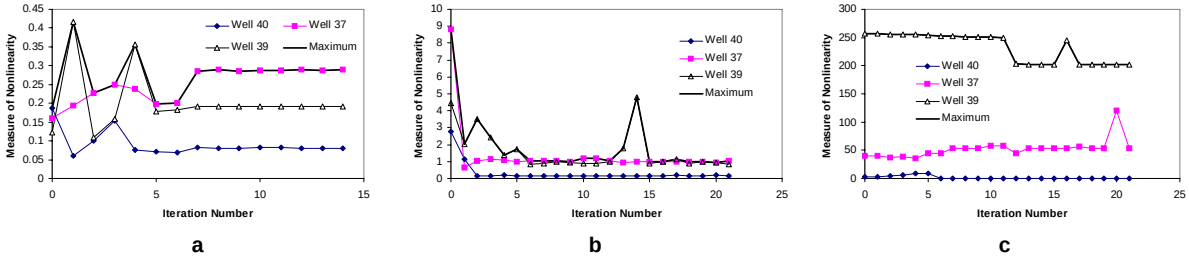

Fig. 20—Measure of nonlinearity for (a) travel-time inversion, (b) generalized travel-time inversion, and (c) amplitude inversion.

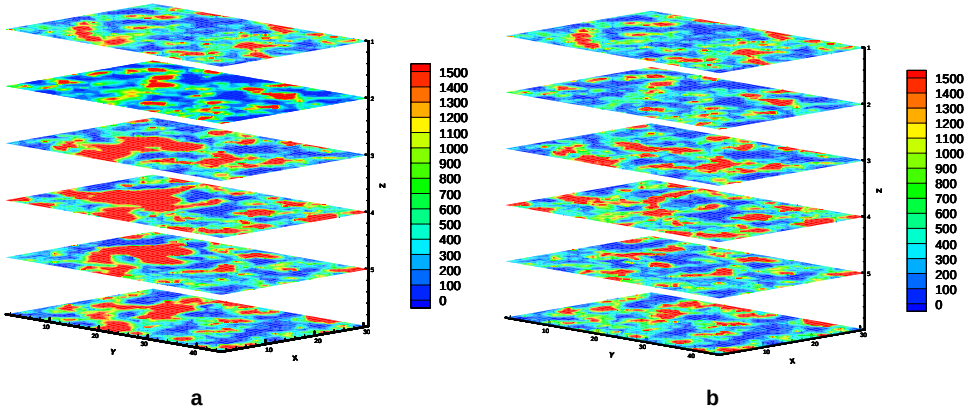

Fig. 21—Derived permeability field after NaSCN concentration match by (a)generalized travel-time inversion and (b) travel-time inversion.

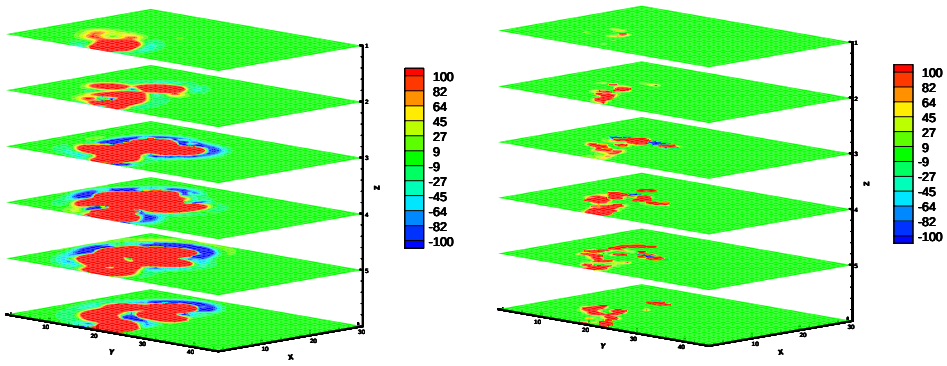

a b

Fig.22—Permeability change after (a) gereralized travel-time match and (b) travel-time match.

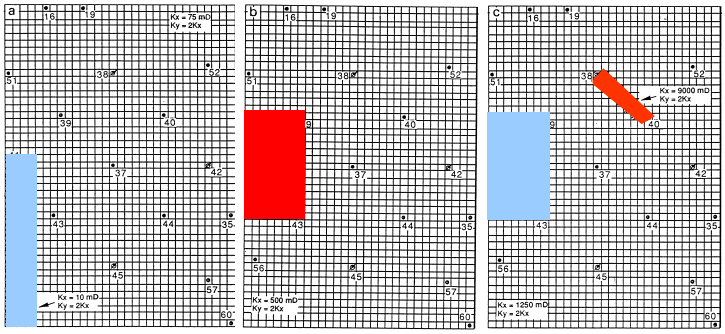

Fig. 23—Permeability multipliers for Layers 1, 2, and 3 from the finite-difference history match (Allison *et al.*[26]).

RESULTS AND DISCUSSION: PART II

Streamline Simulation of Water Injection in Naturally Fractured Reservoirs

Introduction

Streamline-based flow simulation has experienced rapid development and industry acceptance in recent years. The approach has been shown to be highly efficient for modeling fluid flow in large, geologically complex systems where the dominant flow patterns are governed by well positions and heterogeneity.[3-6] Streamline simulation has been applied successfully to a wide range of reservoir engineering problems such as ranking geological models[5,6], 'upscaling' from fine-scale models[7], well- allocation factors and pore volumes[5], integration of water-cut and tracer data into reservoir description[8], and history matching[5,8]. The streamline approach provides sub-grid resolution and minimizes numerical dispersion and grid orientation effects compared to conventional finite-difference methods. Also, it offers efficient use of memory and high computational speed.

Until recently[1,2] streamline simulators have been limited to single-porosity system and thus, are not able to explicitly account for the differences in the matrix/fracture transport and more importantly, matrix/fracture exchange mechanisms that can play an importantly role in naturally fractured systems. A common way to circumvent this limitation is to use the dual media approach whereby the matrix and fractures are treated as separate continua throughout the reservoir.[1,2,9,10] The fracture system is typically associated with high permeabilities and low effective porosities whereas the matrix system is assigned low permeabilitites and high porosities. Thus, fluid flow occurs mostly in fracture system and the matrix serves primarily as fluid storage. Additionally, the matrix and the fracture system interact through exchange terms that depend on the differences in fluid pressure between the two systems. Such matrix-fracture exchange is typically modeled using 'transfer functions'.[9,10]

Several authors have studied the matrix-fracture interactions using experimental and theoretical means. Both capillary and gravitational forces can play important role in determining the matrix-fracture exchange rate. Kazemi *et al*.[9] introduced the first multiphase transfer function. Many authors[10,11,12] have reported successful modeling of fluid flow in fractured systems using this type of transfer functions. In this study, we will refer to such transfer functions as the conventional transfer function (CTF). Sonier *et al*.[13] and Litvak[14] modified the CTF by including the gravitational effects from partially water-filled fractures. When water imbibition is the predominant mechanism for displacing oil from the matrix, empirical transfer functions (ETF) have been used to describe the matrix-fracture exchange mechanisms[15-19]. Such empirical models are conceptually simple and can be calibrated against laboratory experiments. Also, these models can be coupled to Buckley-Leverett equation through a fast convolution to describe displacement in fractures surrounded by matrix block. In our streamline implementation, we will utilize both CTF and ETF to describe flow in naturally fractured systems.

Our objective in this paper is to present a streamline-based approach for modeling fluid flow and transport in naturally fractured reservoirs. We extend the streamline approach to fractured media by deriving the saturation equations for dual porosity dual permeability systems using the streamline time of flight as the spatial coordinate. In the absence of matrix flow, the approach reduces to the commonly used dual porosity system of equations and is identical to the

formulation recently proposed by Di Donato et al.[2] We discuss numerical implementation of the saturation equations within the framework of the current streamline models and validate our results by extensive comparison with a commercial finite- difference simulator under fracture flow conditions.

Mathematical Formulation

Fluid Flow Equations in Naturally Fractured Systems. In naturally fractured reservoirs fluids generally exist in two systems (1) the rock matrix, which provides the main bulk of the reservoir volume and storage and (2) the highly permeable rock fractures which provide the main path for fluid flow. If the fracture system is assumed to provide the main path and storage for fluid, i.e. it is not connected to the matrix system, this can be considered as a single-porosity single-permeability system (SPSP) as in **Fig. 1**. On the other hand, if we assume that the fluid flow in the reservoir takes place primarily through the fracture networks while the matrix-blocks are linked only through the fracture system, this could be regarded as a dual-porosity single-permeability system (DPSP) as in **Fig. 2**. In addition, if there is flow between matrix-blocks, this can be considered as a dual-porosity dual-permeability system (DPDP) as in **Fig. 3**. Clearly, the dual-porosity dual-permeability system is the most general approach to modeling fractured reservoirs and will reduce to the dual-porosity system when flow in the matrix block is assumed to be negligible. The applicability and limitations of these approaches have been discussed by Dean and Lo.[10]

Consider two-phase incompressible flow in a DPDP system. The governing equations that describe fluid flow consist of two sets of equations[9,10,11,12]. The first set deals with the fluid transport in the fractured system, **Eq. 1**, and the second set deals with the fluid transport in the matrix system, **Eq. 2**. Each set consists of one equation for each phase.

$$\begin{aligned}
\nabla \cdot \vec{\vec{k}}_f \cdot \left(\lambda_{of} \nabla P_{of} + \lambda_{ogf} \nabla D\right) - \Gamma_o + q_{of} &= \phi_f \frac{\partial S_{of}}{\partial t} \\
\nabla \cdot \vec{\vec{k}}_f \cdot \left(\lambda_{wf} \nabla P_{wf} + \lambda_{wgf} \nabla D\right) - \Gamma_w + q_{wf} &= \phi_f \frac{\partial S_{wf}}{\partial t}
\end{aligned} \tag{1}$$

$$\begin{aligned}
\nabla \cdot \vec{\vec{k}}_m \cdot \left(\lambda_{om} \nabla P_{om} + \lambda_{ogm} \nabla D\right) + \Gamma_o + q_{om} &= \phi_m \frac{\partial S_{om}}{\partial t} \\
\nabla \cdot \vec{\vec{k}}_m \cdot \left(\lambda_{wm} \nabla P_{wm} + \lambda_{wgm} \nabla D\right) + \Gamma_w + q_{wm} &= \phi_m \frac{\partial S_{wm}}{\partial t}
\end{aligned} \tag{2}$$

The subscripts *m* and *f* represent matrix and fracture system respectively. The mobility of oil and water in each system, λ_o and λ_w, are defined, as follows:

$$\lambda_o = \frac{k_{ro}}{\mu_o}$$
$$\lambda_w = \frac{k_{rw}}{\mu_w} \tag{3}$$

The gravity terms, λ_{og} and λ_{wg}, are defined, as follows:

$$\lambda_{og} = \frac{k_{ro}\rho_o g}{\mu_o}$$
$$\lambda_{wg} = \frac{k_{rw}\rho_w g}{\mu_w} \tag{4}$$

The transfer terms, Γ_o and Γ_w, represent the volumetric oil and water rate transferred between fracture and matrix systems. Clearly, these transfer terms describe the matrix-fracture interactions and we will discuss them in a later section.

Streamline Modeling of Fractured Reservoirs. The underlying principle of streamline simulation is to first trace streamlines through the reservoir using a velocity field and then to transport fluid along these streamlines. In this section, we first discuss the formulation of the pressure equations that form the basis for the velocity fields and streamline trajectories. Next, we transform the saturation equations to the streamline time of flight coordinates to facilitate analytical and numerical calculations of saturations along streamlines.

Pressure Equation for Tracing Streamlines. The first step toward tracing streamlines is to generate a pressure field by solving the pressure equation using a finite difference or finite element scheme. The pressure field can then be converted to a total-velocity field using Darcy's law. Once the total-velocity field is generated, streamlines can be traced easily because they are locally tangential to the total-velocity.[3-6] If we neglect capillarity and add the water-oil equations for each system, we obtain the pressure equations for the fracture and matrix systems as follows:

$$\nabla \cdot \vec{\vec{k}}_f \cdot \left(\lambda_{tf} \nabla P_f + \lambda_{gf} \nabla D\right) - \Gamma_t = -q_{sf} \tag{5}$$

$$\nabla \cdot \vec{\vec{k}}_m \cdot \left(\lambda_{tm} \nabla P_m + \lambda_{gm} \nabla D\right) + \Gamma_t = -q_{sm} \tag{6}$$

where

$$\lambda_t = \lambda_o + \lambda_w$$
$$\lambda_g = \lambda_{og} + \lambda_{wg} \tag{7}$$

The total transfer term, Γ_t, is given as:

$$\Gamma_t = \Gamma_o + \Gamma_w \tag{8}$$

Because we have flow in both matrix and fracture systems in the DPDP formulation, we have to trace streamlines in both the systems. **Eq.5** and **Eq.6** together provide the pressure fields in these systems.

In the DPSP approach, we assume no flow between matrix-blocks. So, the flow and sink terms in **Eq.6** will vanish. **Eq.6** can be written as:

$$\Gamma_t = 0 \tag{9}$$

If we combine **Eq.8** and **Eq.9**, we conclude that the transfer terms, Γ_o and Γ_w, have equal magnitudes and opposite directions.

$$\Gamma_o = -\Gamma_w \tag{10}$$

Because there is no flow in the matrix system, streamlines will be generated and traced only in the fracture system using the following pressure equation:

$$\nabla \cdot \vec{\vec{k}}_f \cdot \left(\lambda_{tf} \nabla P_f + \lambda_{gf} \nabla D\right) = -q_{sf} \tag{11}$$

It is important to point out that the transfer term doesn't appear in the pressure equation. Thus, the transfer term will not affect streamline trajectories and the trajectory computations for the DPSP system is identical to that of a conventional SPSP streamline simulator. However, for the DPDP system, the pressure distribution in the matrix and the fracture system need to be solved for simultaneously in the same manner as in conventional finite-difference simulation and the details have been discussed by Dean and Lo.[10]

Transformation of Saturation Equations to Streamline Coordinates. The equations that describe the evolution of water saturation in a DPDP system (**Eqs. 1** and **2**) can be re-written as follows:

$$\phi_f \frac{\partial S_{wf}}{\partial t} + \vec{u}_{tf} \cdot \nabla f_{wf} + f_{wf} \nabla . \vec{u}_{tf} + \nabla \cdot \vec{G}_f + \Gamma_w = 0 \tag{12}$$

$$\phi_m \frac{\partial S_{wm}}{\partial t} + \vec{u}_{tm} \cdot \nabla f_{wm} + f_{wm} \nabla . \vec{u}_{tm} + \nabla \cdot \vec{G}_m - \Gamma_w = 0 \tag{13}$$

In **Eq.12** and **Eq.13** f_w is the fractional flow of water given by

$$f_w = \frac{\lambda_w}{\lambda_t} \tag{14}$$

and G represents the gravity term defined as,

$$\vec{G} = k \cdot \frac{\lambda_w \lambda_o}{\lambda_t} (\rho_o - \rho_w) g \nabla D \tag{15}$$

To write **Eq.12** and **Eq.13** in terms of streamline time of flight (TOF), the following coordinate transformation is applied[3-6,20]

$$\vec{u}_t \cdot \nabla = \phi \frac{\partial}{\partial \tau} \tag{16}$$

where the TOF, τ, is the time required by a neutral tracer to travel along the streamline, ψ

$$\tau = \int_{along\ \psi} \frac{\phi}{\|u_t\|} \partial \zeta \tag{17}$$

The saturation equations for fracture and matrix systems now reduce to the following

$$\frac{\partial S_{wf}}{\partial t} + \frac{\partial f_{wf}}{\partial \tau_f} + f_{wf} \nabla . \vec{u}_{tf} + \frac{\nabla \cdot \vec{G}_f}{\phi_f} + \frac{\Gamma_w}{\phi_f} = 0 \tag{18}$$

$$\frac{\partial S_{wm}}{\partial t} + \frac{\partial f_{wm}}{\partial \tau_m} + f_{wm} \nabla . \vec{u}_{tm} + \frac{\nabla \cdot \vec{G}_m}{\phi_m} - \frac{\Gamma_w}{\phi_m} = 0 \tag{19}$$

Eq.18 and **Eq.19** can be used to solve for saturation along the streamlines in fracture and matrix systems in a DPDP model. Notice that the terms $f_{wf} \nabla . \vec{u}_{tf}$ and $f_{wm} \nabla . \vec{u}_{tm}$ represent additional cross-flux in the matrix and the fracture system in the DPDP model. Also, $\vec{u}_{tf}$ and $\vec{u}_{tm}$ may not be defined over the entire spatial domain. Under such conditions, we revert back to the total velocity (matrix + fracture) for tracing streamlines.

For the DPSP model the flow in the matrix is ignored and we will trace streamlines only in the fracture system. So, the main transport equation is the saturation equation in the fracture system, **Eq.18**. In addition, the fracture velocity represents the total system velocity which is a conserved quantity, that is $\nabla . \vec{u}_{tf} = 0$. The saturation equations for the fracture and matrix systems for the DPSP model now reduce to the following

$$\frac{\partial S_{wf}}{\partial t}+\frac{\partial f_{wf}}{\partial \tau_f}+\frac{\nabla\cdot\vec{G}_f}{\phi_f}+\frac{\Gamma_w}{\phi_f}=0 \tag{20}$$

$$\Gamma_w=\phi_m\frac{\partial S_{wm}}{\partial t} \tag{21}$$

Finally, for the SPSP system, both fluid flow and storage are assumed to be in the fracture system only and the interaction with the matrix is not included. The saturation equation reduces to the one currently used in conventional streamline simulators.

Matrix-Fracture Transfer Functions

In the previous sections we have discussed the derivation of the saturation equations for the DPDP and the DPSP systems in terms of streamline TOF coordinates. We now focus on describing the interactions between the matrix and the fracture systems through the use of transfer functions. A detailed discussion of several transfer functions and their implementation in streamline simulation can be found in Di Donato et al.[2] The conventional transfer function (CTF), which is the most common form of transfer function used in fractured reservoir simulations, has the following form for water and oil phases[9,10,11,12]:

$$\Gamma_w=F_s k_m \lambda_{wmf}\left(P_{wf}-P_{wm}\right) \tag{22}$$

$$\Gamma_o=F_s k_m \lambda_{omf}\left(P_{of}-P_{om}\right) \tag{23}$$

where

$$\begin{aligned} P_{wf}&=P_{of}-P_{cf}\\ P_{wm}&=P_{om}-P_{cm}\end{aligned} \tag{24}$$

In **Eqs. 22** and **23**, we ignore the gravitational forces and assume a pseudo-steady state behavior in the matrix block. Also, the mobility ratios, λ_{wmf} and λ_{omf}, represent the upstream mobility between fracture and matrix systems and F_s is a shape factor that defines the connectivity between the matrix block and the surrounding fractures.

Note that **Eq.22** and **Eq.23** are functions of phase saturation and pressure. In DPSP system, the dependency of these equations on the phase pressure can be eliminated using **Eq.9** and the capillary pressure relations as follows,

$$\left(P_{of}-P_{om}\right)=\frac{\lambda_{wmf}}{\lambda_{omf}+\lambda_{wmf}}\left(P_{cf}-P_{cm}\right) \tag{25}$$

By substituting **Eq.25** into **Eq.23**, we arrive at the following transfer function for the DPSP streamline simulator,

$$\Gamma_w = F_S k_m \frac{\lambda_{wmf}\lambda_{omf}}{\lambda_{omf} + \lambda_{wmf}}\left(P_{cm} - P_{cf}\right) \tag{26}$$

For a rectangular matrix block with all sides exposed to imbibing water, the shape factor has the following form[9]:

$$F_s = 4\left(\frac{1}{l_x^2} + \frac{1}{l_y^2} + \frac{1}{l_z^2}\right) \tag{27}$$

When countercurrent imbibition is the dominant force for displacing oil from the matrix, empirical transfer functions (ETF) have also been used to describe the matrix-fracture exchange in DPSP systems. The advantage of the ETF is that we can derive an analytical solution to the Buckley-Leverett displacement for saturation calculations in the fracture system.[19] We will utilize the analytical solution to validate our numerical computations of saturations along streamlines. In the ETF, the cumulative oil recovery from a matrix-block surrounded by water can be approximated by the following[21]

$$Q = Q_\infty\left(1 - e^{-\omega t}\right) \tag{28}$$

where ω is a rate constant that is defined as the reciprocal of the time required by the matrix-block to expel 63% of the recoverable oil[19]. This constant can also be determined empirically from laboratory experiments. By differentiating **Eq.28**, the volumetric rate of water transferred from the fracture system to the matrix-blocks is given by:

$$\Gamma_{w@S_w=1.0} = Q_\infty \omega e^{-\omega t} \tag{29}$$

Eq.29 assumes 100% water saturation in the fracture system. This implies that the oil transferred from the matrix is rapidly carried away by the water flowing in the fracture system. To account for changing water saturation in the fracture, a fast convolution can be utilized as suggested by DeSwaan[17]:

$$\Gamma_w = Q_\infty \omega \int_0^t e^{-\omega(t-\varepsilon)} \frac{\partial S_{wf}(\varepsilon)}{\partial \varepsilon} \partial\varepsilon \tag{30}$$

So far we have assumed that the primary recovery mechanism is counter-current imbibition in the DPSP system. This applies when the vertical dimension, l_z of the matrix-block is small. If l_z is large, a gravity head between the matrix-block and the fracture system also will cause fluid movement. **Fig. 4** illustrates the gravity head concept in a single matrix-block surrounded by fractures. If gravity is included in the transfer function, the volumetric oil and water rate can be expressed as[13,14]

$$\Gamma_w = F_s k_m \lambda_{wmf} \left(P_{of} - P_{om} - P_{cf} + P_{mf} + \frac{\Delta P_{gh}}{2} \right)$$
$$\Gamma_o = F_s k_m \lambda_{omf} \left(P_{of} - P_{om} - \frac{\Delta P_{gh}}{2} \right) \tag{31}$$

where

$$\Delta P_{gh} = l_z \left(S_{wnf} - S_{wnm} \right)\left(\rho_w - \rho_o \right) g$$
$$S_{wnf} = \frac{S_{wf} - S_{wcf}}{1 - S_{orf} - S_{wcf}} \tag{32}$$
$$S_{wnm} = \frac{S_{wm} - S_{wcm}}{1 - S_{orm} - S_{wcm}}$$

and S_{wnf}, S_{wnm} are the normalized water saturation in the fracture system and the matrix-block**.**

Finally, utilizing **Eq.9**, the volumetric water transfer rate between fracture and matrix system including gravity is

$$\Gamma_w = F_s k_m \frac{\lambda_{wmf} \lambda_{omf}}{\lambda_{omf} + \lambda_{wmf}} \left(P_{cm} - P_{cf} + \Delta P_{gh} \right) \tag{33}$$

Numerical Solution To Saturation Equations

Dual-Porosity Dual-Permeability System. In the DPDP system, we assume that fluid flow occurs both in the matrix and fracture systems. Thus, we need to generate streamlines for both the systems and compute water saturation along these streamlines. For clarity, we will ignore gravity and cross-flux terms in this discussion. Both of these terms can be included as part of the 'corrective step' in the numerical solution discussed later in this section. Now **Eq.18** and **Eq.19** lead to the following saturation equations for the matrix and fracture systems,

$$\frac{\partial S_{wf}}{\partial t} + \frac{\partial f_{wf}}{\partial \tau_f} + \frac{\Gamma_w}{\phi_f} = 0 \tag{34}$$

$$\frac{\partial S_{wm}}{\partial t} + \frac{\partial f_{wm}}{\partial \tau_m} - \frac{\Gamma_w}{\phi_m} = 0 \tag{35}$$

In general, the streamlines in the fracture and matrix systems will be quite different and this results in difficulties in solving **Eq.34** and **Eq.35** because of their coupling through the transfer terms. We circumvent these difficulties using an operator splitting procedure.[22,23] The underlying idea here is to represent the time derivative in **Eq.34** and **Eq.35** as a convective time step followed by a corrective time step.[24]

$$\begin{aligned} \frac{\partial S_{wf}}{\partial t} &\rightarrow \frac{\partial S_{wf}}{\partial t_1} + \frac{\partial S_{wf}}{\partial t_2} \\ \frac{\partial S_{wm}}{\partial t} &\rightarrow \frac{\partial S_{wm}}{\partial t_1} + \frac{\partial S_{wm}}{\partial t_2} \end{aligned} \tag{36}$$

The convective time-step includes the saturation evolution along the streamlines because of the viscous forces. The corrective time-step incorporates the transfer term between the fracture and the matrix systems.

Thus, the convective terms are given as,

$$\frac{\partial S_{wf}}{\partial t_1} + \frac{\partial f_{wf}}{\partial \tau_f} = 0 \tag{37}$$

$$\frac{\partial S_{wm}}{\partial t_1} + \frac{\partial f_{wm}}{\partial \tau_m} = 0 \tag{38}$$

and the corrective terms are given as,

$$\frac{\partial S_{wf}}{\partial t_2} + \frac{\Gamma_w}{\phi_f} = 0 \tag{39}$$

$$\frac{\partial S_{wm}}{\partial t_2} - \frac{\Gamma_w}{\phi_m} = 0 \tag{40}$$

The convective part can be solved using similar procedures as in single-porosity streamline simulation.[3-6] The streamline saturation resulting form the convective calculations are then mapped back onto the grid and used as initial conditions for the corrective step. The corrective equations accounting for the exchange are then solved on the grid-blocks.

We used an explicit finite-difference scheme to discretize the convective term in the fracture system, **Eq.37**

$$S_{wf,i}^{n+1} - S_{wf,i}^{n} = -\Delta t \frac{f_{wf,i}^{n} - f_{wf,i-1}^{n}}{\Delta \tau_f} \tag{41}$$

Note that *i*-index represents nodes along the streamline. In a similar way, we can discretize the convective term in the matrix system.

We can use the same numerical scheme for the corrective term for the fracture system, **Eq.39**.

$$S_{wf,i}^{n+1} - S_{wf,i}^{n} = -\Delta t \left\{ \begin{array}{l} \left(\frac{F_s k_m}{\phi_f} \right)_i \left(\frac{\lambda_{wmf} \lambda_{omf}}{\lambda_{omf} + \lambda_{wmf}} \right)_i^n \\ \left(P_{cm} - P_{cf} \right)_i^n \end{array} \right\} \tag{42}$$

In **Eq.42**, *i*-index represents the grid-block numbers. Similarly, the same formulation can be used for the corrective term for the matrix system, **Eq.40**. An iterative calculation of matrix-fracture saturations will probably make the approach more robust but is likely to be more time consuming.[2] For example cases presented here, we did not see the need for such an iterative procedure.

As mentioned before, the fracture and matrix saturations from the convective step are mapped onto the grid and used as an initial condition for the corrective step. The following weighted average is used to map fracture saturation,

$$S_{wf,grid} = \frac{\sum_{i=1}^{nsl} S_{wf,i} \Delta \tau_{f,i}}{\sum_{i=1}^{nsl} \Delta \tau_{f,i}} \tag{43}$$

where *nsl* is the number of streamlines passing through a grid-block, $\Delta\tau$ is the time of flight across the grid-block. We use the same averaging scheme to map the matrix saturation back onto the grids.

Dual-Porosity Single-Permeability System. In the DPSP system, streamlines will be generated and traced only through the fracture system. So the convective and transfer terms in the saturation equation can be solved together in a coupled fashion along the streamline and no time-splitting is required. Using the CTF the saturation equation in the fracture system will have the following numerical form:

$$S_{wf,i}^{n+1} - S_{wf,i}^{n} = -\Delta t \left\{ \begin{array}{l} \dfrac{f_{wf,i}^{n} - f_{wf,i-1}^{n}}{\Delta \tau_f} + \\ \left(\dfrac{F_s k_m}{\phi_f} \right)_i \left(\dfrac{\lambda_{wmf} \lambda_{omf}}{\lambda_{omf} + \lambda_{wmf}} \right)_i^n \\ \left(P_{cm} - P_{cf} \right)_i^n \end{array} \right\} \tag{44}$$

Matrix saturation can be calculated from the mass conservation equation, **Eq.21**. The explicit numerical form of this equation is

$$S_{wm,i}^{n+1} - S_{wm,i}^{n} = -\Delta t \left\{ \begin{array}{l} \left(\dfrac{F_s k_m}{\phi_f} \right)_i \left(\dfrac{\lambda_{wmf} \lambda_{omf}}{\lambda_{omf} + \lambda_{wmf}} \right)_i^n \\ \left(P_{cm} - P_{cf} \right)_i^n \end{array} \right\} \tag{45}$$

If the ETF is used in the saturation equations, the fracture saturation equation will have the following numerical form:

$$\begin{aligned} S_{wf,i}^{n+1} - S_{wf,i}^{n} &= \left\{ \begin{array}{l} -\left(\dfrac{1}{\Delta t} + \dfrac{Q_\infty \omega}{\phi_f} e^{-\omega \Delta t} \right)^{-1} \\ \left(\dfrac{f_{wf,i}^{n} - f_{wf,i-1}^{n}}{\Delta \tau_f} + \right. \\ \left. \dfrac{Q_\infty \omega}{\phi_f} SUM^{n-1} e^{-\omega \Delta t} \right) \end{array} \right\} \\ SUM^{n-1} &= \left[SUM^{n-2} + \left(S_{wf,i}^{n} - S_{wf,i}^{n-1} \right) \right] e^{-\omega \Delta t}, n \geq 1 \\ SUM^{n-1} &= 0 \end{aligned} \tag{46}$$

where we have used a difference scheme proposed by Kazemi *et al*.[19] to estimate the convolution term in the ETF. Matrix saturation equation, **Eq.21**, can be solved numerically using similar procedure

$$S_{wm,i}^{n+1} - S_{wm,i}^{n} = -\Delta t \left(\frac{Q_\infty \omega}{\phi_f} SUM^{n-1} e^{-\omega \Delta t} \right) \tag{47}$$

Fracture system water saturation along streamlines can be mapped back onto the grid using **Eq.43**. Matrix saturation along streamlines can be mapped onto the grid-blocks using the following arithmetic average

$$S_{wm,grid} = \frac{1}{nsl}\sum_{i=1}^{nsl} S_{wm,i} \tag{48}$$

If **Eq.46** were used to compute the saturation evolution, the summation term, SUM^{n-1}, is mapped onto the grid-block for the next time update calculations. A weighted average can be used to map the summation term.

$$SUM_{grid}^{n-1} = \frac{\sum_{i=1}^{nsl} SUM_i^{n-1}\Delta\tau_{f,i}}{\sum_{i=1}^{nsl}\Delta\tau_{f,i}} \tag{49}$$

Validating Numerical Solution of the Saturation Equation with ETF. The saturation equation with the ETF for displacement in the fracture can be written as

$$\begin{aligned} &\frac{\partial S_{wf}}{\partial t} + H\frac{\partial S_{wf}}{\partial \tau_f} + \frac{Q_\infty}{\phi_f}\omega\int_0^t e^{-\omega(t-\varepsilon)}\frac{\partial S_{wf}(\varepsilon)}{\partial \varepsilon}\partial\varepsilon = 0 \\ &H = \frac{\partial f_{wf}}{\partial S_{wf}} \end{aligned} \tag{50}$$

with the following initial and boundary conditions:

$$\begin{aligned} &S_{wf}(\tau_f, 0) = 0 \\ &S_{wf}(0, t) = 1 \end{aligned} \tag{51}$$

For constant H, we can solve **Eq.50** analytically for saturation distribution in the fracture.[19] This allows us to validate our numerical computations of saturations along streamlines by comparing the results from the numerical and analytical solutions. The example used to perform this comparison involves water injection in a heterogeneous quarter five-spot pattern. **Fig. 5** shows a 2D permeability field which represents the fracture distribution. Other parameters are presented in **Table 1**. **Fig. 6** shows the fracture-water saturation at two different times for the numerical and the analytical solutions. The results are in excellent agreement which indicates the validity of the numerical solution of the saturation equation.

RESULTS AND DISCUSSION

In this section, we discuss the implementation of the DPSP and DPDP streamline formulation using several examples involving waterflood in five-spot and nine-spot patterns. We examine the effects of the transfer term on the saturation evolution and production histories and compare our results with a commercial DPSP/DPDP simulator viz. ECLIPSE.[25]

Dual-Porosity Single-Permeability System without Gravity Effects. Here we use the CTF without the gravity terms and compare the results from the DPSP streamline simulator with those from the fully implicit DPSP ECLIPSE in terms of water cut and recovery histories and water saturation distributions. The comparison is based on two examples involving waterflood in homogeneous and heterogeneous quarter five spot patterns.

Homogenous Case: Quarter Five Spot Pattern. This example was first presented by Kazemi *et al*.[9] and later used by Thomas *et al*.[12]. **Table 2** shows the reservoir parameters. **Figs. 7** and **8** show relative permeability and capillary pressure curves used in this example. Streamlines for this case are shown in **Fig. 9**. To start with, we investigate the impact of the transfer function on the streamline simulation results. **Figs. 10** and **11** show the water saturation map and the water cut history from the DPSP streamline simulator with and without the CTF. The case without CTF represents the conventional single porosity streamline formulation. Here the water cut is higher and the water saturation advances faster because the interaction with the matrix system is not included. Next, we compare the DPSP streamline simulation to the DPSP ECLIPSE. **Fig. 12** shows water cut and recovery histories from the two simulators indicating an excellent agreement. **Figs. 13** and **14** show the water saturation in fracture and matrix system at two different times from both the simulators. The saturation maps are clearly in good agreement.

Heterogeneous Case: Quarter Five Spot Pattern. We now extend our discussion to a heterogeneous quarter five spot case. The parameters used here are the same as in **Table 2**, except for the fracture permeability. The permeability field is the one shown in **Fig. 5**. **Fig. 15** shows the water saturation in the fracture system with and without the transfer function. As before, the dual porosity formulation slows down the water advancement in the fracture because of the interaction with the matrix. **Fig. 16** compares the water cut response indicating the significance of the dual porosity formulation. The streamline trajectories are shown in **Fig. 17** and reflect the permeability heterogeneity in the fracture system. The water cut and recovery histories for the DPSP streamline simulator and the DPSP ECLIPSE are in good agreement as shown in **Fig. 18**. Similar agreements are found in the fracture and matrix water saturation from both simulators as illustrated in **Fig. 19** and **Fig. 20**. However, the saturation fronts from ECLIPSE are somewhat smeared because of numerical dispersion. The streamline saturation calculations are decoupled from the simulation grid and the effects of permeability heterogeneity on the saturation front are more prominent here.

Dual-Porosity Single Permeability System with Gravity Effects. In this section we examine the impact of gravity terms in the transfer function and again, compare our results with DPSP ECLIPSE using two examples: a homogenous quarter five-spot pattern, and a heterogeneous nine-spot pattern.

Homogenous Case: Quarter Five Spot Pattern. **Table 3** presents the reservoir parameters, and **Fig. 7** and **Fig. 8** show relative permeability and capillary pressure curves used in this example. **Fig. 21** presents the water cut histories for three scenarios using ECLIPSE. These are: (1) no transfer function, (2) a transfer function including the imbibition only, and (3) a transfer function including the gravity and imbibition. As before, the simulation run without transfer function shows the highest water cut response and the earliest breakthrough time. The simulation run with imbibition transfer function shows the lowest water cut response in this case. Including the gravity effects tend to reduce the recovery from the matrix for these examples. **Fig. 22** shows that the DPSP streamline simulator predicts the same behavior as ECLIPSE. In **Fig. 23**, we have superimposed the results indicating the close agreement between the simulators.

Heterogeneous Case: Nine Spot Pattern. We now extend the discussion in the previous section to a heterogeneous nine spot example. The fracture permeability field is the same 2D permeability map shown in **Fig. 5**. **Table 4** presents the reservoir parameters used in this example. We used the same relative permeability and capillary curves as the previous examples. **Fig. 24** shows the streamline pattern in the reservoir. The water cut and recovery histories for the DPSP streamline simulator and the DPSP ECLIPSE are almost identical as shown in **Fig. 25**. For individual wells, the water cut and recovery histories from both simulators are also in good agreement as shown in **Fig. 26**. Fracture and matrix water saturation for both the simulators also show a good match as illustrated in **Fig. 27**. **Fig. 27** again shows the effects of numerical dispersion in the ECLIPSE results leading to smearing of sharp fronts in the saturation map.

Dual-Porosity Dual-Permeability System. We now discuss applications of the dual porosity dual-permeability streamline formulation for modeling fractured systems. Such a model is appropriate when the contrast between the matrix and the fracture permeability is not large enough to justify a DPSP approach.[10] Unlike the previous results, now flow occurs both in the matrix and fracture systems and streamlines need to be generated for both the systems. The saturation advancement along streamlines is carried out using the operator splitting approach as outlined before. We will compare our results with DPDP ECLIPSE for water injection in homogeneous and heterogeneous nine-spot patterns.

Homogeneous Case: Nine-spot Pattern. The reservoir parameters used here are presented in **Table 4** except for the matrix permeability which was increased to 100 md to allow more flow. The fracture permeability used in this example was 500 md. The relative permeability and capillary curves are shown in **Fig. 7** and **Fig. 8**. Recall that in the operator splitting approach, first a time interval is selected during which we update the saturation using the convective term followed by a second update using a corrective step that includes the transfer term. We will refer to this time interval as 'splitting time-step' (SPT). During the SPT, we solve the convective terms using a 'convective time-step' (CVT). Once the convective terms are solved along

streamlines, fracture and matrix water saturations are mapped back onto the grid block. Now the corrective equations can be solved on the grid for the same SPT using a 'corrective time-step' (CRT). The choice of the CVT and CRT depends on the stability of the numerical solution of the convective and corrective terms. The choice of the SPT depends, among others, on transverse fluxes arising from mobility and unsteady state effects and some guidelines are provided by Osako et al.[24]

To start with we choose SPT equal to 250 days. **Fig. 28** shows the water cut response from two producing wells during the convective step for each SPT interval. On the same plot, we indicated the water cut responses after the corrective step. The water cut response shows close agreement with the DPDP ECLIPSE after we incorporate the corrective terms in the saturation calculations. These results clearly indicate the validity of the operator splitting approach. We also examined the sensitivity of the results on the split-time interval using a longer SPT of 500 days. **Fig. 29** shows that this choice of time step clearly leads to erroneous results. However, detailed investigation of error estimates or stability criterion was beyond the scope of this study and remains an area of future research. **Fig. 30** presents a comparison between the DPDP Streamline simulator and ECLIPSE in terms of water saturation distribution after 1000 days. The SPT was chosen to be equal to 250 days. Both simulators show comparable results.

Heterogeneous Case: Nine Spot Pattern. We now extend the discussion for a heterogeneous case with the fracture permeability field in **Fig. 5**. A comparison between the DPDP streamline simulator and the DPDP ECLIPSE in terms of water cut response shows good agreement for all eight producers as shown in **Fig. 31**. Fracture and matrix water saturation from both the simulators also show good match as illustrated in **Fig. 32**. As before, some impact of grid orientation and numerical smearing are evident in the ECLIPSE results.

CPU Time and Scaling. In this section, we compare the CPU time and its scaling behavior for DPSP streamline simulation, fully implicitly DPSP ECLIPSE and IMPES DPSP ECLIPSE. We performed multiple runs on a 3D homogenous case with different number of grid blocks to examine the scaling behavior of the CPU time. **Table 5** shows the parameters used to perform this task.

Fig. 33 shows the CPU time comparison. The CPU time for the IMPES DPSP ECLIPSE has a quadratic relationship with the grid-block numbers. This indicates that using this type of simulation for large models is not computationally efficient. The fully implicit DPSP shows some improvement in CPU time with a scaling exponent of 1.69. On the other, the DPSP streamline simulator CPU time increases linearly as the number of grid-block increases. The results are in agreement with the findings of Di Donato *et al*.[2] and tend to affirm that the streamline simulation will be particularly advantageous for field-scale simulation using high resolution geologic models.

Table 1- Parameters for Quarter Five Spot Example Used to Validate the Numerical Solution of the Saturation Equation with ETF.

Parameters	*Values*
Area, ft2	1,440,000
Thickness, ft	30
Injection and Production Rates, STB/Day	100
ω, 1/Day	0.001
ϕ_f	0.01
ϕ_m	0.16
S_{wcm} & S_{orm}	0.25
k_{rwf}	S_{wf}
k_{rof}	1- S_{wf}
μ_w	1
μ_o	1
k_f, *md*	10000

Table 2-Quarter Five Spot Parameters, Homogenous Case (Imbibition Only).

Parameters	*Values*
Dimension In I-Direction, ft	600
Dimension In J-Direction, ft	600
Thickness, ft	30 ft
Reservoir Grid	40 × 40×1
Injection Rates, STB/Day	210
Production Rate, STB/Day	200
k_m, *md*	1
k_f, *md*	10000
F_s, *ft2*	0.08
ϕ_f	0.01
ϕ_m	0.19
μ_w, *cp*	0.5
μ_o, *cp*	2
ρ_w, *psi/ft*	0.44
ρ_o, *psi/ft*	0.3611
P_i, *psi*	396.89

Table 3-Quarter Five Spot Pattern Parameters, Homogenous Case (Gravity and Imbibition).

Parameters	*Values*
Dimension in I-Direction, ft	2000
Dimension In J-Direction, ft	2000
Matrix-Block Thickness, l_z*, ft*	30 ft
Reservoir Grid	40 × 40×1
Injection Rates, STB/Day	400
Production Rate, STB/Day	400
k_f, *md*	500
k_m, *md*	1
F_s, ft^2	0.12
ϕ_f	0.05
ϕ_m	0.19
μ_w, *cp*	0.5
μ_o, *cp*	2
ρ_w, *psi/ft*	0.44
ρ_o, *psi/ft*	0.3611
P_i, *psi*	4000

Table 4-Nine Spot Pattern Parameters, Heterogeneous Case (Gravity and Imbibition).

Parameters	*Values*
Dimension In I-Direction, ft	2000
Dimension In J-Direction, ft	2000
Thickness, ft	30 ft
Matrix-Block Thickness, l_z*, ft*	30 ft
Reservoir Grid	41 × 41×1
Injection Rates, STB/Day	800
Production Rate for each Well, STB/Day	100
k_m, *md*	1
F_s, ft^2	0.0844
ϕ_f	0.05
ϕ_m	0.2
μ_w, *cp*	0.5
μ_o, *cp*	2
ρ_w, *psi/ft*	0.44
ρ_o, *psi/ft*	0.3611
P_i, *psi*	4000

Table 5-Quarter Five Spot Pattern Parameters, Homogenous Case, CPU Time.

Parameters	*Values*
Dimension In I-Direction, ft	1000
Dimension In J-Direction, ft	1000
Thickness, ft	100 ft
Injection Rates, STB/Day	1000
Production Rate, STB/Day	1000
k_f, *md*	500
k_m, *md*	1
F_s, ft^2	0.05
ϕ_f	0.05
ϕ_m	0.25
μ_w, *cp*	0.5
μ_o, *cp*	2
ρ_w, *psi/ft*	0.44
ρ_o, *psi/ft*	0.3611
P_i, *psi*	4000

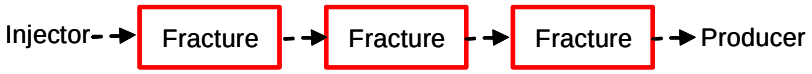

Figure 1-Single-Porosity Single-Permeability System.

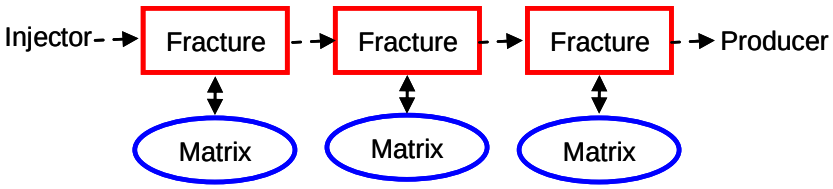

Figure 2-Dual-Porosity Single-Permeability System.

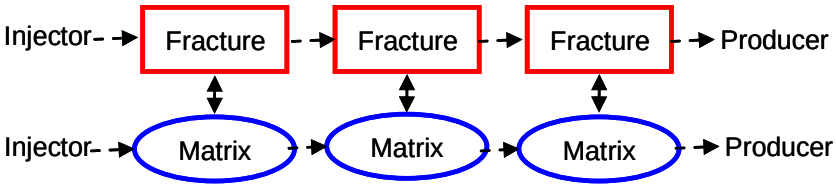

Figure 3-Dual-Porosity Dual-Permeability System.

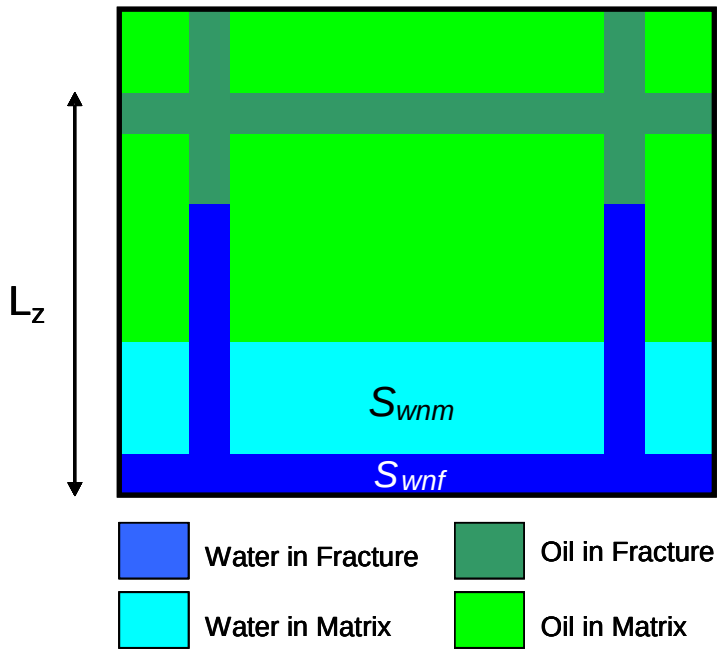

Figure 4 - Gravity Effect in a Single Matrix-Block Surrounded by Fractures Partially Filled with Water.

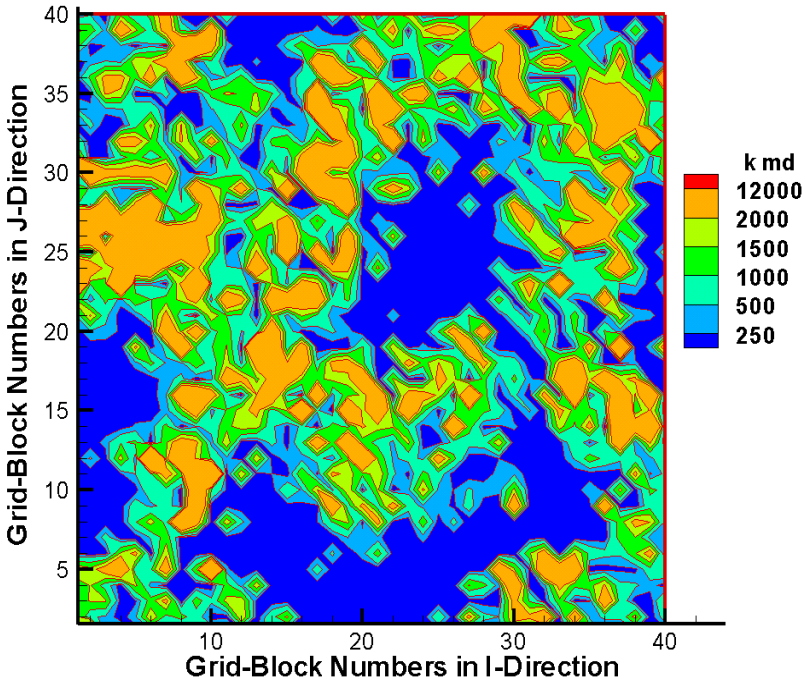

Figure 5 - 2D Fracture Permeability Field

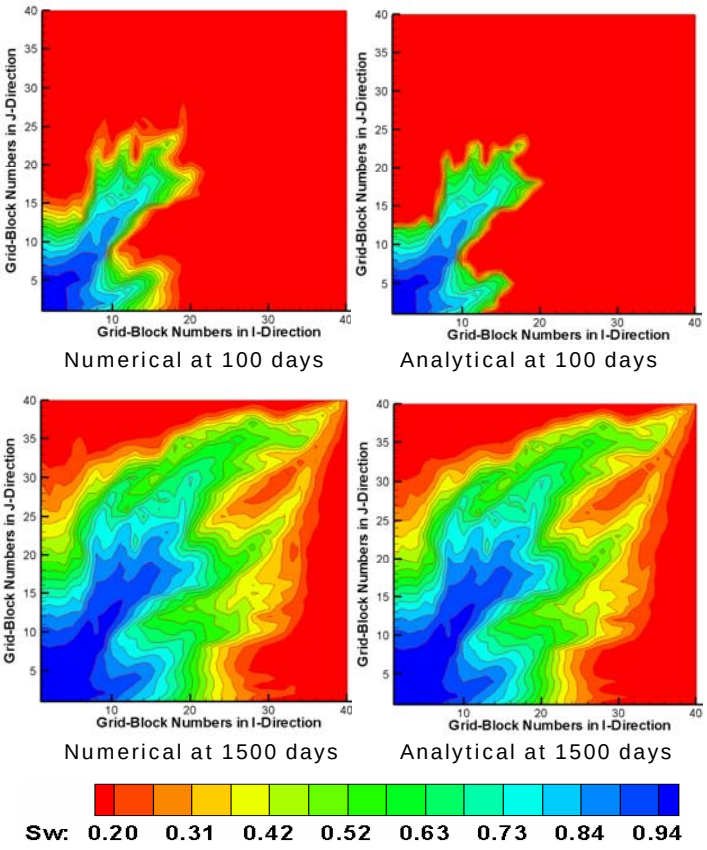

Figure 6-Comparison between the Numerical and Analytical Solutions of the Saturation Equation with ETF.

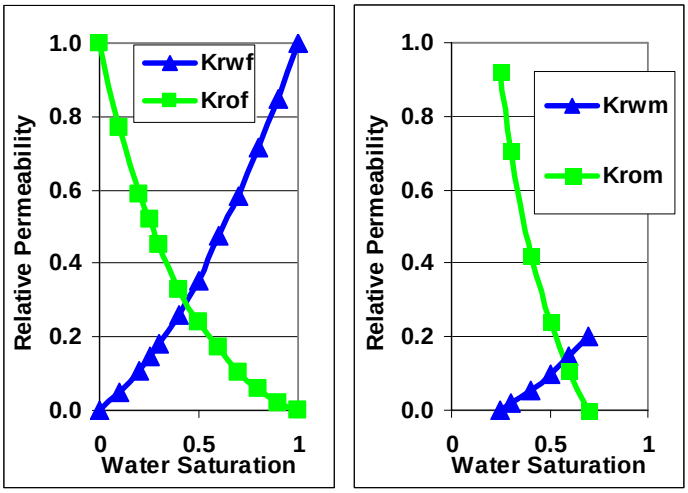

Figure 7-Fracture and Matrix Relative Permeability Curves (after Kazemi et al., 1976).

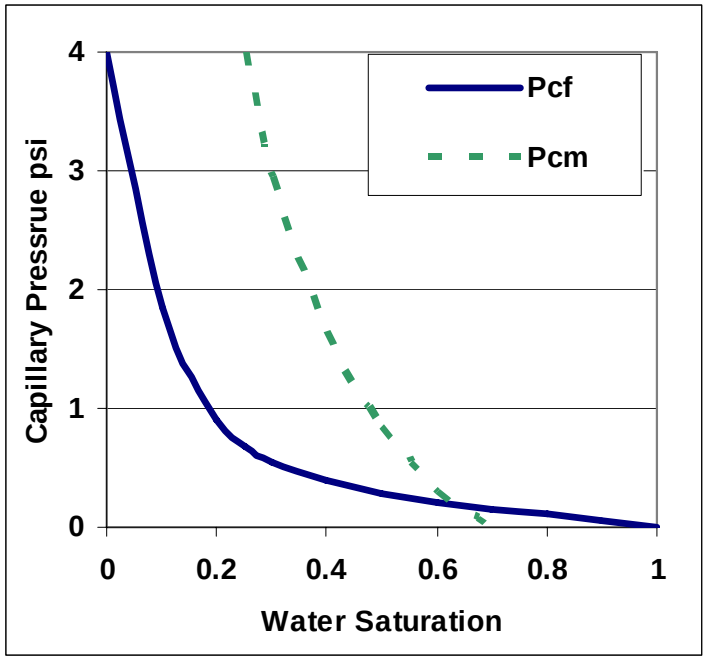

Figure 8-Fracture and Matrix Capillary Pressure Curves (after Kazemi et al. 1976).

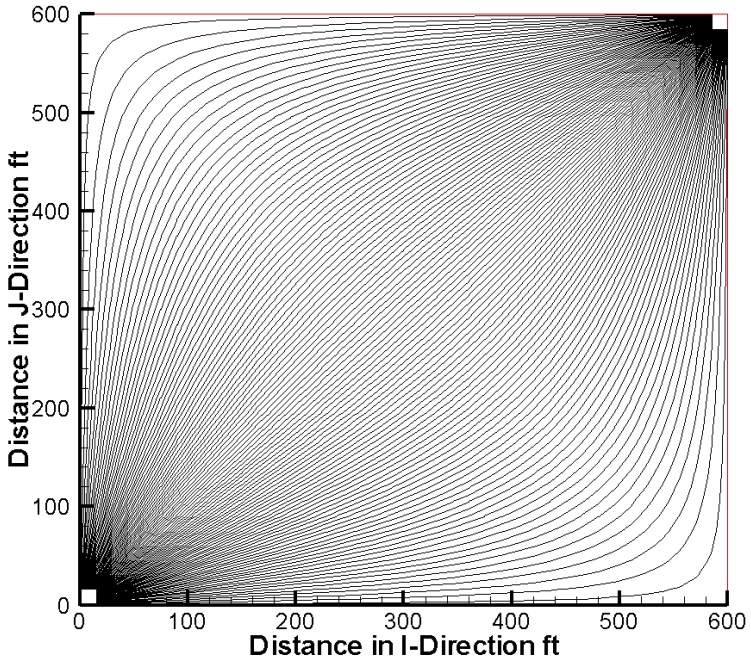

Figure 9-Streamlines in a Quarter Five Spot Pattern, Homogenous Case, Imbibition Process.

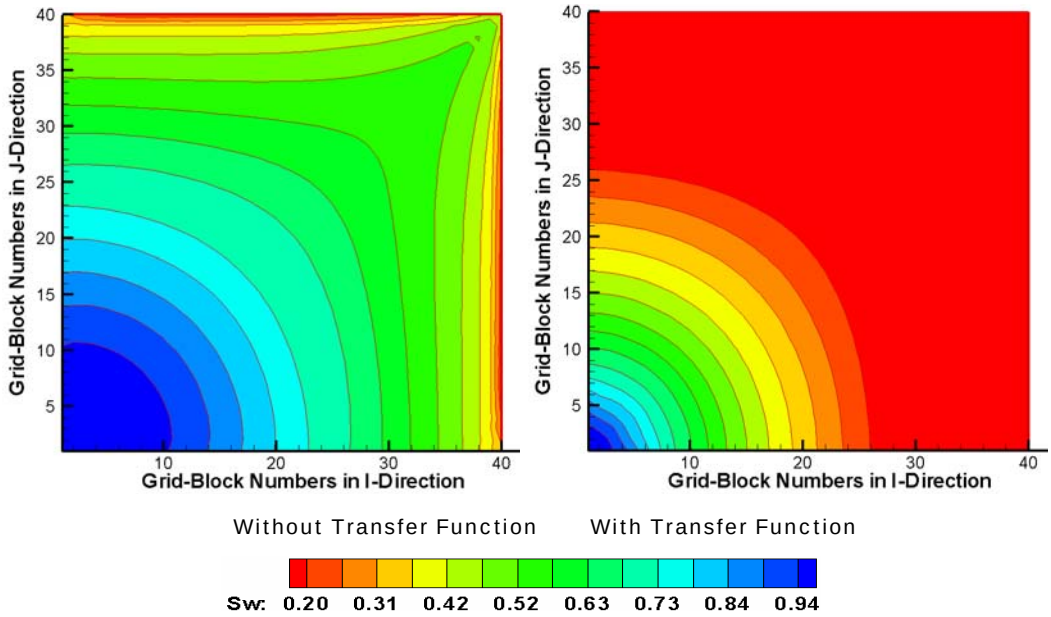

Figure 10-Fracture Water Saturation from DPSP Streamline Simulator with and without Transfer Function at 100 days, Homogenous Case, Imbibition Only.

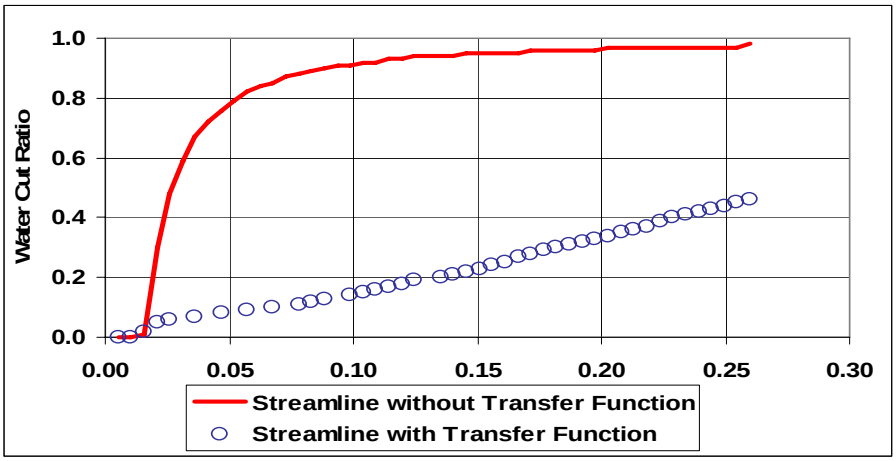

Figure 11-Water-cut Histories From the DPSP Streamline Simulation with and without Transfer Function, Homogenous Case, Imbibition Only.

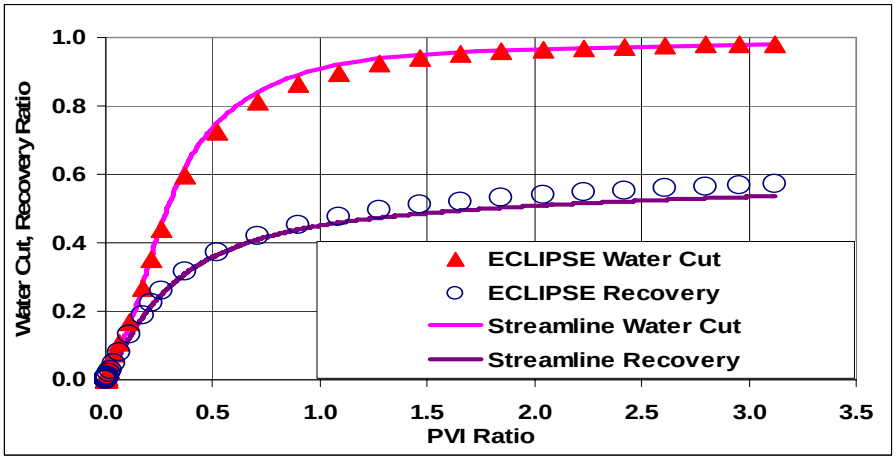

Figure 12-Comparison between the DPSP Streamline Simulator and the DPSP ECLIPSE in Terms of Water Cut and Recovery Histories, Homogenous Case, Imbibition Only.

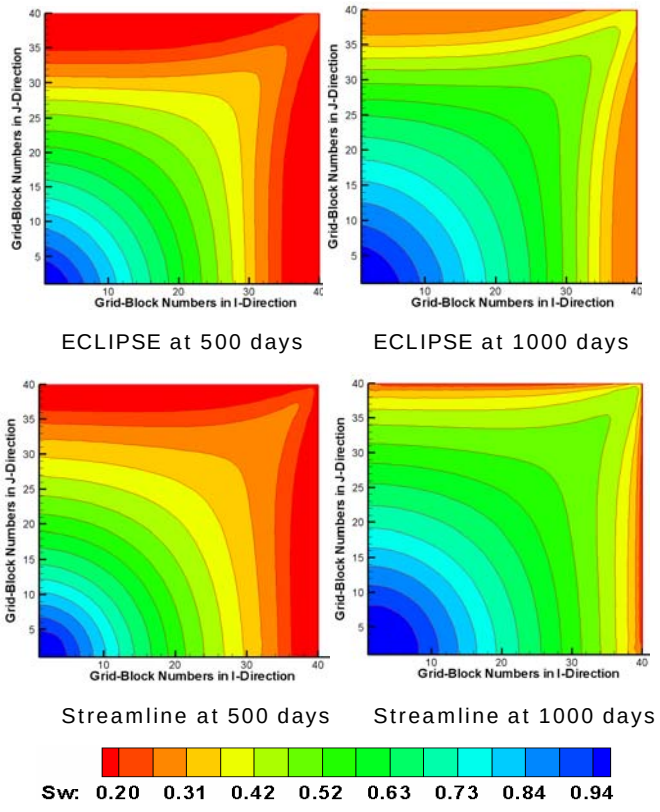

Figure 13-Comparison between the DPSP Streamline Simulator and the DPSP ECLIPSE in Terms of Fracture Water Saturation, Homogenous Case, Imbibition Only.

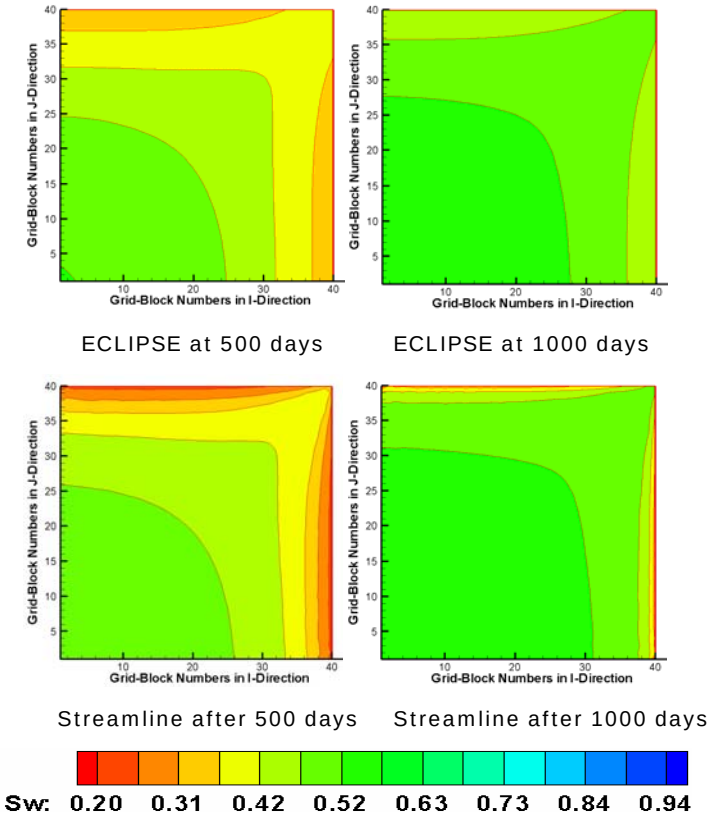

Figure 14-Comparison between the DPSP Streamline Simulator and the DPSP ECLIPSE in Terms of Matrix Water Saturation, Homogenous Case, Imbibition Only.

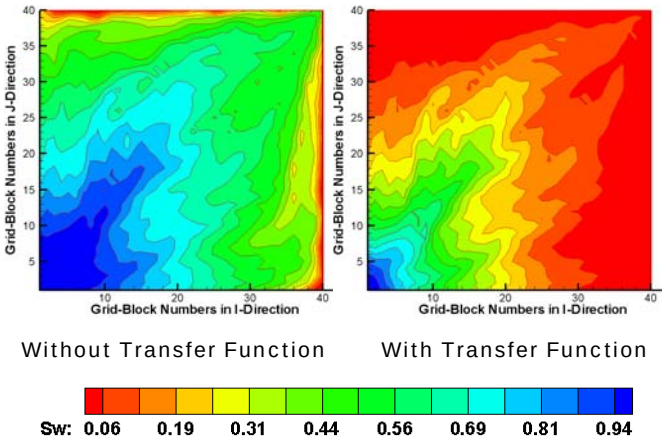

Figure 15- Fracture Water Saturation from the DPSP Streamline Simulator with and without Transfer Function at 100 days, Heterogeneous Case, Imbibition only.

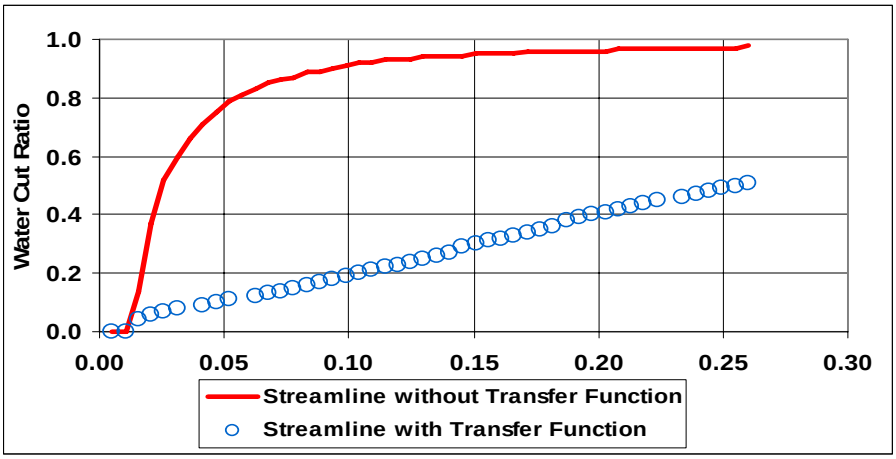

Figure 16-Water-cut Histories From the DPSP Streamline Simulation with and without Transfer Function , Heterogeneous Case, Imbibition Only.

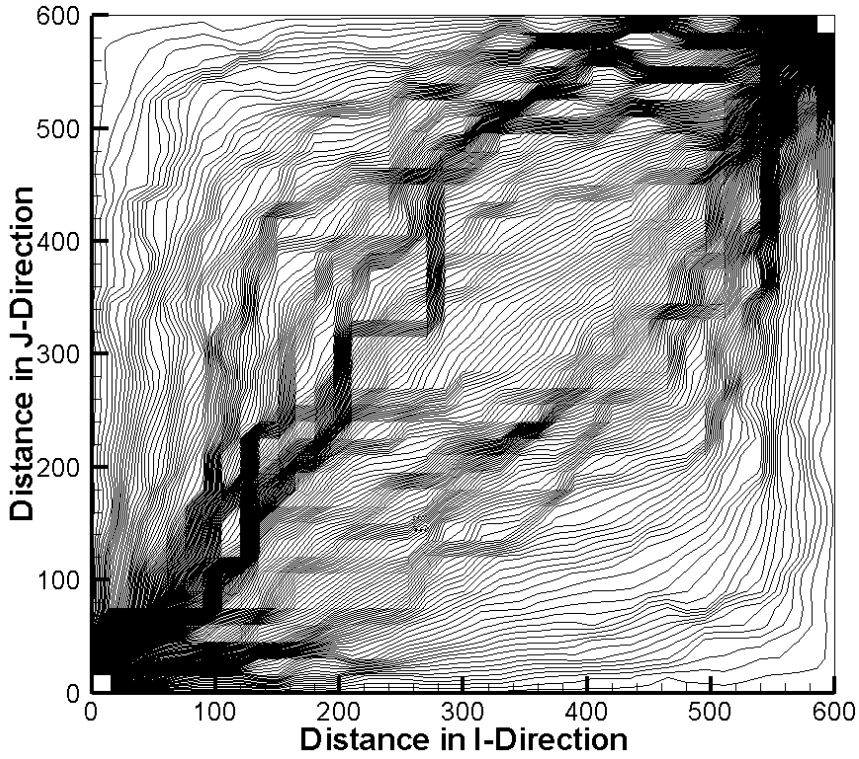

Figure 17-Streamlines in a Quarter Five Spot Pattern, Heterogenous Case, Imbibition Process.

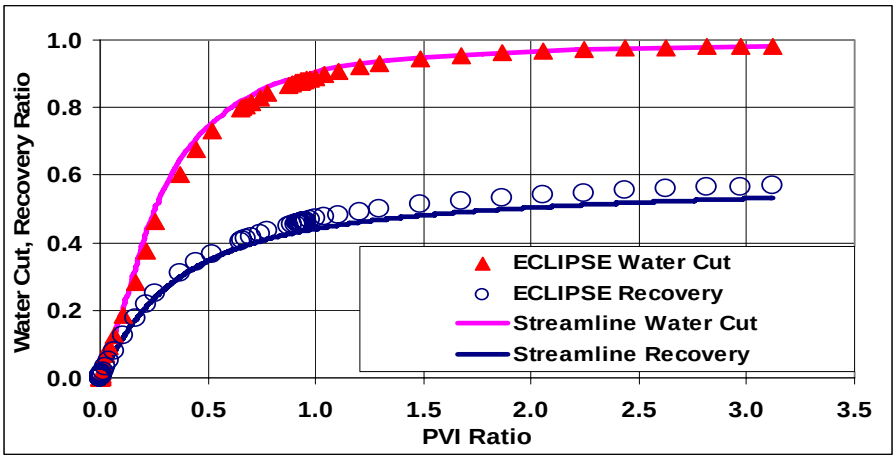

Figure 18-Comparison between the DPSP Streamline Simulator and the DPSP ECLIPSE in Terms of Water Cut and Recovery Ratios, Heterogeneous Case, Imbibition Process.

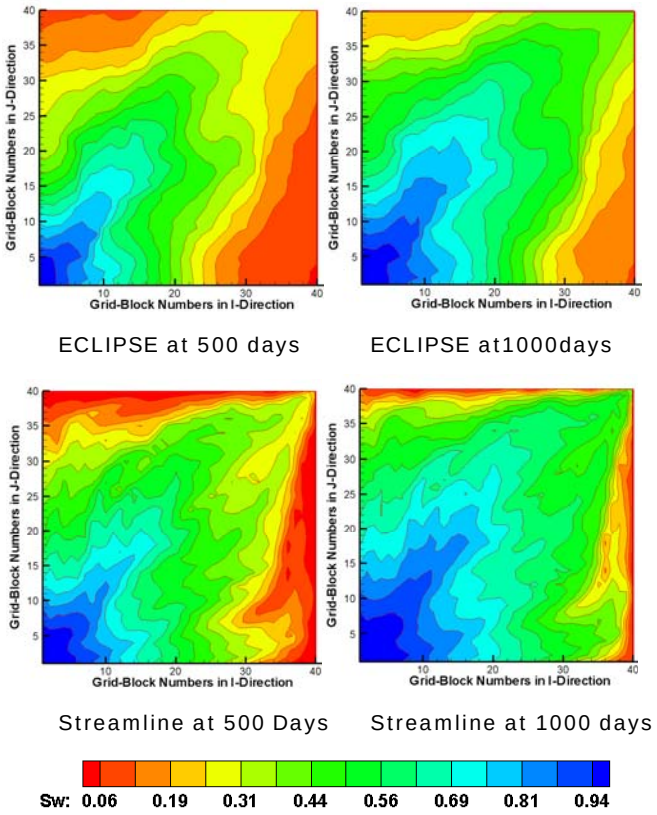

Figure 19-Comparison between the DPSP Streamline Simulator and the DPSP ECLIPSE in Terms of Fracture Water Saturation, Heterogeneous Case, Imbibition Process.

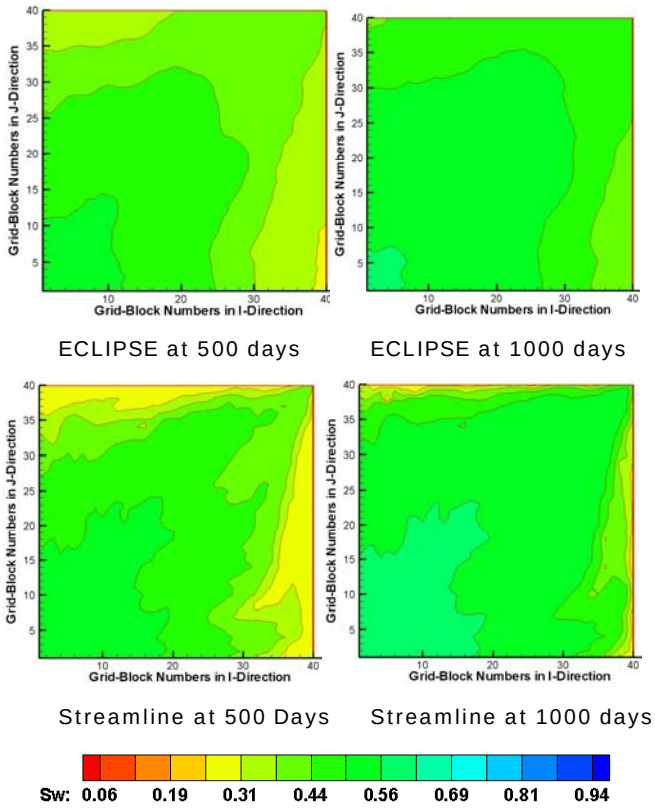

Figure 20-Comparison between the DPSP Streamline Simulator and the DPSP ECLIPSE in Terms of Matrix Water Saturation, Homogenous Case, Imbibition Process.

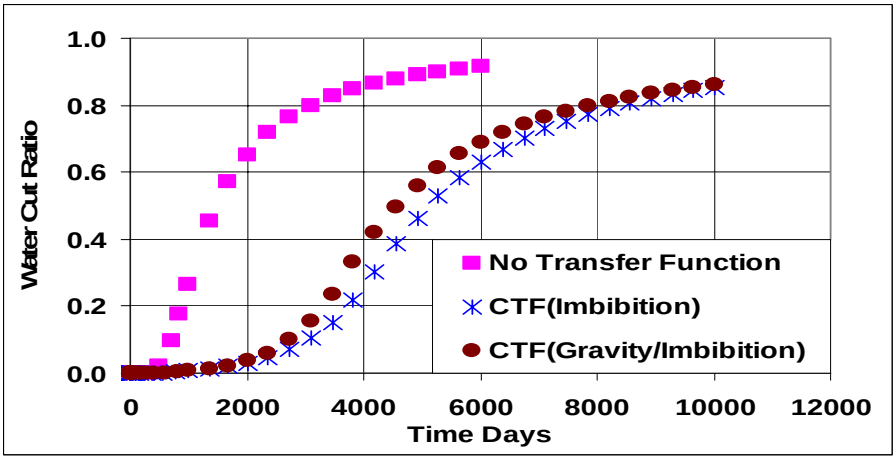

Figure 21-ECLIPSE Water Cut History, Quarter Five Spot Pattern, Gravity/Imbibition Process.

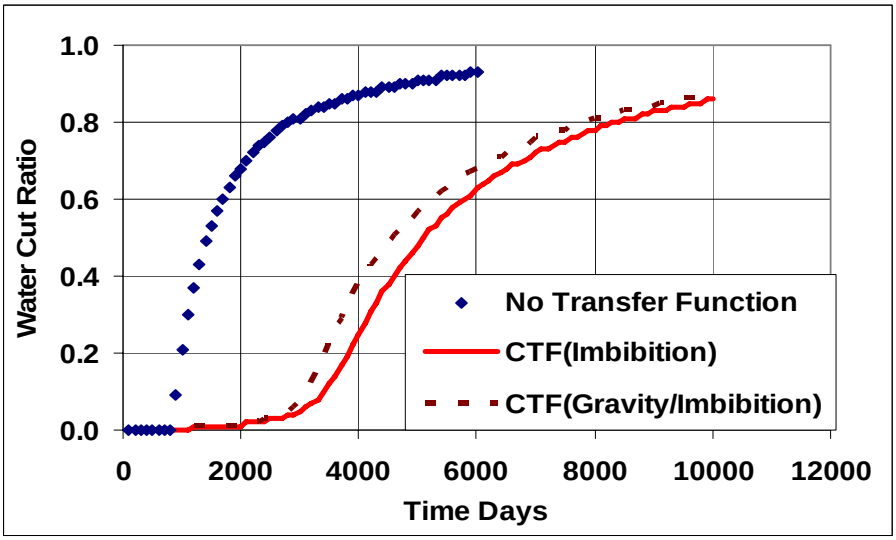

Figure 22-Streamline Simulation Water Cut History, Quarter Five Spot Pattern, Gravity/Imbibition Process.

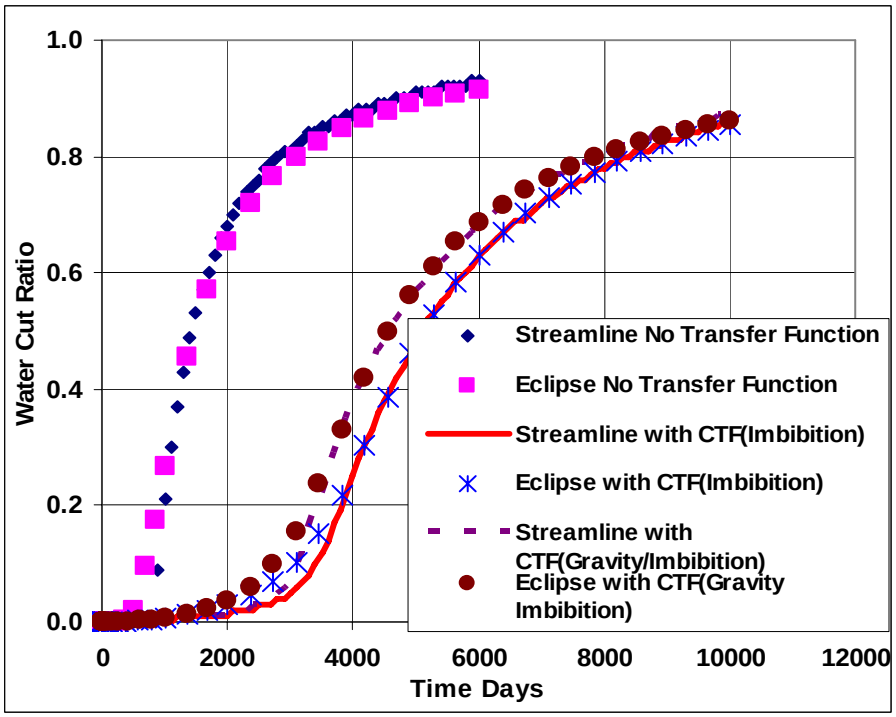

Figure 23- Comparison between the DPSP Streamline Simulator and the DPSP ECLIPSE in Terms of Water Cut History, Quarter Five Spot Pattern, Gravity/Imbibition Process.

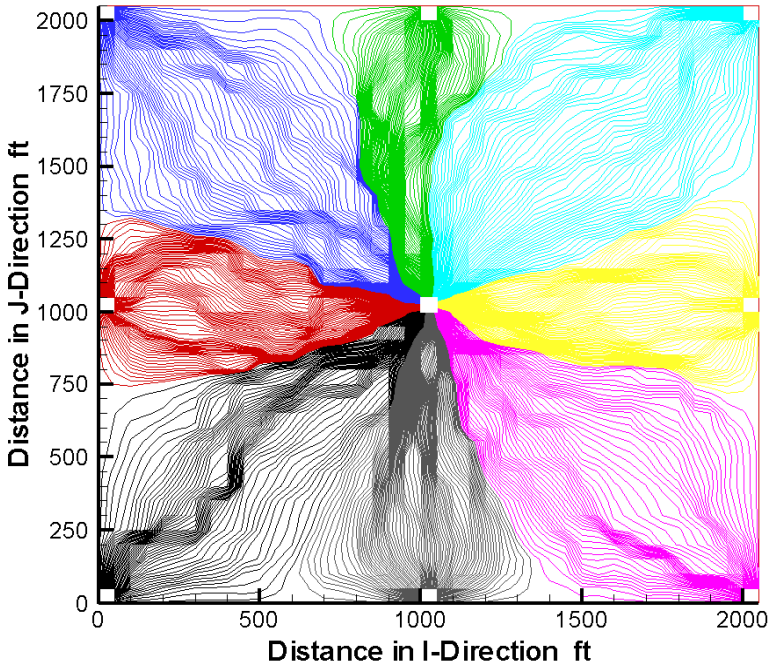

Figure 24-Streamlines in a Nine Spot Pattern, Heterogenous Nine Spot Case, Gravity/Imbibition Process.

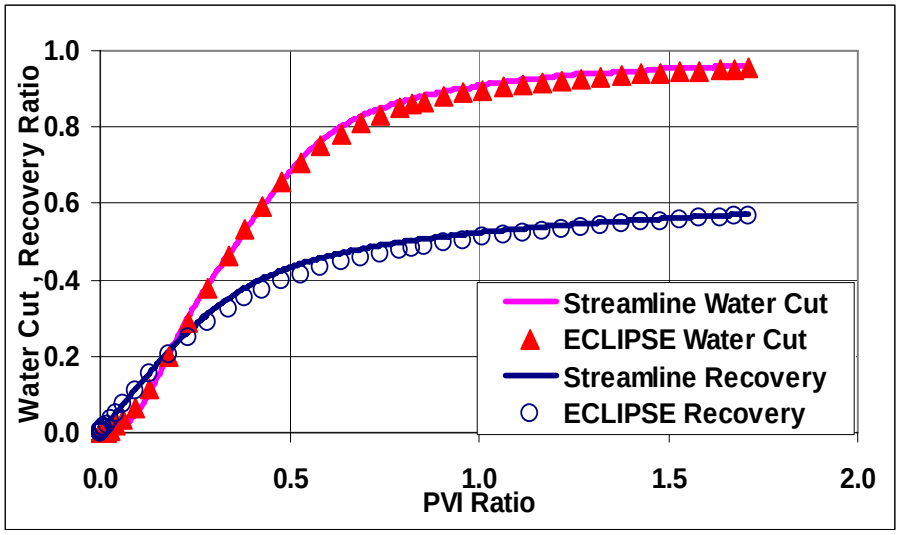

Figure 25- Comparison between the DPSP Streamline Simulator and the DPSP ECLIPSE in Terms of Field Water Cut and Recovery Ratios, Heterogeneous Nine Spot Case, Gravity/Imbibition Process.

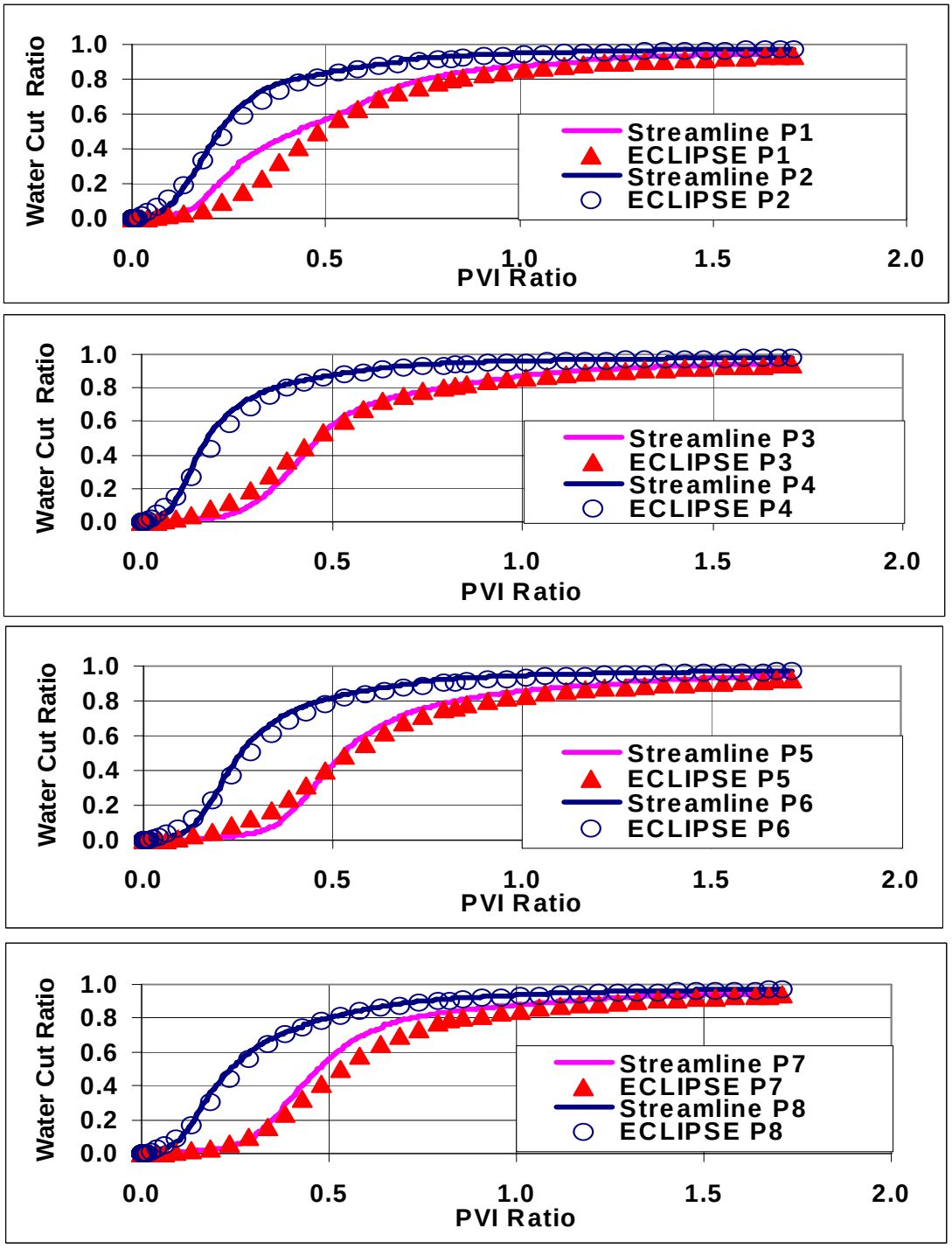

Figure 26- Comparison between the DPSP Streamline Simulator and the DPSP ECLIPSE in terms of Water Cut in Individual Producers, Heterogeneous Nine Spot Case, Gravity/Imbibition Process.

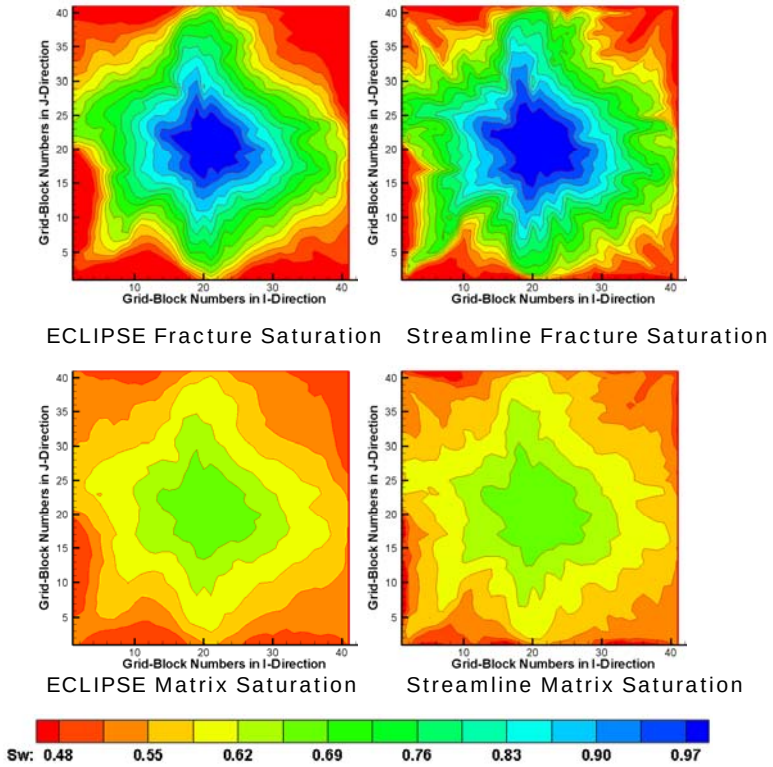

Figure 27- Comparison between the DPSP Streamline Simulator and the DPSP ECLIPSE in terms of Fracture Water Saturation after 6000 Days, Heterogeneous Nine Spot Case, Gravity/Imbibition Process.

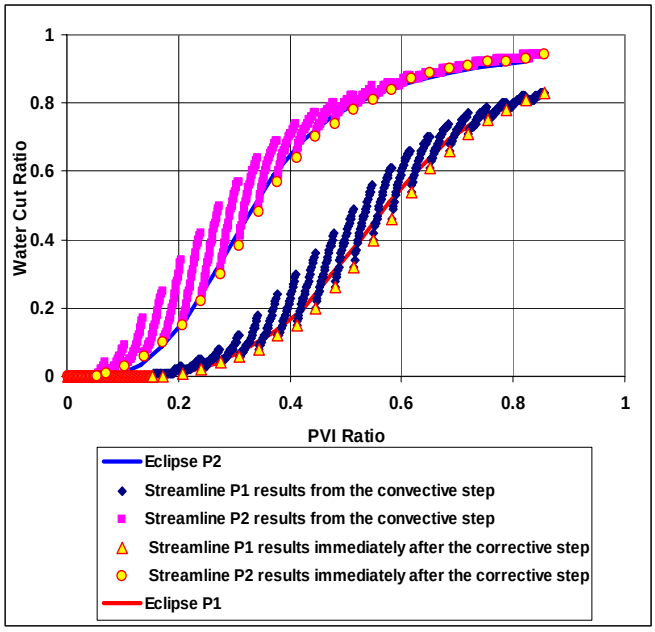

Figure 28-Comparison between the DPDP Streamline Simulator and the DPDP ECLIPSE in terms of Water Cut Ratio, Homogenous Case, Imbibition Process (SPT=250 days).

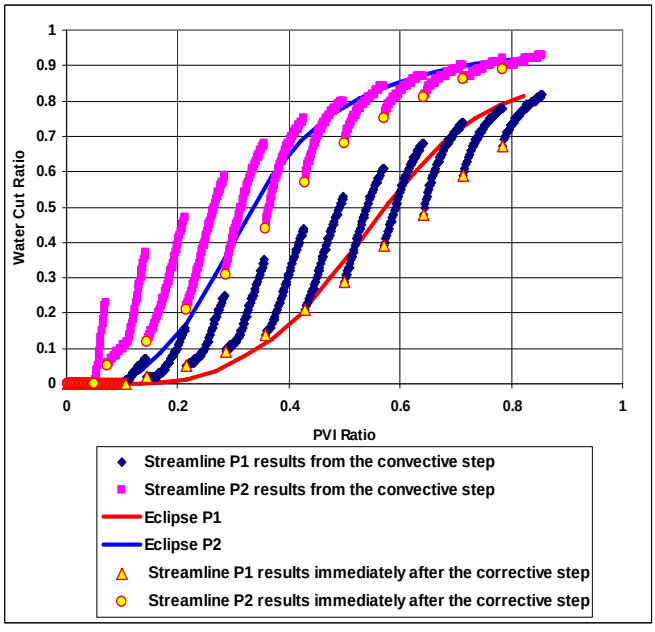

Figure 29-Comparison between the DPDP Streamline Simulator and the DPDP ECLIPSE in terms of Water Cut Ratio, Homogenous Case, Imbibition Process (SPT=500 days).

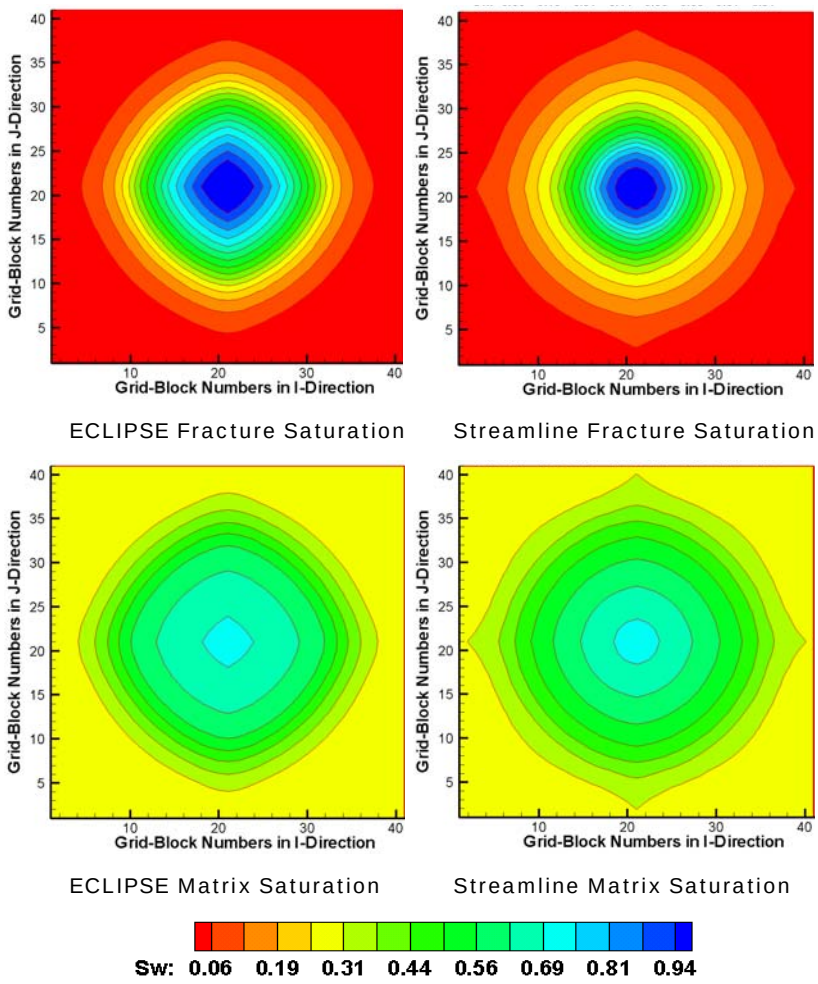

Figure 30-Comparison between the DPDP Streamline Simulator and the DPDP ECLIPSE in terms of Water Saturation after 1000 Days, Homogenous Nine Spot Case, Imbibition Process.

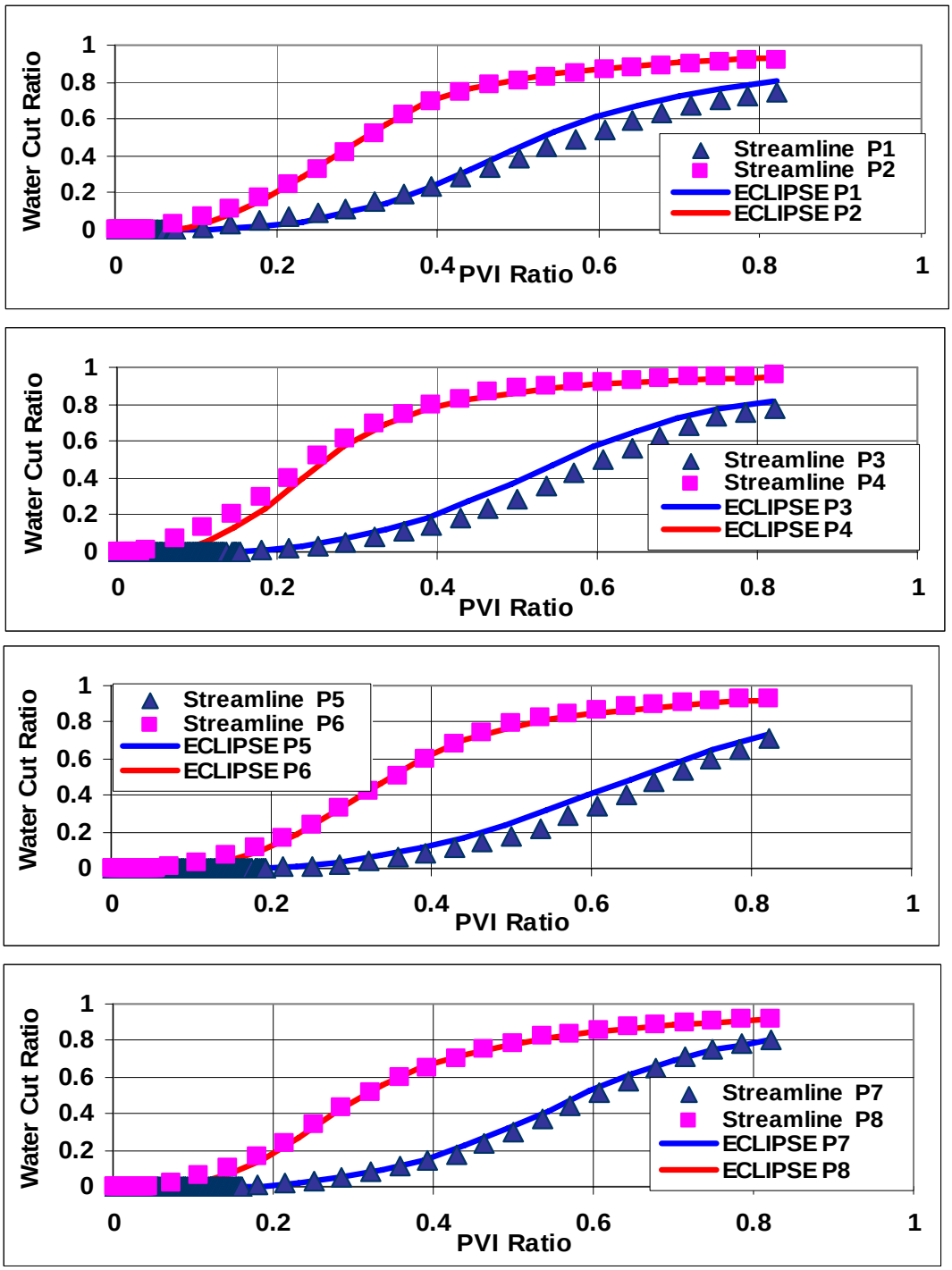

Figure 31- Comparison between the DPDP Streamline Simulator and the DPDP ECLIPSE in Terms of Water Cut Ratio, Heterogeneous Case, Imbibition Process.

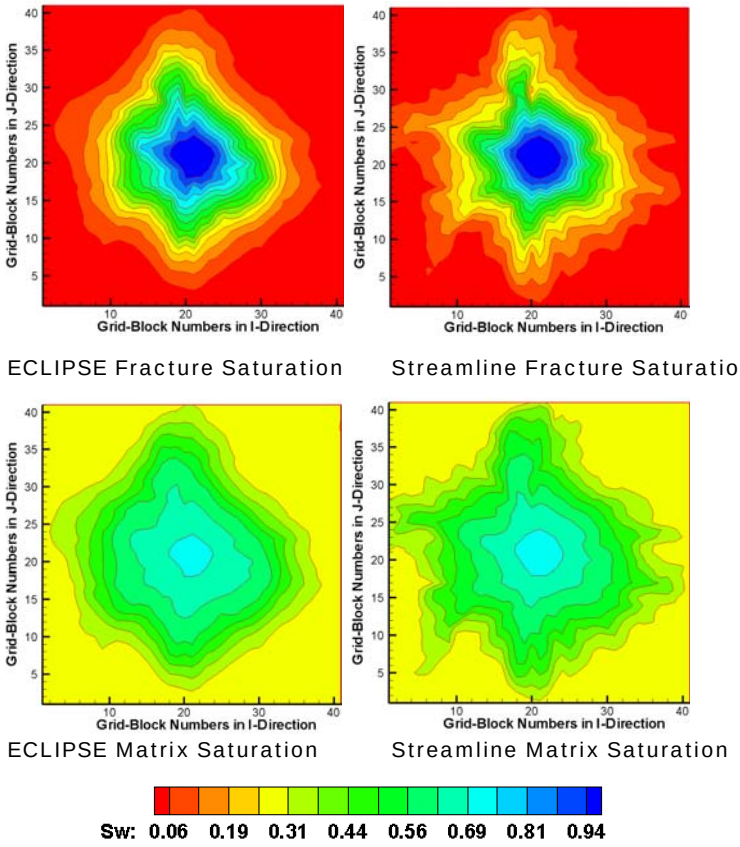

Figure 32- Comparison between the DPDP Streamline Simulator and the DPDP ECLIPSE in terms of Water Saturation after 1000 Days, Heterogeneous Nine Spot Case, Imbibition Process.

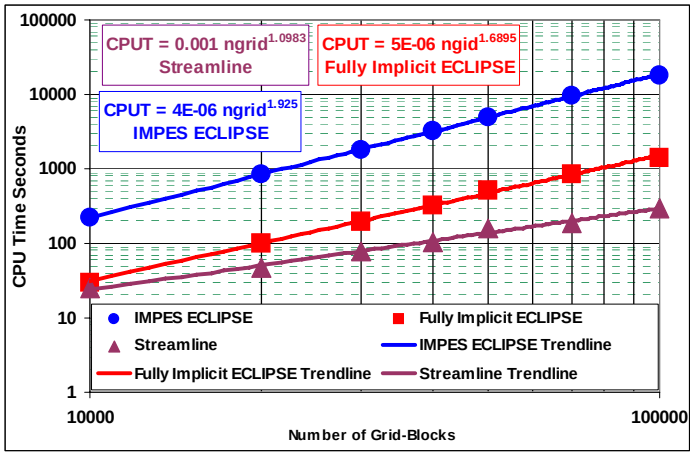

Figure 33-CPU Time Comparison the Fully Implicit DPSP ECLIPSE, The IMPES DPSP ECLIPSE, and the DPSP Streamline Simulation.

RESULTS AND DISCUSSION: PART III

Streamline-Based Production Data Integration in Naturally Fractured Reservoirs

Introduction

Natural fractures are known to play a significant role in subsurface flow and transport of fluids. In recent years, advances in key technologies such as seismic imaging and horizontal drilling revealed the true extent of fractures in many reservoirs and enabled operators to utilize novel ways to use fracture connectivity to enhance recovery. The number of reservoirs that are now considered to be naturally fractured has also risen significantly in recent years and there is a greater need for more robust fracture characterization methods that can integrate both static and dynamic data in an efficient manner.[1]

Of late, discrete fracture network (DFN) techniques have gained increasing attention in the oil industry.[2,3] The DFN is based on mapping fracture planes in 3D space using statistical properties of fracture swarms, fracture network geometry and flow characteristics. The advantage of the DFN models is the ability to incorporate complex fracture patterns based on field data such as cores, well logs, borehole images, seismic data and geomechanics. Although the DFN models can reproduce very realistic fracture geometry, it is important to condition these models to dynamic data such as well test, tracer and production data to reproduce the flow behavior in the reservoir. Such conditioning is particularly important for fractured reservoirs because only a small fraction of the fractures in the DFN model might carry bulk of the fluid flow.[4,5]

Streamline models have shown great potential in integrating dynamic data into high resolution geologic models.[6-10] A unique feature of streamline models has been the ability to efficiently compute the sensitivity of the production data to reservoir parameters such as porosity and permeability. These sensitivities are partial derivatives that quantify how the production response will be affected by changes in reservoir properties. Integrating dynamic data into reservoir models typically involve the solution of an inverse problem and the sensitivities play a key role here. In our previous works, we have utilized the streamline-based sensitivities in conjunction with a generalized travel time inversion method to efficiently integrate production data into geologic models.[7] Our approach has been successfully applied to a large number of field cases including a giant middle-eastern carbonate reservoir.[8]

Until recently, streamline models have been limited to single porosity systems and thus, were not suitable for modeling fluid flow in fractured reservoirs, particularly accounting for matrix-fracture interactions. A common way to model fluid flow in fractured reservoirs is through the dual media approach whereby the fracture and the matrix are treated as separate continua that are connected through a transfer function.[11-13] The transfer functions that describe the exchange of fluids between the matrix and the fracture system can be easily implemented within the framework of the current single porosity streamline models.[14,15] This allows us to utilize much of the techniques related to production data integration developed for single porosity streamline models. However, compared to the single porosity systems, the propagation of the saturation front in the fracture is retarded significantly because of the exchange of fluid with the matrix in dual porosity systems. These effects must be accounted for while computing the travel time sensitivities for saturation fronts. The streamline-derived sensitivities can also be applied in conjunction with dual porosity finite difference simulators and allow us to combine the

efficiency of the streamline approach with the versatility of finite difference simulation. The streamlines can be obtained from the fluid fluxes that are readily available during finite-difference simulation. This significantly broadens the applicability of the streamline-based approach in terms of incorporating compressibility effects and complex physics.[16]

The organization of this report is as follows. First we outline the major steps in our proposed approach and illustrate the procedure using a 2-D synthetic example. Next, we briefly describe the streamline-based dual porosity simulation and how to include matrix-fracture transfer mechanisms within the framework of single porosity streamline simulation. We then describe the extension of streamline-based sensitivity computations to fractured reservoirs and production data integration via generalized travel time inversion. Finally, we demonstrate the power and utility of our method using a realistic 3-D example whereby we use a finite-difference dual porosity simulator and streamline-derived sensitivities to integrate over 20 years of water-cut history.

Approach

Our approach for integrating dynamic data in fractured reservoirs is based on a previously proposed generalized travel time inversion for production data integration.[17] The approach has been shown to be computationally efficient, robust and suitable for large-scale field applications.[7,18] The unique aspect here is the extension and validation of streamline-based analytic travel time sensitivity computations for fractured medium and accounting for matrix-fracture exchange mechanisms. The travel time sensitivities can be applied to both streamline and finite difference simulators. Thus, we can exploit the computational efficiency of the streamline approach and the versatility of the finite difference simulators in terms of handling compressibility and complex physics. The main steps used in our approach are as follows.

- **Dual Porosity Fracture Flow Simulation**. For modeling fluid flow in fractured reservoirs, we can use either a 3D dual porosity streamline simulator or a finite difference simulator. The streamline models have recently been extended to fractured reservoirs using the dual media approach.[14,15] In particular, the dual porosity streamline models can be considerably faster than conventional finite-difference simulators when the primary exchange mechanism between the matrix and the fracture system is capillary imbibition. However, in the presence of strong coupling between the matrix and the fracture system, the streamline models may not offer significant advantage and we revert to conventional finite difference dual porosity flow simulation. The use of finite-difference models allows us to incorporate compressibility and other relevant physical mechanisms without any significant loss in computational efficiency.

- **Generalized Travel-Time and Sensitivity Computations**. The misfit between the observed and computed production response is quantified using a previously proposed generalized travel time.[7,17] A critical aspect of production data integration is calculation of sensitivities that define the relationship between production response and reservoir parameters. We compute these sensitivities analytically as one-dimensional integrals along streamline trajectories. For streamline simulators, these trajectories are readily available. However, for finite difference models an additional step is necessary to compute the streamlines and time of flight based on the finite difference velocity field. These one dimensional calculations scale very favorably with respect to number of grid blocks. Thus, our approach is particularly well-suited for high resolution geologic models.

- **Data Integration Using Generalized Travel Time Inversion**. For history matching, we have used a generalized travel time inversion approach that utilizes the analytical sensitivities is used in conjunction with an iterative optimization scheme to minimize the travel time shift between calculated and observed data.[17] Additional constraints are imposed to integrate prior information and also retain plausibility of the solution. These include a prior covariance model or equivalently a 'roughness' constraint to preserve the spatial correlation of the fracture permeability and a 'norm' constraint to retain the prior geologic features.[17] The generalized travel time inversion has many favorable characteristics including quasi-linear properties that make it attractive for field applications.[7,15]

An Illustration of the Procedure. To illustrate our approach, we will use an example that involves integration of water cut data in a 9-spot pattern. The reference fracture permeability field was derived from a discrete fracture network (DFN) model shown in **Fig 1a**. The model exhibits complex connectivity patterns common to naturally fractured reservoir where the distribution of fracture swarms determines the shape and intensity of fractured regions. A moving window is used to calculate the fracture density for each grid cell which is then converted to a fracture permeability multiplier using a non-linear transform.[20] The fracture permeability is calculated using the multiplier and a predetermined fracture permeability range. The reference fracture permeability distribution is shown in **Fig. 1b.** We used a dual porosity streamline simulator for modeling fluid flow in the fractured medium for this example.

We can randomly extract various percentages of fracture swarms and fractures within the swarms to generate prior models with varying degrees of fracture information. Because production data is more appropriate for characterizing large scale features, fracture swarms location is more critical than the detailed connectivity of individual fractures within a cell. We generate a 2D prior model of fracture patterns by randomly drawing 50% of the fracture swarm and 50% of fractures inside each swarm. **Fig. 2a** shows the prior fracture permeability model.

We match the water cut response from the reference model for the first 500 days using the generalized travel time inversion. Starting with the prior model, we minimize the travel time shift at each producer iteratively to match the reference production data. **Fig. 2b** shows the final fracture permeability model. **Fig 3** shows the observed data, initial model response and the matched response after performing the generalized travel time inversion. The process has not only matched the breakthrough times but also the amplitude of the water cut response for all the wells. Also, **Fig. 2b** shows that after inversion we are able to recover the permeability contrast in the reference model and reproduce the dominant fracture connectivity while retaining most of the features of the prior model. For example, integration of production data has connected the two distinct high permeability regions in the prior model. This is clearly an important feature in the reference model in terms of fluid flow response. Finally, **Fig. 4** shows the convergence of the inversion algorithm. The data misfit is reduced by almost an order of magnitude in only five iterations.

Mathematical Formulation

Dual Porosity Streamline Simulation. Streamline models have recently been generalized to model fluid flow in fractured reservoirs including matrix-fracture interactions.[14,15] A common approach to include such interactions has been through the dual porosity conceptualization whereby the fluid flow is assumed to occur primarily through the high permeability fracture system and the matrix acts as the fluid storage.[11-13] A matrix-fracture transfer function is used to exchange fluid

between the matrix and the fracture systems. If we consider incompressible flow in a non-deformable media, then the conservation equations for the fracture and the matrix in a dual porosity system can be written as follows, [12-15]

$$\phi_f \frac{\partial S_{wf}}{\partial t} + \vec{u}_t \bullet \nabla f_{wf} + \nabla \bullet \vec{G} + \Gamma_w = 0 \quad \text{.....(1)}$$

$$\Gamma_w = \phi_m \frac{\partial S_{wm}}{\partial t} \quad \text{.....(2)}$$

In **Eqs. 1** and **2**, the subscripts *f* and *m* represent the fracture and the matrix systems, respectively. In addition, the fractional flow, f_{wf} and the gravity term, G are defined as follows,

$$f_{wf} = \frac{\lambda_{wf}}{\lambda_{wf} + \lambda_{of}} \quad \text{.....(3)}$$

$$\vec{G} = k \cdot \frac{\lambda_{wf}\lambda_{of}}{\lambda_t}(\rho_o - \rho_w)\vec{g}\nabla D \quad \text{.....(4)}$$

where,

$$\lambda_{wf} = \frac{k_{rwf}}{\mu_w} \quad \text{.....(5a)}$$

$$\lambda_{of} = \frac{k_{rof}}{\mu_o} \quad \text{.....(5b)}$$

$$\lambda_t = \lambda_{of} + \lambda_{wf} \quad \text{.....(6)}$$

We can rewrite **Eq. 1** in terms of the streamline time of flight coordinate by introducing the coordinate transformation[21],

$$\vec{u}_t \cdot \nabla = \phi \frac{\partial}{\partial \tau} \quad \text{.....(7)}$$

where the time of flight τ is the transit time of a neutral tracer along a streamline,[22]

$$\tau = \int \frac{\phi}{\|u_t\|} \partial \zeta \quad \text{.....(8)}$$

The saturation equation for the fracture system, **Eq.1**, now takes the following form,

$$\frac{\partial S_{wf}}{\partial t} + \frac{\partial f_{wf}}{\partial \tau} + \frac{\nabla \bullet \vec{G}}{\phi_f} + \frac{\Gamma_w}{\phi_f} = 0 \quad \text{.....(9)}$$

Eq. 9 together with the matrix saturation **Eq. 2** describes the streamline transport equations for the dual porosity system.

It is important to note that because the fluid flow occurs only in the fracture system, we need to trace streamlines only for the fractured medium. The tracing of streamlines for the dual porosity system is identical to that of the single porosity system.[23] The form of the pressure equation remains unchanged when the primary transfer mechanism between the matrix and the fracture system is counter-current imbibition and the transfer terms cancel out. The transfer function for counter-current imbibition can be described by the following,[14,15,24]

$$\Gamma_w = F_s k_m \frac{\lambda_{wf}\lambda_{om}}{\lambda_{wf}+\lambda_{om}}\left(P_{cm}-P_{cf}\right) \quad \text{.....(10)}$$

The basic steps for streamline simulation in a DPSP system can be summarized as follows: (1) Starting with the fracture permeability field (**Fig. 5a)**, source/sink configuration and boundary conditions, a pressure field is generated as in conventional finite-difference simulation (**Fig. 5b**) (2) Next, the velocity distribution in the reservoir is obtained using Darcy's law and the streamlines are traced using the Pollock approach[23] (**Fig. 5c**). The time of flight or travel time along streamlines are also obtained at this stage and the isochrones represent the front propagation (**Fig. 5d**) (3) The fracture saturation distribution is obtained by solving the 1-D saturation **Eq. 9** (without the gravity term) along each streamline as shown in **Fig. 6a**. Gravity effects can be accounted for in the same manner as in single porosity streamline simulation viz. using operator splitting techniques.[25] **Fig. 6b** shows the saturation distribution along a streamline as a function of matrix-fracture transfer rate in **Eq. 10**. For $F_s = 0$, there is no interaction with the matrix and the solution reverts back to the single porosity formulation. Clearly, the net effect of the matrix-fracture transfer function is to retard the water saturation front in the fracture system. The matrix saturation equation is solved along the streamline at the same time and is shown in **Fig. 6c**. (4) The matrix and fracture saturations are then mapped back onto the grid (**Fig. 6e** and **6f**). Again, the rapid propagation of the saturation front in the fracture system in the absence of transfer to the matrix ($F_s = 0$) can be clearly seen in **Fig. 6d**. (5) The streamlines may be updated to account for changing well conditions such as infill drilling, rate changes etc. As in single porosity simulation, fracture and matrix saturations are mapped from streamlines onto the grid before each update, followed by pressure solution, streamline generation and re-initialization.

Generalized Travel Time Inversion. Production data integration via generalized travel time inversion has three major elements to it: representation of the data misfit, relating production data with reservoir parameters via sensitivities and history matching and model updating via an optimization procedure. We briefly discuss these steps here.

Data Misfit Calculation. The first step in the production data integration approach is quantification of the data misfit. We define a 'generalized travel time' at each well for this purpose. In this approach, we seek an optimal time-shift Δt at each well so as to minimize the production data misfit at the well.[17] This is illustrated in **Fig. 7a** where the calculated water-cut response is systematically shifted in small time increments towards the observed response and the data misfit is computed for each time increment. The optimal shift will be given by the Δt that minimizes the misfit function,

$$J = \sum_{i=1}^{Nd}\left[y^{obs}(t_i+\Delta t) - y^{cal}(t_i)\right]^2 = f(\Delta t, m) \quad \text{.....} \quad (11)$$

Or, alternatively maximizes the coefficient of determination given by the following

$$R^2(\Delta t) = 1 - \frac{\sum\left[y^{obs}(t_i+\Delta t) - y^{cal}(t_i)\right]^2}{\sum\left[y^{obs}(t_i) - \overline{y^{obs}}\right]^2} \quad \text{.....(12)}$$

Thus, we define the generalized travel time as the 'optimal' time-shift $\Delta\tilde{t}$ that maximizes the R^2 as shown in **Fig. 7b**. It is important to point out that the computation of the optimal shift does not require any additional flow simulations. It is carried out as a post-processing at each well

after the calculated production response is obtained from flow simulation. The overall production data misfit can now be expressed in terms of a generalized travel time misfit at all wells as follows

$$E = \sum_{j=1}^{Nw} (\Delta\tilde{t}_j)^2 \quad \text{.....(13)}$$

The generalized travel time approach has been successfully applied to many field cases. Furthermore, it leads to a robust and efficient inversion scheme because of its quasi-linear properties.[7,17]

Analytic Sensitivity Computation and Verification. One of the important advantages of the streamline approach is the ability to analytically compute the sensitivity of the generalized travel time with respect to reservoir parameters, for example, fracture permeability. These sensitivities form an integral part of our data integration algorithm.

We have seen that during generalized travel time computation we shift the entire fractional flow curve by a constant time. Thus, every data point in the fractional-flow curve has the same shift time, $\delta t_1 = \delta t_2 = \cdots = \Delta\tilde{t}$ (**Fig. 7a**). We can average the travel time sensitivities of all data points to obtain a rather simple expression for the sensitivity of the generalized travel time with respect to reservoir parameters *m* as follows,[7]

$$\frac{\partial \Delta\tilde{t}_j}{\partial m} = -\frac{\sum_{i=1}^{N_{dj}} \left(\partial t_{i,j} / \partial m\right)}{N_{dj}} \quad \text{.....(14)}$$

All that remains now is to calculate the sensitivity of the arrival times of various water-cut at the producing well, $\partial t_{i,j} / \partial m$. These sensitivities can be easily obtained in terms of the sensitivities of the streamline time of flight,[7]

$$\frac{\partial t}{\partial m} = \frac{\dfrac{\partial \tau}{\partial m}}{\dfrac{\partial f_w}{\partial S_w}}. \quad \text{.....(15)}$$

In the above expression, the fractional-flow derivatives are computed at the saturation of the outlet node of the streamline.[7] For dual porosity streamline models, the saturation evolution along streamlines in the fractured system is carried out in two steps: a predictor step that involves transport along streamlines (identical to the single porosity calculations) and a corrector step that involves the matrix-fracture exchange as follows,[15]

$$\frac{\partial S_{wf}}{\partial t} + \frac{\partial f_{wf}}{\partial \tau} = 0 \text{ : Predictor} \quad \text{.....(16)}$$

$$\frac{\partial S_{wf}}{\partial t} + \frac{\Gamma_w}{\phi_m} = 0 \quad \text{ : Corrector} \quad \text{.....(17)}$$

The fractional flow in **Eq. 15** is computed after the saturation is updated to account for matrix-fracture exchange. If gravity is included, then an additional updating is required to account for gravity segregation before the sensitivities are computed.[25]

Finally, the time-of-flight sensitivities can be obtained analytically in terms of simple integrals along streamline. For example, the time-of-flight sensitivity with respect to permeability will be given by[6]

$$\frac{\partial \tau}{\partial k(\mathbf{x})} = \int_{\Sigma} \frac{\partial s(\mathbf{x})}{\partial k(\mathbf{x})} dx = -\int_{\Sigma} \frac{s(\mathbf{x})}{k(\mathbf{x})} dx, \quad \text{.....(18)}$$

where the integrals are evaluated along the streamline trajectory, and the 'slowness' which is the reciprocal of interstitial velocity, is given by

$$s(\mathbf{x}) = \frac{\phi(\mathbf{x})}{\lambda_t k(\mathbf{x}) |\nabla P(\mathbf{x})|} \quad \text{.....(19)}$$

Note that the quantities in the sensitivity expressions are either contained in the initial reservoir model or are available after the forward simulation run.

In order to verify our DPSP travel time sensitivity in **Eq. 15** we compared our results with sensitivities obtained by numerical perturbation. For this purpose, we simulated water injection in a quarter five-spot pattern. A dual porosity medium with homogeneous fracture permeability represented by 21x21 grid cells was used for this comparison. We perturbed every grid block permeability by 5%, one grid block at a time and numerically computed the partial derivative of the arrival time of a fixed water cut with respect to permeability. **Fig. 8** shows the results for water cuts of 0.10 and 0.20. Clearly, we obtain a good agreement between analytical travel time sensitivities calculated from **Eq. 15** and numerical travel time sensitivities. The perturbation method shows some artifacts partly because the results depend on the magnitude of perturbation whereas the analytical sensitivities are symmetric and smooth. The differences are also because of the approximations inherent in the analytical computations, particularly the assumption that the streamlines do not shift because of small perturbation in reservoir properties. Nevertheless, as we will see later, the streamline-based sensitivities are adequate for history matching purposes under a wide variety of conditions.

Data Inversion Various approaches have been proposed in the literature for the integration of production data via inverse modeling.[26-30] These can be broadly classified into 'deterministic' and 'Bayesian' methods. Both methods have been successfully applied to history matching of field data. In this work, we have adopted a Bayesian formulation whereby we minimize the following penalized misfit function,

$$\frac{1}{2}(m - m_p)^T C_M^{-1}(m - m_p) + \frac{1}{2}\left[\Delta \tilde{\boldsymbol{t}}\right]^T C_D^{-1}\left[\Delta \tilde{\boldsymbol{t}}\right] \text{.....(20)}$$

In **Eq. 20**, $\Delta\tilde{\mathbf{t}}$ is the vector of generalized travel-time shift at the wells; C_D and C_M are the data error covariance and the prior model parameter covariance, respectively. The minimum in **Eq. 20** can be obtained by an iterative least-squares solution to the linear system[31]

$$\begin{bmatrix} \mathbf{C}_D^{-1/2}\mathbf{G} \\ \mathbf{C}_\mathbf{M}^{-1/2} \end{bmatrix} \delta \mathbf{m} = \begin{bmatrix} \mathbf{C}_D^{-1/2}\left(\Delta\tilde{\mathbf{t}}\right) \\ \mathbf{C}_\mathbf{M}^{-1/2}\left(\mathbf{m_p} - \mathbf{m}\right) \end{bmatrix}. \quad \text{.....(21)}$$

where G is the sensitivity matrix containing the sensitivities of the generalized travel time with respect to the reservoir parameters and m_p represents the prior model. We use an iterative sparse matrix solver, LSQR, for solving the augmented linear system in **Eq. 21**. The LSQR

algorithm is well suited for highly ill-conditioned systems and has been widely used for large-scale tomographic problems in seismology.[32]

An important consideration in the solution of **Eq. 21** is calculation of the square-root of the inverse of the prior covariance matrix. We have used a numerical stencil that allows for an extremely efficient computation of $C_M^{-1/2}$ and is applicable to a wide range of covariance/variogram models.[33]

Application and Results

In this section we demonstrate the feasibility of our approach for field studies by application to a large-scale 3-D example. For modeling fluid flow in the reservoir we have used a commercial finite-difference simulator (ECLIPSE[34]) for this case. The dual porosity two phase model used is completely general and accounts for all relevant mechanisms such as fracture-matrix transfer, compressibility, gravity and capillary effects and other cross-streamline fluxes. As mentioned before, we use streamlines and time of flight derived from the finite difference simulator to compute the sensitivity of the production data with respect to reservoir parameters. It is important to note that we do not need to solve the 1-D transport equations along streamlines for computing the sensitivities. Instead, the saturation of the outlet block from the finite difference solution is used directly to compute the fractional flow derivative in **Eq. 15**. This makes the sensitivity computation very fast even for finite-difference simulators and the additional work required involves only streamline generation, computation of the time of flight and the solution of 1-D integrals along streamlines to compute the travel time sensitivities. We must emphasize here that the streamline-derived sensitivities are only approximate, particularly in the presence of compressible flow and strong matrix-fracture coupling. Nevertheless, our experience shows these sensitivities are adequate for inversion purposes and do not have any noticeably adverse impact on the convergence of the solution. Our hybrid workflow capitalizes on the strengths of the two approaches to make fracture flow inversion efficient and at the same time broadly applicable. A flow chart depicting the outline of our procedure is shown in **Fig. 9**. There are 4 main steps involved in the iteration loop

- Fluid flow simulation using a dual porosity finite difference simulator.
- Use of finite-difference velocity field to obtain streamlines, time of flight and travel time sensitivities at specified time intervals, particularly at changes in well events.
- Use of generalized travel time to quantify data misfit.
- Iterative minimization for model updating and history matching until convergence.

Large-Scale 3D Example. This synthetic example is designed after a carbonate reservoir in west Texas. The dual porosity reservoir model used here has a mesh size of 58x53x10 with a total of 30,740 grid cells that represent the fracture permeability distribution. To start with, we generated a reference fracture pattern distribution using a discrete fracture network (DFN) model. The DFN model was generated on a layer by layer basis using pre-specified distributions that control fracture length, height, aperture and azimuth inside elliptical fracture swarms. The motivation behind using the DFN model is that we can use fracture parameters derived from seismic lineament maps, image logs, regional stress studies etc. to generate realistic fracture distribution constrained to field data. The discrete fracture pattern was then converted to a continuum model using grid block permeability multipliers as discussed before. **Fig. 10** shows the reference fracture permeability for the ten layers. Clearly, the layers 2, 4, 7 and 9 are highly fractured and will have a significant impact on the flow behavior. For comparison purposes, **Fig. 11** shows the

discrete fracture networks for layers 2, 4 and 7. The fracture permeability varies over three orders of magnitude from a minimum of 2.5 md to a maximum of 1600 md. The matrix permeability was fixed at 1 md.

There are 31 producers and 11 injectors in the model which consist of 11 inverted 5-spot patterns covering 320 acres. The detailed production rates and well schedule including infill drilling, well conversion and well shut-ins can be found elsewhere.[7] **Fig. 12** shows the well locations and the streamlines at the end of 7500 days of simulation. Just as in streamline simulation, we generate the streamlines only when there are significant changes in the well events or boundary conditions. These streamlines are then used to compute the time of flight and travel time sensitivities in **Eq. 15.** For this example we used 11 streamline updates to account for changing well conditions during the sensitivity computations.

For demonstration of our production data integration approach, we will start with two different prior models and match the water-cut history obtained from the reference permeability field. The first model was generated using 50% of the fractures and fracture swarms in the reference fracture distribution (**Fig. 11**). Thus, the prior model contained altogether about a quarter of all the fractures in the reference model. The second model contained 75% of the fracture and fracture swarm information and thus had approximately half of all the fractures in the reference model. The fracture porosity was kept fixed at 0.03.

Prior Model-1: 50% Fracture Information. In this example we retain 50% of the information in the reference fracture pattern (**Fig. 11**). Both the fracture swarm location and the fracture density within the swarms were included as part of the prior information. The discrete fracture pattern generated is shown in **Fig. 13** for layers 2, 4 and 7. The prior permeability distribution is shown in **Fig. 14**. As expected, the prior model exhibits less connectivity and fewer preferential flow paths compared to the reference model. The final permeability field after matching water-cut response at the producers is shown in **Fig. 15**. The water-cut response from the prior model for 30 producers is shown in **Fig. 16**. In the same figure we have superimposed the water-cut response from the reference model. Clearly, we see a large discrepancy in the production response because of the lack of fracture connectivity and permeability contrast in the prior model. After inversion, a close agreement is obtained between the reference and the calculated production response as shown in **Fig. 16**. On comparison of the final permeability field with the reference permeability distribution, we see that we are able identify the dominant flow paths in the reference model through the integration of production data. For example, in layers 2 and 7 (**Fig. 17)**, the inversion process re-establishes the high contrast and recovers some of the connected pathways seen in the reference model. We can see similar effects across many of the layers. However, the results also underscore the inherent non-uniqueness in the solution, particularly in 3-D because of the large degree of freedom for these flow paths. This makes prior information vital to the success of the inversion. Finally, **Fig. 18** shows the convergence of the inversion as a function of number of iterations. Both travel time misfit and overall water-cut misfit are reduced significantly after 20 iterations. The entire history matching took 3.2 hours in a PC (Intel Xeon 3.06 GHz Processor).

Prior Model-2 : 75% Fracture Information. The prior model for this example was generated by retaining 75% of the information regarding fracture swarms and fracture density within swarms. Again, the discrete fracture network generated for layers 2, 4, and 7 are shown in **Fig. 19**. The permeability distribution is shown in **Fig. 20**. As expected, the prior model for this case

shows a closer resemblance to the reference permeability field. This is also reflected in the computed water-cut response shown in **Fig. 22**. Clearly, the production response for this model is much closer to the reference production history compared to the previous model. Although many of the wells show good match, the lack of fracture connectivity and permeability contrast still impacts the production response of several wells, for example, wells 2, 3, 8, 9 and 14, among others. After inversion, we obtain excellent agreement for all wells as shown in **Fig. 22**. The final permeability field after inversion is shown in **Fig. 21.** On closer observation, for example, layers 3 and 5 (**Fig. 23**), we see that we are able to match the production data with minimum deviation from the prior model. This is expected because of the higher fracture information in the prior model. Also the inverse algorithm by design attempts to preserve prior information to maintain geologic realism.[31] **Fig. 24** shows the misfit reduction as a function of the number of iterations for this example. Again, the misfit is reduced by almost an order of magnitude.

Finally, on comparing the results of inversion using the two different prior models, we can clearly see the role of prior information in our ability to predict fluid flow through fractured reservoirs. Although we were able to match the production history reasonably well starting with 50% fracture information, the results improved significantly when additional fracture data were incorporated. This observation is true for inverse modeling in general; however, the impact is expected to be more pronounced for fractured reservoirs because of the high contrast between the fracture and matrix permeability and the role of preferential fracture flow paths on the overall flow behavior. The inverse problem is ill-posed and we can not expect to reproduce the details of the fracture pattern in the reference model. However, we can reduce the non-uniqueness by anchoring the solution close to the prior model. By starting with different prior models and matching different 'realizations' of the production data, we can explore the uncertainty space by sampling from the posterior distribution.[35]

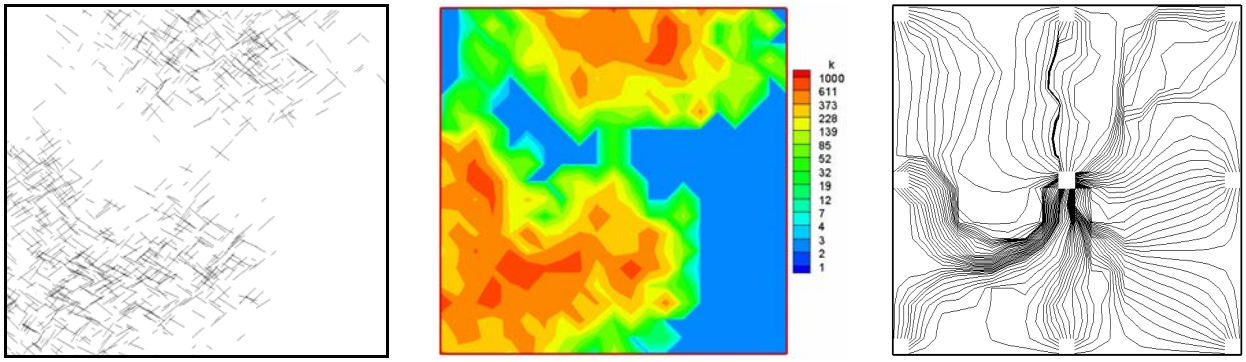

(a) Discrete fracture network (b) Reference fracture permeability (c)Streamline pattern

Fig. 1— Reference model for the 9-spot 2D case

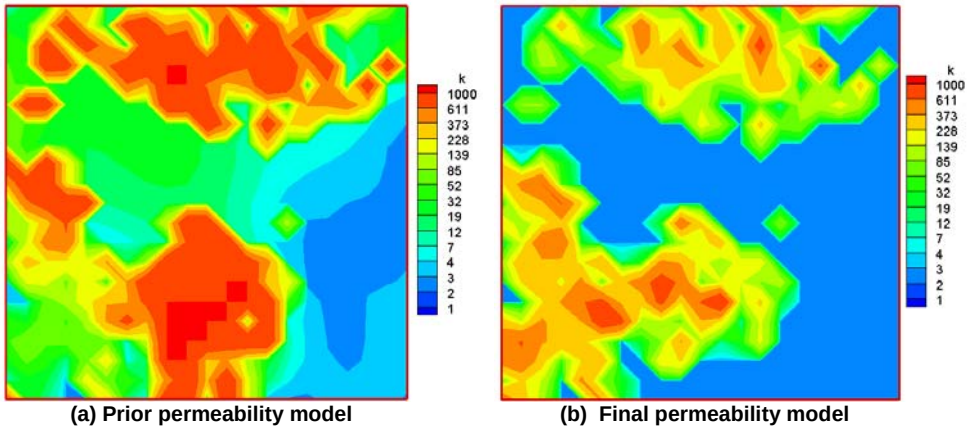

(a) Prior permeability model (b) Final permeability model

Fig. 2— Prior and final permeability models after integrating water cut data.

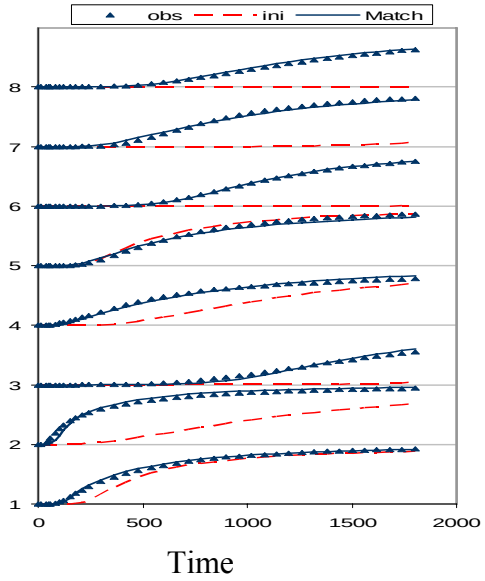

Fig. 3— Initial and final water cut match.

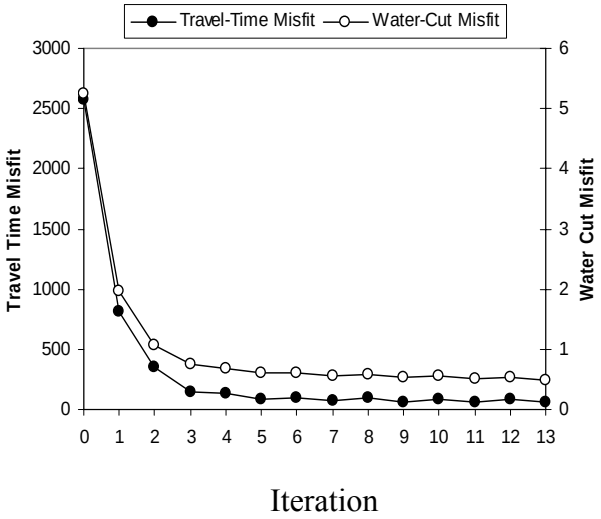

Fig. 4— Data misfit vs. number of iterations.

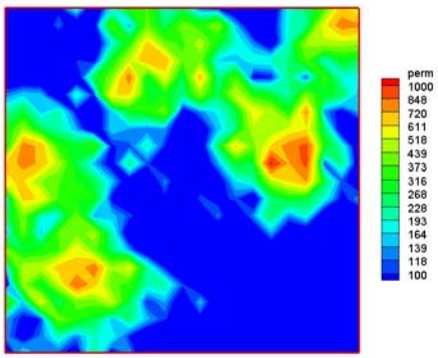

(a) Permeability field

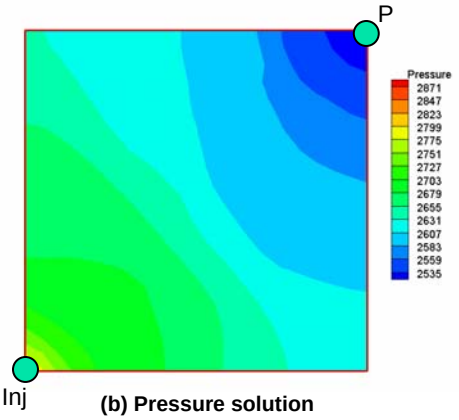

(b) Pressure solution

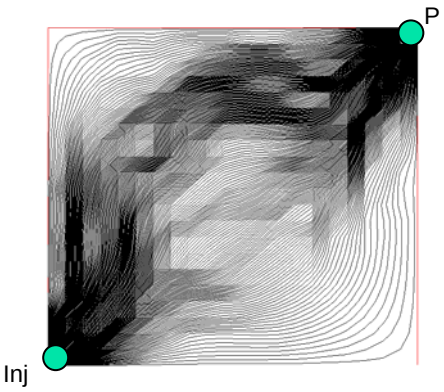

(c) Streamlines

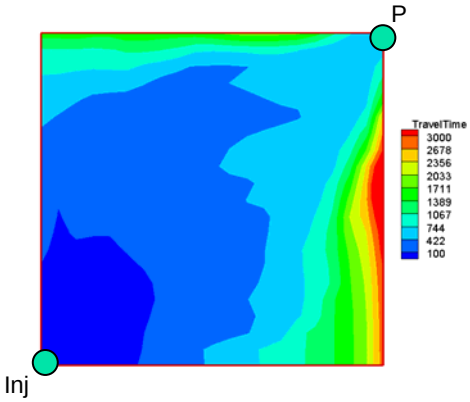

(d) TOF map

Fig. 5— Streamline and time of flight (TOF) calculations.

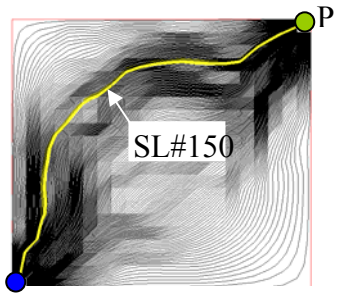

(a) 1-D streamline solution

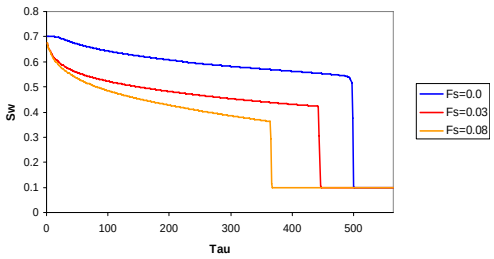

(b) Fracture Saturation

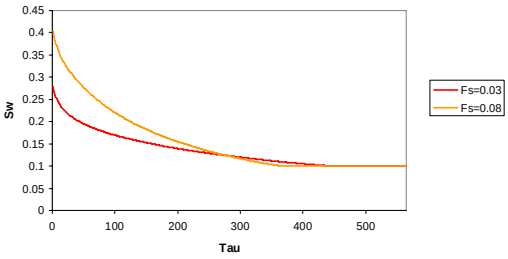

(c) Matrix Saturation

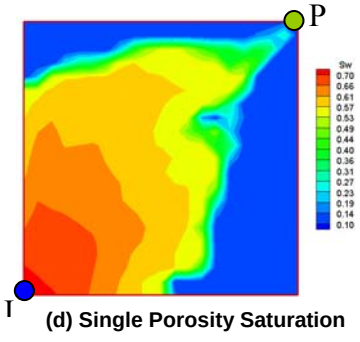

(d) Single Porosity Saturation

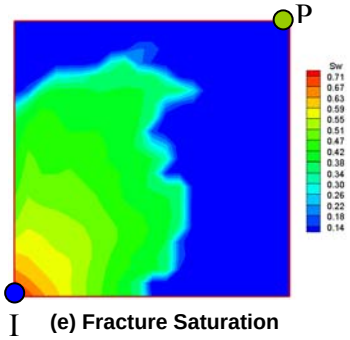

(e) Fracture Saturation

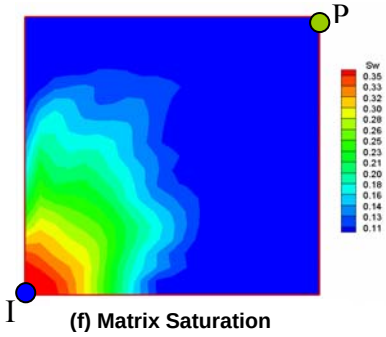

(f) Matrix Saturation

Fig. 6 —Saturation evolution along streamlines – single and dual porosity examples.

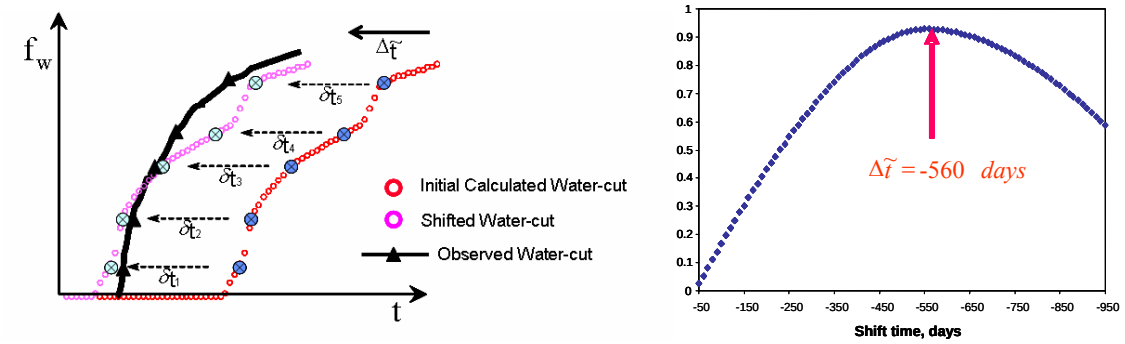

(a) Time shift (b) Maximizing correlation

Fig. 7—Illustration of generalized travel-time inversion: (a) History-matching by systematically shifting the calculated water-cut to the observed history, (b) Best shift-time that maximizes the correlation function.

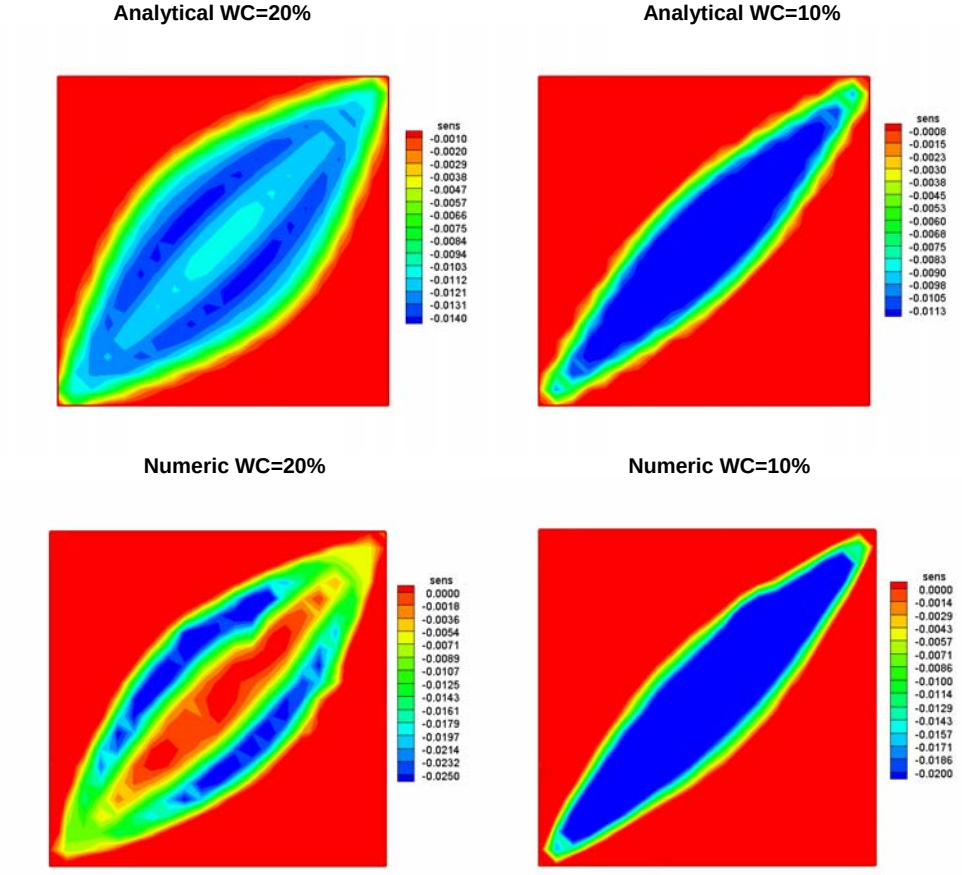

Fig. 8— Comparison of numerical and analytical sensitivities in a ¼-five spot pattern.

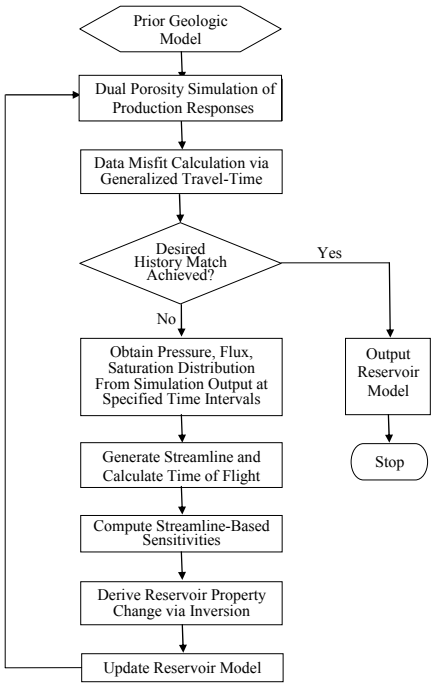

Fig. 9—— Flowchart for history matching dual porosity finite-difference models using streamline-derived sensitivities.

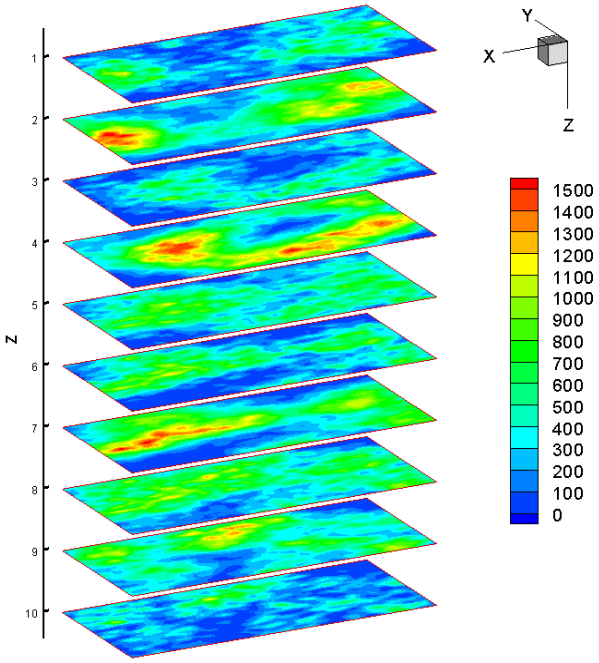

Fig. 10—Reference fracture permeability distribution.

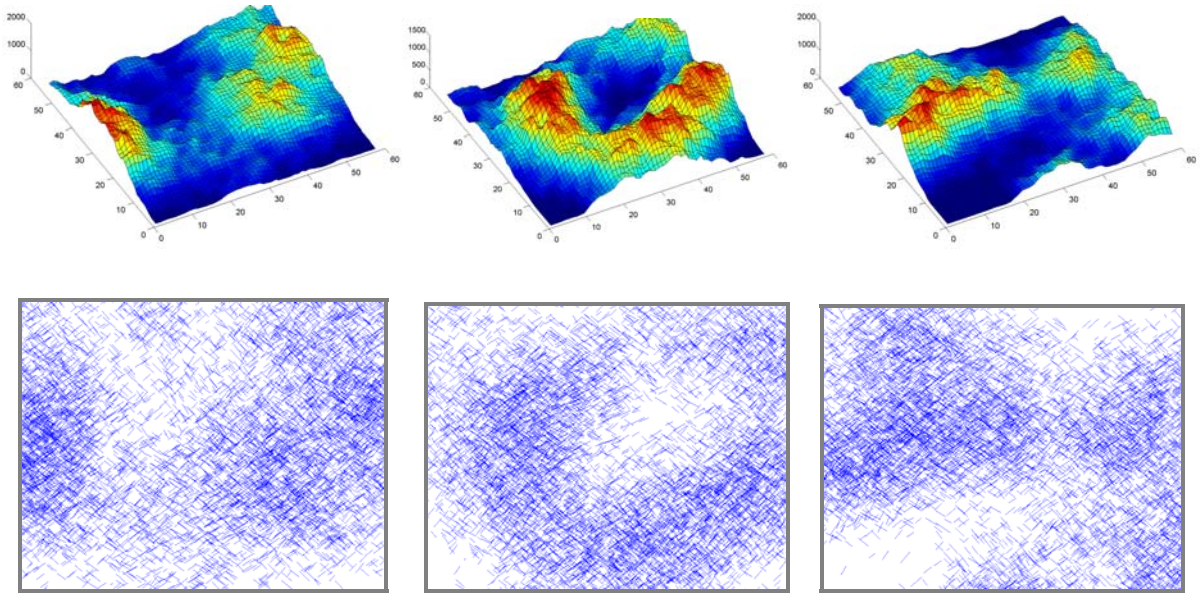

(a) Layer 2 **(b) Layer 4** **(c) Layer 7**

Fig. 11—Discrete fracture layers converted to permeability (upper panel) using fracture intensity

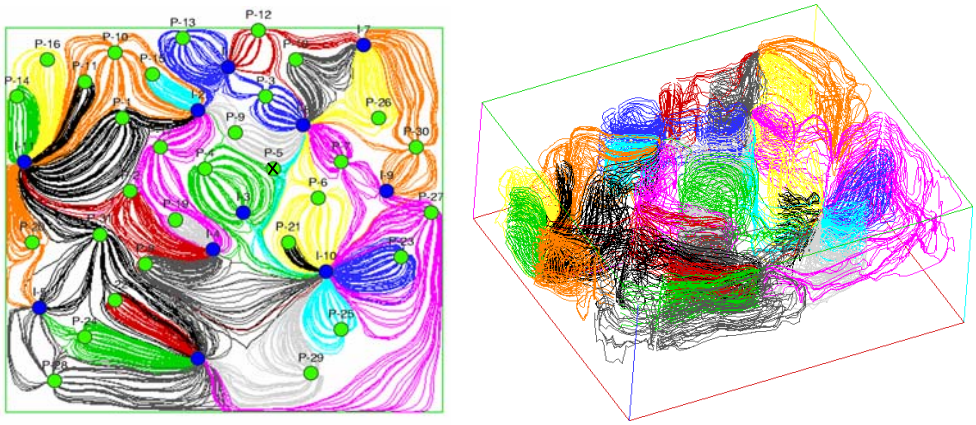

(a) Well locations and streamlines

(b) 3D Streamlines

Fig. 12—(a) Top view shows well locations and streamlines at the end of the last update. (b) 3D streamlines traverse layers in 3D space.

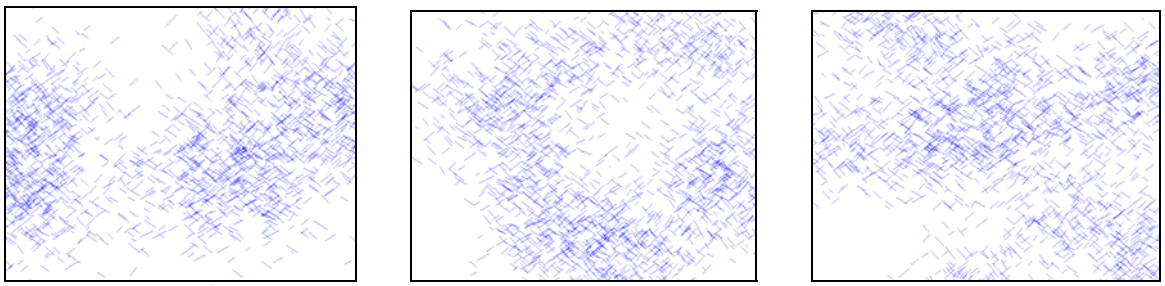

Layer#2 Layer#4 Layer#7

Fig. 13—Discrete fracture networks for 3 different layers with 50% fracture information.

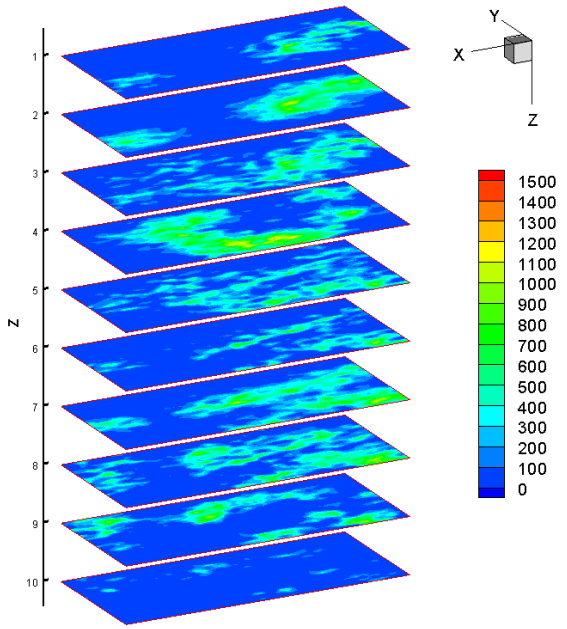

Fig. 14— Permeability distribution for prior model with 50% fracture information.

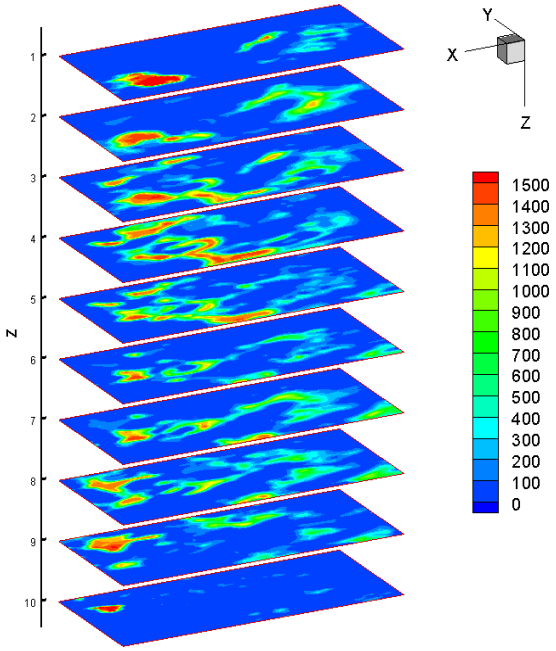

Fig. 15—Final permeability distribution after water cut integration.

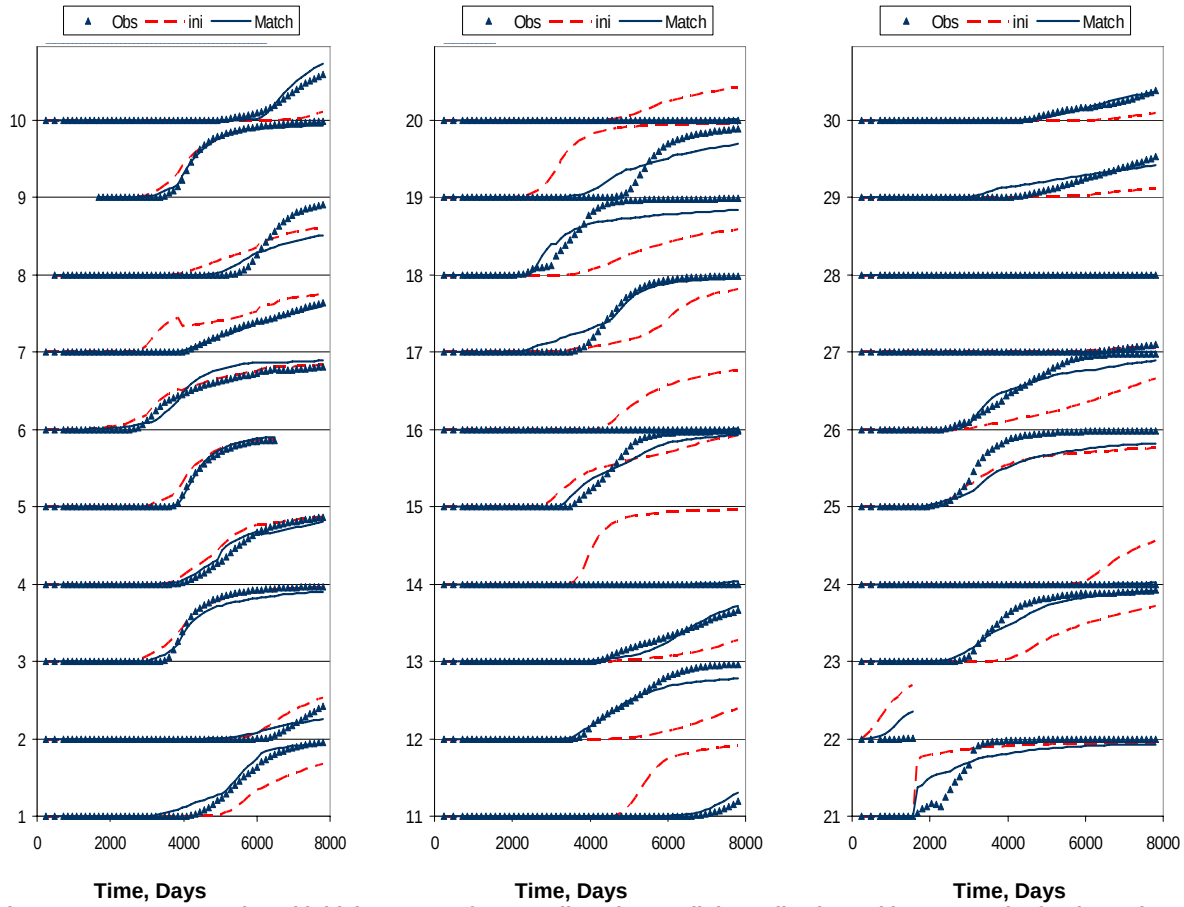

Fig. 16— Water cut match and initial response for 30 wells. Almost all the wells showed better match after inversion.

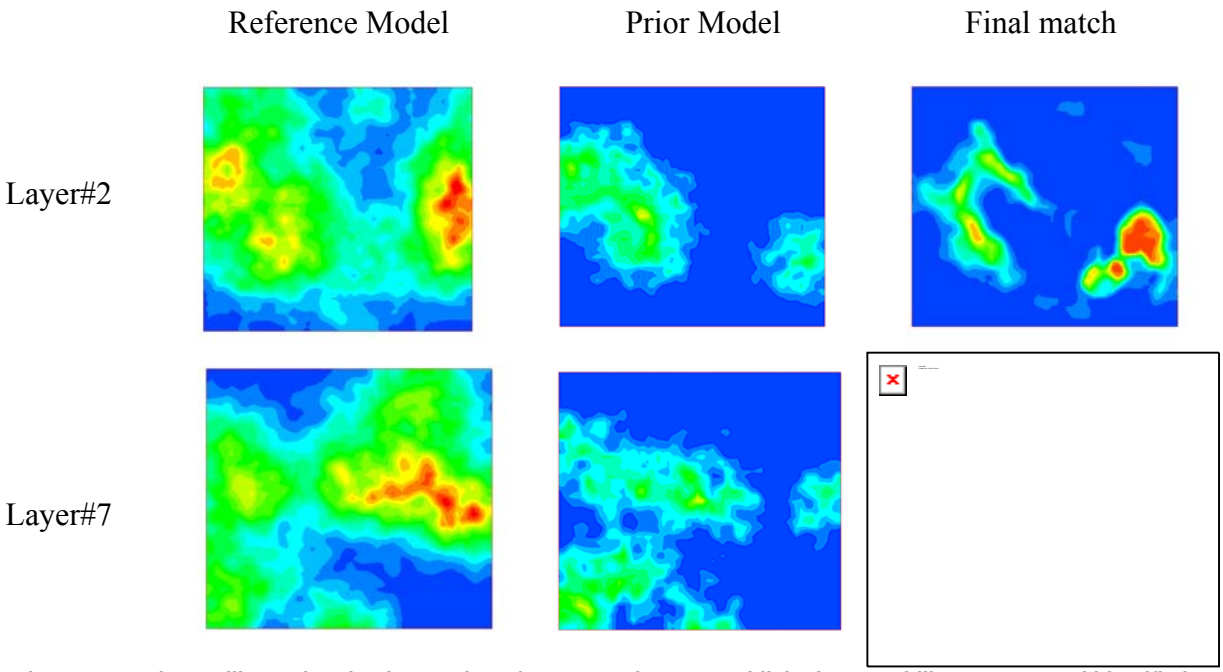

Fig. 17— Two layers illustrating that integration of water cut data re-established permeability contrast and identified major flow paths while preserving the prior information.

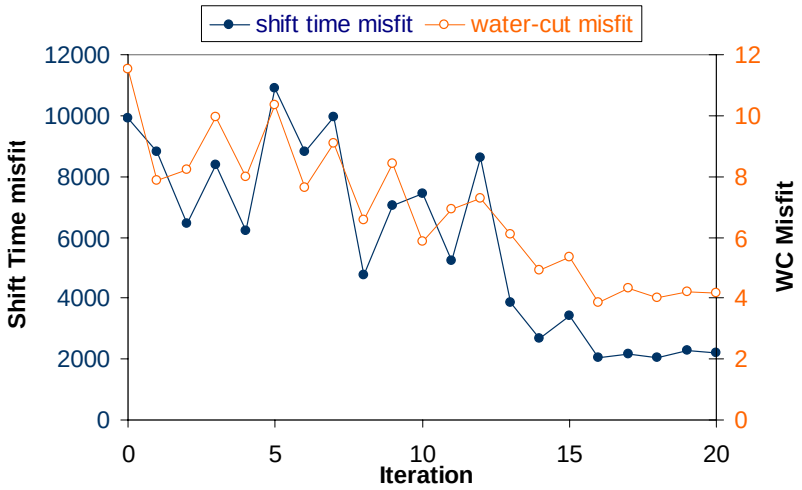

Fig. 18—Data misfit vs. iterations (prior model-1)

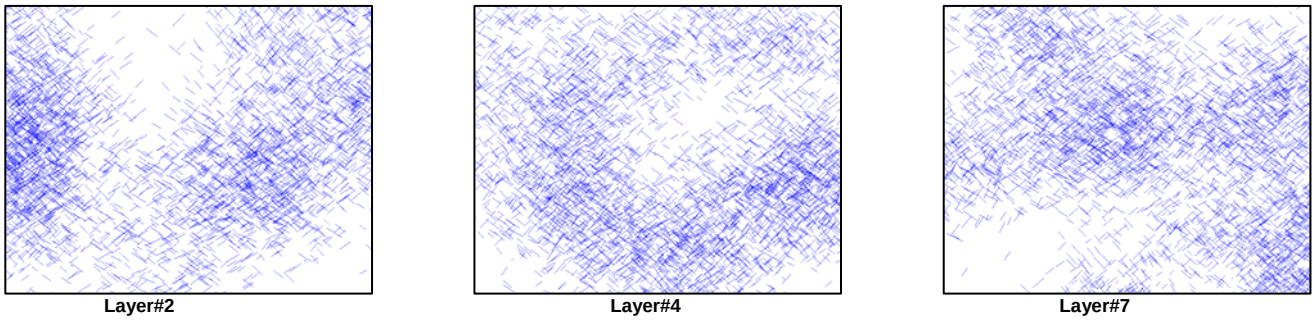

Fig. 19—Discrete fracture network for 3 layers with 70% fracture information

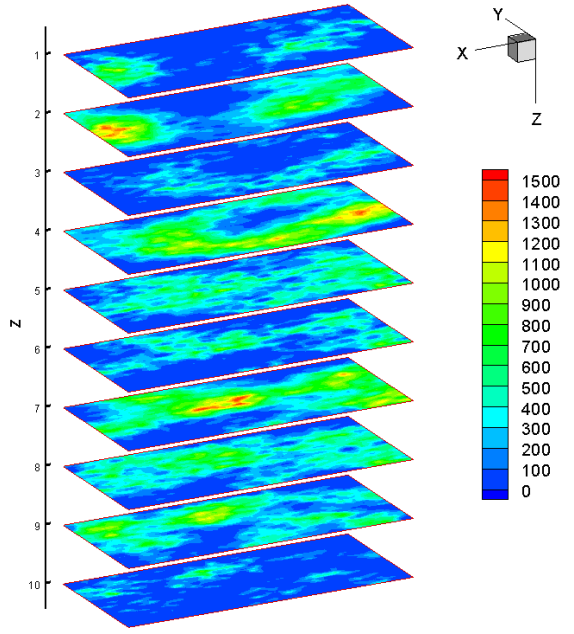

Fig. 20— Permeability distribution for the prior model with 75% fracture information.

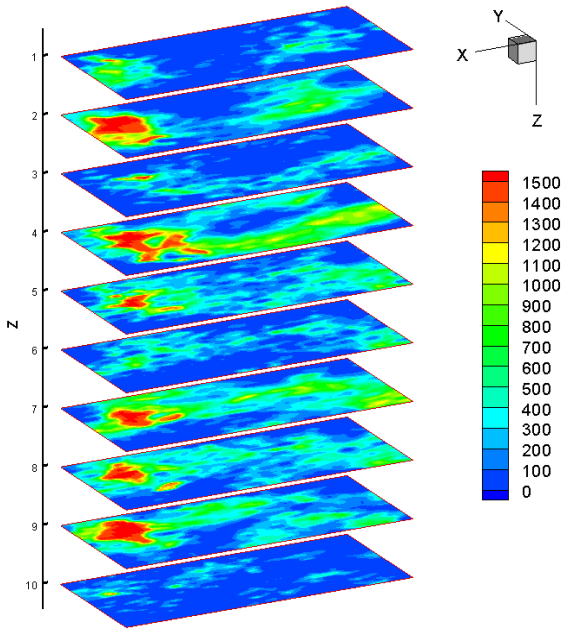

Fig. 21—Final permeability distribution after water cut integration.

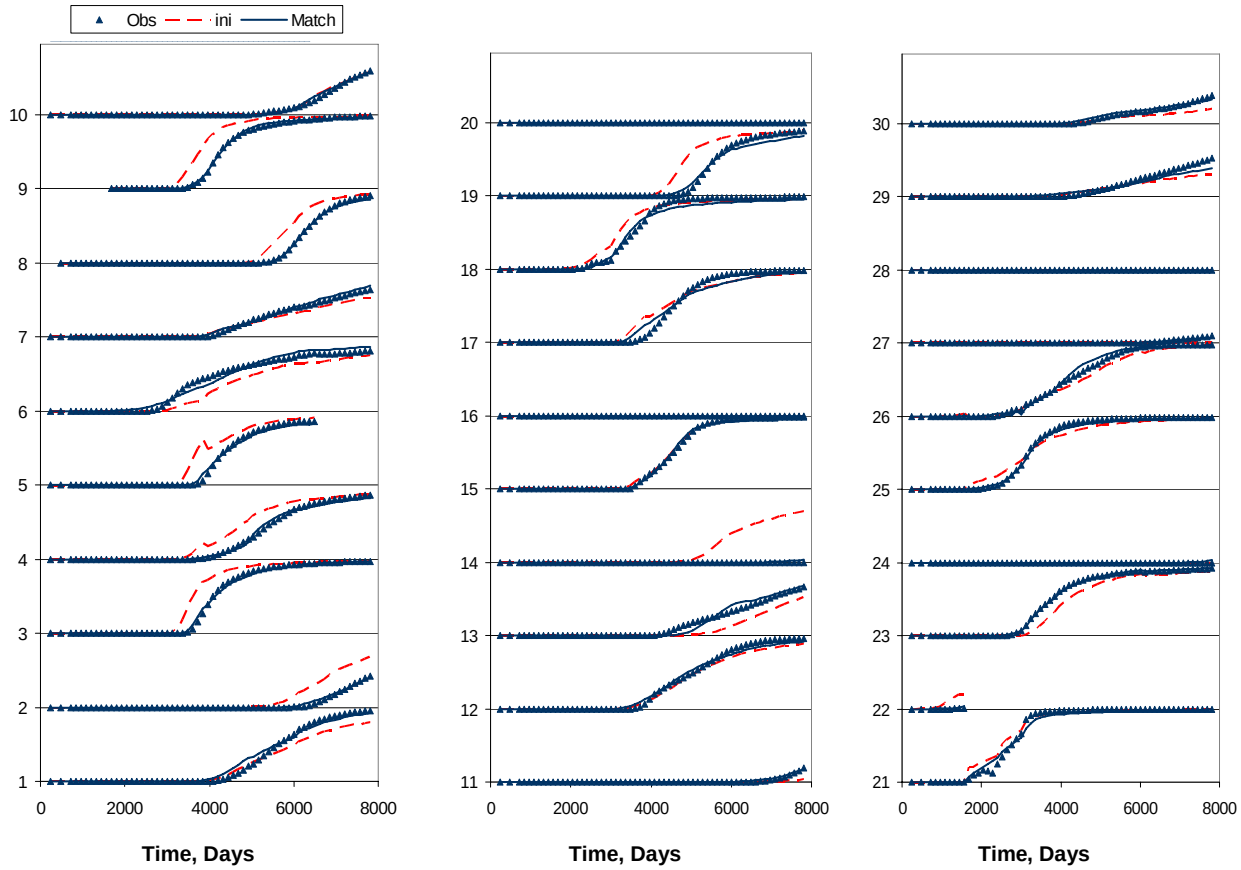

Fig. 22— Water cut Match and initial response for 30 wells for prior model-2.

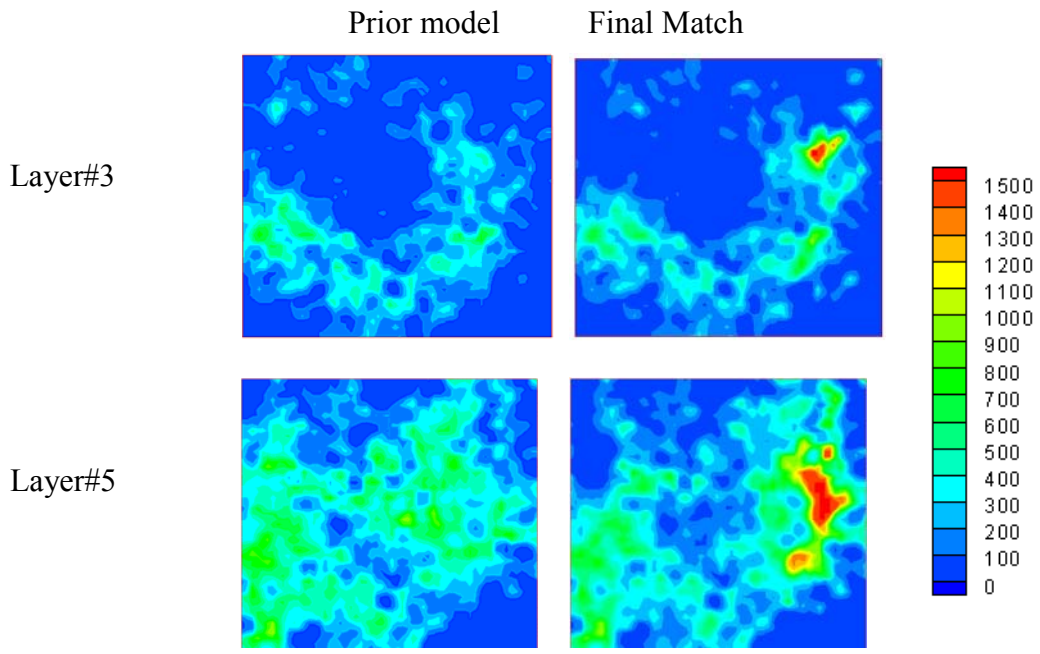

Fig. 23— Two layers illustrating changes to the prior model for matching production data. Note that much of the prior model remains unchanged to preserve geologic realism.

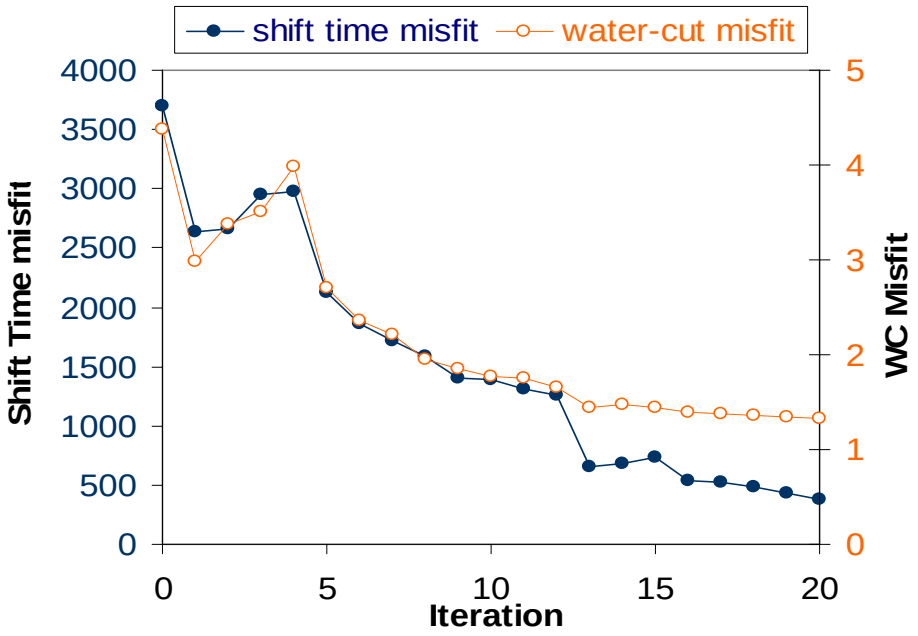

Fig. 24—Misfit vs. number of iterations (prior model-2)

RESULTS AND DISCUSSION: PART IVA

Field-Scale Design Optimization via Numerical Simulation: Use of Downhole Samplers for Test Design

Introduction

The past several years have seen a great increase in the development, deployment and application of permanent in-well fiber optic monitoring systems. In-well fiber optic sensors are either currently available or under active development for measuring pressure, temperature, flow rate, phase fraction, strain, acoustics, and sand production. Potential future sensor developments include measurement of density and fluid chemistry (Kragas et al., 2001). This study is a preliminary investigation of the use of downhole sensors to enhance the value of Partitioning Interwell Tracer Tests (PITTs). The idea being investigated is to measure the tracer concentrations in real time at multiple depths using downhole sensors. These tracer concentration data could be used to estimate oil saturations at the corresponding depths using the method of moments (Zemel, 1995) and/or inverse modeling (Yoon et al., 1999, Wu et al., 2002).

Preliminary Results

Partitioning interwell tracer tests were simulated for two cases. In each case, a tracer slug was injected and the produced tracer concentrations were measured for several layers corresponding to several depths in these production wells. Residual oil saturations were estimated and a vertical distribution of oil saturation was generated.

The first case illustrated is based upon a carbonate outcrop called Lawyer Canyon in the San Andres formation. The outcrop geology is quite similar to the oilfields of West Texas and consists of highly cyclic Permian dolomitized shallow water platform carbonates (Jennings et al., 2000). Figure 1 shows the location of the outcrop and the associated geology. A vertical cross-section of 150 feet long by 100 feet wide by 10 feet thick was simulated. The geometrically averaged horizontal permeability is 13 md and the porosity is 0.15. Residual oil saturation distributions were generated using an exponential relation with the permeability. The average residual oil saturation is 0.35. Figures 2 and 3 show the permeability and residual oil saturation profiles. The residual oil saturation was averaged for each simulation layer and is shown versus depth in figure 6.A tracer slug consisting of a conservative tracer and two partitioning tracers of partitioning coefficients 0.5 and 1.0 was injected. The injected volume of the tracer slug was 0.7 PV. Figures 4 and 5 show the tracer concentration curves for the top and bottom simulation layers The.bottom low permeability layers have greater tracer transit times, evident from figure 5. The method of moments (Zemel, 1995) was used to calculate the residual oil saturation for each layer from the simulated tracer concentrations. The major assumptions of the method are that the average oil saturation in the reservoir is constant with time and the partition coefficients of the tracers do not change during the test.

The average oil saturation in the swept volume can be calculated from PITT data using the following equations. The partition coefficient for tracer i between the oil phase and the mobile water phase is

$$K_i = \frac{C_{2i}}{C_{1i}}$$

where C2i is the concentration of tracer i in the oil phase and C1i is the concentration of tracer i in the water phase. The mean residence volume for a tracer i in a slug tracer injection is

$$\overline{V}_i = \frac{\int_0^\infty V C_{Di} dV}{\int_0^\infty C_{Di} dV} - \frac{V_{slug}}{2}$$

In the above equation V_{slug} is the volume of the injected tracer slug, C_{Di} is the normalized concentration of tracer i at the producer and V is the cumulative volume of fluid injected.
The oil saturation can be calculated by

$$S_o = \frac{\overline{V}_2 - \overline{V}_1}{(K-1)\overline{V}_1 + \overline{V}_2}$$

$\overline{V}_2$ is the mean residence volume of the partitioning tracer, $\overline{V}_1$ is the mean residence volume of the conservative tracer and K is the partition coefficient of the partitioning tracer.

Figure 6 shows the close match between the estimated and model oil saturations, for simulation runs with different vertical permeability values. The accuracy in estimation increases with decrease in vertical permeability due to decreased cross flow.

The second illustration is for a three-dimensional oil reservoir. The simulated field is a quarter of a 40 acre five-spot well pattern. For the permeability realization, the standard deviation in the natural logarithm of permeability was 1.61, the geometrically averaged permeability was 345 md, the correlation length in the vertical z-direction was 10 ft, and the correlation lengths in the horizontal directions were 100 ft. An exponential variogram was used to generate the permeability data. The permeability and oil saturation distributions have been presented in Figures 7 and 8. The injected volume of the tracer slug was 0.9 PV. Figure 9 shows the tracer concentration outputs for the first simulation layer. Figure 10 shows the close match between the estimated and model oil saturations. The same trend, as in the two-dimensional case of higher accuracies with decreasing vertical permeability is observed.

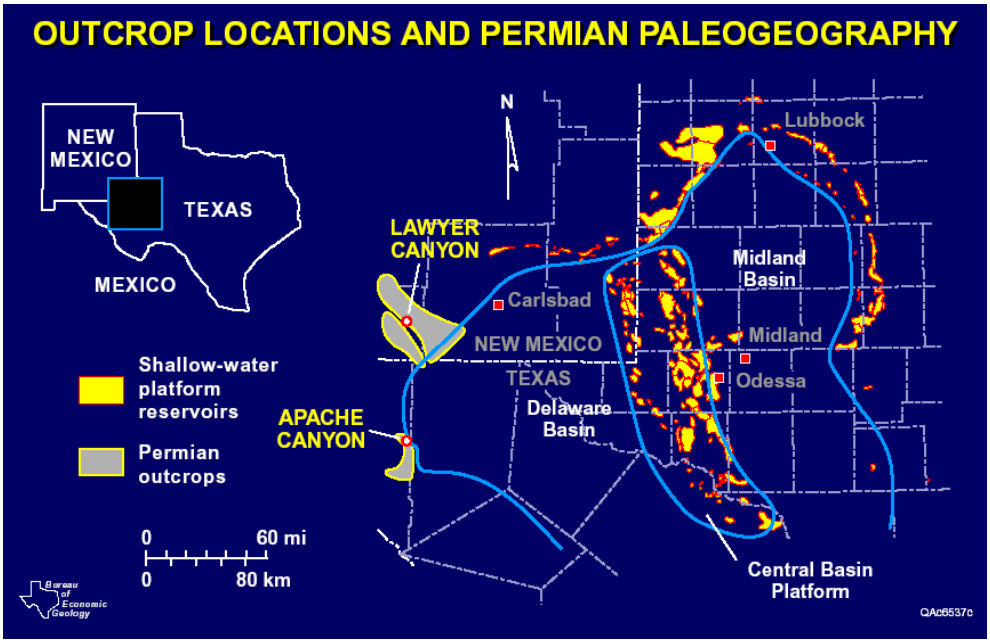

Figure 1**:** Map of geology and carbonate outcrop location of West Texas

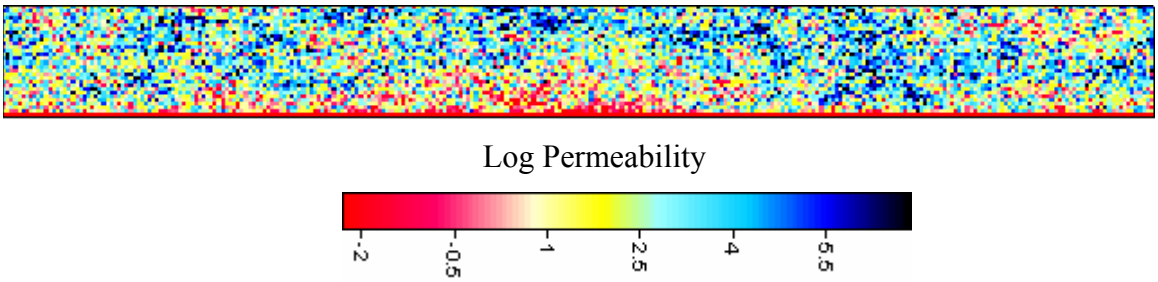

Figure 2: Horizontal permeability profile of Lawyer Canyon

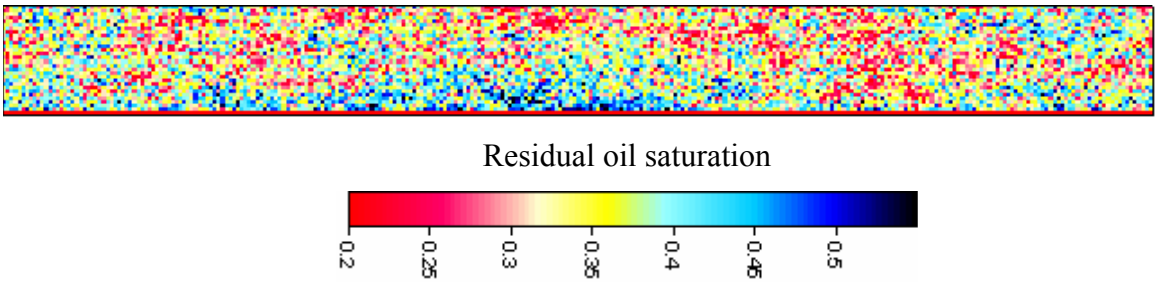

Figure 3: Residual oil saturation profile of Lawyer Canyon

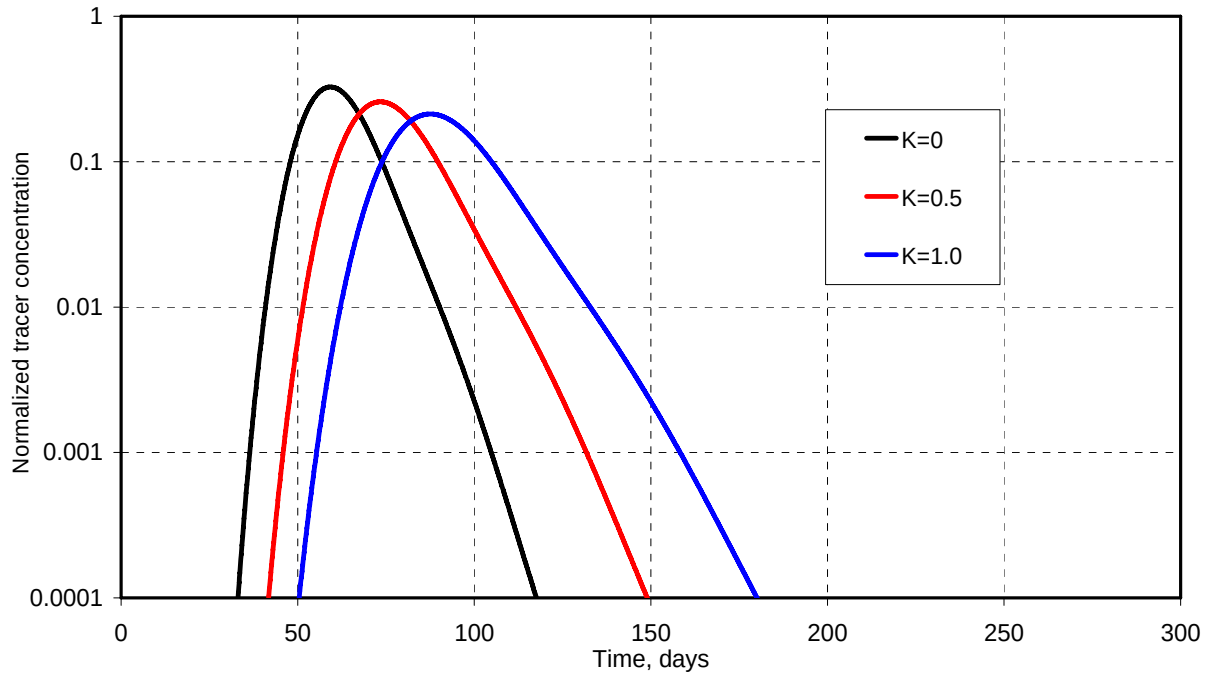

Figure 4: Normalized tracer concentrations for simulation layer 1 for Lawyer Canyon

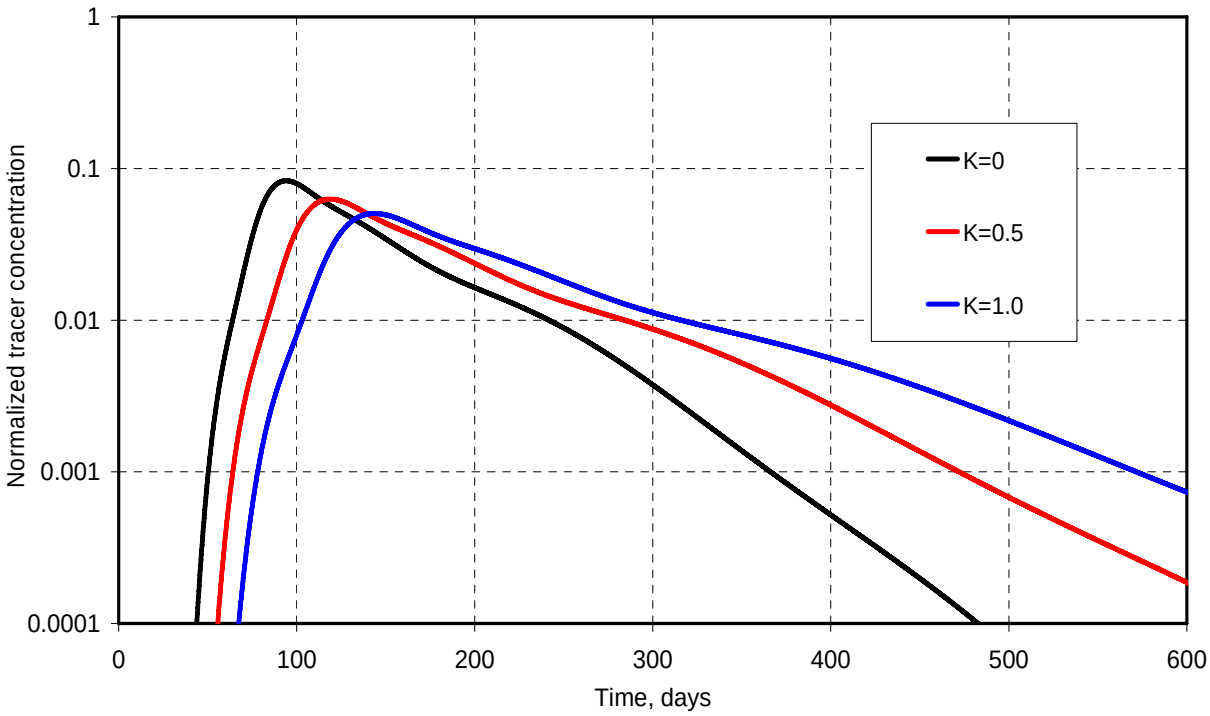

Figure 5: Normalized tracer concentrations for simulation layer 30 for Lawyer Canyon

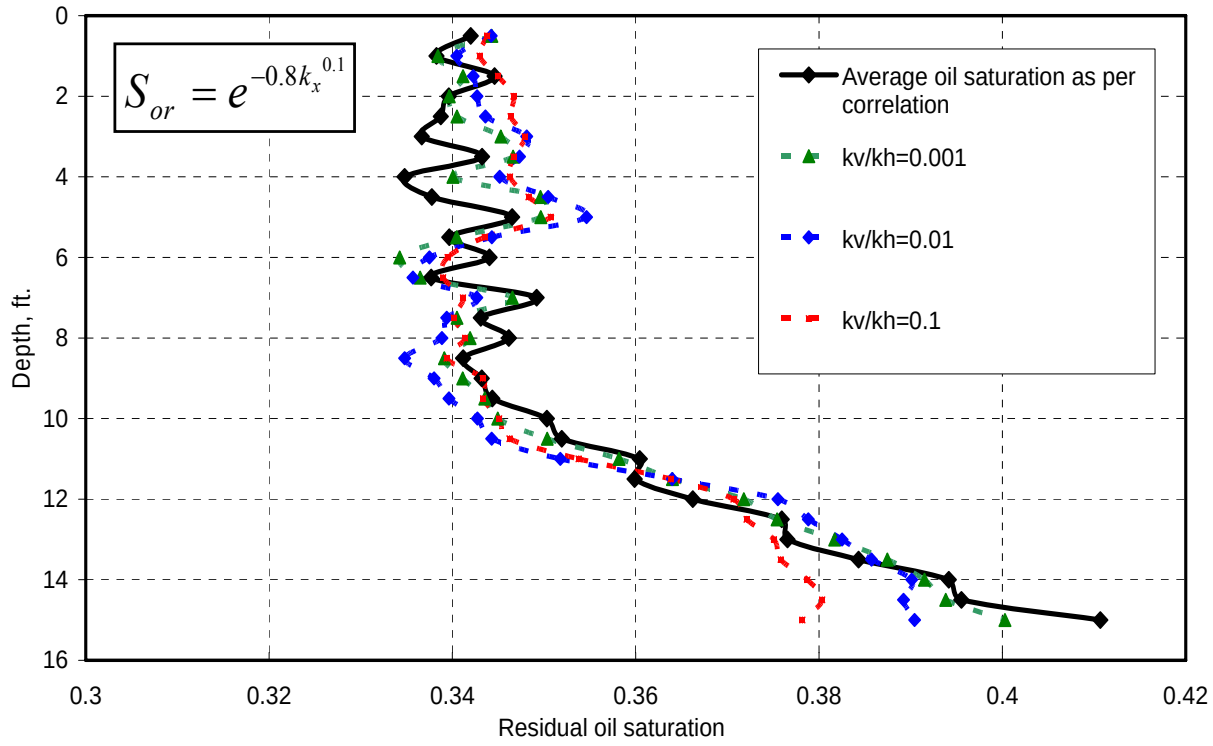

Figure 6: Estimated oil saturations for different vertical permeabilities for Lawyer Canyon

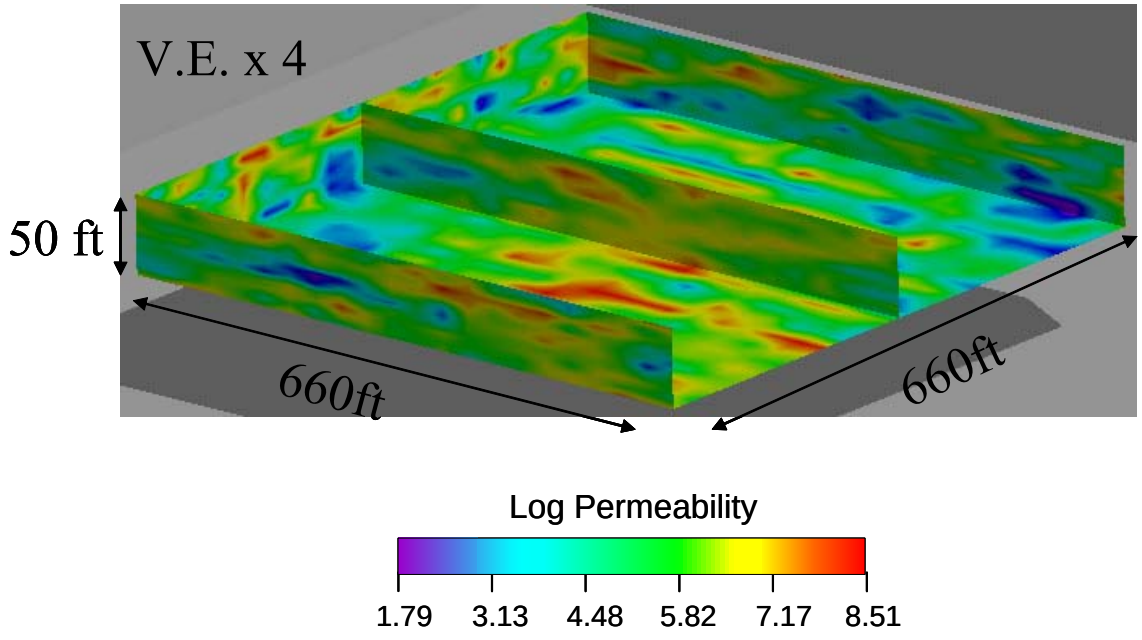

Figure 7: Permeability profile of the three-dimensional reservoir

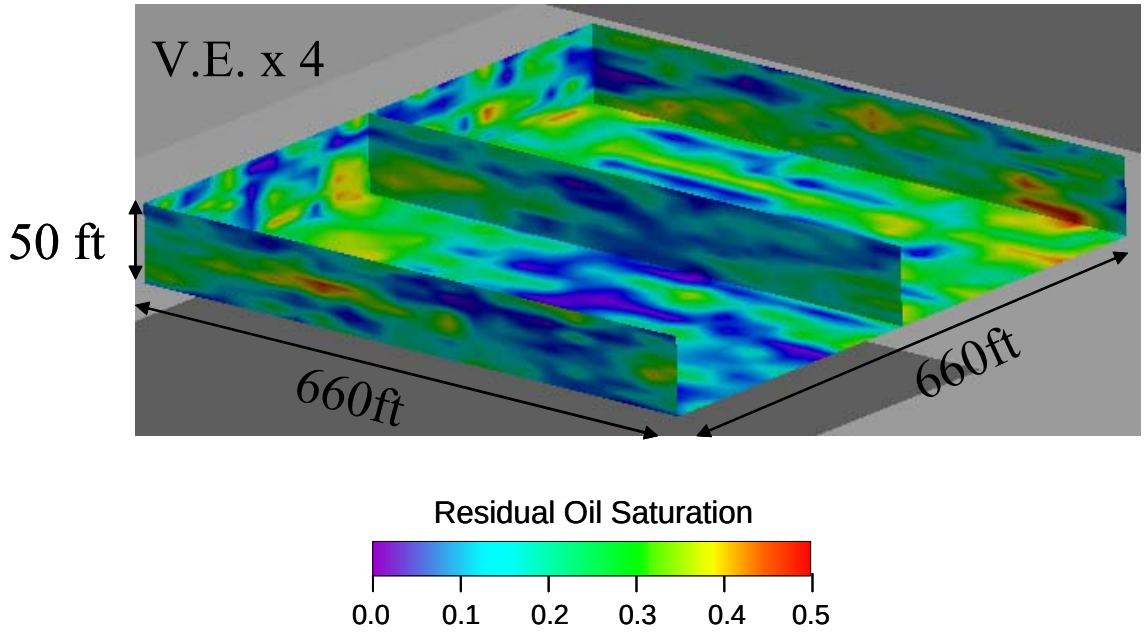

Figure 8: Residual oil saturation profile of the three-dimensional reservoir

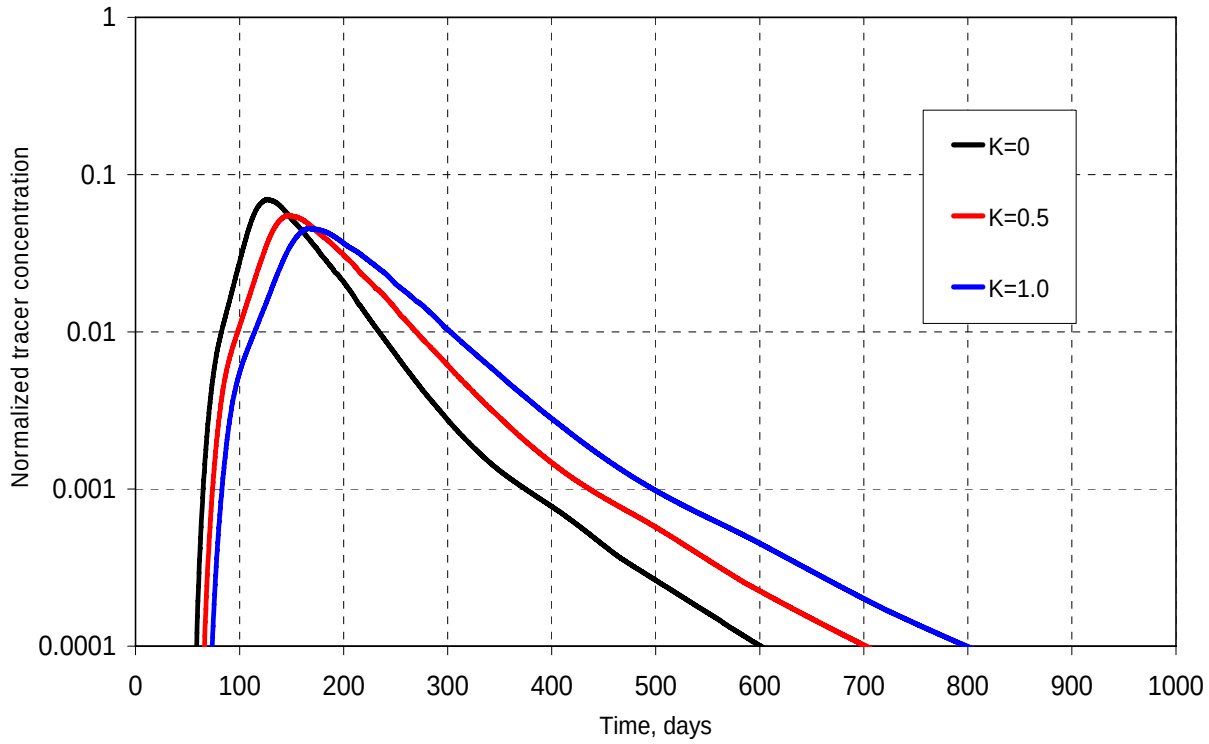

Figure 9: Normalized tracer concentrations at the producer for simulation layer 1 of the three-dimensional reservoir

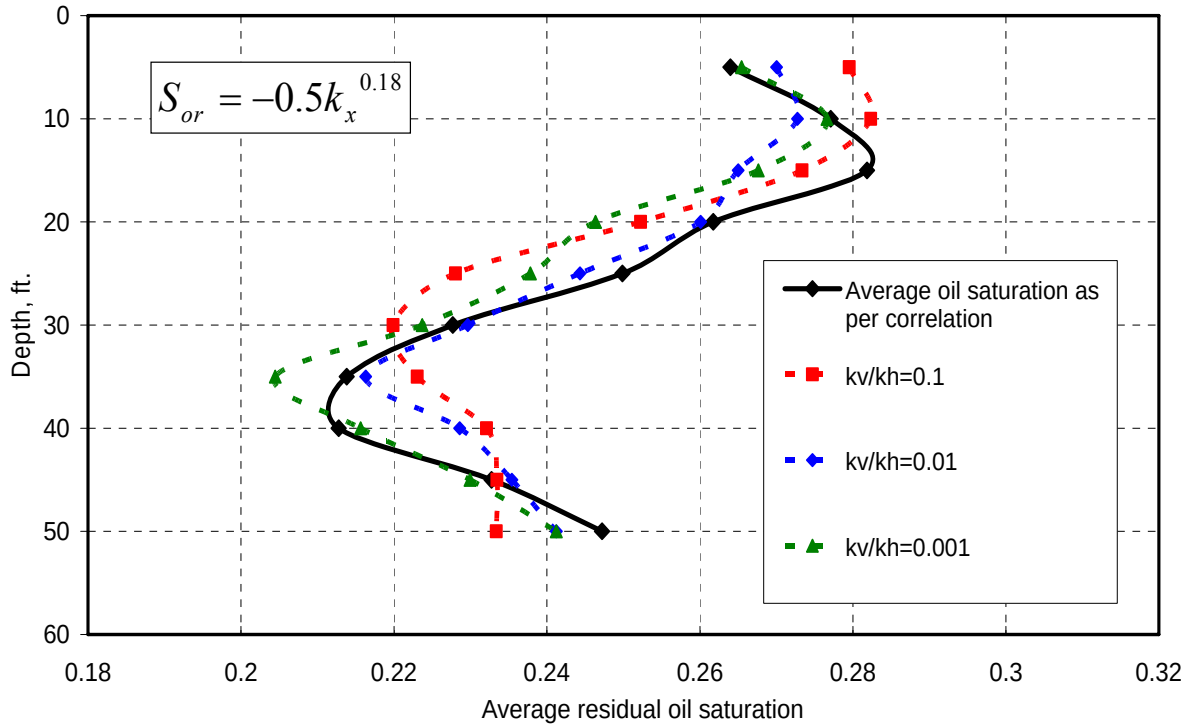

Figure 10: Estimated oil saturation for different vertical permeabilities for the 3 dimensional reservoir

RESULTS AND DISCUSSION: PART IVB

Field-Scale Design Optimization via Numerical Simulation: Use of Natural Tracers for PITT Design

Introduction

Crude oil is a mixture of organic components of varying water solubility. A novel idea being investigated in this research is to use some of the more water-soluble components of crude oil as natural partitioning tracers to estimate oil saturations and swept pore volumes, and hence as a substitute for injected tracers. The rate at which these components will dissolve into water will depend upon their partition coefficients under reservoir conditions. In this study we have identified some of the common components of crude oils that might be used as natural partitioning tracers. Equations have been derived to estimate pore volumes and average oil saturations in a reservoir for both single-phase and multiphase flow and two simulations used to illustrate their validity under the assumed conditions.

Preliminary Results

Water-soluble components of crude oil have been studied for various geochemical applications (Bennet et al., 1997; Larter et al., 1995; Taylor et al., 1997; Kharaka et al., 2000). Some of the most soluble components are phenols, benzoic acids, quinolines and aliphatic acids. Table 1 lists some representative partition coefficients (Bennet et al., 1997, Reinsel et al., 1994 and Taylor et al., 1997) with a wide range of values from 0.009 to 31.

The mass conservation equations can be integrated under remarkably general reservoir conditions to estimate oil saturations and pore volumes. The major assumptions are that the partition coefficients are constant and the volume of each component dissolved into the water is small compared to total oil volume, so that its dissolution has negligible effect on the saturations. In general, the equations can be applied to heterogeneous reservoirs with multiphase flow.

The first case illustrated is based upon a carbonate outcrop called Lawyer Canyon, reference of which has been made in the first part of the report. The field was simulated with single phase flow and a uniform residual oil saturation of 0.30. The residual oil was modeled as a mixture of four partitioning components. Table 2 outlines the components and their initial concentrations. A waterflood was simulated and component concentrations were measured at the producer. Figure 1 shows the concentration of the crude oil components at the producer. The concentration of these compounds decrease with time as they are stripped out of the oil phase in the reservoir. Concentration of any two compounds can be used for the estimation of pore volumes and average oil saturations. In the cases illustrated, butyric acid and phenol concentrations have been used for the estimation. Figures 2 and 3 show the comparison between the estimated and reservoir oil saturations and pore volumes.

The second illustration is a waterflood of a quarter of a 40 acre five spot well pattern. The standard deviation in the natural logarithm of permeability was 1.61, the geometrically averaged permeability was 277 md, the correlation length in the vertical direction was 10 ft, and the correlation lengths in the horizontal directions were 100 ft. An exponential variogram was used to generate the permeability data. Figure 4 shows the permeability profile for the simulation field. The field was simulated with a uniform initial oil saturation of 0.7. The oil was modeled as four partitioning components as in the previous illustration. Figure 5 shows the fluid production rates of the simulated water flood. Figure 6 shows the concentrations of the crude oil compounds

at the producer in the water phase. Figures 7 and 8 show the close match between the estimated and actual oil saturations and pore volumes.

Compound	**Partition Coefficient**
Acetic Acid	0.009
Butyric Acid	0.084
Phenol	1.3
p-Cresol	3.6
o-Cresol	5.2
2,4 Dimethyl Phenol	15
3 Isopropyl Phenol	31

Table 1: Partition Coefficients of crude oil compounds

Compound	**Partition Coefficient**	**Initial concentration in the oil phase, mg/l**
o-Cresol	5.2	7.5
Phenol	1.3	1.5
Butyric Acid	0.084	1
Acetic Acid	0.009	1

Table 2: Oil compounds modeled in the illustrated simulations

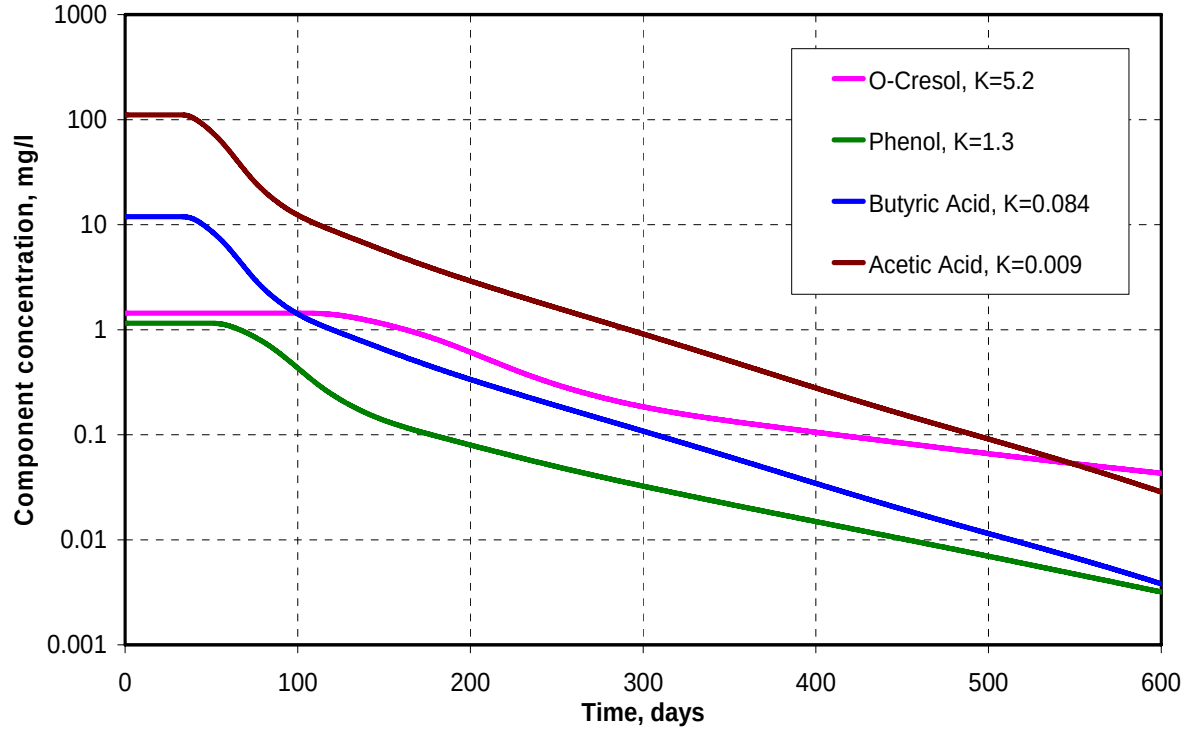

Figure 1: Total component concentrations at the producer for Lawyer Canyon

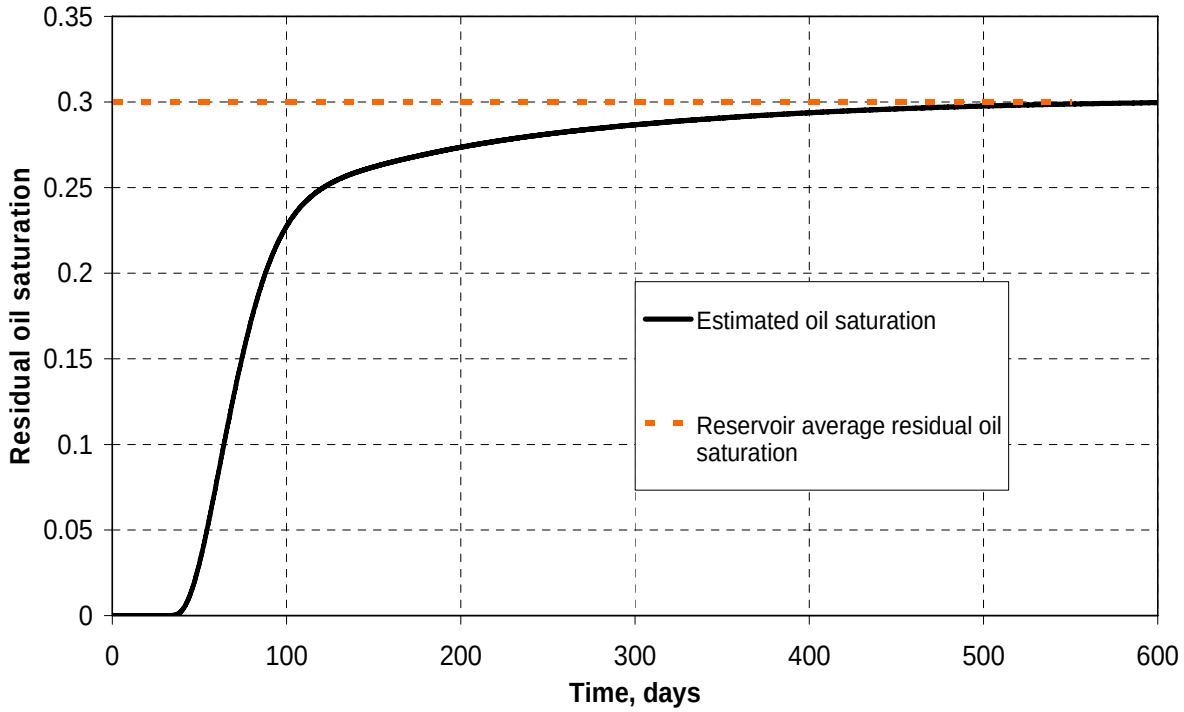

Figure 2: Estimated residual oil saturation for Lawyer Canyon using concentrations of Phenol and Butyric Acid

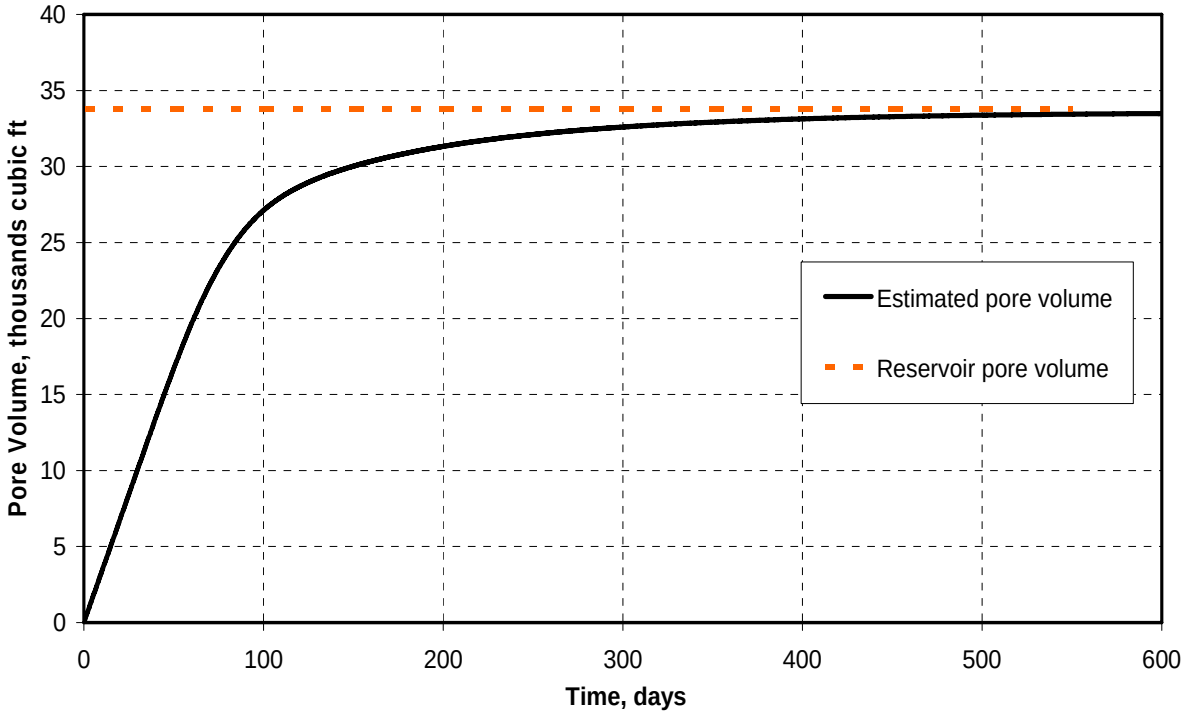

Figure 3: Estimated pore volume for Lawyer Canyon using concentrations of Phenol and Butyric Acid

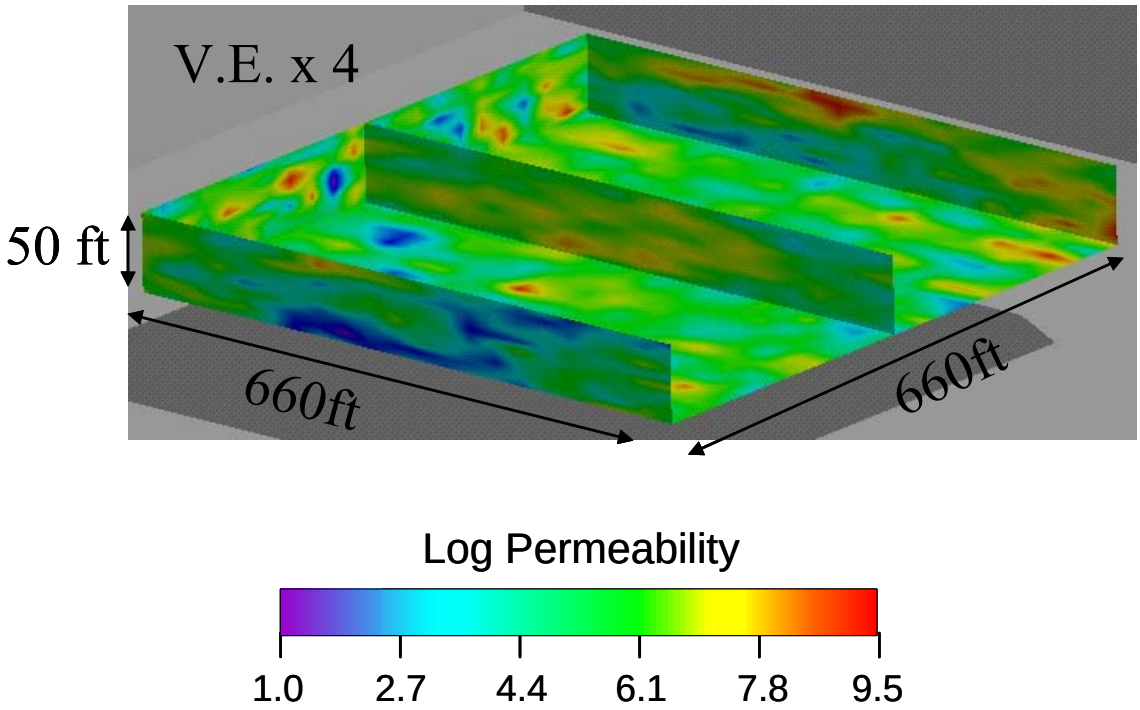

Figure 4: Permeability Profile for the 3 dimensional simulation

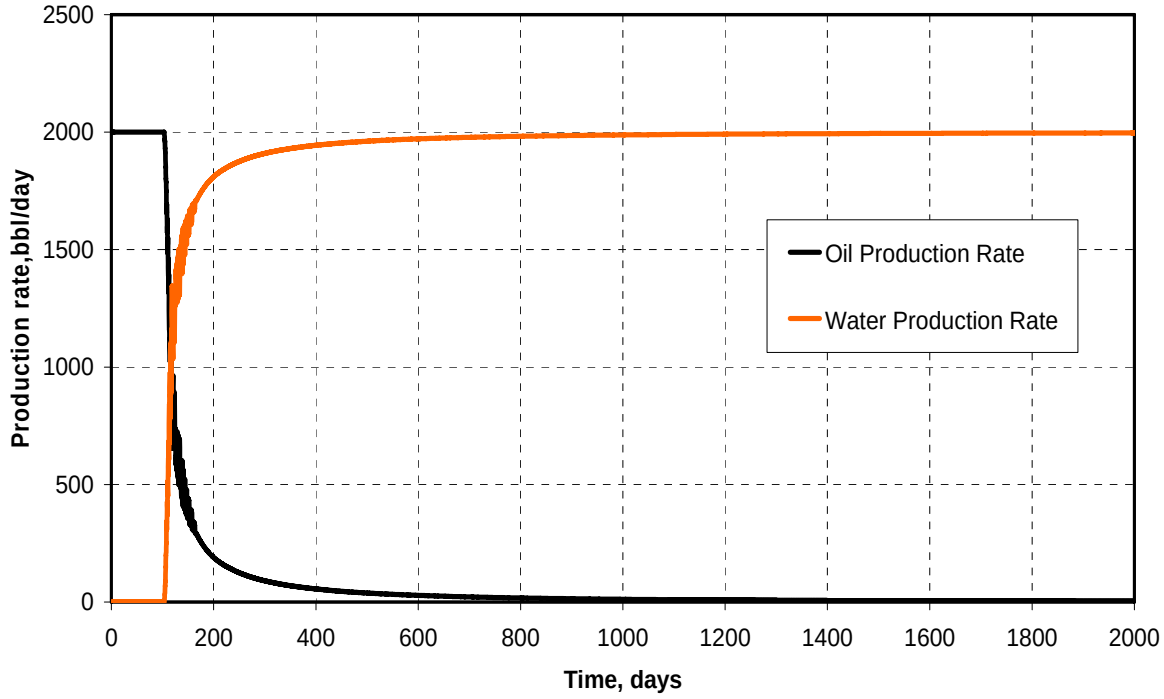

Figure 5: Fluid production rates for the 3 dimensional simulation

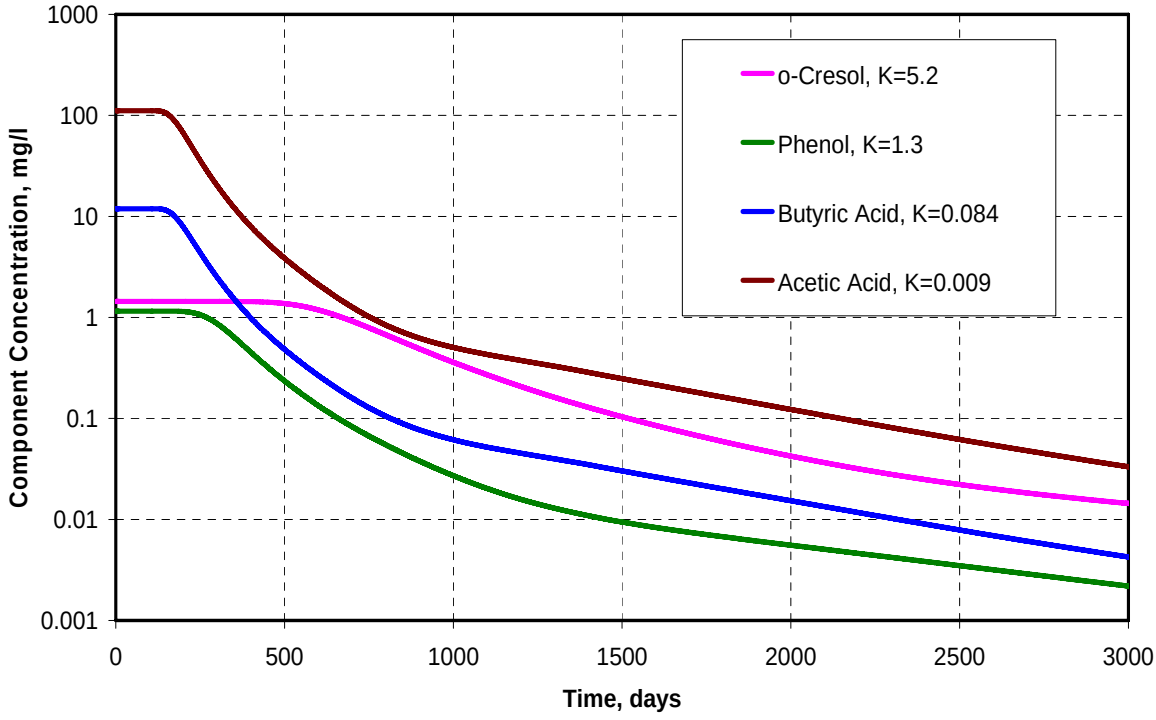

Figure 6: Component concentrations in the water phase at the producer for the 3 dimensional simulation

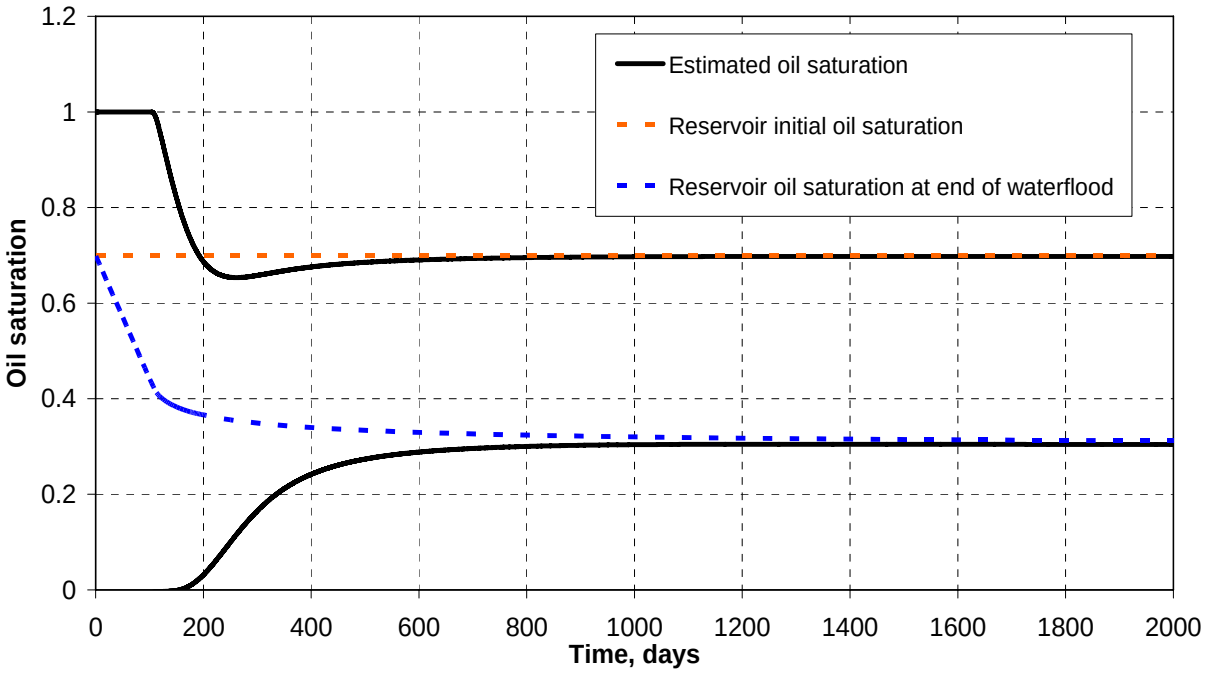

Figure 7: Estimated oil saturations using concentrations of Phenol and Butyric Acid for the 3 dimensional simulation

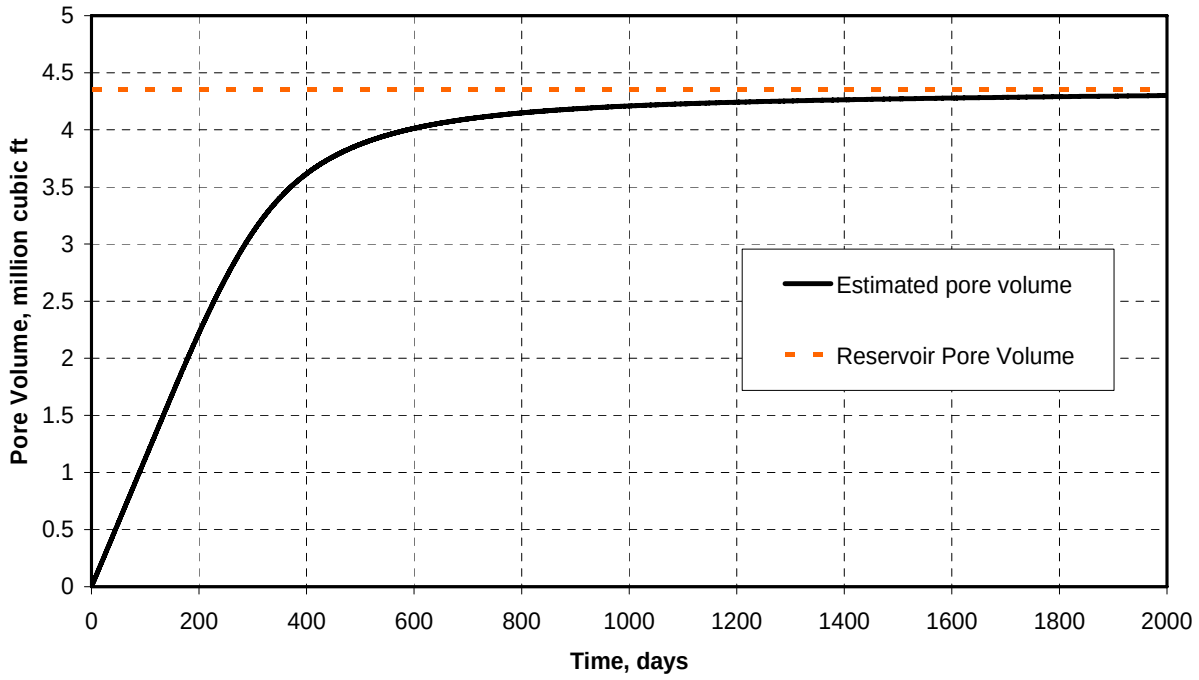

Figure 8: Estimated pore volume using concentration of Phenol and Butyric Acid for the 3 dimensional simulation.

RESULTS AND DISCUSSION: PART IVC

Field-Scale Design Optimization via Analytic Methods and Numerical Simulation

Introduction

Tracer tests have been used in the reservoirs for many years for evaluation of reservoir characteristics such as well communication, flow barriers, preferential flow paths, rate of movement of injected fluids, oil saturations and sweep efficiencies (Zemel, 1995). Partitioning interwell tracer tests have the advantage over single well tracer tests that they can be used to quantify the volume of both mobile and residual oil over the entire reservoir volume swept by the interwell tracers (Tang et al., 1991a, Tang et al., 1991b and Allison, 1998) rather than just the near well region. It is often the unswept oil far from the injection wells that is of most interest to reservoir engineers rather than the values at or even below residual oil saturation near the injection wells. During the past ten years, PITTs have been used extensively to measure the volume of organic liquid contaminants and/or average oil saturation in groundwater as well as in the soil above the water table.

The method of moments was developed for the analysis of both swept pore volume and the average oil saturation within swept pore volumes from PITT data in aquifers (Jin et al., 1995 and Jin et al., 1997). Dwarakanath et al. (1999) estimated the uncertainty in the oil saturation calculated by the method of moments caused by errors in experimental data. Jayanti (2003) studied the impact of heterogeneity on the accuracy of the oil saturation derived from tracer data. In this part of the report, we further develop and apply the method of moments to interpret partitioning interwell tracer data under a variety of oil field conditions.

Derivation of the Method of Moments

The derivation of the method of moments was been generalized to include the calculation of mobile oil saturation (two-phase flow) in three-dimensional, heterogeneous reservoirs including even naturally fractured reservoirs. The swept pore volume is defined as the pore volume of the reservoir contacted by the injected fluid. In general, a tracer is eventually produced at more than one producing well, so the concept must be associated with the volume swept between a particular injection well and a particular production well. Tracers can also be injected in different vertical intervals of the reservoir, so the swept pore volume must also be associated with the injection and production interval. The value of oil saturation must be associated with this swept pore volume to be meaningful. The swept pore volume is also of interest per se since the sweep efficiency is directly proportional to it.

The key equations needed to calculate swept pore volume and oil saturation are given below along with the key steps in the derivation of the method of moments. The mass conservation equations can be integrated under remarkably general conditions to estimate oil saturation and swept pore volume. The assumptions in the derivation of the equation are (1) the partition coefficient of each tracer is constant during the test, which is a very good approximation since very low tracer concentrations are used in practice (2) diffusion at the well boundaries is negligible, which has no practical effect on the results (3) there is no mass transfer of the tracers across the boundaries of the swept volume of interest and (4) the tracers are chemically stable during the test.

The mass conservation equation for tracer i flowing in the reservoir is

$$\frac{\partial \phi C_i}{\partial t} + \nabla \cdot \vec{N}_i = 0 \tag{1}$$

Where

$$C_i = \sum_{j=1}^{n_p} S_j C_{ij} \tag{2}$$

$$\vec{N}_i = \sum_{j=1}^{n_p} \left(C_{ij} \vec{u}_j - \phi S_j \vec{\vec{K}}_{ij} \cdot \nabla C_{ij} \right) \tag{3}$$

For a tracer slug injection over time period $0 \le t \le t_{slug}$

$$\begin{cases} C_{it}\big|_{injector} = C_{iJ}, & 0 \le t \le t_{slug} \\ C_{it}\big|_{injector} = 0, & t \ge t_{slug} \end{cases} \tag{4}$$

Multiplying Eq. (1) by time and integrating over time

$$-\phi m_{0i} + \nabla \cdot \int_0^\infty t \vec{N}_i \, dt = 0 \tag{5}$$

Where

$$m_{0i} = \int_0^\infty C_i \, dt \tag{6}$$

Integrating Eq. (5) over the reservoir volume of interest

$$-\iiint \phi m_{0i} \, dV + \iiint \nabla \cdot \left(\int_0^\infty t \vec{N}_i dt \right) dV = 0 \tag{7}$$

Applying divergence theorem to Eq. (7)

$$-\iiint \phi m_{0i} \, dV + \iint \left(\int_0^\infty t \vec{N}_i \, dt \right) \cdot \vec{n} \, dA = 0 \tag{8}$$

Since mass transfer occurs only at the wells

$$-\iiint \phi m_{0i} \, dV + \left(q m_{1i} \right)\big|_{wells} = 0 \tag{9}$$

Where

$$m_{1i} = \int_0^\infty t\left(\sum_{j=1}^{n_p} f_j C_{ij}\right) dt \tag{10}$$

This equation could be applied to a variety of water, oil and gas combinations. For the specific case of just oil and water, it can be written as follows:

$$\begin{aligned}
&\iiint \phi m_{0i}\, dV \\
&= \iiint \phi \int_0^\infty (S_w C_{iw} + S_o C_{io})\, dt\, dV \\
&= \iiint \phi \int_0^\infty (S_w + K_i S_o) C_{iw}\, dt\, dV \\
&= \iiint \phi \left(\hat{S}_w + K_i \hat{S}_o\right) \int_0^\infty C_{iw}\, dt\, dV \\
&= \iiint \phi \left(\hat{S}_w + K_i \hat{S}_o\right) m_{0iw}\, dV
\end{aligned} \tag{11}$$

Where the partition coefficient is defined as:

$$K_i = \frac{C_{io}}{C_{iw}}$$

And

$$\hat{S}_j = \frac{\int_0^\infty S_j C_{iw}\, dt}{\int_0^\infty C_{iw}\, dt} \tag{12}$$

Equation (9) can be used to show that:

$$-\iiint \phi \left(\hat{S}_w + K_i \hat{S}_o\right) m_{0iw} dV + m_{0iw}\big|_{producer} \overline{V_i} = 0 \tag{13}$$

Where the mean residence volume of tracer i is given as

$$\overline{V_i} = \frac{\int_0^\infty q C_{it} t\, dt}{\int_0^\infty C_{iw}\, dt} - \frac{V_{slug}}{2} \tag{14}$$

Assuming $\hat{S}_j$ is not different between tracers and that m_{0iw} is not a function of space, it follows from Eq. (13) that:

$$-\iiint \phi\left(\hat{S}_w + K_i \hat{S}_o\right) dV + \overline{V}_i = 0 \tag{15}$$

Equation (15) can be used to show that the average oil saturation is given by:

$$\bar{\hat{S}}_o = \frac{\overline{V}_1 - \overline{V}_2}{\overline{V}_2(K_1 - 1) - \overline{V}_1(K_2 - 1)} \tag{16}$$

And the swept pore volume is given by:

$$V_s = \frac{\overline{V}_2(K_1 - 1) - \overline{V}_1(K_2 - 1)}{K_1 - K_2} \tag{17}$$

Since the average oil saturation $\bar{\hat{S}}_o$ is at the mean residence time of the conservative tracer $\bar{t}_1$, the average oil saturation at the end of the PITT is given by subtracting the volume of oil produced after the mean residence time, which is:

$$\overline{S}_o = \frac{V_s \bar{\hat{S}}_o - \int_{\bar{t}_1}^{\infty} q_o \, dt}{V_s} \tag{18}$$

The mean residence volume for each tracer i calculated from Eq. (14) between a particular injection well with injection rate Q and a particular production well n should be calculated using the flow rate q corresponding to the rate in the swept volume of interest. This rate can be calculated by proportioning the mass of tracer produced m_n at the producer n of interest with the total mass of the tracer injected (M) as follows:

$$q = \frac{m_n}{M} Q \tag{19}$$

Where

$$m_n = \int_0^{\infty} q_n C_{it} \, dt \tag{20}$$

$$M = \int_0^{t_{slug}} Q C_{iJ} \, dt = C_{iJ} Q t_{slug} = C_{iJ} V_{slug} \tag{21}$$

Once the mean residence volumes are obtained, the swept pore volume between wells and the average oil saturation in each swept pore volume is performed with the same equations

as that with one injector and one producer. The average oil saturation $\bar{\hat{S}}_o$ calculated from Eq. (16) is the average oil saturation at the mean residence time of the conservative tracer, $\bar{t}_1$, before correction for produced oil. For a reservoir with multiple wells, produced oil can be contributed from multiple injectors and the oil production rate needs to be divided into well pairs so that the moment analysis can be performed for each well pair. The oil production rate is assumed to be proportional to the tracer swept volume. For example, for the case of one producer with streamlines from 4 injectors, the oil production rate corresponding to swept volume 1 is given by:

$$q_o = \frac{V_{s1}}{V_{s1} + V_{s2} + V_{s3} + V_{s4}} Q_o \tag{22}$$

where Q_o is the total oil production rate for this production well and V_{s1} is the swept pore volume of interest. The average oil saturation corrected for produced oil within a particular swept volume is then calculated from Eq. (18) as before.

Simulation Results for Conventional PITTs

In this first example, a slug of tracers in water at residual oil saturation was simulated using the UTCHEM simulator. The 3D simulation domain is a quarter of a five-spot well pattern with dimensions of 660 ft long, 660 ft wide and 50 ft thick (Table 1). A heterogeneous permeability field was stochastically generated using FFT software (Jennings et al., 2000). The permeability field has a log mean permeability of 344 md and a Dykstra-Parsons coefficient of 0.81. The correlation lengths are 100 ft in the horizontal direction and 10 ft in the vertical direction.

Figure 1 shows the permeability and residual oil saturation for a vertical cross-section of the reservoir at J = 1. A residual oil distribution was generated assuming an exponential relation with permeability.14 Regions of high permeability have low oil saturation and vice versa. The average oil saturation in the reservoir is 0.245. The reservoir has a uniform porosity of 0.2. A tracer slug consisting of a conservative tracer and three partitioning tracers with partition coefficients of 0.5, 1.0 and 2.0 was injected for 0.1 pore volumes (PV) followed by water.

Figure 2 shows the tracer concentration curves at the producer. In order to obtain the response curve of a partitioning tracer (the produced concentrations) in a reasonably short time and yet ensure good separation of the conservative and partitioning tracers, the partition coefficients should be within a certain range. The retardation factor for partitioning tracer i relative to the conservative tracer is defined as follows:

$$R_{fi} = 1 + \frac{K_i S_{or}}{1 - S_{or}}$$

Jin (1995) recommended retardation factors between 1.2 and 4.0 for groundwater applications. Times and distances are much longer in the oil field, so retardation factors between 1.2 and 1.5 are more likely to be optimum. The oil saturation calculated from the produced tracer concentrations as a function of time is shown in Fig. 3. The oil saturation was estimated using a conservative tracer and a partitioning tracer with a partition coefficient of 1.0. The oil saturation

calculated from the method of moments gradually approaches the true average value of residual oil saturation used in the simulation and by 800 days is very close to it.
Figure 4 shows the tracer concentration histories for the same case except the tracers were injected continuously rather than as a slug. For a continuous tracer injection, the mean residence volume is the swept pore volume and gradually increases with time. The sweep efficiency as a function of time can be calculated by dividing the swept pore volume by the total pore volume if the partition coefficient is 1.0. Figure 5 illustrates the sweep efficiency calculated using such a tracer. Converting swept pore volumes to sweep efficiency is simple in a confined well pattern such as in this example. For more complicated cases, the total pore volume of interest must first be defined before the swept pore volume can be used to calculate the sweep efficiency.

Table 1: Summary of Reservoir Conditions

Reservoir dimensions	**660 ft x 660 ft x 50 ft**
Number of gridblocks	**22x22x10**
Porosity	**0.2**
Residual oil saturation	**0.25**
Residual water saturation	**0.30**
Water end point relative permeability	**0.15**
Oil end point relative permeability	**0.85**
Corey exponent for water	**1.5**
Corey exponent for oil	**2.0**
Density of oil	**52.88 lb/cu. ft**
Density of water	**62.4 lb/cu. ft**
Viscosity of oil for mobility ratio of 0.5	**1.5 cp**
Viscosity of oil for mobility ratio of 1.2	**5 cp**
Viscosity of oil for mobility ratio of 5.2	**15 cp**
Viscosity of water	**0.7 cp**
Longitudinal dispersivity	**0.3 ft**
Transverse dispersivity	**0.03 ft**

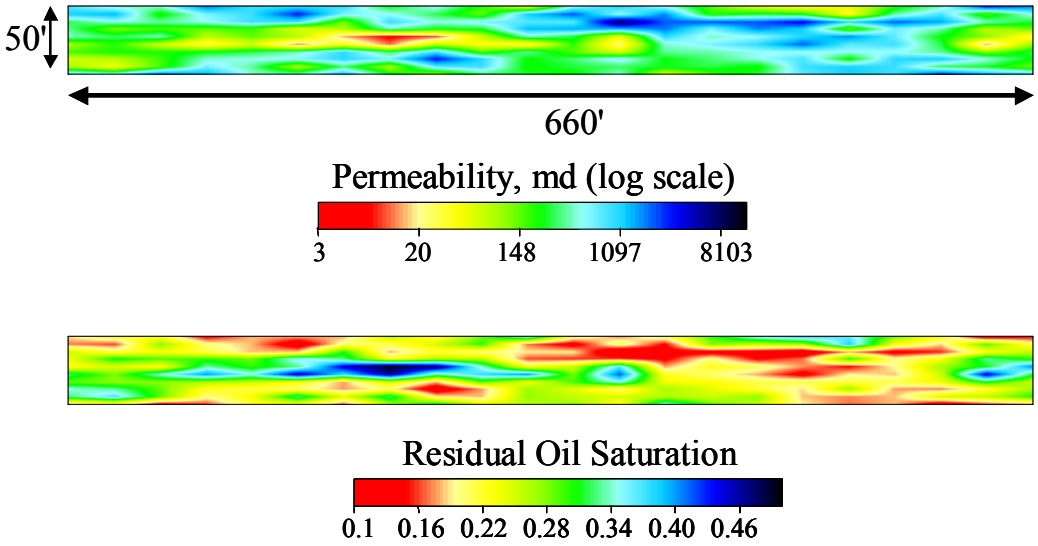

Figure 1- Permeability and oil saturation profiles for the three-dimensional heterogeneous reservoir.

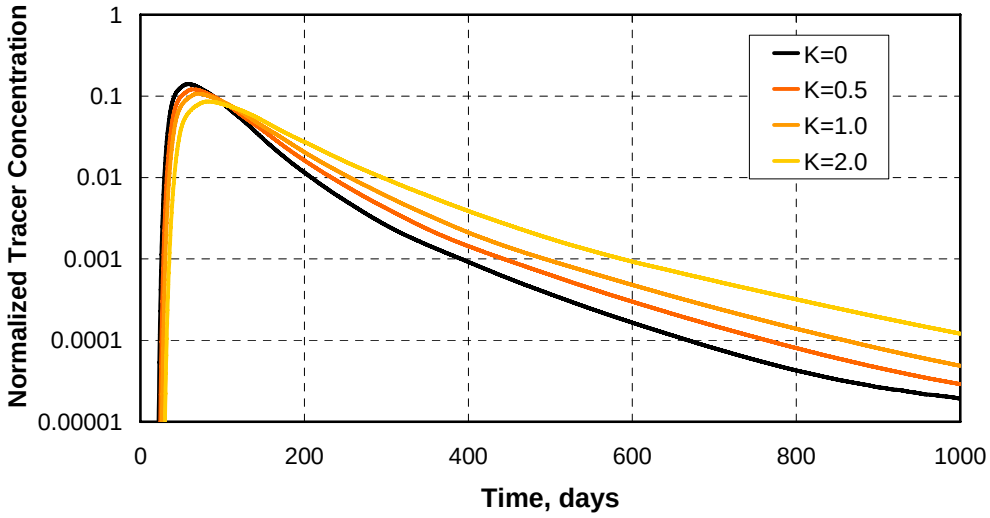

Figure 2- Tracer concentration curves for the three dimensional heterogeneous simulation.

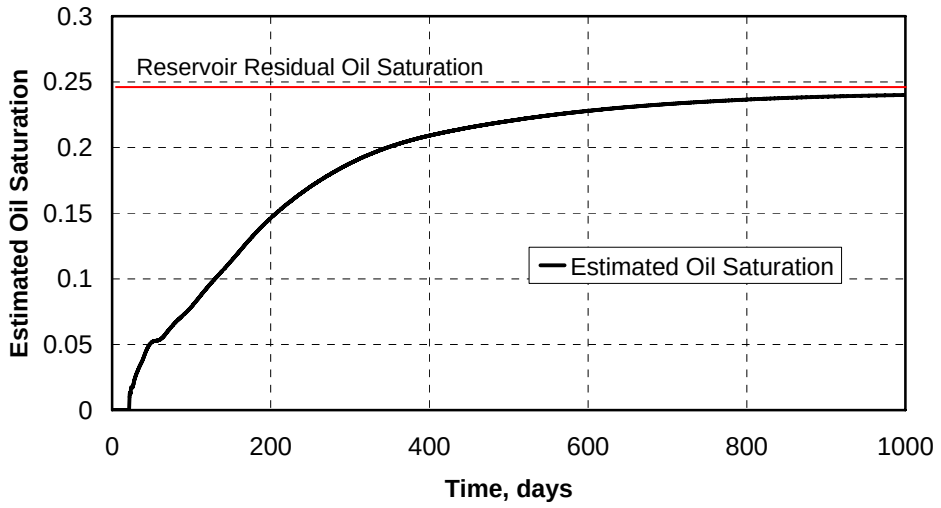

Figure3—Estimated oil saturation using the method of moments.

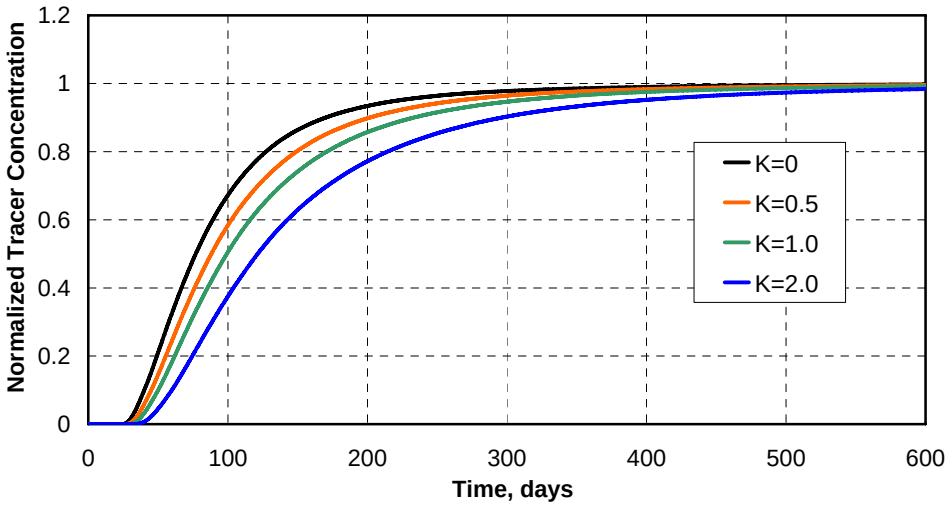

Figure 4- Tracer concentrations for a continuous tracer injection.

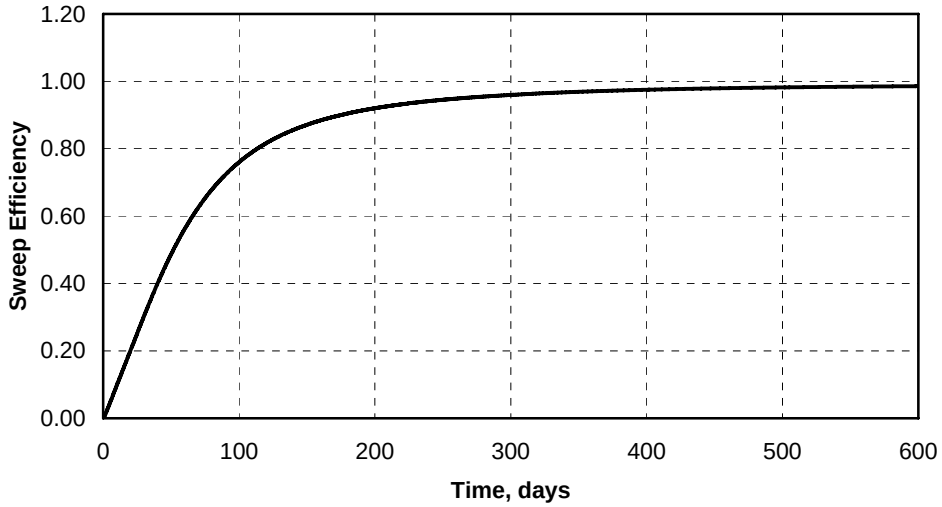

Figure 5- Sweep efficiency calculated using tracer concentrations for a partitioning tracer (K=1) injected continuously.

Oil Saturation as a function of depth

If downhole sensors could be used for real time tracer measurements at different depths in the well during a partitioning interwell tracer test, then such tracer data could be used to generate the vertical distribution of oil saturation in addition to the average oil saturation in the swept volume of the reservoir between well pairs. Sampling at different depths could also be used to provide such data at discrete times. The potential value of obtaining these data is illustrated in the following simulation example.

A slug of tracers in water at residual oil saturation was simulated using the UTCHEM simulator. The 3D simulation domain is a quarter of a five-spot well pattern with dimensions of 660 ft long, 660 ft wide and 50 ft thick (Table 1). A heterogeneous permeability field was stochastically generated using FFT software (Jennings et al., 1997). The permeability field has a log mean permeability of 344 md and a Dykstra-Parsons coefficient of 0.81. The correlation lengths are 100 ft in the horizontal direction and 10 ft in the vertical direction. Figure 1 shows the permeability and residual oil saturation for a vertical cross-section of the reservoir at J = 1. A residual oil saturation distribution was generated assuming an exponential relation with permeability (Sinha, 2003). Regions of high permeability have low oil saturation and vice versa. The average oil saturation in the reservoir is 0.245. The reservoir has a uniform porosity of 0.20.

Tracer concentration data at various depths in the reservoir were used to make the calculations. Figure 2 shows the tracer concentrations at the producer at a depth of 12.5 ft from the top of the reservoir. A sensitivity study was carried out with various values of vertical to horizontal permeability ratio to study its effect on the oil saturation.

Figure 3 shows a comparison between the average oil saturation in the reservoir and the oil saturation estimated from the PITT as a function of depth. The oil saturations estimated from the tracer data are within 0.02 of the true values within each layer of the reservoir and capture the general trend with depth. The accuracy in the results increases with a decrease in vertical to horizontal permeability ratio corresponding to lower cross flow between layers.

Table 2—Summary of Reservoir Conditions

Reservoir dimensions	660 ft x 660 ft x 50 ft
Number of gridblocks	22x22x10
Porosity	0.2
Residual oil saturation	0.25
Residual water saturation	0.30
Water end point relative permeability	0.15
Oil end point relative permeability	0.85
Corey exponent for water	1.5
Corey exponent for oil	2.0
Density of oil	52.88 lb/cu. ft
Density of water	62.4 lb/cu. ft
Viscosity of oil for mobility ratio of 0.5	1.5 cp
Viscosity of oil for mobility ratio of 1.2	5 cp
Viscosity of oil for mobility ratio of 5.2	15 cp
Viscosity of water	0.7 cp
Longitudinal dispersivity	0.3 ft
Transverse dispersivity	0.03 ft

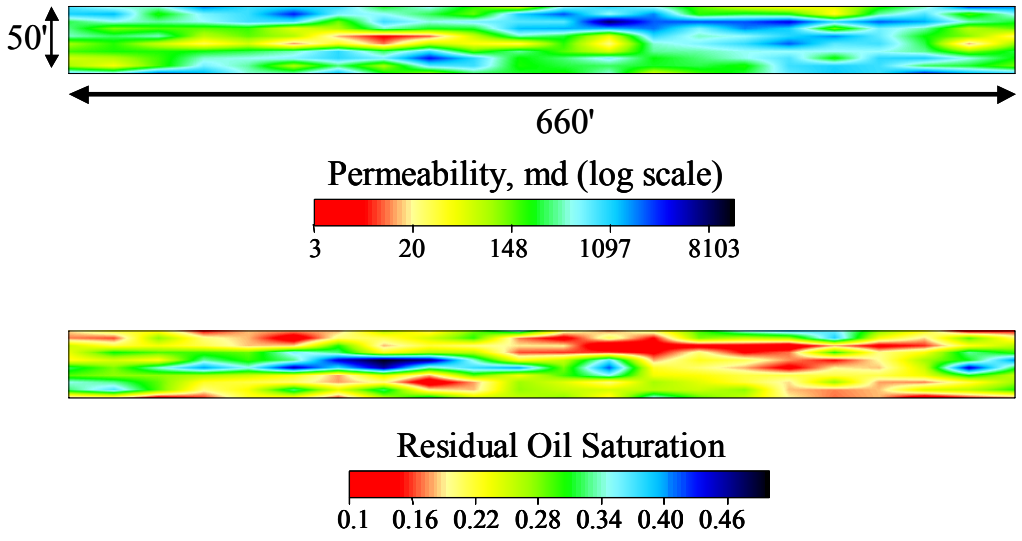

Figure 1- Permeability and oil saturation profiles for the three-dimensional heterogeneous reservoir.

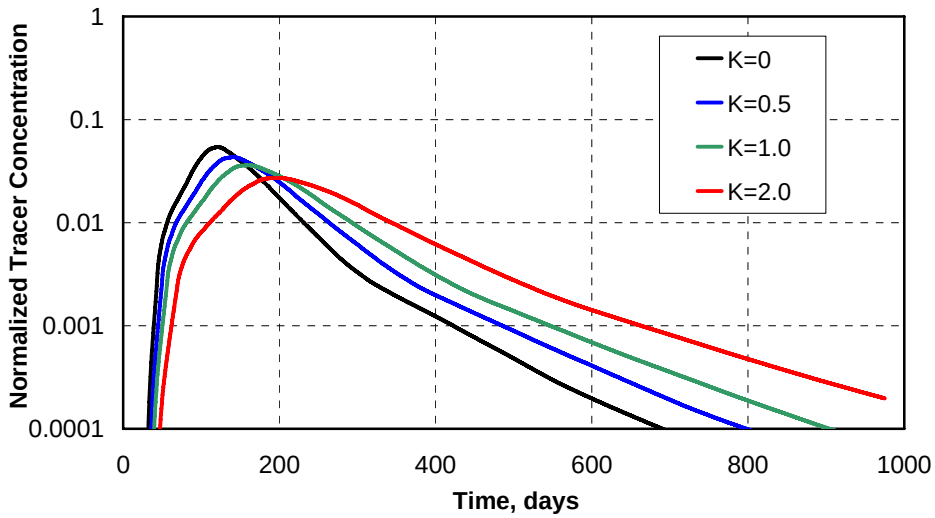

Figure 2- Tracer concentrations at 12.5 ft from the top of the reservoir.

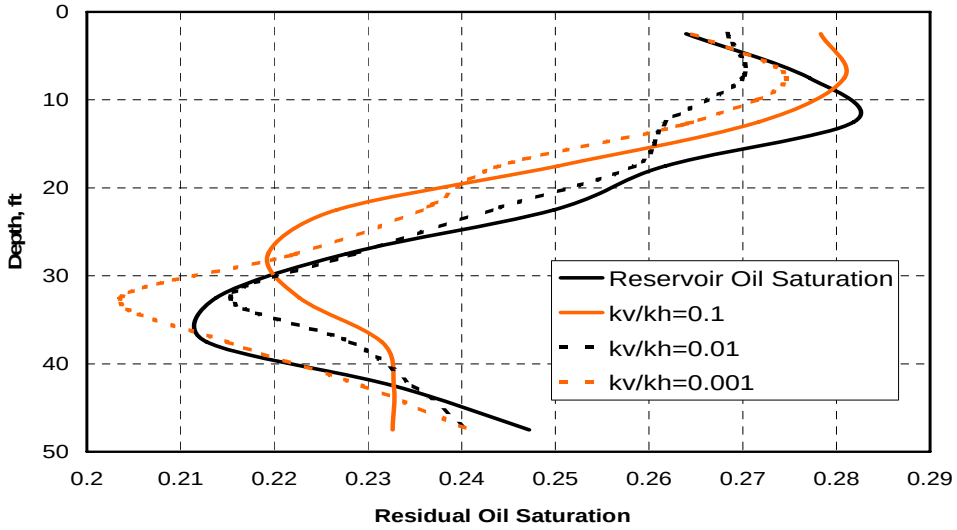

Figure 3- Estimated vertical distribution in oil saturation for various kv/kh ratios.

Simulation of Tracer Tests with Mobile Oil

Although inverse modeling is very useful and much faster computationally than in the past, there is still a lot of advantages in using the simpler method of moments to get average values of oil saturation including its usefulness to condition an inverse calculation or history match with a reservoir simulator. The following examples show that the method of moments can be used to accurately calculate oil saturation even under two-phase flow in the reservoir. Such calculations are very fast and simple compared to inverse modeling.

In this example, the same tracer slug case as before was simulated except the tracers were injected during the waterflood while there was still mobile oil present in the reservoir. In the

previous cases, the residual oil saturation was correlated with permeability so it varied throughout the reservoir. In this example, a uniform residual oil saturation of 0.25 was used.

To simulate tracer tests with different volumes of mobile oil initially in the reservoir, tracer tests were started at different stages of the waterflood. The tracer tests were started after 0.5, 1.0, 1.5, 2.0, 2.5 and 3.0 pore volumes (PV) of water injection. The oil saturation is estimated after 7.0 PV of water injection using the method of moments. In practice, shorter times could be used with some extrapolation of the tracer concentration data (Jin et al., 1995, Jin et al., 1997 and Dwarakanath et al., 1999). A sensitivity study was carried out with waterflood end point mobility ratios of 0.5, 1.2 and 5.2.

Figure 1 shows the oil production rate for the waterflood simulation with an end point mobility ratio of 1.2. Since oil is being produced and partitioning tracers are used, some of the tracer is in the oil as well as in the water. Figures 2 and 3 show the tracer concentration curves for water and oil for a simulation with tracer injection starting at 0.5 PV after the start of the waterflood. Equation (18) was used to calculate the oil saturation using the total tracer concentration rather than the aqueous tracer concentration as in previous examples. The total tracer concentration can be obtained by either directly measuring the tracer concentrations in both the produced water and oil, or by measuring only the concentrations in the water and then calculating the oil concentration from the measured partition coefficient, but this would mean more uncertainty in the estimate.

Figure 4 shows the total tracer concentrations for the same case. Figures 5 to 7 show a comparison between the estimated oil saturation and the oil saturation using total tracer concentrations for mobility ratios of 0.5, 1.2, and 5.2. The maximum difference between the average oil saturation during the PITT and the oil saturation estimated from the PITT is 0.01. Some adjustment in the oil saturation would be needed to estimate the oil saturation at the end of the PITT rather than an average value during the PITT. In these examples, the differences are small. One approach would be to use the PITT estimates to condition a simulation and then predict the oil saturation at other times using the simulator, ideally incorporating other conditioning data at the same time.

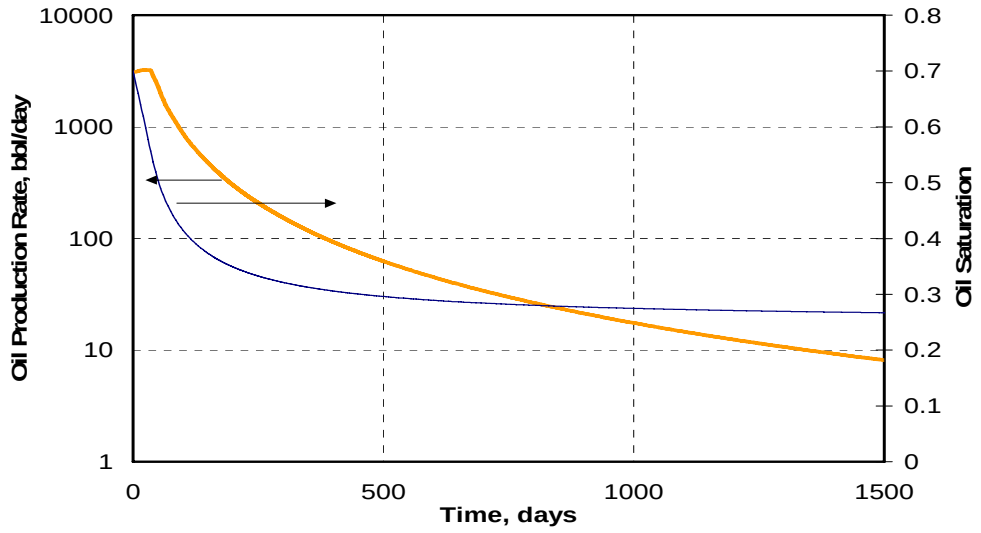

Figure 1- Oil production rate for the simulation with a mobility ratio of 1.2.

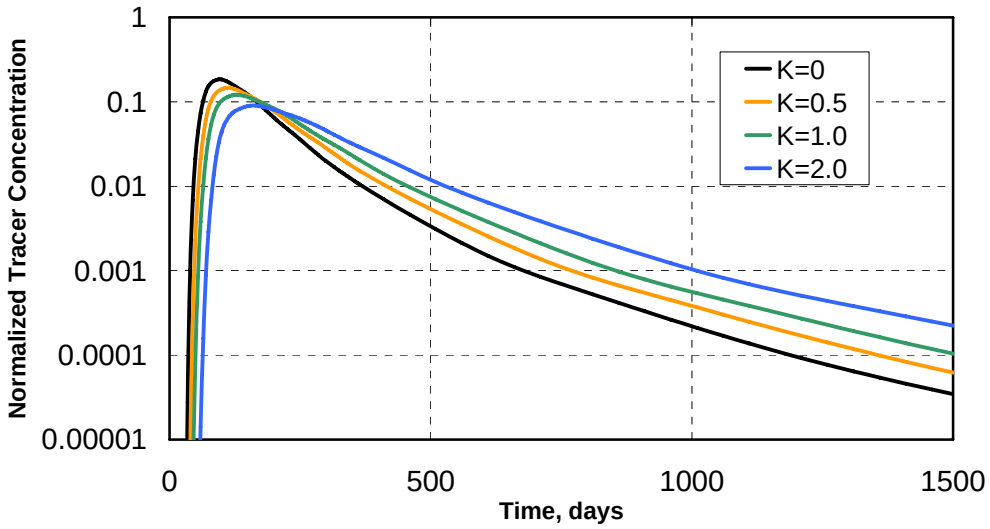

Figure 2- Water phase tracer concentrations for a PITT at 0.5 PV with an end point mobility ratio of 1.2.

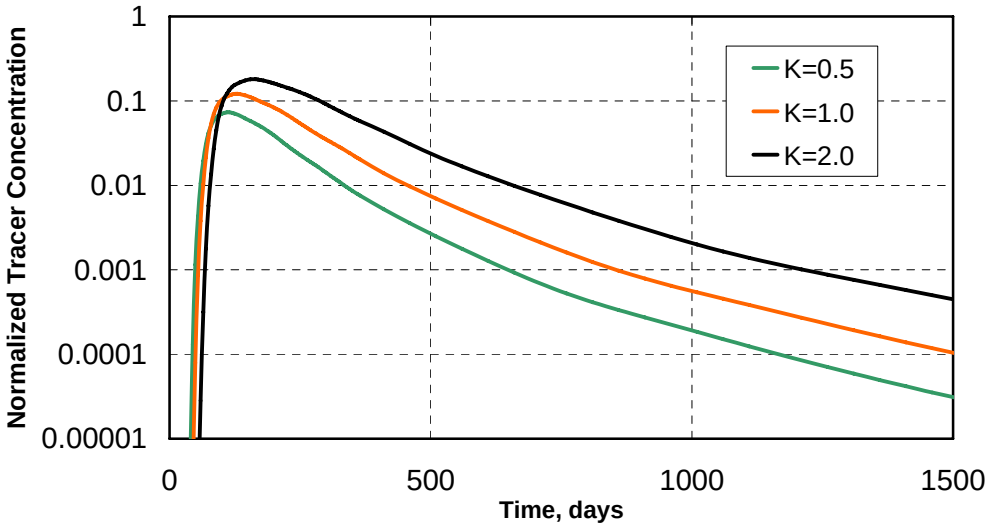

Figure 3- Oil phase tracer concentrations for a PITT at 0.5 PV with an end point mobility ratio of 1.2.

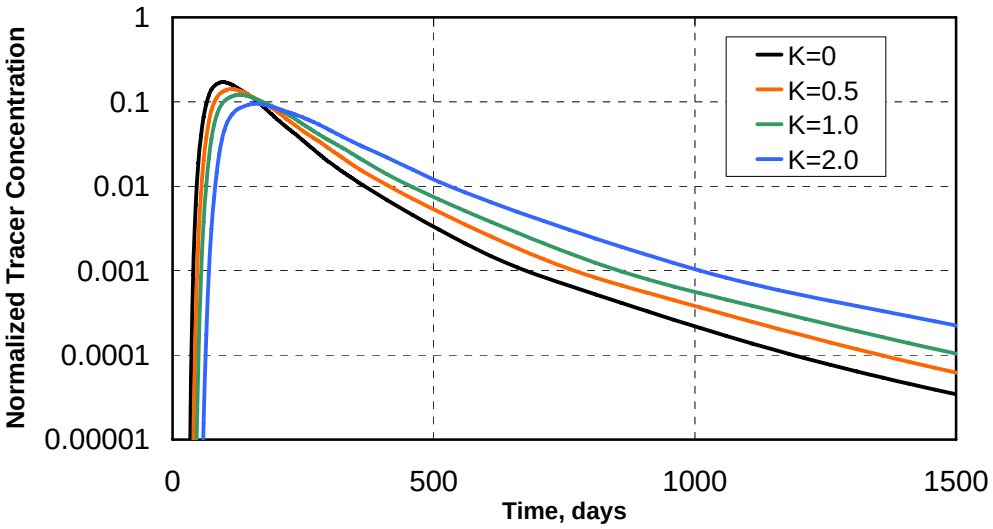

Figure 4- Total tracer concentrations for a PITT at 0.5 PV with an end point mobility ratio of 1.2.

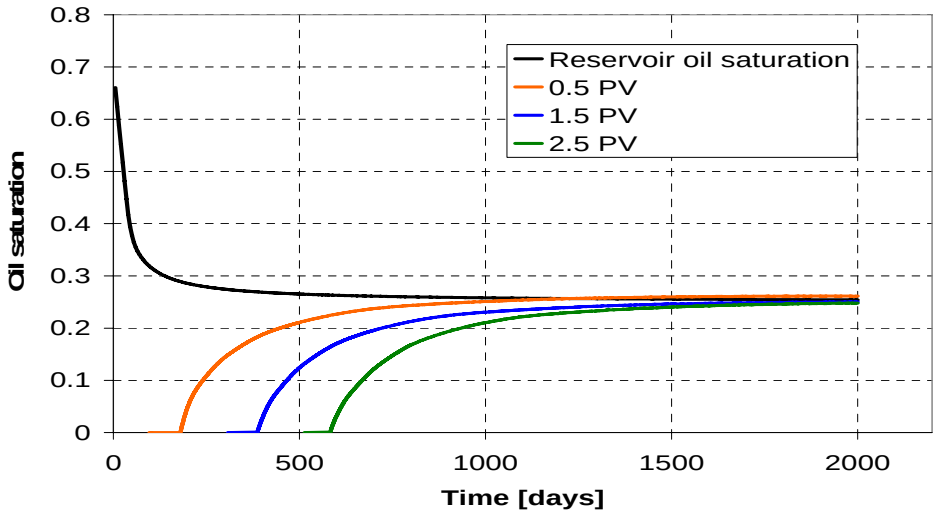

Figure 5- Estimated oil saturation using total tracer concentrations for an end point mobility ratio of 0.5

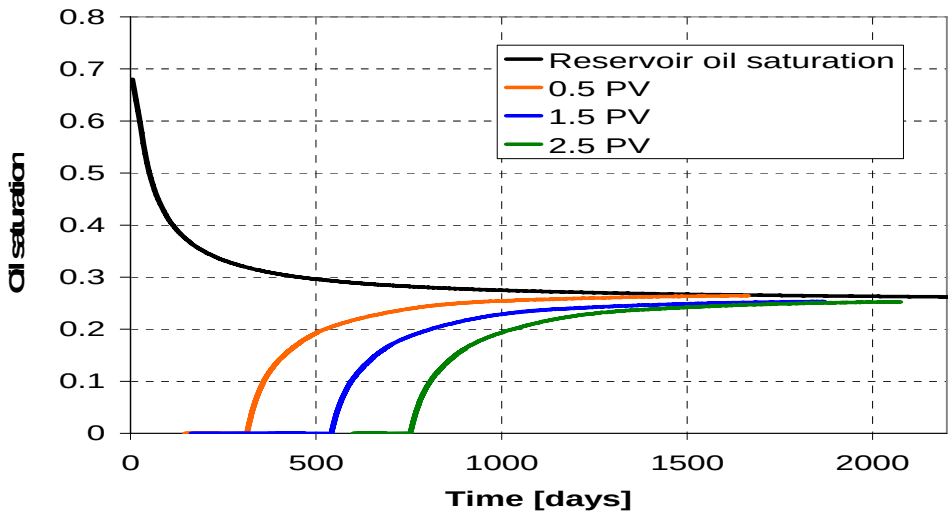

Figure 6- Estimated oil saturation using total tracer concentrations for an end point mobility ratio of 1.2.

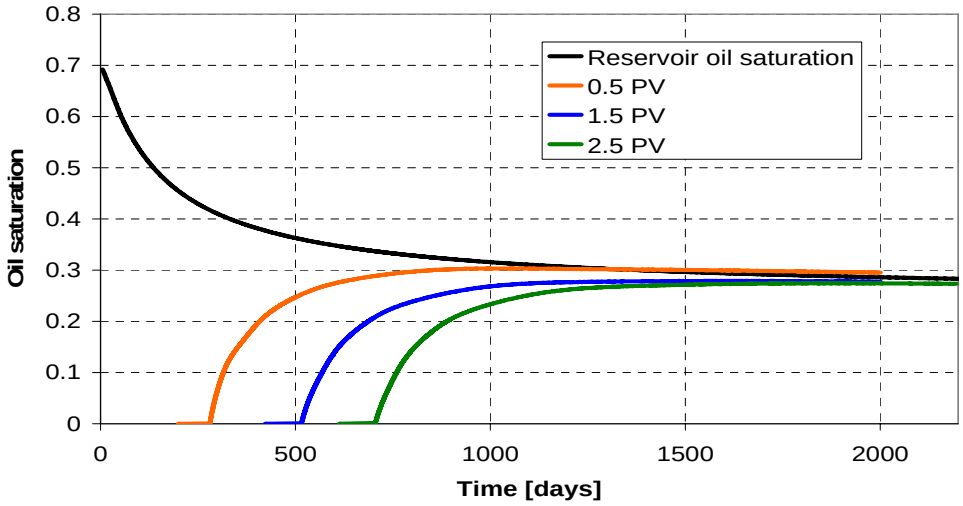

Figure 7- Estimated oil saturation using total tracer concentrations for an end point mobility ratio of 5.2.

In example INVO2-run4, a PITT was simulated in an inverted, confined, 40 acre five-spot well pattern (Table 1). A constant injection rate of 6000 bbl/day was used. The producer was constrained to produce at a constant bottom hole pressure of 2000 psi. A stochastic permeability field with the properties shown in Table 1 was generated using FFT method.

Figure 1 is a plot of the permeability field with a Dystra-Parsons coefficient of 0.81. Figures 2 and 3 show the permeability distribution of the most and the least permeable layers. The reservoir was water flooded for 2000 days before the tracer injection (99% water cut). The oil production rate from the start of tracer injection is shown in Figure 4. Total simulation time

is 6000 days (12 PVs). Four tracers were injected as a slug for 50 days (0.1 PV) with partition coefficients of 0, 0.5, 1, and 2. The results illustrated below were calculated using the partition coefficient of 2.

Tracer concentration plots for each production well are given in Figures 5 to 8. In Figures 5 and 7, tracer breakthrough is quite early and the tracer curves have sharp peaks. This can be explained with the high permeable channels around production wells 1 and 3. Early breakthrough of the tracers in these production wells is clearly seen in Figures 9 and 10, which show the tracer concentration profiles 35 days after the tracer injection in layers 1 and 8.

Figure 20 shows the oil saturation calculated between the injector and each producer using the method of moments. Table 2 shows the difference between these results and the reservoir oil saturation values in each quadrant at the end of the simulation. In the first row of table 2, the residual oil saturation in the reservoir is given as 0.234. This value is calculated by subtracting the amount of oil produced (ECLIPSE output) from the initial oil saturation and is smaller than the input value of 0.25, which implies there is some numerical error in this result.

The difference between the method of moment results and the reservoir values vary between -0.035 and -0.001. The biggest difference is seen in the oil saturation between the injector and producer 1 although the swept pore volume is quite high for this well as it can be seen in Figure 21. This is because of the unrecovered tracer around this well. Figure 22 shows the remaining tracer (partition coefficient K=2) around production well 1. Table 3 shows the swept pore volumes between the injector and each producer. After 6000 days of simulation, 98.4% of the reservoir is swept and oil saturations for each quadrant were estimated with acceptable errors. Figures 23 and 24 have the oil saturation distribution profiles in the 1st and the 2nd layers at the end of the simulation.

Table 1. Reservoir description for Case INVO2-run4

Grid	**44x44x10**
Grid block size, ft	**30x30x5**
Reservoir dimensions, ft	**1320x1320x50**
Area of the reservoir, acres	**40**
Reservoir pore volume, bbl	**3,103,117**
Porosity	**0.2**
Horizontal correlation lengths, ft	**100**
Correlation length in the z direction, ft	**10**
Dykstra-Parsons coefficient	**0.81**
Standard deviation of log permeability	**1.65**
Log mean of permeability, md	**312**
Initial water saturation Swi	**0.3**
Residual water saturation Swr	**0.3**
Residual oil saturation Sor	**0.25**

Table 2. Comparison of Oil Saturations

	Well-1	*Well-2*	*Well-3*	*Well-4*
MOM results for So	0.223	0.247	0.240	0.253
Average So of the reservoir in each quadrant	0.258	0.261	0.254	0.254
Difference	-0.035	-0.013	-0.014	-0.001
Difference %	-3.5%	-1.3%	-1.4%	-0.1%
Sor in the reservoir calculated from ECLIPSE production data	0.234			

Table 3. Swept pore volume

	Well-1	*Well-2*	*Well-3*	*Well-4*
Vswept, bbl	1,052,168	555,314	886,385	558,286
Total Vswept, bbl	3,052,153			
Vswept/Vreservoir	0.339	0.179	0.286	0.180
VsweptTotal/Vreservoir	0984			

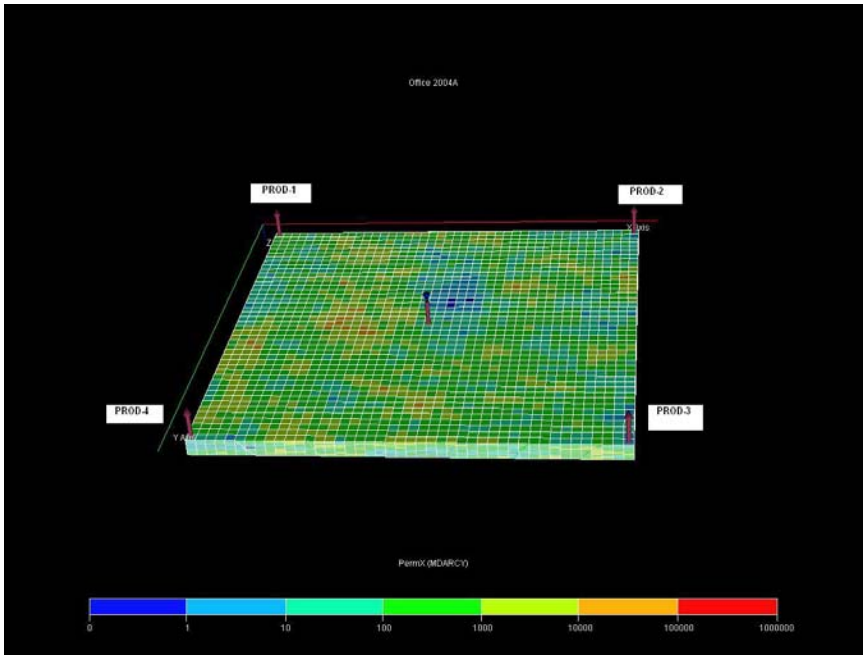

Figure 1- The permeability distribution

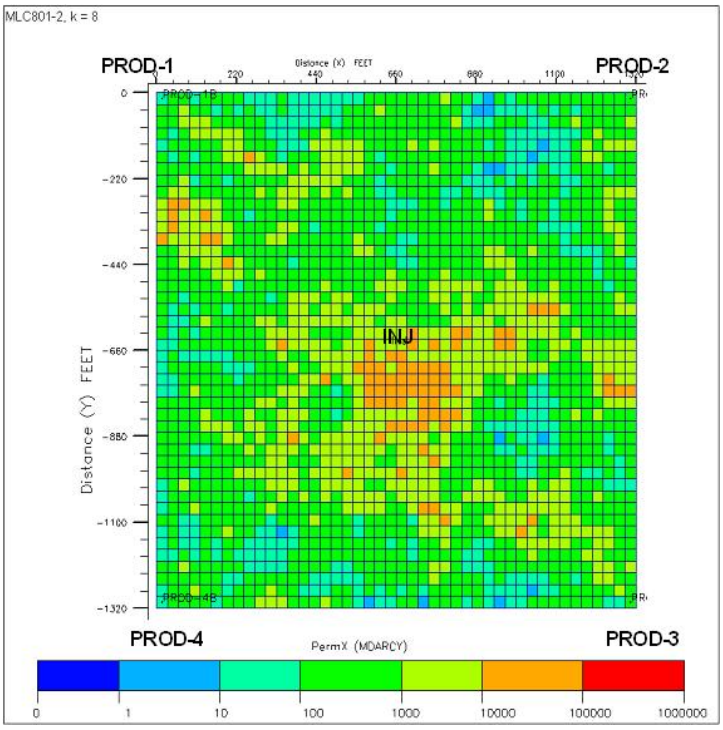

Figure 2- Logarithmic permeability distribution in layer 8 (most permeable layer)

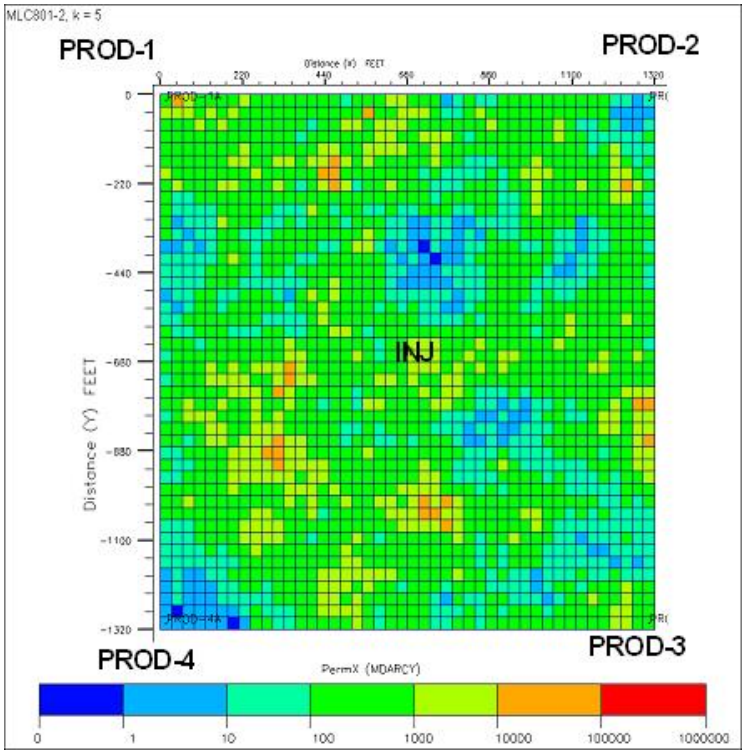

Figure 3- Logarithmic permeability distribution in layer 5 (least permeable layer)

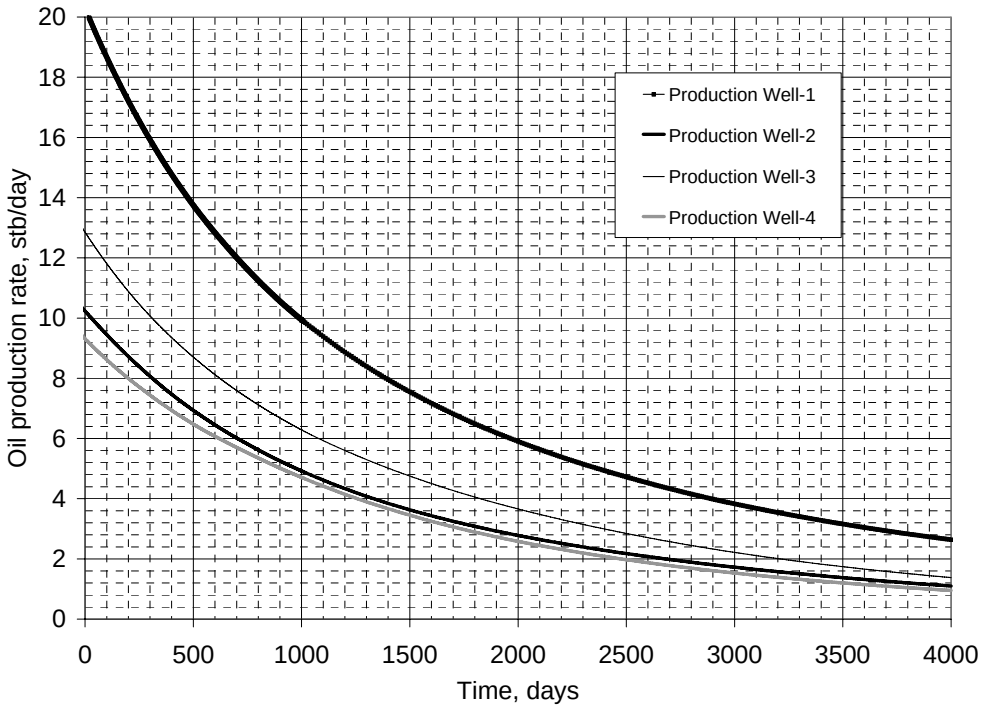

Figure 4- Oil Production rate

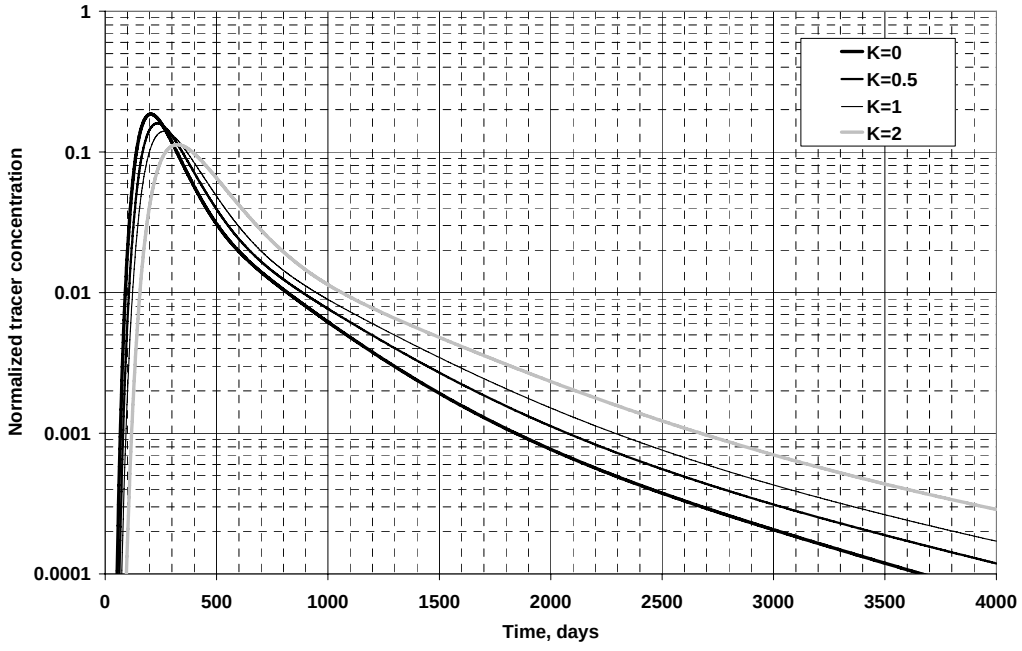

Figure 5- Normalized tracer concentration at production well 1

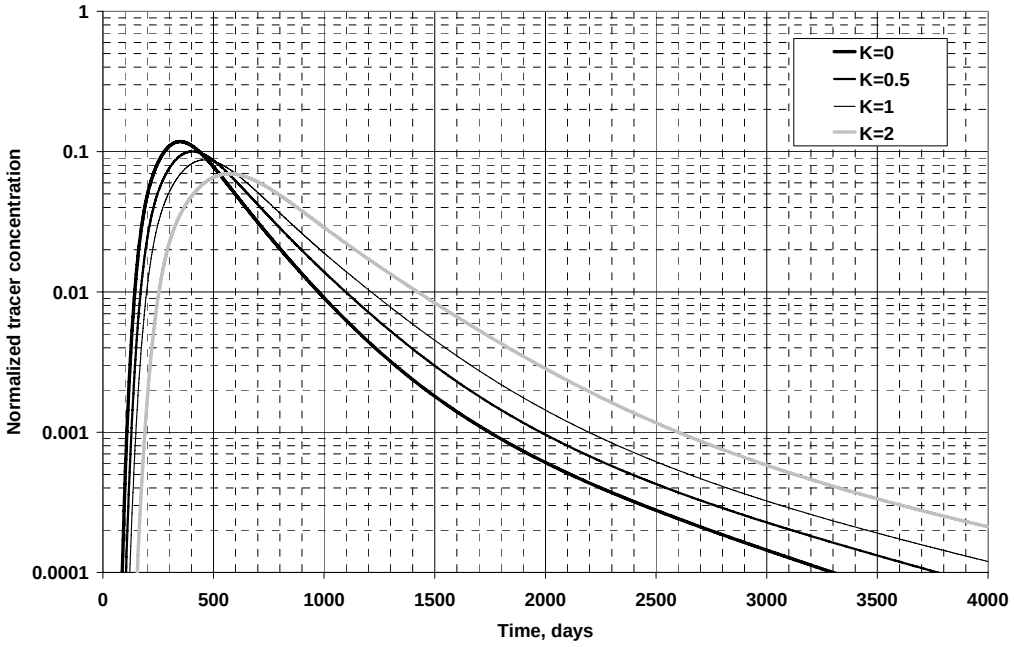

Figure 6- Normalized tracer concentration at production well 2

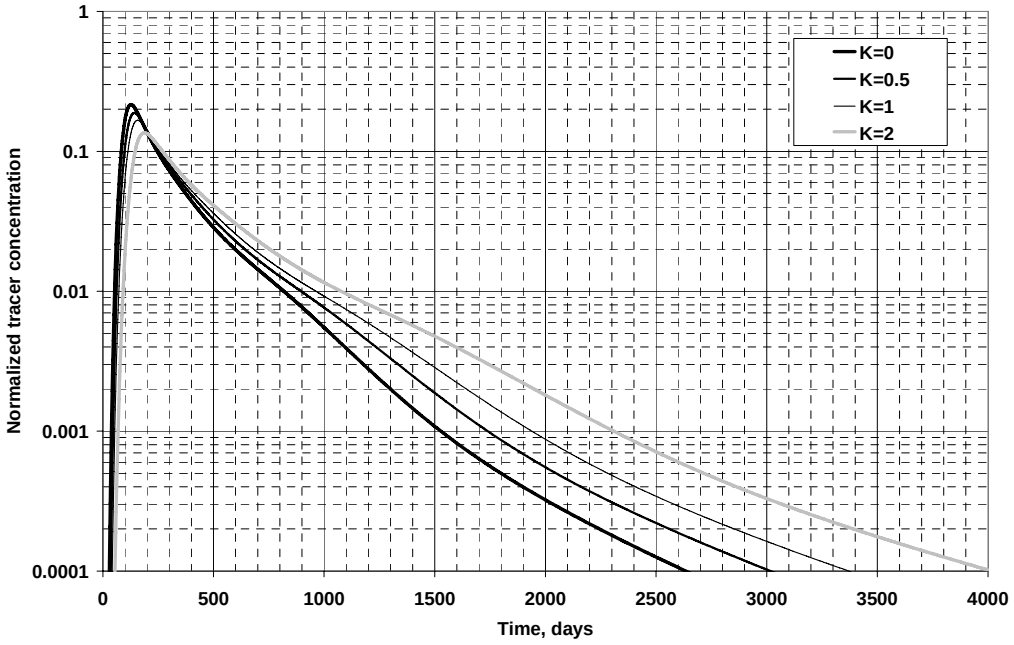

Figure 7- Normalized tracer concentration at production well 3

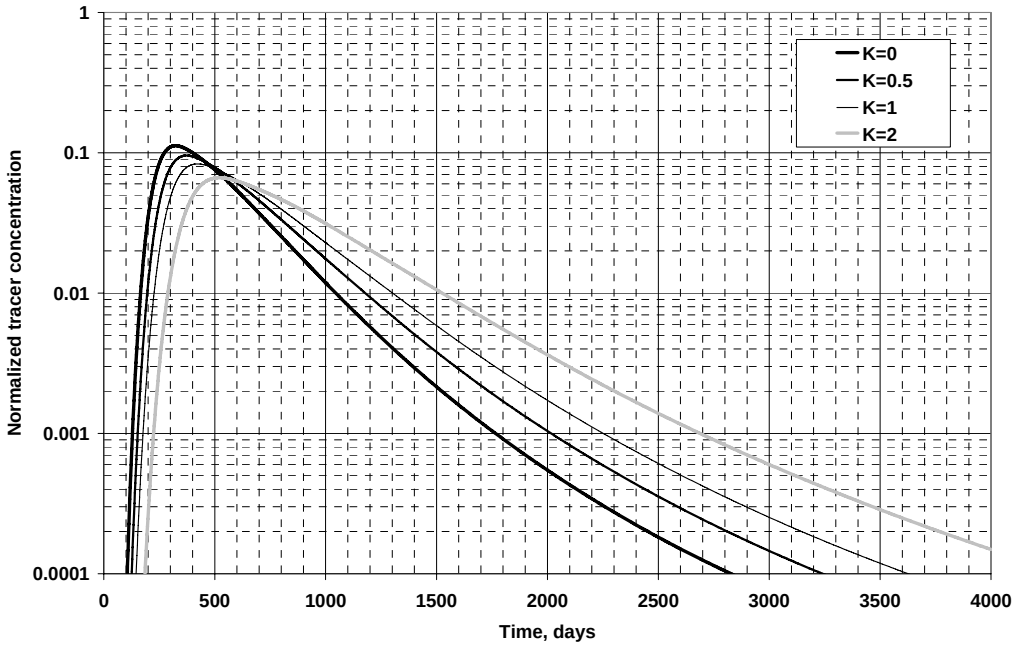

Figure 8- Normalized tracer concentration at production well 4

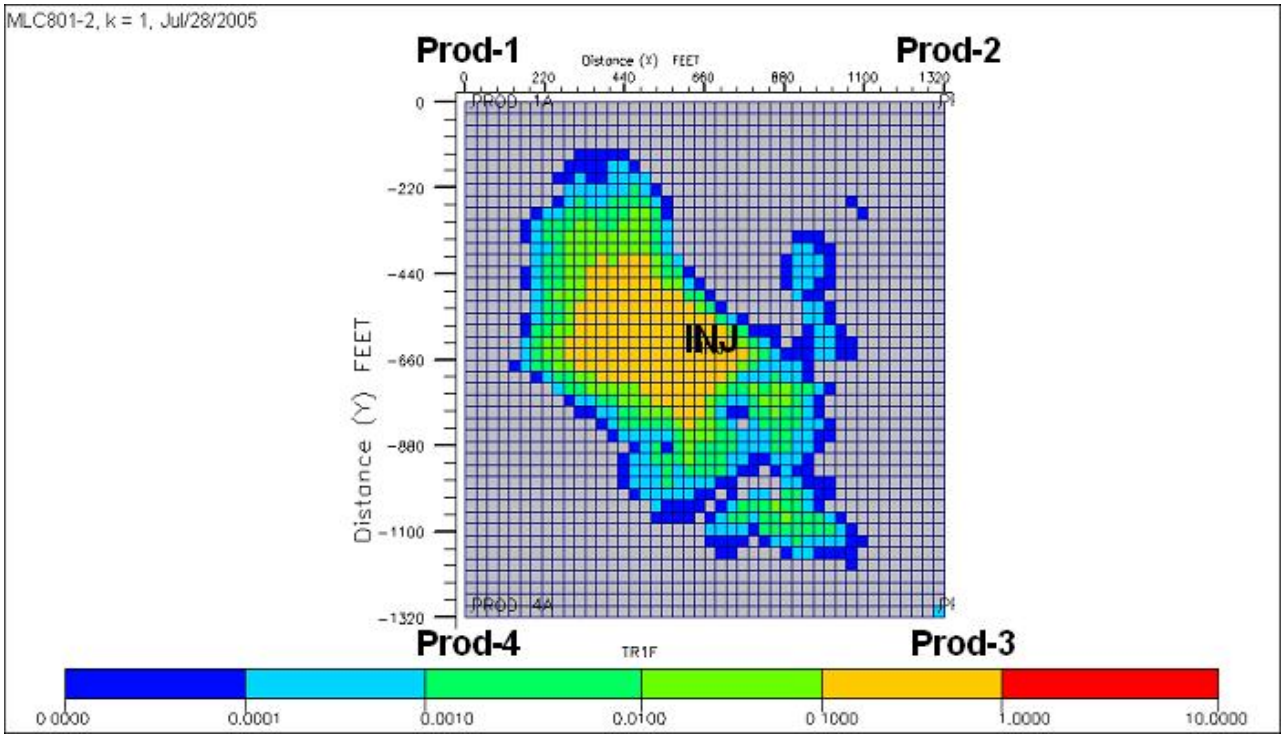

Figure 9- Conservative tracer concentration profile (logarithmic scale) in layer 1 after 35 days of tracer injection

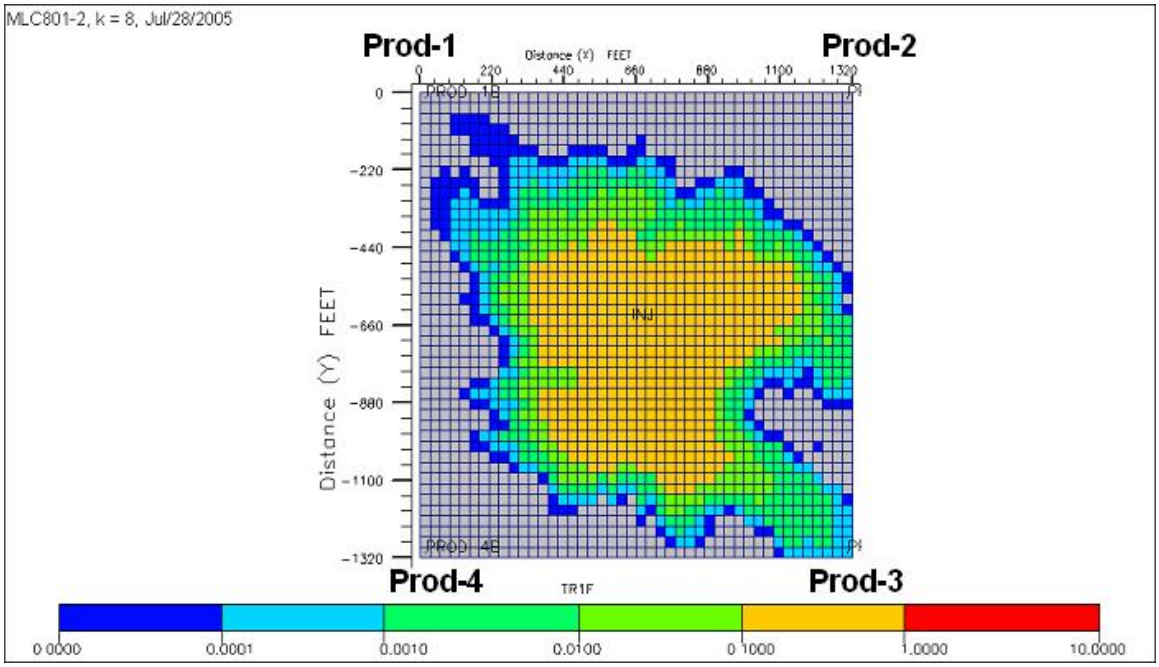

Figure 19- Conservative tracer concentration profile (logarithmic scale) in layer 8 after 35 days of tracer injection

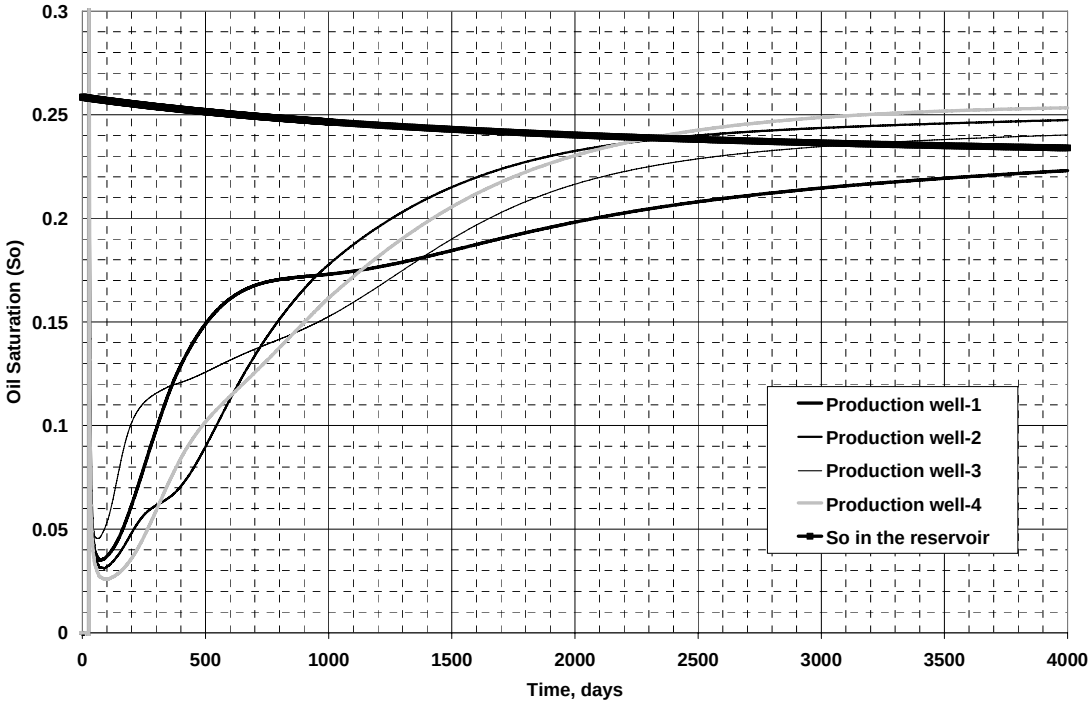

Figure 20- Oil Saturation Calculated from the Method of Moments

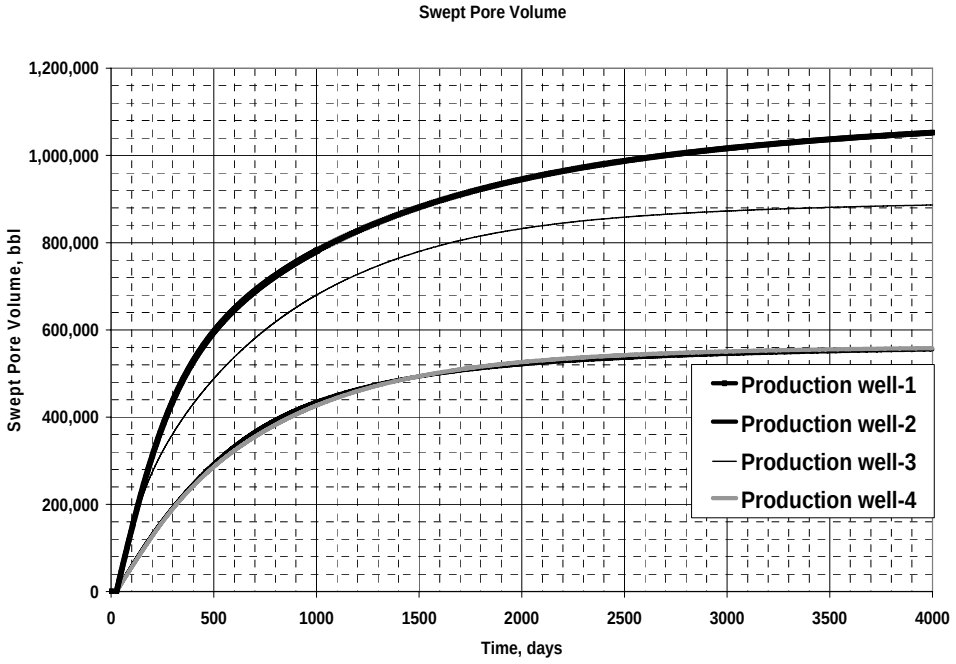

Figure 21- Swept pore volume between the injector and the each production well.

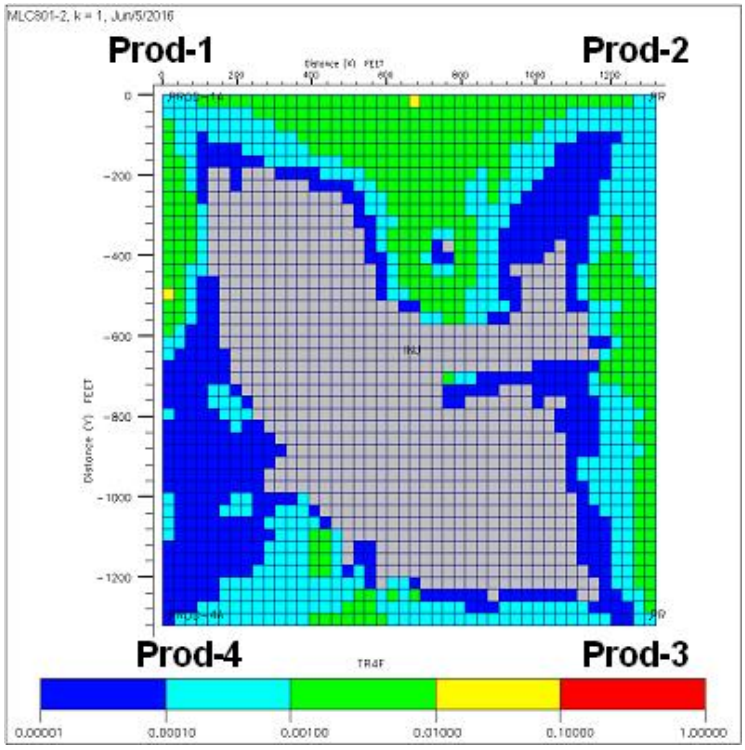

Figure 22- Tracer concentration profile (Partition coefficient=2) in layer 1 at the end of the simulation

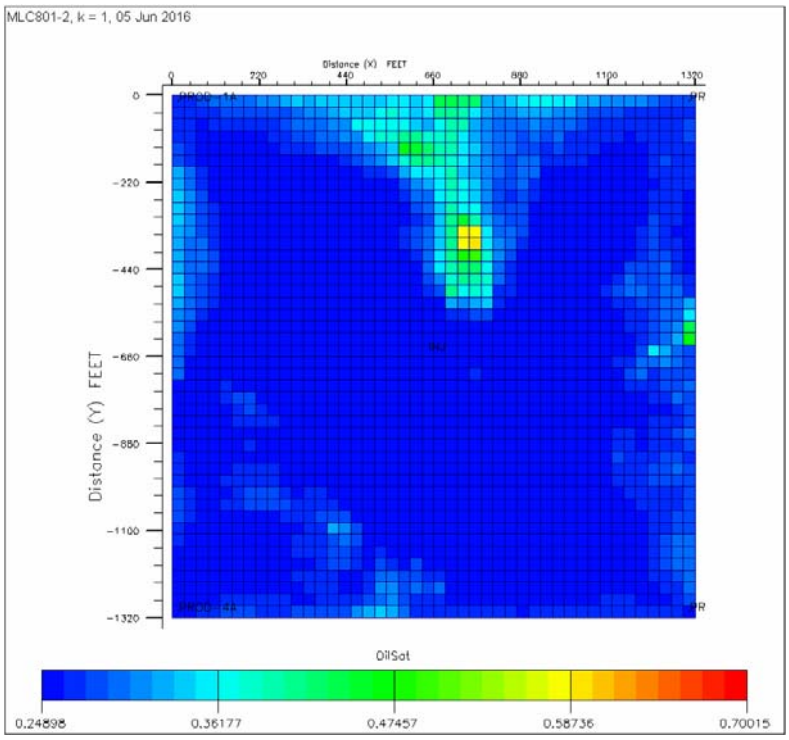

Figure 23- Oil saturation distribution in layer 1 at the end of the simulation

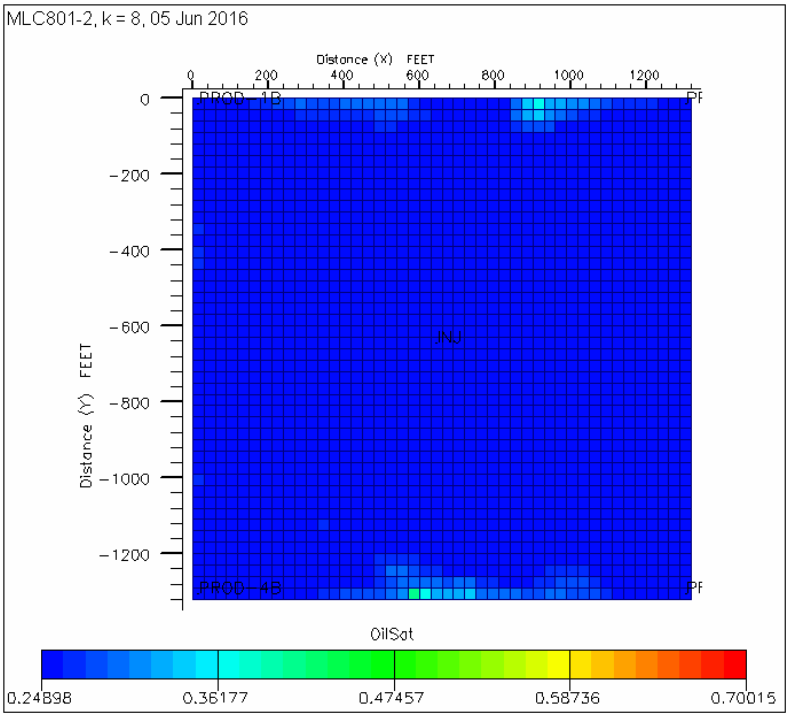

Figure 24- Oil saturation distribution in layer 8 at the end of the simulation

In this example INVO2-run5, all parameters were kept the same as the previous run except the Dykstra-Parsons coefficient was increased to 0.90 to see how this would affect the PITT results. Figures 1 and 2 show the permeability distribution of the most and the least permeable layers. The reservoir was water flooded for 2000 days (99% water cut) before the PITT. A slug with four tracers was injected for 50 days (0.1 PV). The oil saturation distribution at the beginning of the PITT is shown in Figures 3 and 4. Tracer production concentration curves are shown from Figures 5 to 8. Figures 9 and 10 show the tracer concentration profiles for layers 1 and 8 for the tracer with a partition coefficient of 2. Table 1 compares the oil saturations for each swept pore volume. The results are still good even though the reservoir is much more heterogeneous than the first case. Table 2 shows the swept pore volumes and sweep efficiency at the end of the PITT.

Table 1. Comparison of Oil Saturations for Case INV02-run5

So at the end of the tracer inj.	*Well-1*	*Well-2*	*Well-3*	*Well-4*
MOM results	0.230	0.240	0.240	0.237
So of the reservoir in each quadrant	0.254	0.253	0.253	0.255
Difference	-0.024	-0.013	-0.014	-0.018
Difference %	-2.4%	-1.3%	-1.4%	-1.8%
Sor in the reservoir calculated from ECLIPSE production data	0.235			

Table 2. Swept pore volume

	Well-1	*Well-2*	*Well-3*	*Well-4*
Vswept, bbl	589,444	818,921	888,288	735,376
Total Vswept, bbl	3,032,029			
Vswept/Vreservoir	0.190	0.264	0.286	0.237
VsweptTotal	0.977			

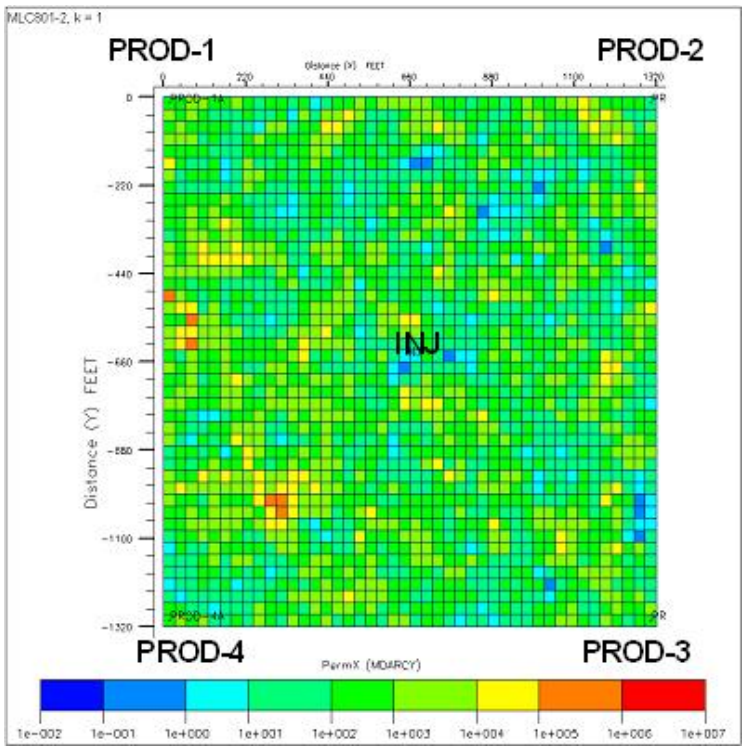

Figure1- Permeability in the least permeable layer 1

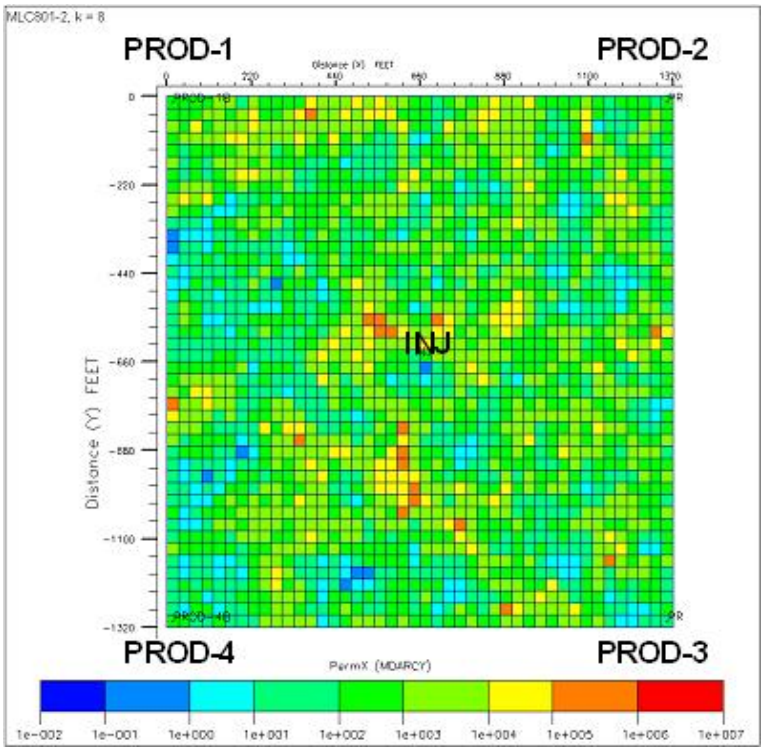

Figure 2- Permeability in the most permeable layer 8

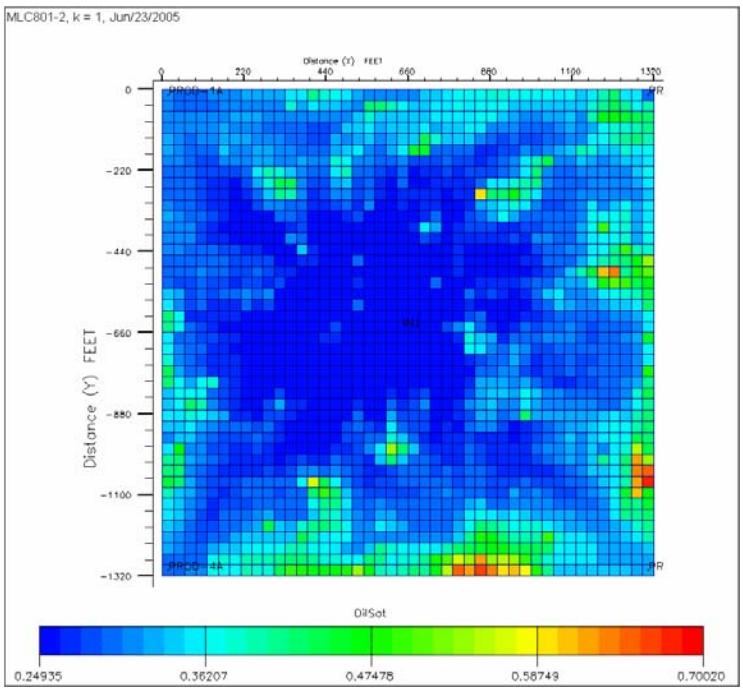

Figure 3- Oil saturation distribution in layer 1 at the beginning of the tracer injection

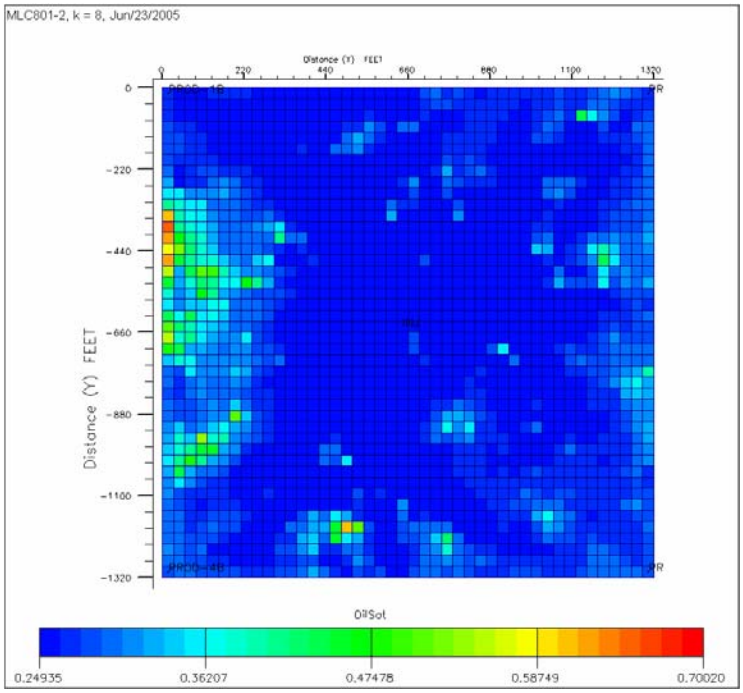

Figure 4- Oil saturation distribution in layer 8 at the beginning of the tracer injection

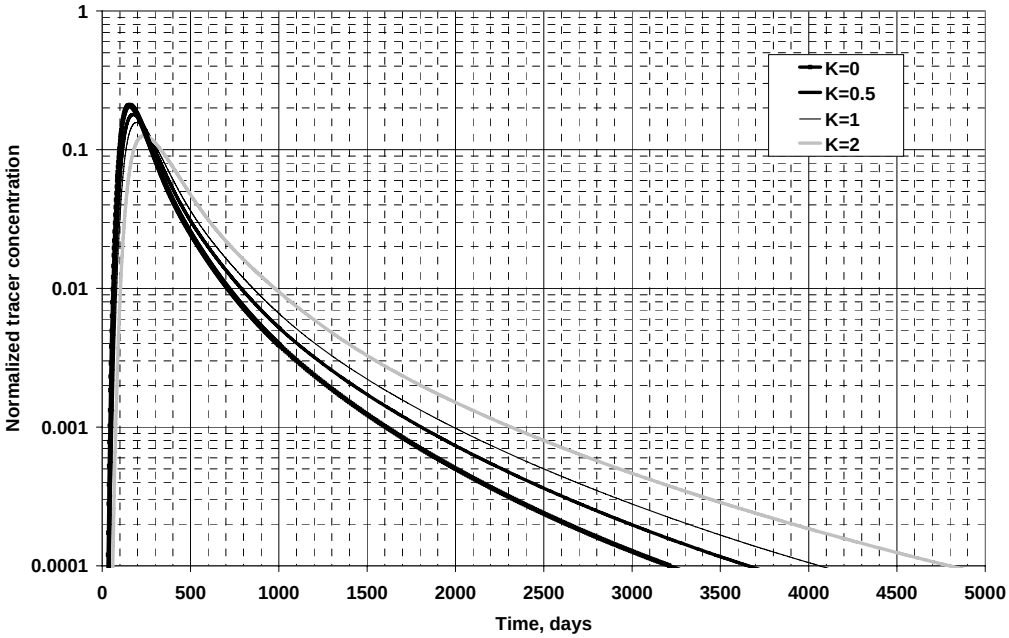

Figure 5- Normalized tracer concentration at production well 1

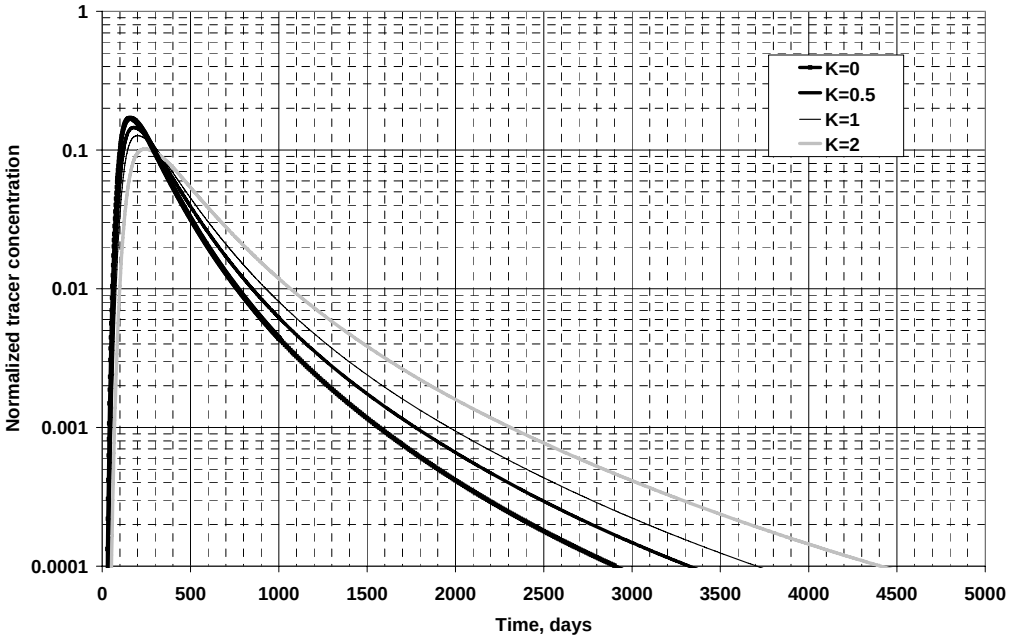

Figure 6- Normalized tracer concentration at production well 2

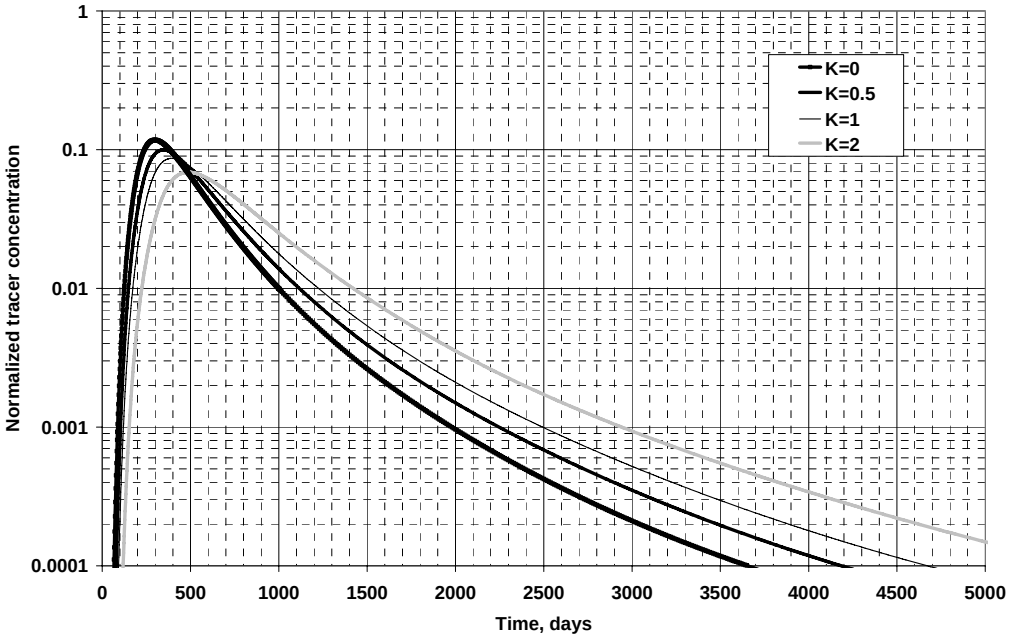

Figure 7- Normalized tracer concentration at production well 3

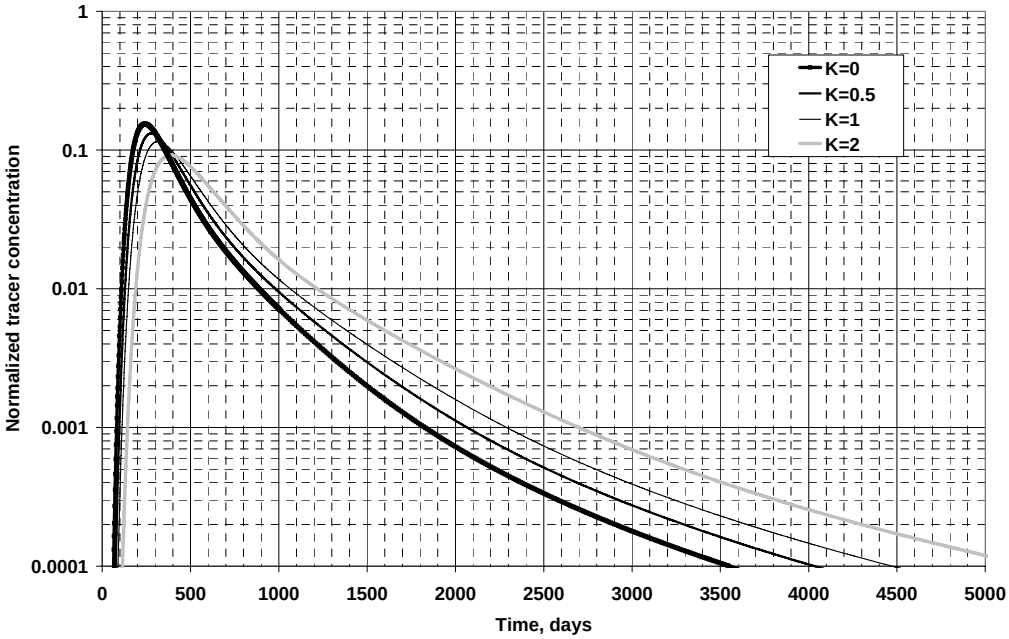

Figure 8- Normalized tracer concentration at production well 4

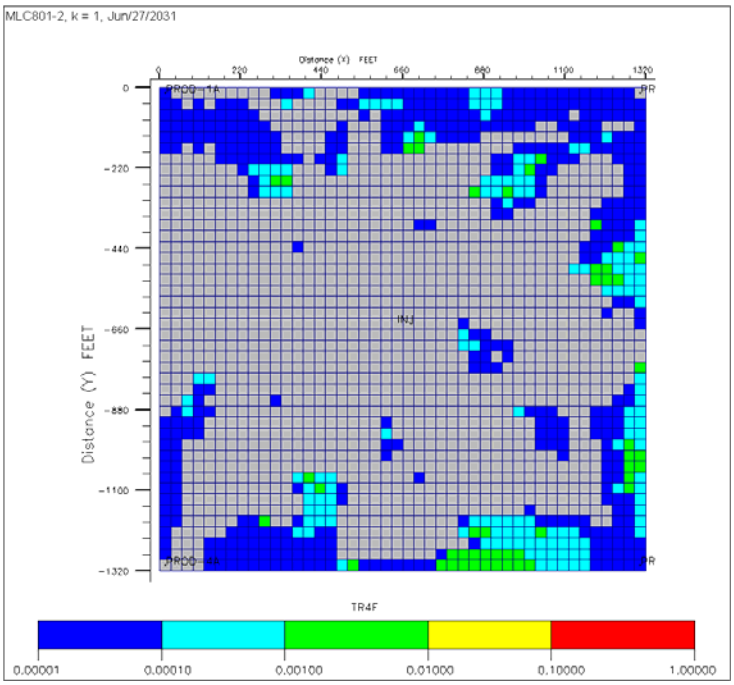

Figure 9- Tracer concentration profile in layer 1 at the end of the PITT

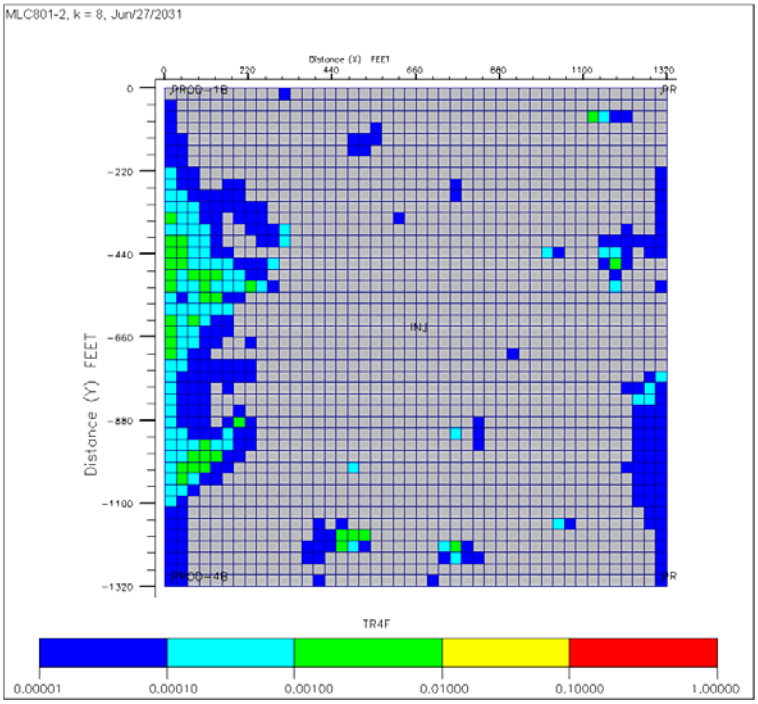

Figure 10- Tracer concentration profile in layer 8 at the end of the PITT

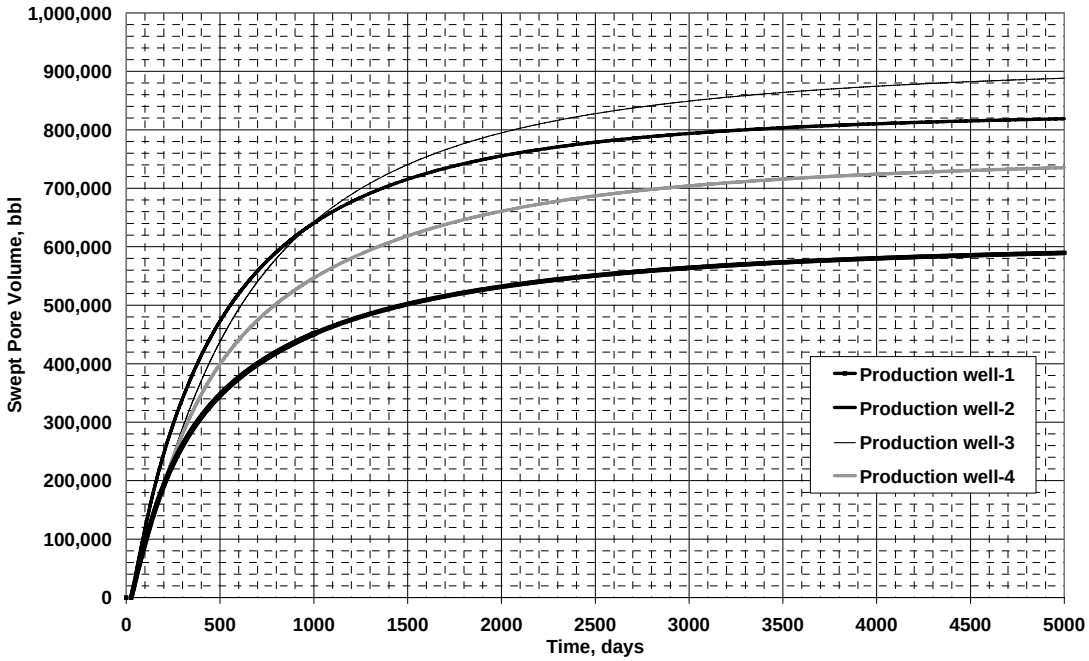

Figure 11- Swept pore volume between the injector and the each production well.

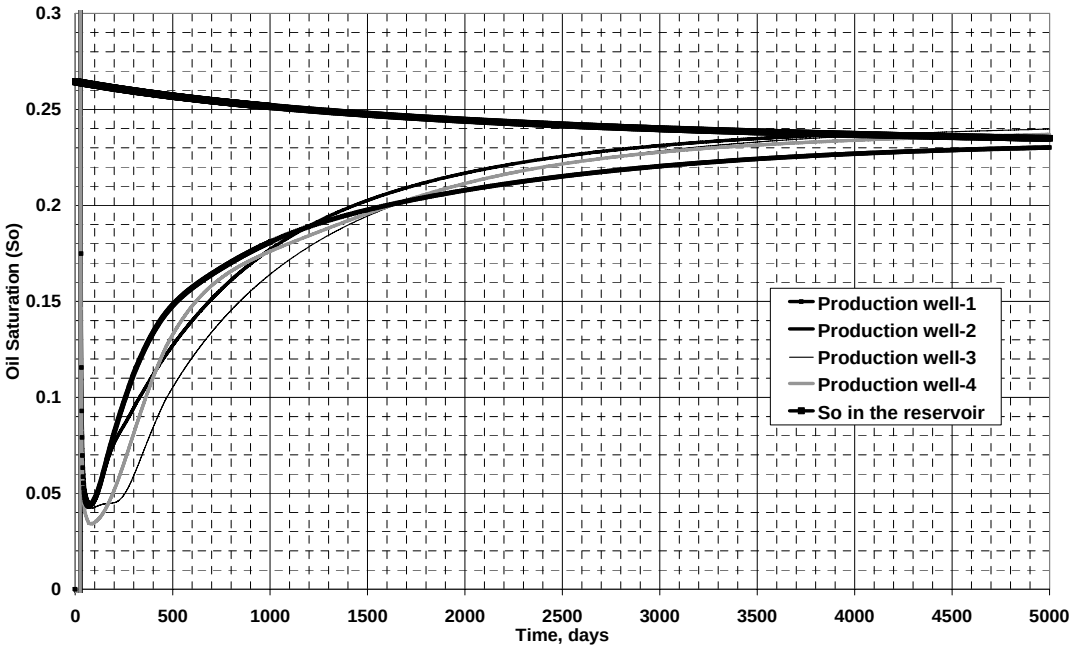

Figure 12- Oil Saturation calculated from the method of moments

In this example INVO2-run7, an unconfined, inverted 20 acre five-spot well pattern was simulated with the same reservoir parameters used in the confined 5-spot well pattern with a Dystra-Parsons coefficient of 0.81. The reservoir was water flooded for 1000 days (99% water cut) and then a tracer slug was injected for 50 days (0.1 PV). Total simulation time was 6000 days. Figures 1 and 2 show the oil saturation in the least and most permeable layers (layers 5 and 8) at the beginning of the tracer injection. Figures 3 and 4 show the conservative tracer concentration in those 2 layers at 50 days. Figures 5 and 6 show the conservative tracer concentration at 6000 days.

Figures 7 to 10 show the tracer concentration history of the partition coefficient of 0, 0.5, 1, and 2 for 4 producers, respectively. Regarding to the tracer breakthrough time, only tracer with partition coefficient of 2 shows the difference from the conservative tracer. The separations in the tails are noticeable among tracers.

Figure 11 shows the swept pore volume and the ratio of volume swept in the reservoir. The swept pore volume is increased even after 5000 days because the tracers sweeping between the outer boundary and they haven't been produced yet. Figure 12 shows the sweep efficiency, combined for all of the producers. The oil saturations in each swept pore volume are shown in Figure 13 and Table 1. The largest error in the estimated oil saturation is for the swept pore volume between the injector and production well 2, which has a very low permeability region. Table 2 summarizes the swept pore volumes.

Table 1: Oil saturation

So at the end of the tracer inj.	*Well-1*	*Well-2*	*Well-3*	*Well-4*
MOM results	0.210	0.202	0.234	0.225
So of the reservoir in each quadrant	0.269	0.276	0.263	0.261
Difference	-0.059	-0.074	-0.028	-0.036
Difference %	-5.9%	-7.4%	-2.8%	-3.6%
Sor in the reservoir calculated from ECLIPSE production data	0.240			

Table 2: Swept pore volumes

	Well-1	*Well-2*	*Well-3*	*Well-4*
Vswept, bbl	780,465	663,622	736,652	674,832
Total Swept Pore Volume	2,855,570			
Vswept/Vreservoir	0.25	0.21	0.24	0.22
VsweptTotal/Vreservoir	0.92			

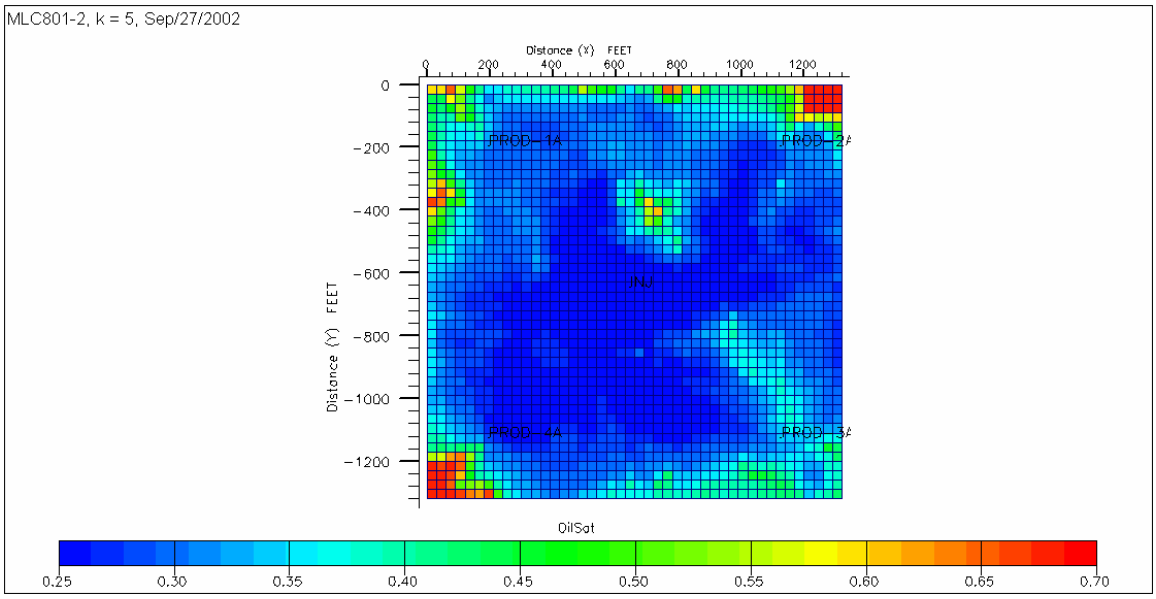

Figure 1- Oil saturation distribution at the start of tracer injection on Layer5 (least permeable layer)

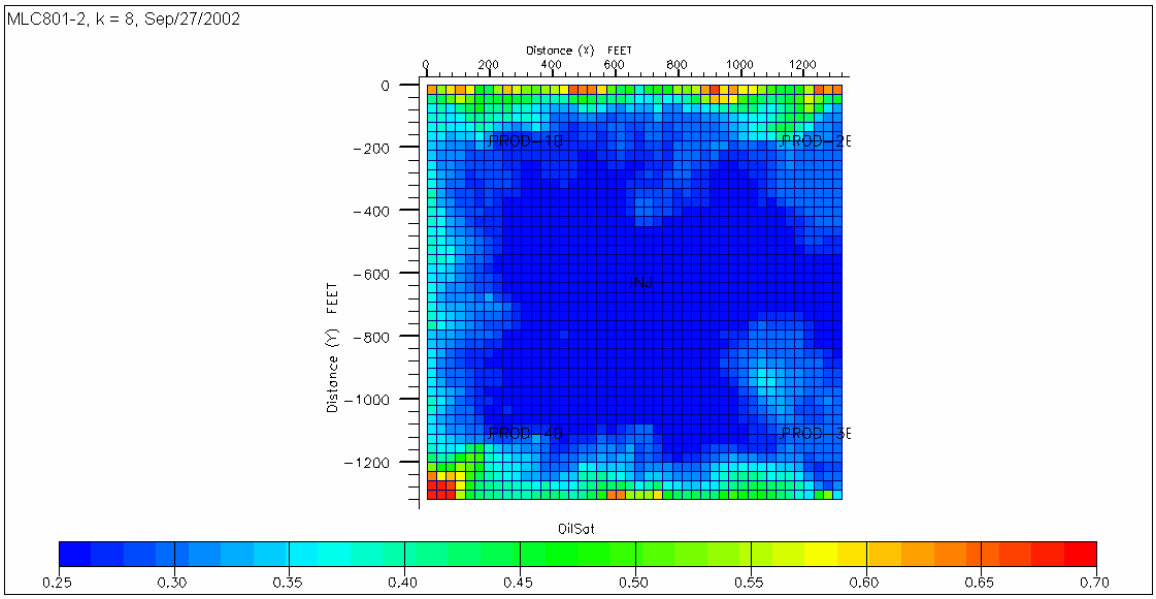

Figure 2- Oil saturation distribution at the start of tracer injection on Layer8 (most permeable layer)

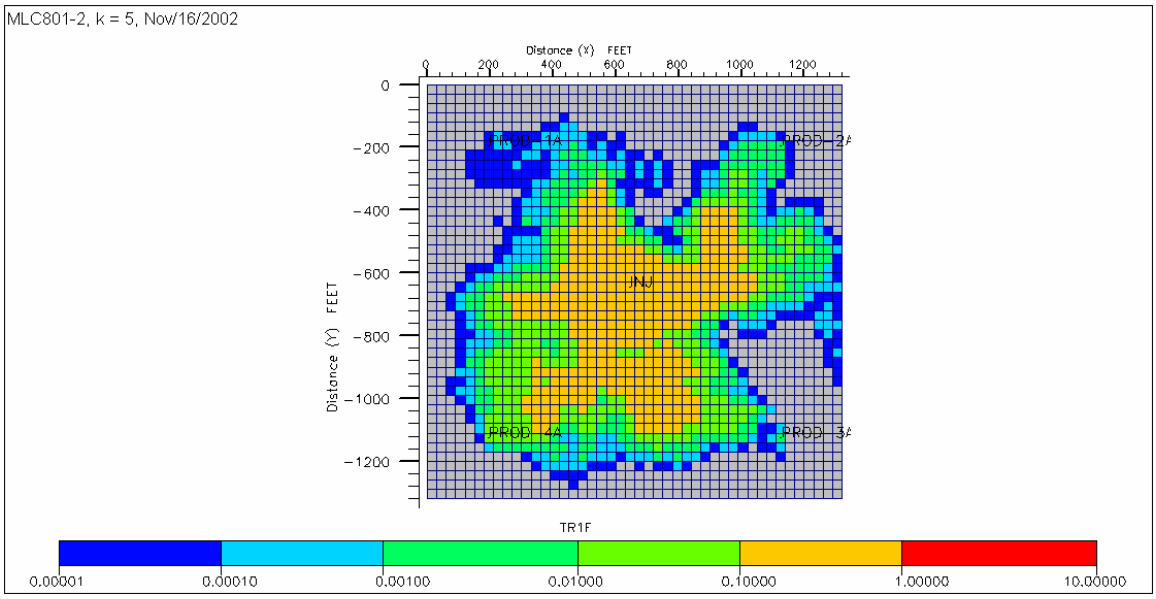

Figure 3- Conservative tracer concentration at 50 days in layer5 (least permeable layer)

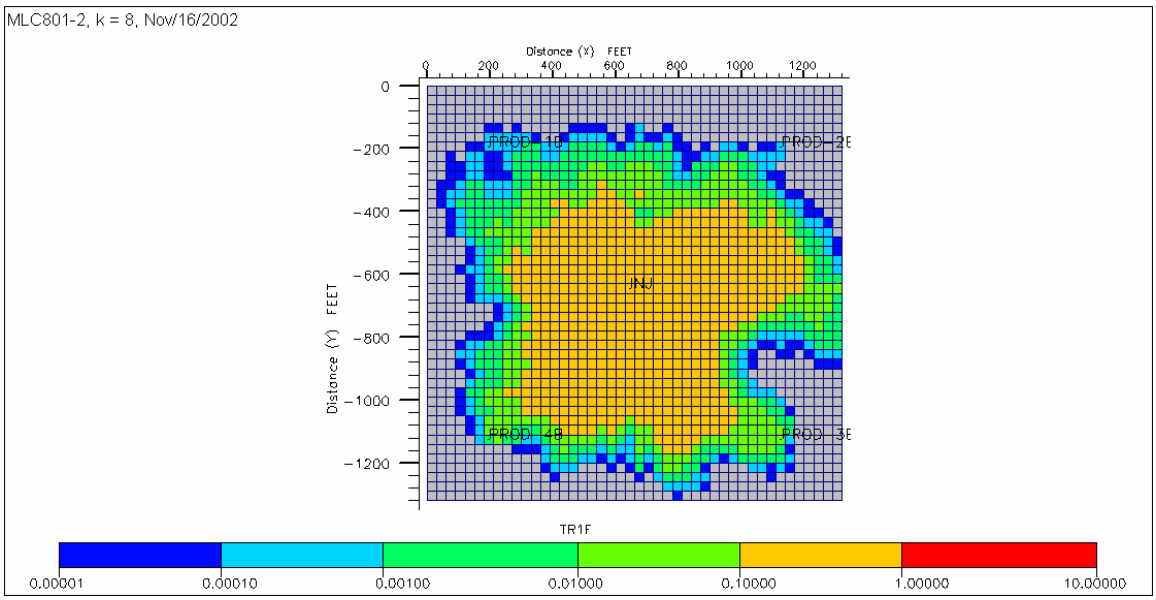

Figure 4- Conservative tracer concentration at 50 days in layer8 (most permeable layer)

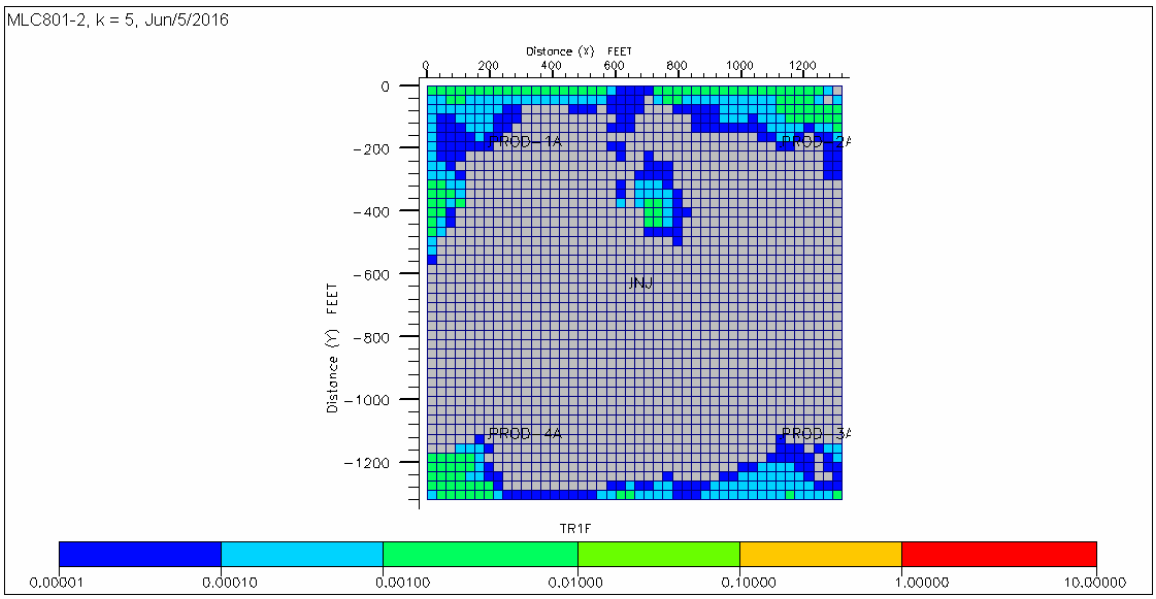

Figure 5- Conservative tracer concentration at 5000 days in layer 5 (least permeable layer)

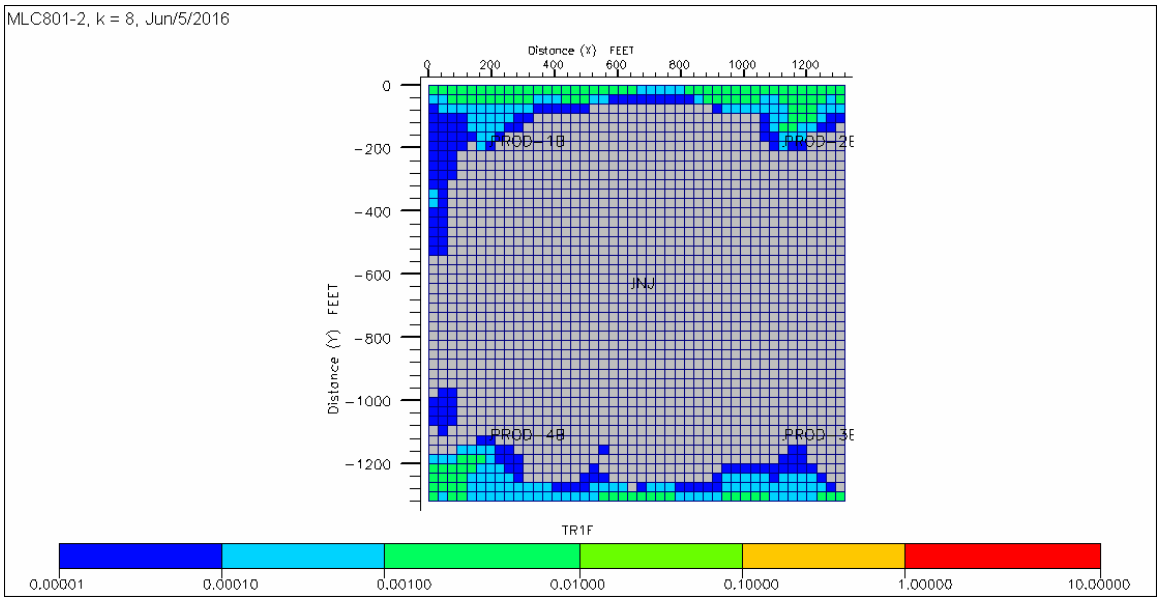

Figure 6- Conservative tracer concentration at 5000 days in layer8 (most permeable layer)

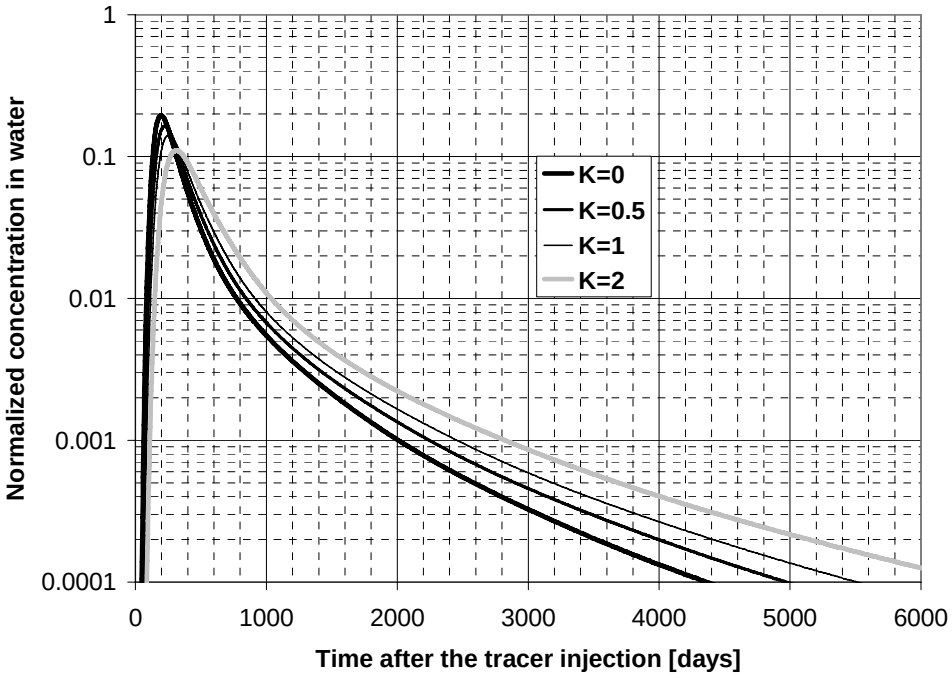

Figure 7- Tracer concentration history at Producer 1

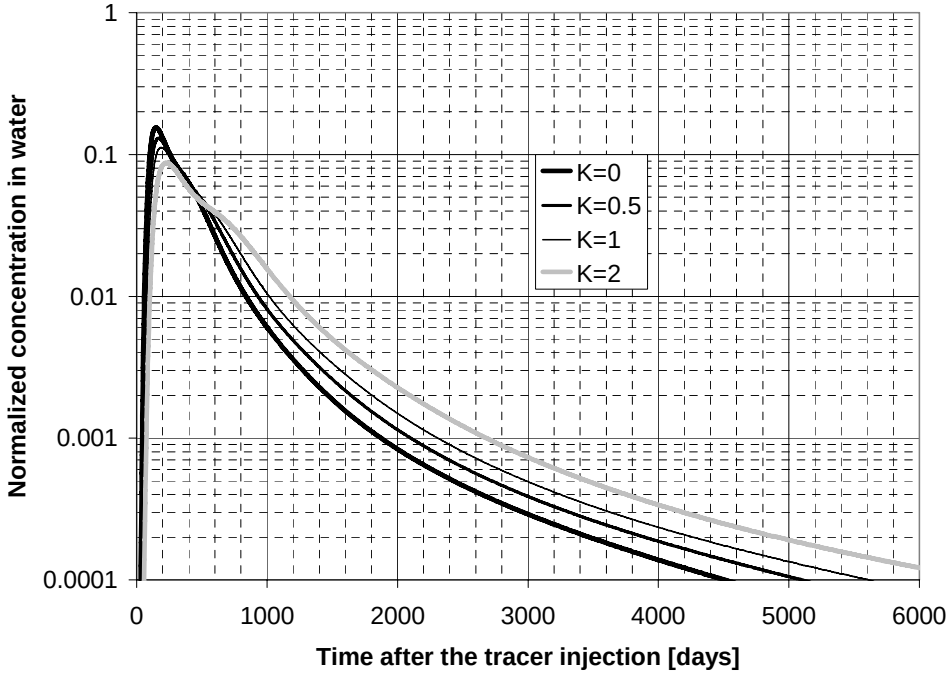

Figure 8- Tracer concentration history at Prod2

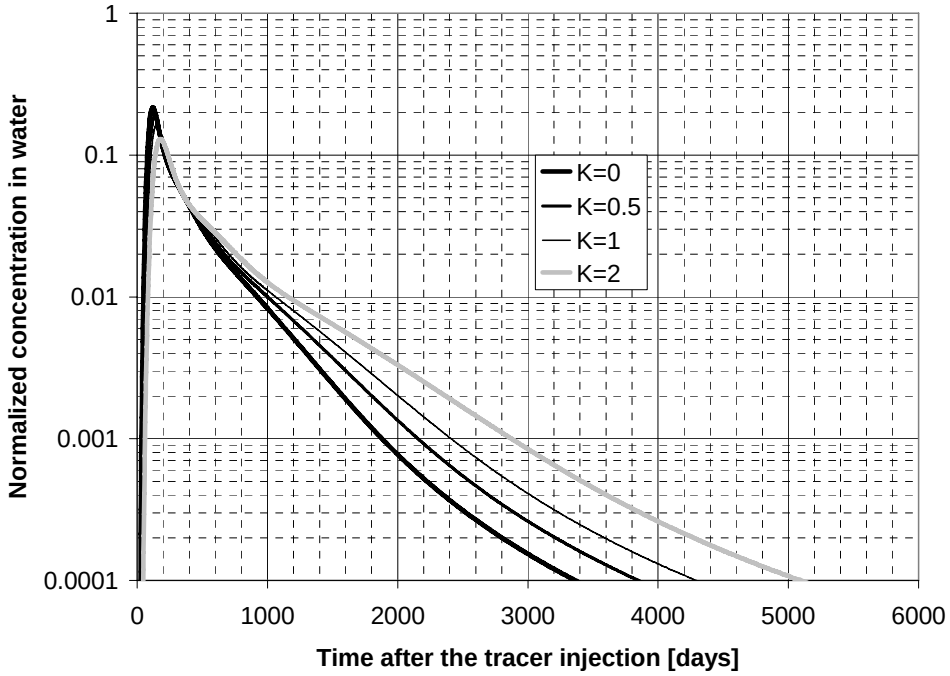

Figure 9- Tracer concentration history at Prod3

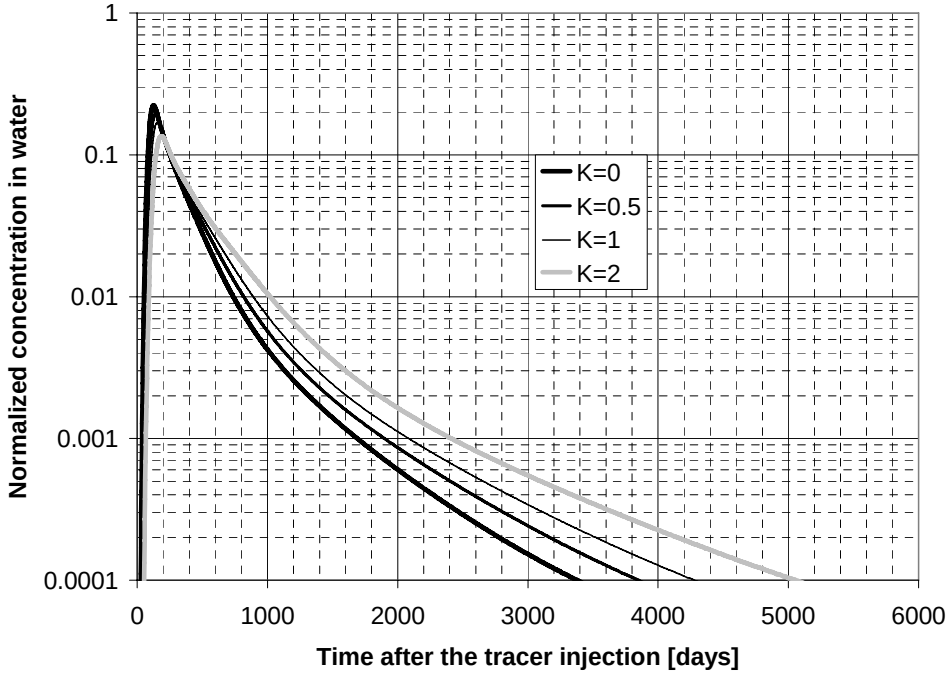

Figure 10- Tracer concentration history at Prod4

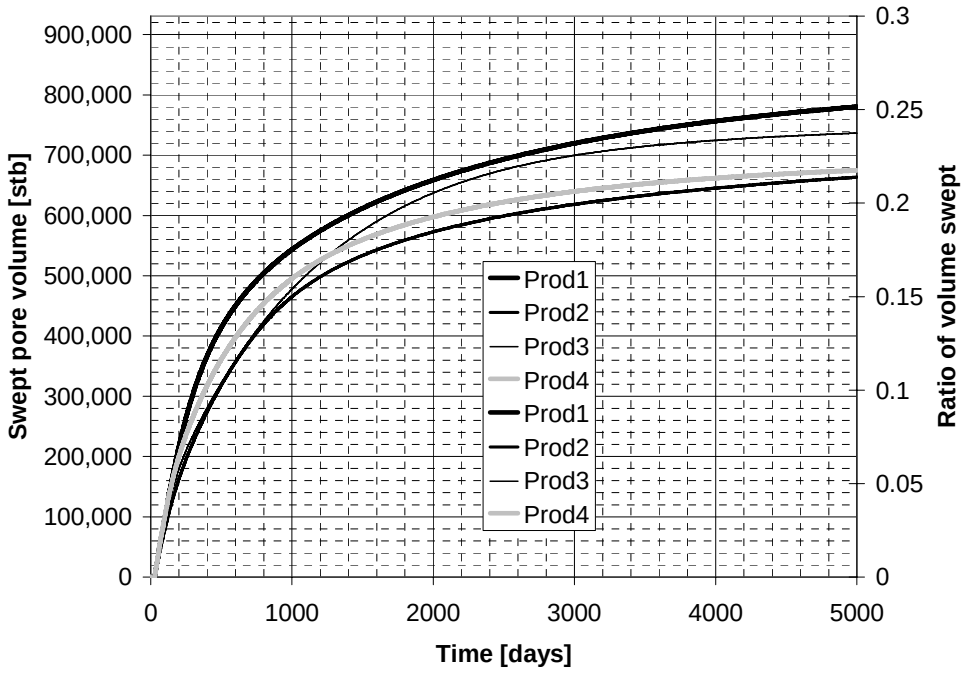

Figure 11- Swept pore volume and the ratio of volume swept

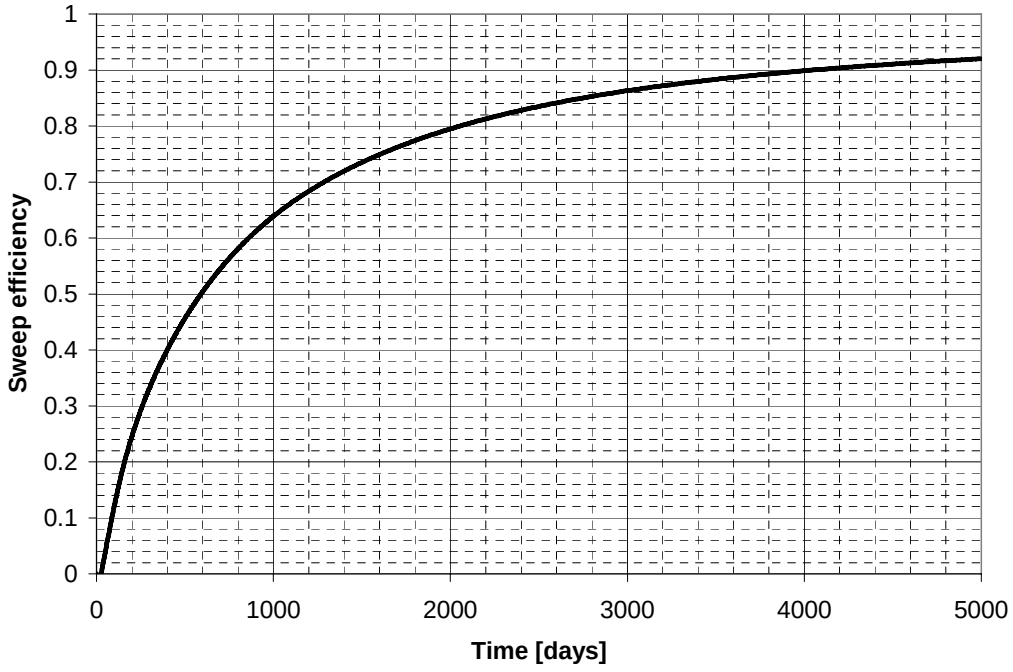

Figure 12- Sweep efficiency in the reservoir

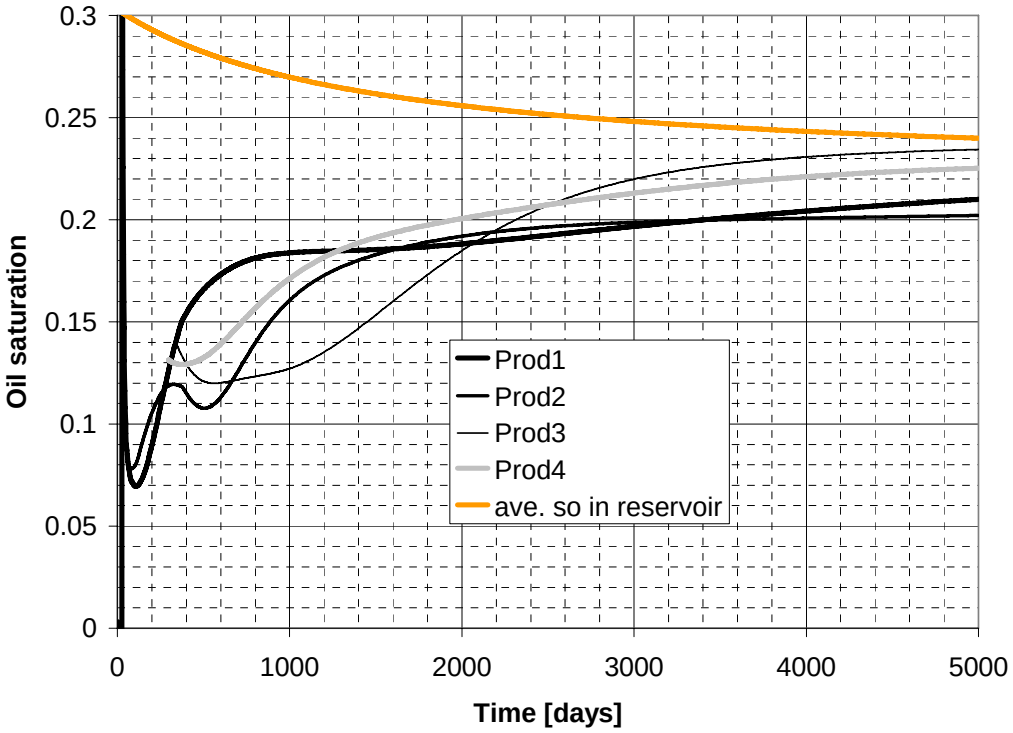

Figure 13- Oil saturation calculated from the method of moments

In this example INVO2-run8, tracer injection began after 250 days of water flooding (0.5 PV and 77% water cut). The purpose of this example was to test the method of moments for a case with more mobile oil to verify that the generalized method as derived in this report can be used to give a good approximation to the oil saturation even if it is far above residual oil saturation.

Figures 1 and 2 show the oil saturation in the reservoir at the beginning of the tracer flood. Figures 3 to 6 show the tracer concentrations for each production well. In Figures 4 to 6, early tracer breakthrough is observed. Figure 8 shows the tracer concentration in layer 5 after 25 days of tracer flooding and also shows the early breakthrough at production wells 2, 3 and 4. Figures 9 and 10 show the tracer concentration in layers 8 and 5 at the end of the simulation. Most of the tracer was recovered except past the four production wells.

Figures 11 and 12 show the swept pore volumes and the oil saturations calculated from the method of moments. Table 1 summarizes the oil saturation values. Table 2 shows the swept pore volumes. Although the tracer injection started at 77% water cut, mobile oil in the reservoir didn't increase the error in the estimated oil saturations compared to the previous example with the PITT starting at 99% water cut.

Table 1. Oil saturations INVO2-run8

So at the end of the simulation	*Well-1*	*Well-2*	*Well-3*	*Well-4*
MOM results for So	0.226	0.197	0.251	0.226
Average So of the reservoir in each quadrant	0.269	0.276	0.263	0.261
Difference	-0.044	-0.079	-0.012	-0.036
Difference %	-4.4%	-7.9%	-1.2%	-3.6%
Sor in the reservoir calculated from ECLIPSE production data	0.24			

Table 2. Swept pore volumes

	Well-1	*Well-2*	*Well-3*	*Well-4*
Vswept, bbl	781,780	659,269	727,266	671,643
Total Vswept, bbl	2,839,958			
Vswept/Vreservoir	0.252	0.212	0.234	0.216
VsweptTotal/Vreservoir	0.915			

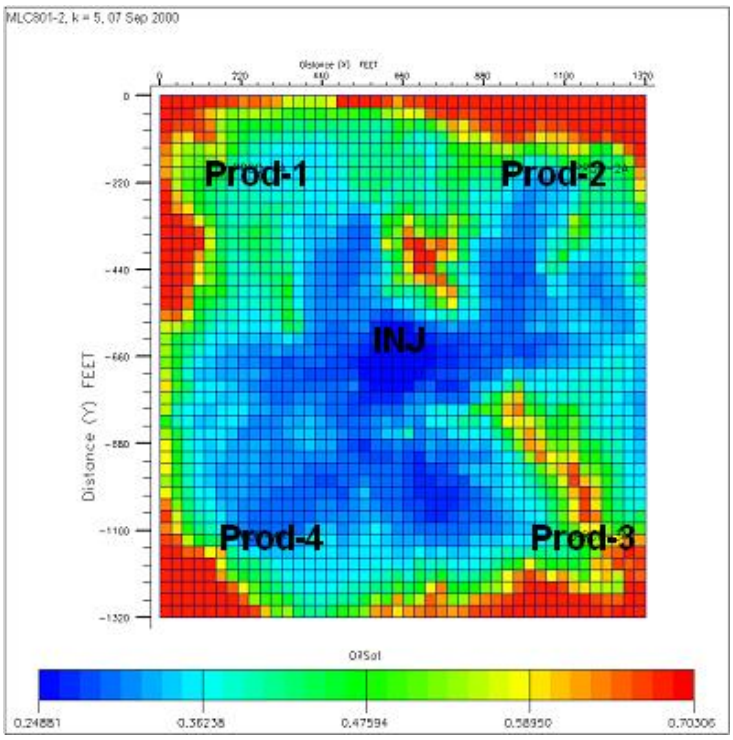

Figure 1- Oil saturation distribution in layer 5 at the beginning of the tracer injection

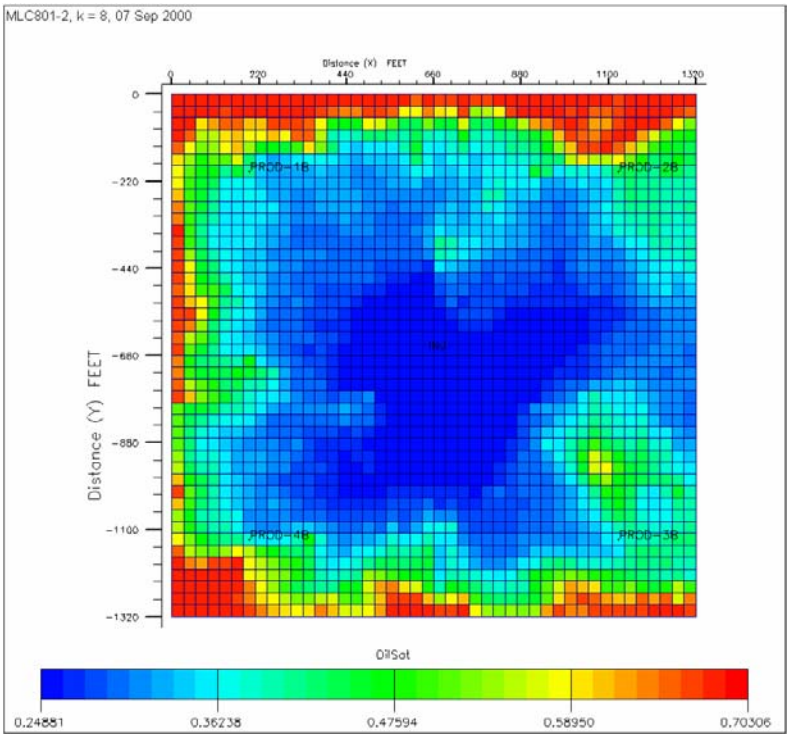

Figure 2- Oil saturation distribution in layer 8 at the beginning of the tracer injection

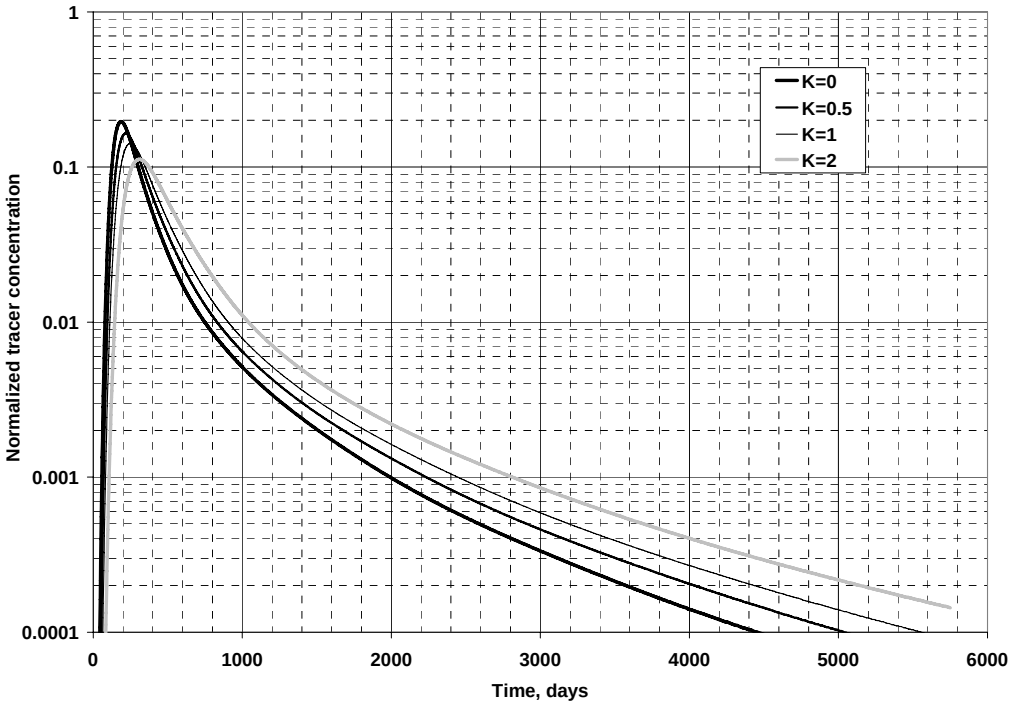

Figure 3- Normalized tracer concentration at production well 1

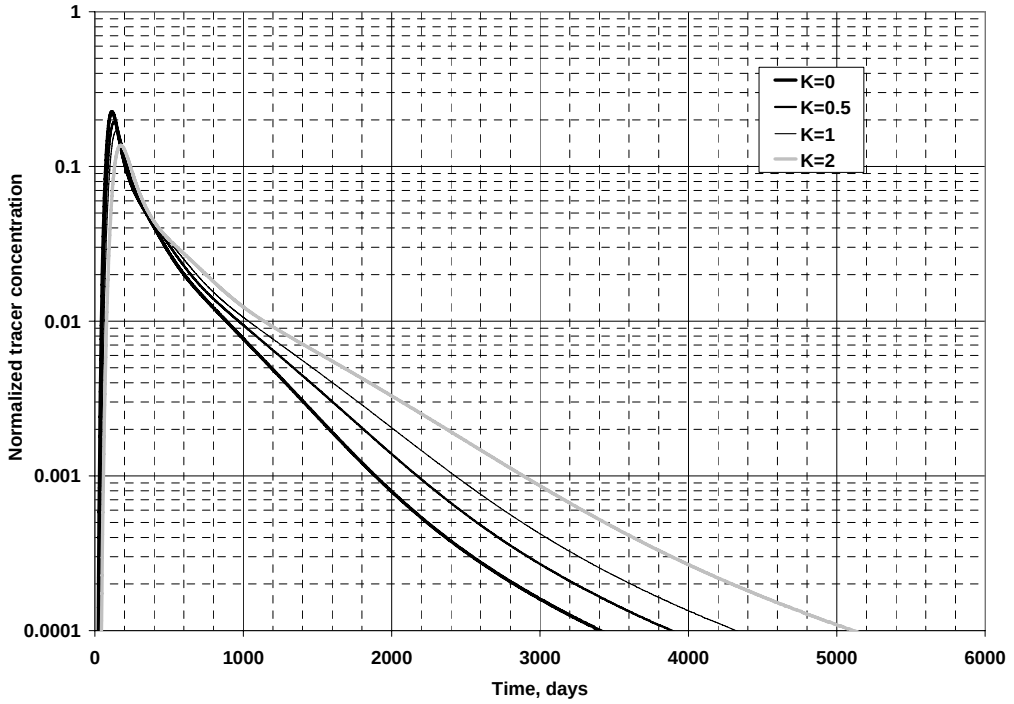

Figure 4- Normalized tracer concentration at production well 2

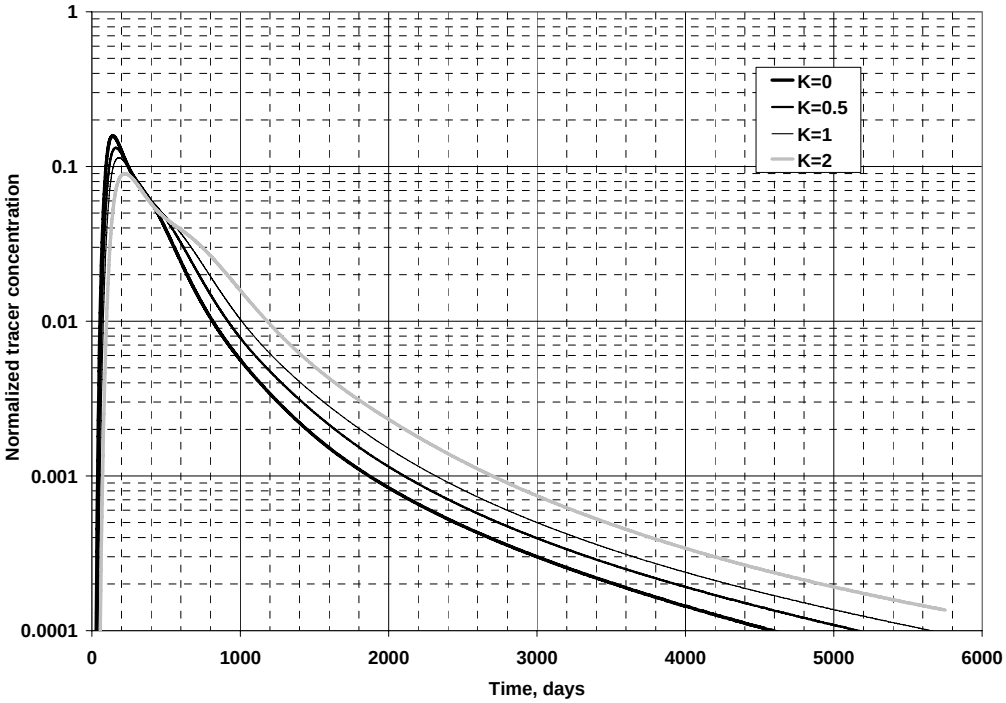

Figure 5- Normalized tracer concentration at production well 3

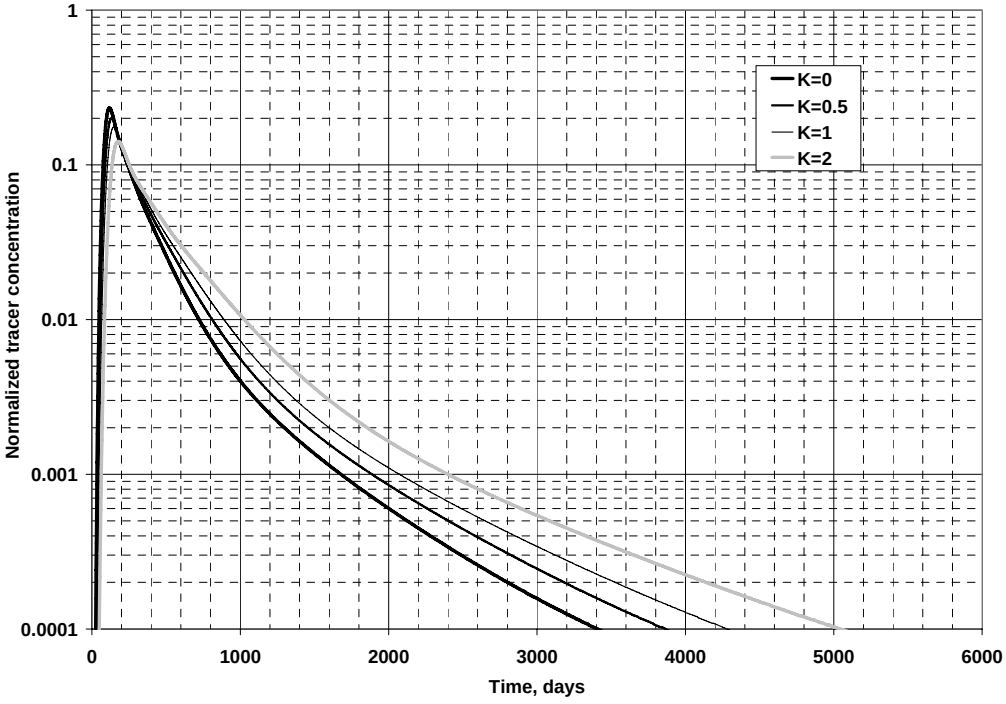

Figure 6- Normalized tracer concentration at production well 4

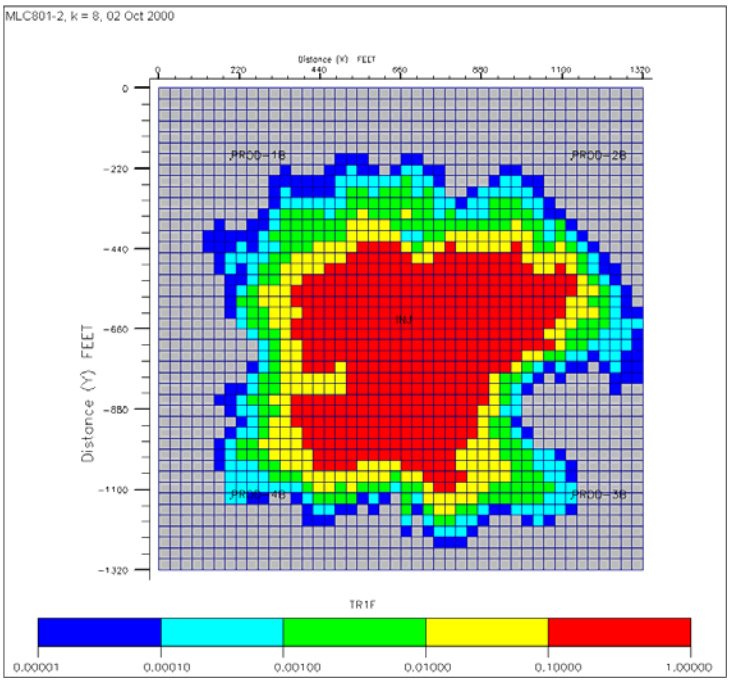

Figure 7- Tracer concentration (partition coefficient 2) profile in logarithmic scale after 25 days of tracer injection in layer 3

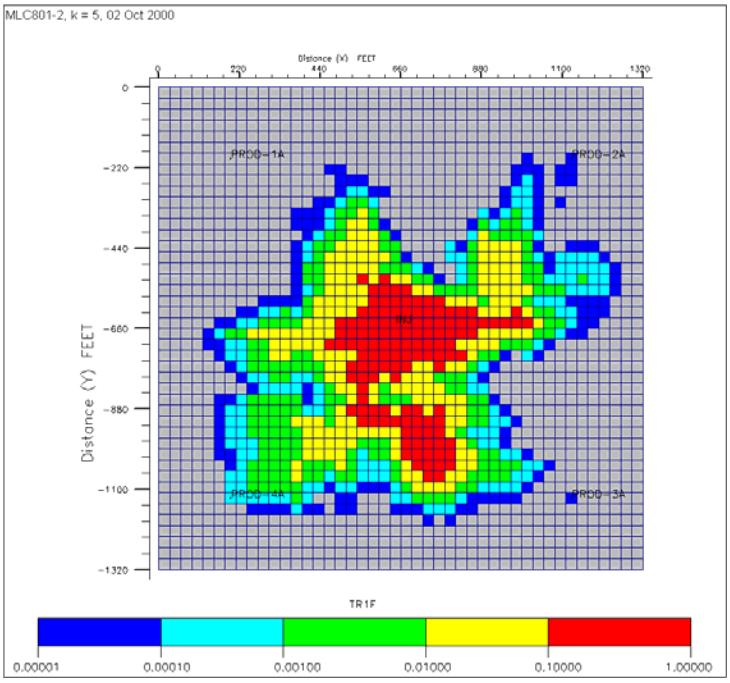

Figure 8- Tracer concentration profile (partition coefficient 2) in layer 5 after 25 days of tracer injection

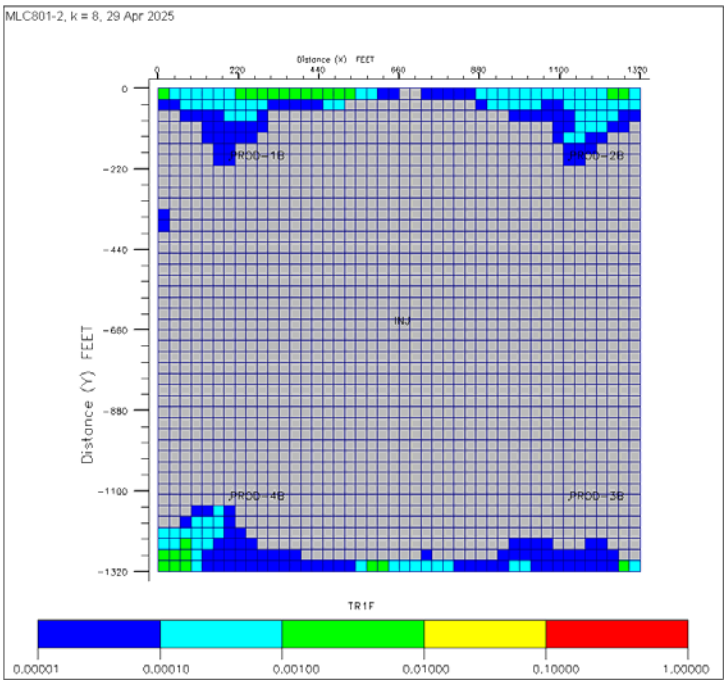

Figure 9- Tracer concentration profile (partition coefficient 2) in layer 8 at the end of the simulation

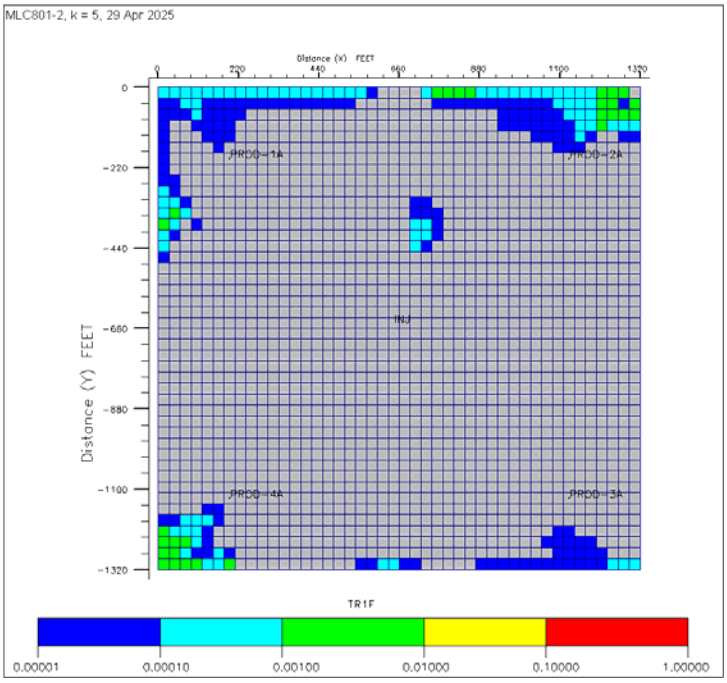

Figure 10- Tracer concentration profile (partition coefficient 2) in layer 5 at the end of the simulation

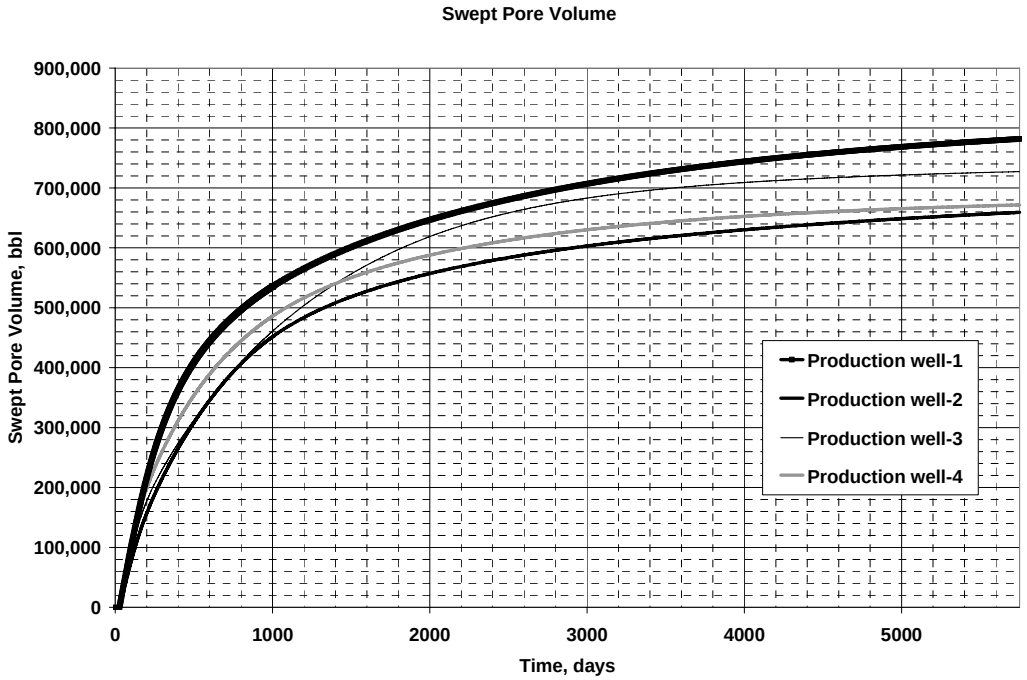

Figure 11- Swept pore volume between the injector and the each production well.

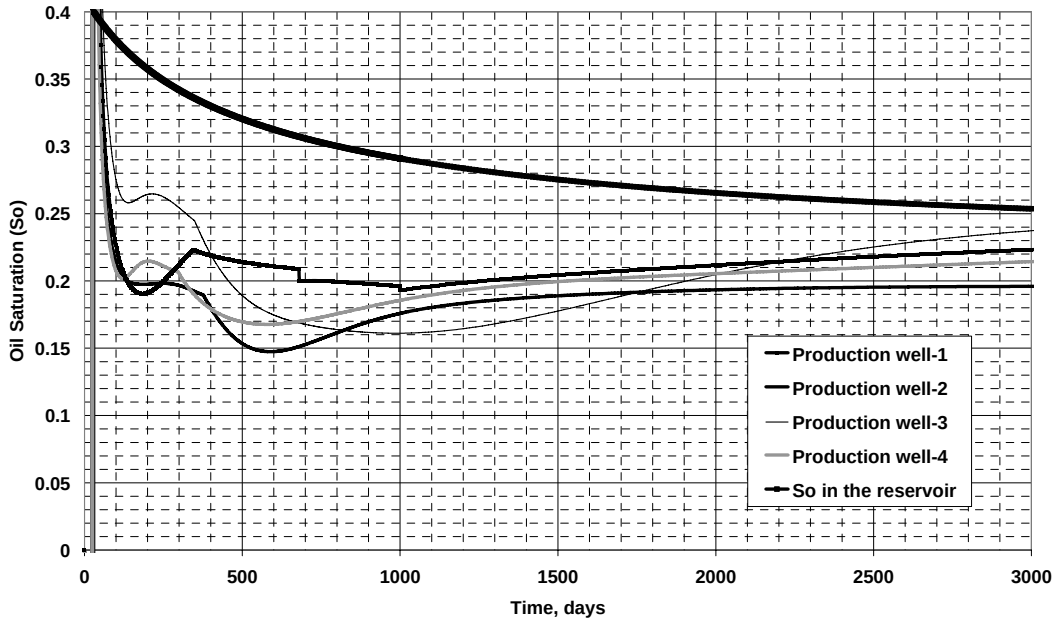

Figure 12- Oil saturation calculated from the method of moments

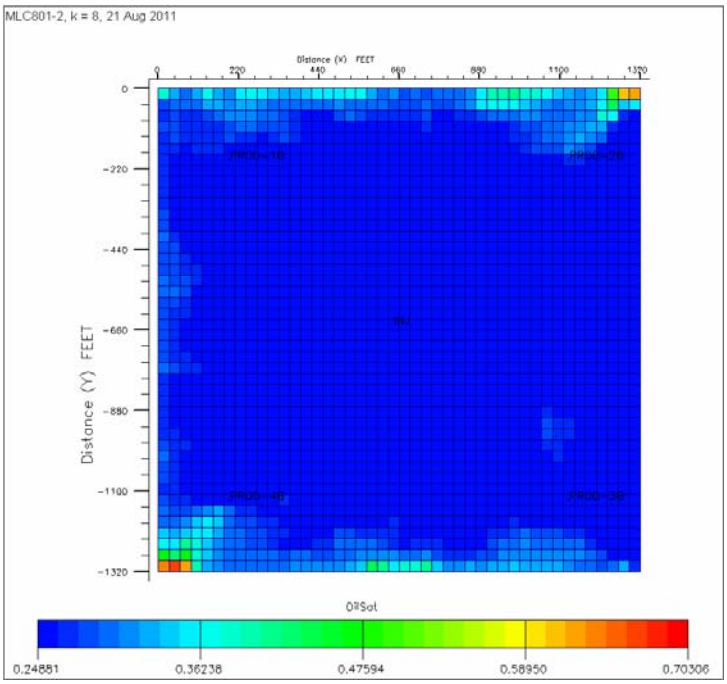

Figure 13- Oil saturation distribution in layer 8 at the end of the simulation

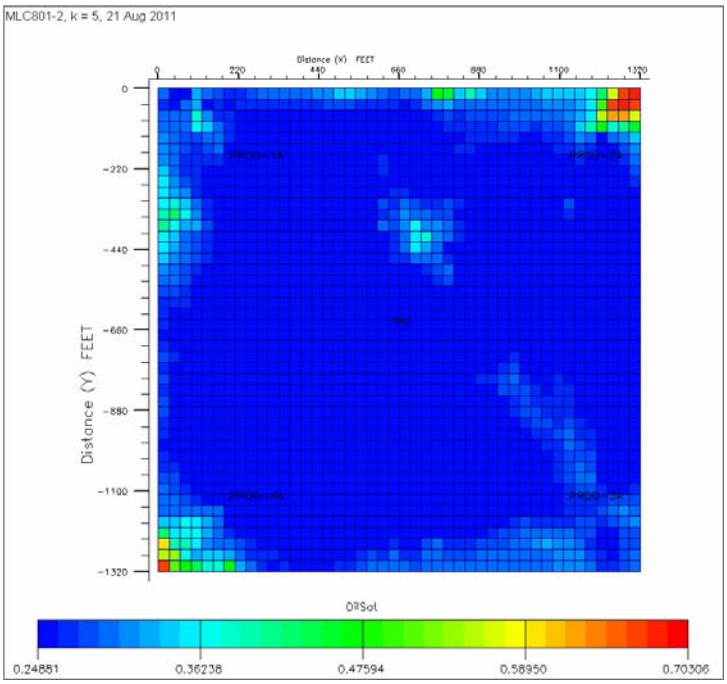

Figure 14- Oil saturation distribution in layer 5 at the end of the simulation

Tracer Tests using Natural Tracers

Crude oil is a mixture of organic components. These components have varying solubilities in water. Partition coefficients and concentrations of aliphatic acids and alkyl phenols present in crude oil are in publications (Reinsel et al., 1994 and Taylor et al., 1997). We have investigated the possibility of using some of the more soluble components as natural tracers to estimate oil saturation and swept pore volumes. The goal is to achieve a low cost alternative to a conventional PITT.

The same heterogeneous permeability field used for the previous simulations has been used to illustrate the production of natural tracers. The initial oil saturation is 0.70. The oil is modeled as five components of different water solubilities. Data for the modeled components was obtained from publications (Reinsel et al., 1994 and Taylor et al., 1997). Table 1 shows the oil components and their initial concentrations. One pore volume of water is injected in 388 days.

Figure 1 shows the concentrations in the produced brine for the components in the crude oil that partition into the brine during a simulated waterflood. As the components are stripped out of the oil phase, their concentrations in both the oil and the water phases decrease with time. The decrease in concentration depends upon the partition coefficient of the component at reservoir conditions. Lower partition coefficients correspond to higher solubility in water and hence a faster decrease in produced concentrations. Figure 14 shows the normalized concentration for phenol. The concentrations are normalized by the initial aqueous phase concentration C_{iwI} assuming local equilibrium between the crude oil and the water. The normalized concentration is defined as follows:

$$C_{niw} = \frac{C_{iwI} - C_{iw}}{C_{iwI}}$$

The normalized tracer curves look similar to tracer curves in a continuous tracer injection. Figure 2 also shows a comparison between a natural tracer and a continuous injection of partitioning tracers. Therefore, the simulation of a continuous tracer with the same partition coefficient gives the same result as simulating a dissolved component i.e. a natural tracer. Although UTCHEM can be used either way, many simulators do not include an option for the dissolution of components of the crude oil into the brine, so they could not be used to model natural tracers directly. But they might be able to model such tracers indirectly in this way.

The measured concentrations of any two partitioning components can be used to estimate oil saturation and swept pore volumes rather than the conventional use of the conservative tracer and one or more partitioning tracers. This is critical to this application because there is no conservative tracer available for the case of natural tracers. Actually, some anionic components of the brine such as the chloride anion are conservative, but not likely to be synchronized with the dissolved components and therefore not useful for calculating oil saturation. Figure 3 shows the estimated initial oil saturations using the various components. Since the initial concentration of the components in the water phase is needed, the choice of oil components will depend upon when the concentration measurements are initiated. For example, if measurement of organic component concentrations were started after 500 days of water injection, the obvious choice of components would be o-cresol and 2,4 -dimethyl phenol. Figure 4 shows a comparison between the estimated swept pore volume and the reservoir pore volume. Since the initial oil saturation and swept pore volumes have been estimated, the oil saturation at the end of a waterflood can be

calculated. Figure 5 shows the estimated oil saturation at the end of a waterflood. The estimated oil saturations and pore volumes match the reservoir values closely.

Naturally Fractured Reservoirs

PITTs in naturally fractured reservoirs will typically take longer and the tracer concentrations will be lower than for single porosity reservoirs due to matrix transfer.14 Therefore, the possibility of using natural tracers in fractured reservoirs has been researched as an alternative to injected tracers since it would cost less than injecting tracers. Natural tracers were simulated for a waterflood in a quarter of a five-spot well pattern with dimensions of 111.5 ft long by 111.5 ft wide by 17 ft thick. The reservoir has a fracture spacing of 3 ft in both the horizontal and vertical directions, which is typical of carbonate beds of equivalent thickness (Nelson, 1985). We modeled the fractures explicitly as distinct gridblocks with the properties of the fracture rather than use the traditional dual porosity approach. The matrix has a porosity of 0.10. The fracture occupies 0.1 % of the total reservoir pore volume. The permeabilities of the fracture and matrix are 1000 and 1 md, respectively. One pore volume of water is injected in 1 year. The oil was modeled as four soluble components initially in equilibrium with the water. This simulation was performed using ECLIPSE.

Figure 6 shows the produced component concentrations. Figure 7 shows the oil saturations calculated from the produced tracers. One of the obvious differences compared to a single porosity simulation is the longer time required to estimate the oil saturation due to the lower rate of decline in the concentrations at the producers. However, the estimates of the oil saturation are ultimately as accurate as for the single porosity cases. At earlier times, the estimated oil saturations are low compared to the matrix values, but even this information could be useful. It might be possible to use inverse modeling to greatly shorten the time required to give useful estimates of the remaining oil saturation.

Table 1—Component Concentrations and Partition Coefficients for the Natural Tracer Simulation

Component	*Initial Concentration in Oil, mg/l*	*Partition Coefficient*
acetic acid	1.0	0.009
butyric acid	1.0	0.084
phenol	1.5	1.3
o-cresol	7.5	5.2
2,4-dimethyl phenol	8.5	15

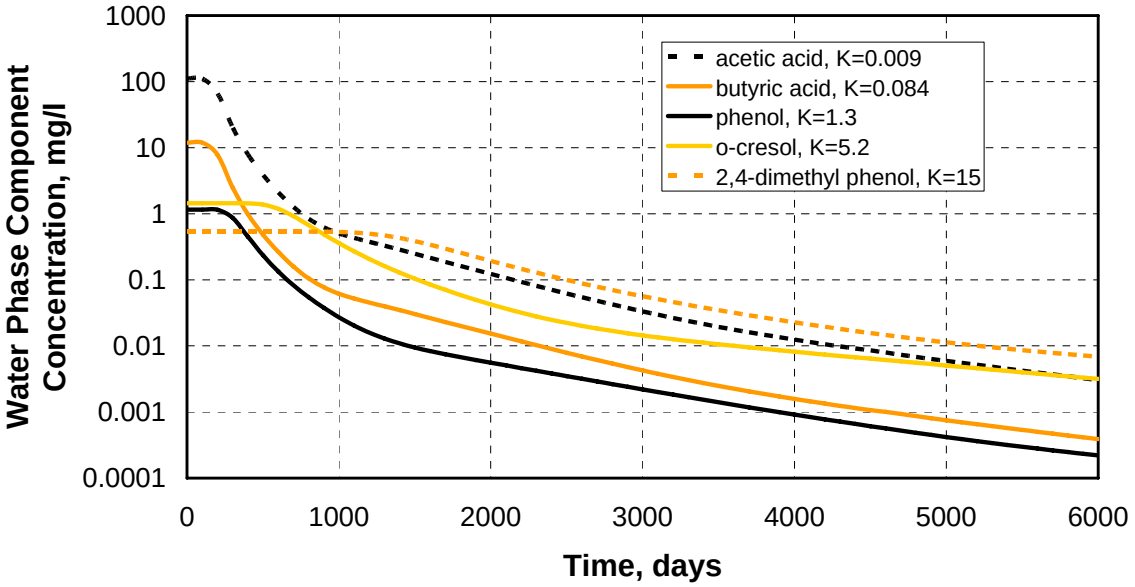

Figure 1- Component concentrations in the water phase.

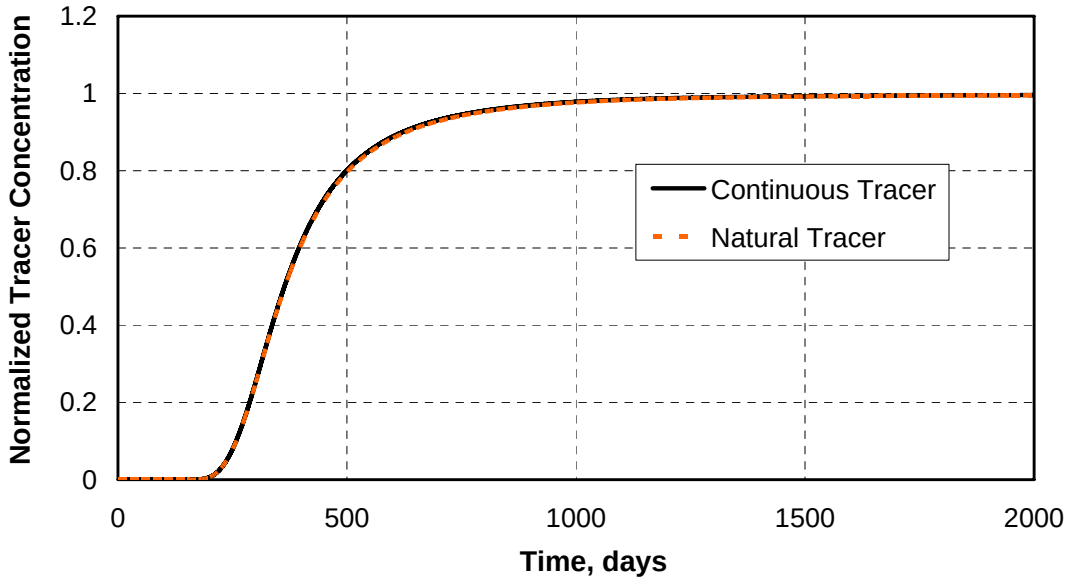

Figure 2- Comparison between natural and continuous tracer injection.

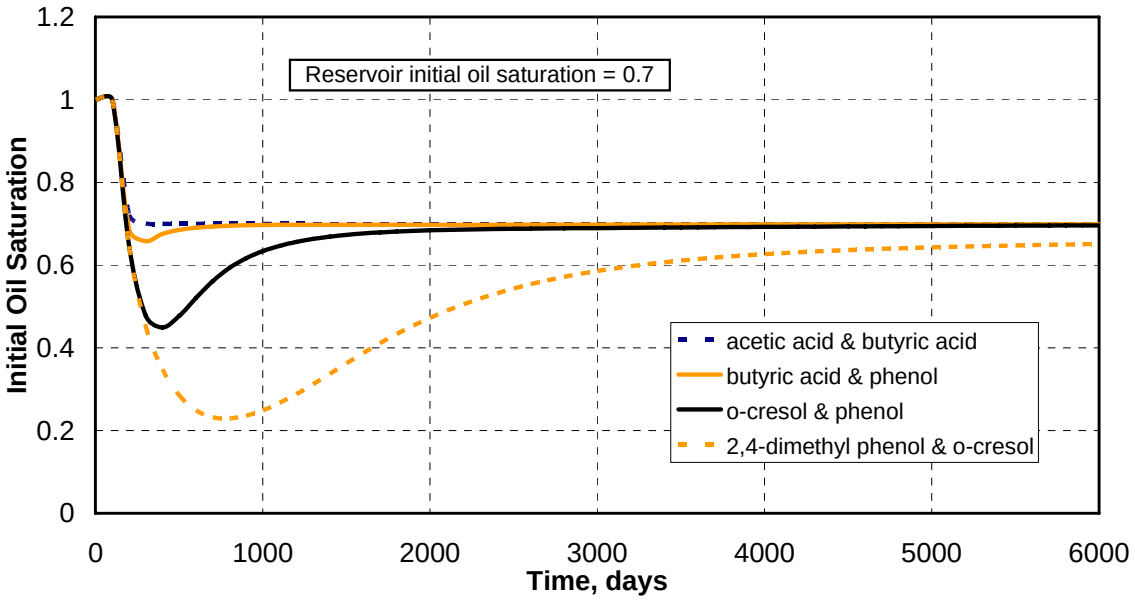

Figure 3- Estimated initial oil saturation using various components for the natural tracer test.

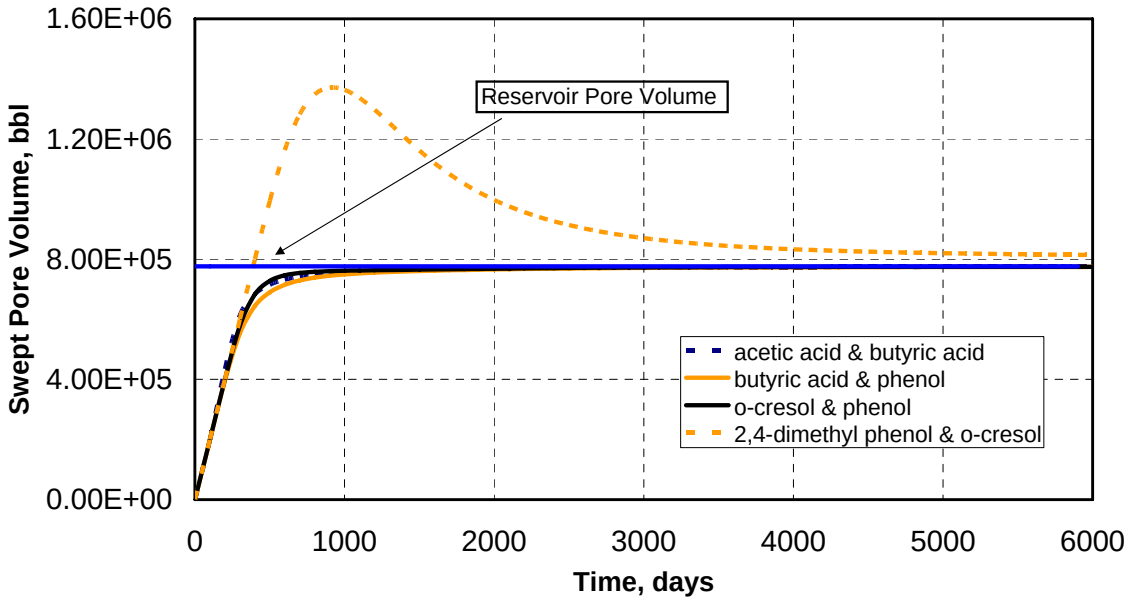

Figure 4- Estimated swept pore volume using various components for the natural tracer test.

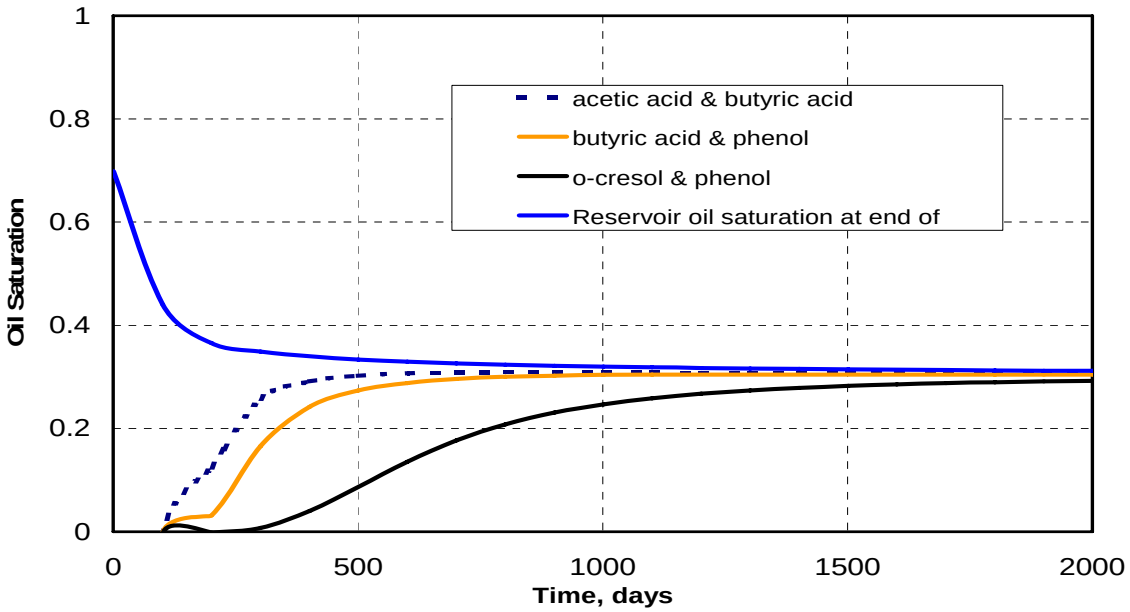

Figure 5- Estimated oil saturation at end of waterflood for the natural tracer test.

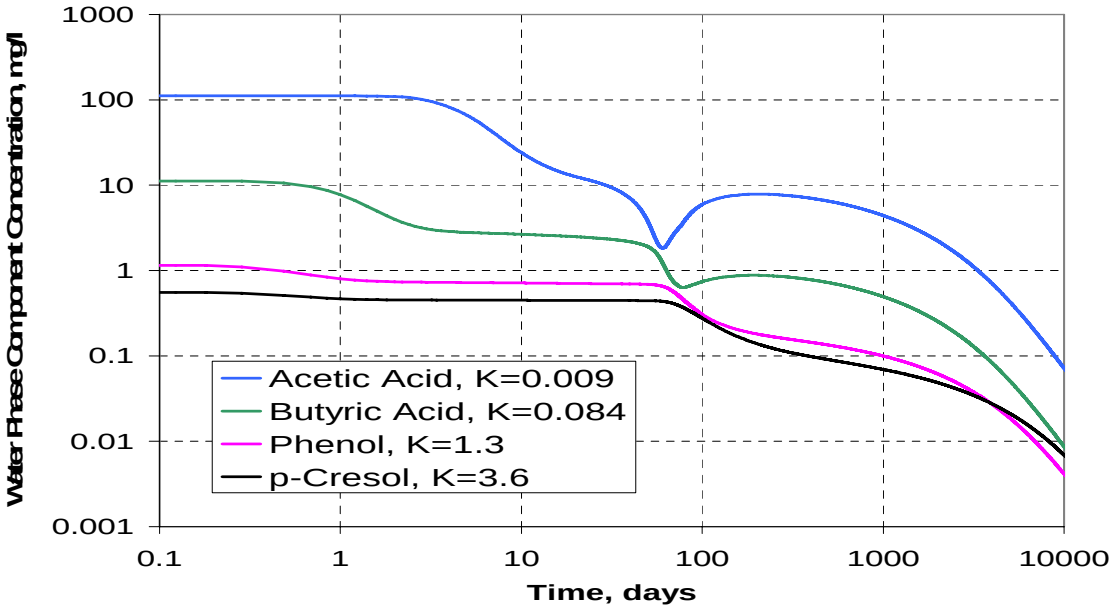

Figure 6- Component concentrations for the fractured reservoir.

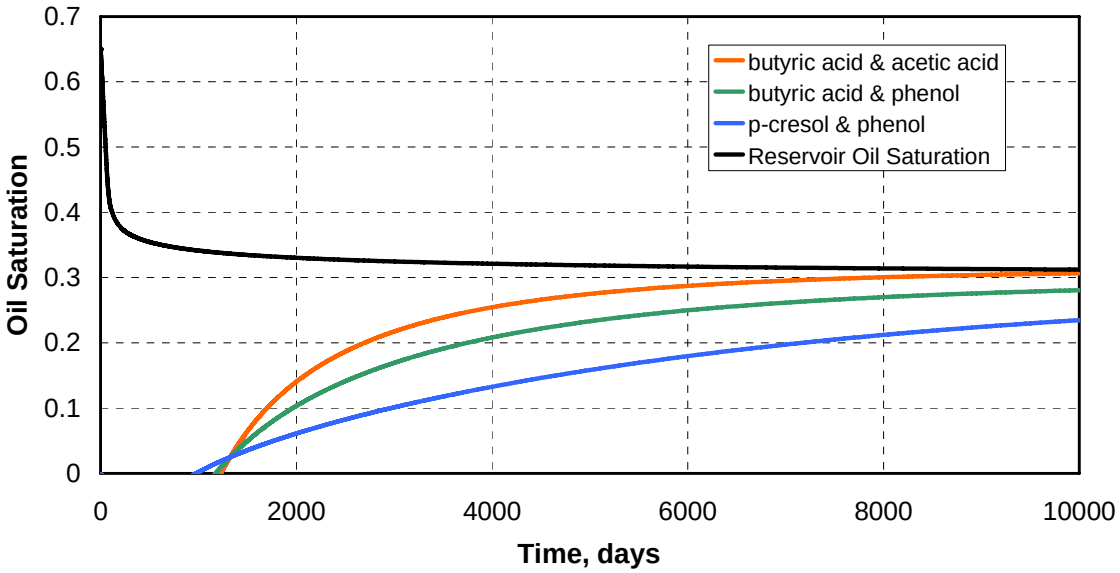

Figure 7- Estimated oil saturations for the fractured reservoir.

Summary

These results discuss several alternative ways of using partitioning interwell tracer tests (PITTs) in oil fields for the calculation of oil saturation, swept pore volume and sweep efficiency, and assesses the accuracy of such tests under a variety of reservoir conditions. The method of moments is used for the interpretation of PITTs in heterogeneous reservoirs with spatially variable residual oil saturation and extends the method to cases with mobile oil saturation. The feasibility of using partitioning tracers to estimate oil saturation at different depths in the reservoir was investigated assuming that the tracer concentrations could be measured with downhole chemical sensors or any other suitable method. The possibility of using natural organic tracers (dissolved components of the crude oil) as a low-cost alternative to injected tracers was also simulated and the method of moments was used to interpret the results for both single porosity and dual porosity reservoirs. All of these applications point to a much greater potential for the PITT technology than is commonly recognized or practiced in the oil field. The results clearly demonstrate that the method of moments is a very simple, fast and robust method to estimate oil saturation and swept pore volumes from either injected or natural partitioning tracer data.

CONCLUSIONS

Part-I

We have presented three approaches to tracer and production data integration and examined their relative merits using quantitative measures of non-linearity. These are travel time, generalized travel time and the commonly used amplitude inversion. The travel-time inversion of production data is robust and computationally efficient. Unlike conventional amplitude matching that can be highly nonlinear, the travel-time inversion has quasilinear properties. This makes the method particularly attractive for field-scale applications where the prior geologic model might be far from the solution. The generalized travel-time inversion appears to retain most of the desirable features of the travel-time inversion and also accomplishes the amplitude match. Some specific findings from this study can be summarized as follows:

1. We have quantitatively investigated the non-linearities associated with travel time and amplitude inversion for production data integration. The non-linearity is expressed in terms of a simple and intuitive geometric measure of curvature as proposed by Bates and Watts[16] and later used by Grimstad and Mannseth.[17]
2. The non-linearity in travel time inversion is found to be orders of magnitude smaller than the conventional amplitude inversion. As a result, the travel time inversion has better convergence properties and is less likely to be trapped in local minimum.
3. Travel time sensitivity is more uniform between the wells. In contrast, the amplitude sensitivity can be localized near the wells. The higher magnitude of the travel time sensitivity also contributes to its quasilinearity and improved convergence properties.
4. The generalized travel time inversion effectively combines travel time and amplitude inversion while retaining most of the desirable properties of the travel time inversion. For the field example studied here, the generalized travel time inversion outperformed both travel time and amplitude inversion.

Part-II

We have presented a general dual porosity dual permeability formulation for streamline simulation of water injection in naturally fractured reservoirs. Our approach accounts for the matrix-facture interactions via transfer functions and reduces to the dual porosity streamline formulation proposed by Di Donato et al.[2] when flow in the matrix is neglected. The proposed approach can be easily implemented within the framework of the conventional single porosity streamline simulators while retaining most of its computational advantages over finite difference models. Some specific conclusions arising from this work can be summarized as follows:

- Streamline simulation can be easily generalized for naturally fractured reservoirs using a dual media approach. As in finite-difference simulation, the matrix and fracture systems are treated as two separate continua interlinked via a transfer function.
- The dual permeability formulation requires streamline generation for both the matrix and the fracture systems. The streamline saturation equations have been presented in the time of flight coordinate that decouples the saturation calculations from the underlying grid. The matrix-fracture transfer function appears simply as a source term in these equations.
- An operator splitting approach is presented to efficiently solve the saturation equation for the dual porosity dual permeability systems. The procedure involves a ‘convective step’ along

streamlines followed by a 'corrective step' on the grid to account for the matrix-fracture interaction.

- We have modeled the matrix-fracture interactions using the conventional transfer function and also an empirical transfer function. For the empirical transfer function, the streamline saturation calculations have been validated using an analytic solution.
- We have compared our streamline-based formulation with ECLIPSE for both dual porosity single permeability (DPSP) and dual-porosity dual-permeability (DPDP) models. In all cases, an excellent agreement is obtained both in terms of water-cut histories and water saturation profiles. Streamline results are shown to be less impacted by numerical dispersion and thus preserves saturation fronts better compared to ECLIPSE.
- A comparison of the scaling of the CPU time with respect to the number of grid blocks shows that the streamline simulator is likely to offer significant computational advantage over finite difference models for large-scale field applications.

Part-III

We have proposed a streamline-based production data integration technique for naturally fractured reservoirs using the dual porosity approach. The principal features of our method are the extension of streamline-derived analytic sensitivities to account for matrix-fracture interactions and the use of our previously proposed generalized travel time inversion for history matching. Our proposed workflow has been demonstrated by using both a dual porosity streamline simulator and a commercial finite difference simulator. The approach is computationally efficient and well suited for large scale field applications in naturally fractured reservoirs with changing field conditions. The use of the generalized travel time concept enabled us to match both the breakthrough and amplitude of the reference response in one step. The main findings of our study are summarized as follows.

- Streamline-based analytic sensitivity computations have been extended to naturally fractured reservoirs using the dual porosity approach. The matrix-fracture interactions are accounted for using predictor-corrector steps that involve convection along streamline followed by matrix-fracture exchange.
- A comparison of the streamline-based sensitivities with those computed using the numerical perturbation method shows close agreement, indicating the validity of our approach. The streamline-based sensitivity computation is extremely efficient and requires a single forward simulation.
- We have used the streamline-derived sensitivities in conjunction with a previously proposed generalized travel time inversion for integration of production data in fractured reservoirs. The generalized travel-time inversion is robust, computationally efficient and eliminates much of the time-consuming trial-and-error associated with manual history matching.
- We have combined the streamline-derived sensitivities with a dual porosity finite-difference simulator to exploit the efficiency of the streamline approach and the versatility of the finite-difference simulator. Use of finite-difference simulation allows us to include compressibility effects, strong matrix fracture coupling and cross-streamline mechanisms.
- We have demonstrated the power and efficiency of our proposed method using 2-D and 3-D examples designed after realistic field conditions. For the 3-D application, the results indicate

the role of production data and prior information in terms of reproducing the fracture connectivity and fluid flow response in the reservoir.

Part-IV

- An initial effort has been made in simulating the use of downhole sensors in tracer tests. Fields quite similar in characteristics to common oil fields were considered for the study. The initial results are very positive and show that partitioning tracers measured as a function of depth with downhole sensors can in principle be used for estimating the vertical distribution of oil saturation during or after a waterflood. With permanent downhole sensors, the potential exists to make these measurements numerous times during a waterflood to update the sweep efficiency and consider targeting poorly swept oil using profile control, targeted infill drilling and other technologies and/or improved oil recovery methods.
- The concept of natural tracers in oil fields has been introduced as a potentially cost-effective substitute for injected tracers. Phenols and aliphatic acids have been identified as some of the components of crude oil that might be used as natural partitioning tracers. Equations to calculate average oil saturations and pore volumes have been derived for single as well as multiphase flow and their accuracy has been illustrated with simulations.
- An analytical derivation based on the method of moments has been presented to calculate oil saturations and swept pore volumes using produced tracer concentrations. The general derivation is applicable for three-dimensional heterogeneous reservoirs with mobile oil in the reservoir. The estimated results were quite accurate when compared to the true reservoir values.
- (Simulations indicate that partitioning interwell tracer tests can be used to accurately estimate the vertical distribution of oil saturation in a reservoir, provided a means such as downhole sensors is available for measuring the tracer concentrations as a function of time and depth in the reservoir. The method of moments is a simple and accurate way to calculate the average oil saturation for each layer in the reservoir.
- The method of moments has been validated for calculating oil saturation in reservoirs with mobile oil. The procedure is the same as for applications at residual oil saturation except total tracer concentrations are used rather than aqueous phase concentrations. The difference between the average oil saturation during the tracer test and the estimated values was less than 0.01 for all cases simulated.
- The possibility of using some of the more soluble oil components as tracers for the estimation of oil saturation was investigated. Natural tracers may in some cases provide a low-cost alternative for injected tracers and extend the practical use of the concept of partitioning tracers. In this study, some of the soluble oil components that might be used as natural tracers have been identified based upon their partitioning into water. Oil saturations calculated from the generalized method of moments were in excellent agreement with the actual values even with mobile oil. This method is also not limited to residual oil saturation.
- The theoretical use of natural tracers was also extended to naturally fractured reservoirs. The values calculated from the generalized method of moments was also in good agreement with the actual values from the simulation in this case, but much longer waterflood times are required to give good estimates of the oil saturation compared to single porosity reservoirs. However, if natural tracers could be measured over long time periods, this method would

give useful results without injecting tracers and other methods such as inverse modeling might greatly shorten the time required to get useful estimates of the remaining oil saturation.

REFERENCES

Part-I

1. Bissel, R.C.: "Calculating Optimal Parameter for History Matching," *Proc*. 4th European Conference on the Mathematics of Oil Recovery, Topic E: History Match and Recovery Optimization, 1994.
2. Vasco, D.W., Yoon, S., and Datta-Gupta, A.: "Integrating Dynamic Data Into High-Resolution Reservoir Models Using Streamline-Based Analytic Sensitivity Coefficients," *SPE Journal* (December 1999) 389.
3. Oliver, D. S.: "Incorporation of Transient Pressure Data into Reservoir Characterization," *In Situ* 18 (3), 243-275 1994.
4. Datta-Gupta, A. *et al.*: "Streamlines, Ray Tracing and Production Tomography: Generalization to Compressible Flow," *Petroleum Geoscience* (May 2001), 75.
5. Yoon, S., Malallah, A.H., Datta-Gupta, A. and Vasco, D.W..: "A Multiscale Approach to Production Data Integration Using Streamline Models," *SPE Journal*, 6(2), 182-192, June (2001).
6. Landa, J.L., Kamal, M.M., Jenkins, C.D., and Horne, R.N.: Reservoir Characterization Constrained to Well Test Data: A Field Example," paper SPE 36511, Presented the 1996 SPE Annual Technical Conference and Exhibition, Denver 6-9 October.
7. Milliken, W.J. *et al.*: "Application of 3-D Streamline Simulation to Assist History Matching," paper SPE 63155 presented at the 2000 SPE Annual Technical Conference and Exhibition, Dallas, 1-4 October.
8. Wang, Y. and Kovscek, A.R.: "A Streamline Approach to History Matching Production Data," paper SPE 59370 presented at the 2000 SPE/DOE Symposium on Improved Oil Recovery, Tulsa, 3-5 April.
9. Wu, Z. and Datta-Gupta, A.: "Rapid History Matching Using a Generalized Travel Time Inversion Method," *SPE Journal*, 7(2), 113-122, June (2002)..
10. Reynolds, A. C., He, N., and Oliver, D.S.: "Reducing Uncertainty in Geostatistical Description with Well Testing Pressure Data," in *Proc*., 1997 International Reservoir Characterization Conference, Houston, 2-4 March.
11. Landa, J.L. and Horne, R.N.: "A Procedure to Integrate Well Test Data, Reservoir Performance History and 4-D Seismic Information into a Reservoir Description," paper SPE 38653 presented at the 1997 SPE Annual Technical Conference and Exhibition, San Antonio, TX, Oct. 5-8.
12. He, Z., Datta-Gupta, A., and Yoon, S.: "Streamline-Based Production Data Integration with Gravity and Changing Field Conditions*," SPE Journal*, 7(4), 423-436, December (2002).
13. King, M.J. and Datta-Gupta, A.: "Streamline Simulation: A Current Perspective," *In Situ* (1998) **22**, No. 1, 91.
14. Wen, X. *et al.*: "High Resolution Reservoir Models Integrating Multiple-Well Production Data," paper SPE 38728 presented at the 1997 SPE Annual Technical Conference and Exhibition, San Antonio, Texas, 5-8 October.
15. Luo, Y. and Schuster, G.T.: "Wave-Equation Traveltime Inversion," *Geophysics* (1991) **56,** No. 5, 645.
16. Bates, D.M. and Watts, D.G.: "Relative Curvature Measures of Nonlinearity," *J. R. Statist. Soc. B* (1980) **42**, No. 1, 1.

17. Grimstad, A.-A. and Mannseth, T.: "Nonlinearity, Scale, and Sensitivity for Parameter Estimation Problems," *SIAM J. Sci. Comput.* (2000) **21**, No. 6, 2096.
18. Mannseth, T. *et al.*: "Functional Representation and Model Nonlinearity in Estimation of Porous Media Properties From Laboratory Experiments," presented at the Fourth SIAM Conference on Mathematical and Computational Issues in the Geosciences, Albuquerque, NM, 16-19 June, 1997.
19. Yeh, W. W-G: "Review of Parameter Identification Procedures in Groundwater Hydrology: The Inverse Problem," *Water Resources Research* (1986) **22**, No. 2, 95.
20. Bissel, R.C. *et al.*: "Reservoir History Matching Using the Method of Gradients," paper SPE 24265 presented at the 1992 SPE European Petroleum Computer Conference, Stavanger, 25-27 May.
21. Sun, N-Z and Yeh, W. W.-G.: "Coupled Inverse Problems in Groundwater Modeling, I, Sensitivity Analysis and Parameter Identification," *Water Resources Research* (1990) **26**, 2507.
22. Datta-Gupta, A. and King, M.J.: "A Semianalytic Approach to Tracer Flow Modeling in Heterogeneous Permeable Media," *Advances in Water Resources* (1995) **18**, No. 1, 9.
23. Parker, R.L.: *Geophysical Inverse Theor*y, Princeton University Press, 1994.
24. Paige, C.C. and Saunders, M. A.: "LSQR: An Algorithm for Sparse Linear Equations and Sparse Least Squares," *ACM Trans. Math. Software* (1982) **8**, No. 1, 43.
25. Nolet, G.: "Seismic Wave Propagation and Seismic Tomography," in *Seismic Tomograph*y, G. Nolet (Ed.), D. Reidel, Dordrecht, (1987) 1-23.
26. Lichtenberger, J.: "Field Application of Interwell Tracers for Reservoir Characterization of Enhanced Oil Recovery Pilot Areas," paper SPE 21652 presented at the 1991 SPE Production Operations Symposium, Oklahoma City, 7-9 April.
27. Allison, S.B., Pope, G.A., and Sepehrnoori, K., "Analysis of Field Tracers for Reservoir Description," *J. Pet. Sci. Eng.* (1991), **5,** 173-186.
28. Iliassov, P.A. *et al.*: "Field-Scale Characterization of Permeability and Saturation Distribution Using Partitioning Tracer Tests: The Ranger Field, Texas," *SPE Journal*, 7(4), 409-423, December (2002).
29. Deutsch, C.V. and Journel, A.G.: *GSLIB: Geostatistical Software Library and User's Guide*, Oxford University, 1998.

Part-II

1. Al-Huthali, A.H.: "Streamline-Based Simulation of Water Injection in Naturally Fractured Reservoirs," MS thesis, Texas A&M U., College Station, TX (August 2003).
2. Di Donato, G., Huang, W., and Blunt, M.J.: " Streamline-Based Dual Porosity Simulation of Fractured Reservoirs," paper SPE 84036 presented at the 2003 Annual Technical Conference and Exhibition, Denver, CO, 5-8 October.
3. Bratvedt, F., Bratvedt, K. Buchholz, C. F, Gimes, T., Holden, H., Holden, L. and Risebro, N. H.: "FRONTLINE and FRONTSIM. Two Full Scale, Two-Phase, Black oil Reservoir Simulators Based on Front Tracking," Surv. Math. Ind., 3, 185 (1993).
4. Crane, M. J. and Blunt, M. J., "Streamline-based Simulation of Solute Transport," *Water Resour. Res.*, 35(10), 3061-3078, 1999.
5. Datta-Gupta, A., "Streamline Simulation: A Technology Update," SPE Distinguished Author Series, *Journal of Petroleum Technology*, 68-73 (December 2000).

6. King, M.J. and Datta-Gupta, A.: "Streamline Simulation: A Current Perspective," *In Situ* (1998) **22**, No.1, 91.
7. King, M.J. and Mansfield, M. "Flow Simulation Through Geologic Models," SPE 38877 in Proceedings of the SPE Annual Technical Conference, San Antonio, TX, October 5-8, 1997.
8. Vasco, D.W., Yoon, S., and Datta-Gupta, A.: "Integrating Dynamic Data Into High-Resolution Reservoir Models Using Streamline-Based Analytic Sensitivity Coefficients," paper SPE 49002 presented at the 1998 SPE Annual Technical Conference and Exhibition, New Orleans, LA, 27-30 September.
9. Kazemi, H. *et al.*: "Numerical Simulation of Water-Oil Flow in Naturally Fractured Reservoirs," *SPEJ* (December 1976) 317-26: *Trans*., AIME **261**.
10. Dean, R.H. and Lo, L.L.: "Simulations of Naturally Fractured Reservoirs," *SPERE* (May 1988) 638-48.
11. Saidi, A.M.: "Simulation of Naturally Fractured Reservoirs," paper SPE 12270 presented at the 1983 SPE Symposium on Reservoir Simulation, San Francisco, California, 15-18 November.
12. Thomas, L. K., Dixon, T.N., and Pierson, R.G.: "Fractured Reservoir Simulation," *SPEJ* (February 1983) 42-54.
13. Sonier, F., Souillard, P., Blaskovich, F.T.: "Numerical Simulation of Naturally Fractured Reservoirs", SPE paper 15627 presented at the 1986 SPE Annual Technical Conference and Exhibition, New Orleans, 5-8 October.
14. Litvak, B.L.: "Simulation and Characterization of Naturally Fractured Reservoirs", Proceedings of the 1985 Reservoir Characterization Technical Conference, Dallas, April 29-May

Part-III

1. Nelson, R. A. : Geological Analysis of Naturally Fractured Reservoirs, Gulf Publishing Company, Houston (1985).
2. Dershowitz, W., *et al.*: "Integration of Discrete Fracture network Methods with Conventional Simulator Approaches," *SPE Res. Eval. & Eng.*, 165-170, (April 2000).
3. Tamagawa, T., Matsuura, T., Anraku, T., Tezuka, K. and Namikawa, T., "Construction of Fracture Network Model Using Static and Dynamic Data," SPE 77741 presented at the SPE Annual Technical Conference and Exhibition, San Antonio, TX, Sept. 29-Oct. 2, 2002.
4. Long, J. C. S., Doughty C., Datta-Gupta, A., Hestir, K. and Vasco, D. W., "Component Characterization: An Approach to Fracture Hydrogeology," Subsurface Flow and Transport: The Stochastic Approach, G. Dagan and S. P. Neuman (Eds.), Cambridge University Press, 179-195 (1997).
5. Datta-Gupta, A., Vasco, D. W. and Long, J. C. S., "Detailed Characterization of a Fractured Limestone Formation Using Stochastic Inverse Approaches," *SPE Formation Evaluation*, 10 (3), 133-140 (1995).
6. Vasco, D.W., Yoon, S., and Datta-Gupta, A.: "Integrating Dynamic Data Into High-Resolution Reservoir Models Using Streamline-Based Analytic Sensitivity Coefficients," *SPE Journal* (1999), **4**(4), 389-399.

7. He, Z., Datta-Gupta, A., and Yoon, S.: "Streamline-Based Production Data Integration with Gravity and Changing Field Conditions," *SPE Journal*, 7(4), 423-436, December (2002).
8. Qassab, H, Khalifa, M, Pavlas, R., Khargoria, A., He, Z., Lee, S. H. and Datta-Gupta, A.: "Streamline-based Production Data Integration Under Realistic Field Conditions: Experience in a Giant Middle-Eastern Oil Reservoir," SPE 84079 presented at the SPE Annual Technical Conference and Exhibition, Denver, CO, October 5-8, 2003.
9. Wang, Y. and Kovscek, A.R.: "A Streamline Approach to History Matching Production Data," paper SPE 59370 presented at the 2000 SPE/DOE Symposium on Improved Oil Recovery, Tulsa, 3-5 April.
10. Milliken, W.J. *et al.*: "Application of 3-D Streamline Simulation to Assist History Matching," paper SPE 63155 presented at the 2000 SPE Annual Technical Conference and Exhibition, Dallas, 1-4 October.
11. Barenblatt, G.E., Zheltov, Iu. P., and Kochina, I.N.: "Basic Concepts in the Theory of seepage of homogenous Liquids in Fissured Rocks," j. Appl. Math. And Mech. Eng. Transl., 1286-1303, 1960.
12. Kazemi, H. et al.: "Numerical Simulation of Water-Oil Flow in Naturally Fractured Reservoirs," *SPEJ* (December 1976) 317-26: *Trans*., AIME 261.
13. Dean, R.H. and Lo, L.L.: "Simulations of Naturally Fractured Reservoirs," *SPERE* (May 1988) 638-48.
14. Di Donato, G., Huang, W., and Blunt, M.J.: " Streamline-Based Dual Porosity Simulation of Fractured Reservoirs," paper SPE 84036 presented at the 2003 Annual Technical Conference and Exhibition, Denver, CO, 5-8 October.
15. Al-Huthali, A.H.: "Streamline Simulation of Counter-current Imbibition in Naturally Fractured Reservoirs," Journal of Petroleum Science and Engineering, 2004 (in press).
16. Cheng, H, Khargoria, A., He, Z. and Datta-Gupta, A., "Fast History Matching of Finite-difference Models Using Streamline-derived Sensitivities," SPE 89447 presented at the SPE/DOE fourteenth symposium on Improved Oil Recovery, Tulsa, OK, April 17-21, 2004
17. Wu, Z. and Datta-Gupta, A.: "Rapid History Matching Using a Generalized Travel Time Inversion Method," *SPE Journal*, 7(2), 113-122, June (2002).
18. Cheng, H., Wen, X, Milliken, W. and Datta-Gupta, A., "Field Experiences with Assisted and Automatic History Matching Using Streamline Models," SPE 89857 presented at the SPE Annual Technical Conference and Exhibition, Houston, TX, September 26-29, 2004.
19. Oliver, D. S., Reynolds, A. C., Bi, Zhuoxin and Abacioglu, Y., "Integration of Production data Into Reservoir Models," Petroleum Geoscience, (7), S65-S73, 2001..
20. Guerreiro, L. *et al.*: "Integrated Reservoir Characterization of a Fractured Carbonate Reservoir." SPE 58995, SPE Inter. Petroleum Conf. and Exhib., Villahermosa, Mexico, (Feb. 2000).
21. King, M.J. and Datta-Gupta, A.: "Streamline Simulation: A Current Perspective," *In Situ* (1998) **22**, No.1, 91.
22. Datta-Gupta, A. and King, M.J: "A Semi-analytic Approach to Tracer Flow Modeling in Heterogeneous Permeable Media," *Advances in Water Resources* (1995) **18**, 9-24.
23. Pollock, D. W., "Semianalytical Computation of Pathlines for Finite-Difference Models," Groundwater, 26 (6), 743 (1988).

24. Kazemi, H. et al.: "Analytical and Numerical Solution of Oil Recovery From Fractured Reservoirs with Empirical Transfer Functions," *SPEJ* (May 1992) 219.
25. Bratvedt, F., Gimse, T. and Tegnander, C., "Streamline Computations for Porous Media Flow Including Gravity," Transport in Porous Media, 25, 63 (1996).
26. Bissel, R.C. *et al.*: "Reservoir History Matching Using the Method of Gradients," paper SPE 24265 presented at the 1992 SPE European Petroleum Computer Conference, Stavanger, 25-27 May.
27. Landa, J.L. and Horne, R.N.: "A Procedure to Integrate Well Test Data, Reservoir Performance History and 4-D Seismic Information into a Reservoir Description," paper SPE 38653 presented at the 1997 SPE Annual Technical Conference and Exhibition, San Antonio, TX, Oct. 5-8.
28. Wen, X. *et al.*: "High Resolution Reservoir Models Integrating Multiple-Well Production Data," paper SPE 38728 presented at the 1997 SPE Annual Technical Conference and Exhibition, San Antonio, Texas, 5-8 October.
29. Reynolds, A. C., He, N., and Oliver, D.S.: "Reducing Uncertainty in Geostatistical Description with Well Testing Pressure Data," in *Proc*., 1997 International Reservoir Characterization Conference, Houston, 2-4 March.
30. Anterion, F., Eymard, R. and Karcher, B. : "Use of Parameter Gradients for Reservoir History matching," paper SPE 18433 presented at the 1989 SPE Symposium on Reservoir Simulation, Houston, February 6-8.
31. Vega, L., Rojas, D. and Datta-Gupta, A.: "Scalability of the Deterministic and Bayesian Approaches to Production Data Integration into Field-Scale Reservoir Models," SPE 79666 presented at the 2003 SPE Reservoir Simulation Symposium, Houston, 3-5 February.
32. Paige, C.C. and Saunders, M. A.: "LSQR: An Algorithm for Sparse Linear Equations and Sparse Least Squares," *ACM Trans. Math. Software* (1982) **8**, No. 1, 43.
33. Vega, L., An Efficient Bayesian Formulation for Production Data Integration into Reservoir Models, Ph. D. Dissertation, Texas A&M University (December 2003).
34. Schlumberger GeoQuest: ECLIPSE User Guide 2003A.
35. Liu, N., Betancourt, S., and Oliver, D.S.: "Assessment of Uncertainty Assessment Methods," paper SPE 71624 presented at the 2001 SPE Annual Technical Conference and Exhibition, New Orleans, 30 September-3 October.

Part-IVA

1. Jennings, J. W. Jr., S.C. Ruppel, W. B. Ward: "Geostatistical Analysis of Permeability Data and Modeling of Fluid-Flow Effects in Carbonate Outcrops", SPE Reservoir Evaluation and Engineering Vol. 3, No. 4, August 2000
2. Kragas, Tor K., Brock A. Williams, Gregory A. Myers: "The Optic Oil Field: Deployment and Application of Permanent In- well Fiber Optic Sensing Systems for Production and Reservoir Monitoring", paper SPE 71529 presented at the 2001 SPE Annual Technical Conference and Exhibition, New Orleans, Louisiana, 30 September-3 October
3. Wu, Zhan, Akhil Datta Gupta: "Rapid History Matching Using a Generalized Travel-Time Inversion Method", SPE Journal, Vol. 7, No. 2, June 2002

4. Yoon, S., I. Barman, A. Datta-Gupta, and G.A. Pope: "In-Situ Characterization of Residual NAPL Distribution Using Streamline-Based Inversion of Partitioning Tracer Tests," SPE 52729 Proceedings of the 1999 SPE/EPA Exploration & Production Environmental Conference, Austin, TX, 28 February - 3 March.
5. Zemel, B.: " Tracers in the Oil Field", Developments in Petroleum Science, Vol. 43, Elsevier Science, 1995

Part-IVB

1. Benett, B. and S. R. Larter: "Partition behavior of alkyl phenols in crude oil/brine systems under subsurface conditions", Geochimica et Cosmochimica Acta, Vol. 61, No. 20, 1997
2. Kharaka, Yousif K., Paul D. Lundegard and Thomas H. Giordano: " Distribution and origin of organic ligands in subsurface waters from sedimentary basins", Ore Genesis and Exploration: The Roles of Organic Matter, Reviews in Economic Geology, Vol. 9, 2000
3. Larter, S.R., and A. C. Aplin: "Reservoir geochemistry: Methods, applications and opportunities", The geochemistry of reservoirs, Geological Society Special Publication, No. 86, 1995
4. Reinsel, Mark A., John J. Borkowski and John T. Sears: " Partition coefficients for Acetic, Propionic and Butyric Acids in a crude oil/water system", Journal of Chemical Engineering Data, 39, 1994
5. Taylor, P., Steve Larter, Martin Jones, Jason Dale and Idar Horstad: " The effect of oil-water-rock partitioning on the occurrence of alkyl phenols in petroleum systems", Geochimica et Cosmochimica Acta, Vol. 61, No. 9, 1997

Part-IVC

1. Allison, S. B., "Analysis and Design of Field Tracers for Reservoir Description," MS thesis, The University of Texas at Austin, 1988.
2. Datta-Gupta, A., Yoon, S., Vasco, D.W. and Pope, G.A., "Inverse modeling of partitioning interwell tracer tests: A streamline approach," Water Resources Research, 38(6), 15.1-15.15, 2002.
3. Delshad, M., Asakawa, K., Pope, G. A. and Sepehrnoori, K., "Simulations of Chemical and Microbial Enhanced Oil Recovery Methods," paper SPE 75237, presented at the SPE/DOE Thirteenth Improved Oil Recovery Symposium, Tulsa, OK, 2002.
4. Delshad, M., Pope, G. A. and Sepehrnoori, K., "A compositional simulator for modeling surfactant enhanced aquifer remediation, Part 1 Formulation," Journal of Contaminant Hydrology, 23, 303-327, 1996.
5. Dwarakanath, V., Deeds, N. and Pope, G. A., "Analysis of Partitioning Interwell Tracer Tests," Environmental Science and Technology, 33, 3829-3836, 1999.
6. ECLIPSE Reference Manual (2002a), Schlumberger Geoquest, Geoquest Reservoir Technologies, Houston, TX, 2002.
7. Jennings, J. W, Ruppel, S. C and Ward, W. B., "Geostatistical Analysis of Permeability Data and Modeling of Fluid-Flow Effects in Carbonate Outcrops," SPE Reservoir Engineering, 3(4), August 2000.

8. Jin, M., Delshad, M., Dwarakanath, V., McKinney, D. C., Pope, G. A., Sepehrnoori, K., Tilburg, C. E., and Jackson, R. E., "Partitioning tracer test for detection, estimation, and remediation performance assessment of subsurface nonaqueous phase liquids," Water Resources Research 31(5), 1201-1211, 1995.
9. Jin, M., "A Study of Nonaqueous Phase Liquid Characterization and Surfactant Remediation," Ph.D. dissertation, The University of Texas at Austin, August 1995.
10. Jin, M., Jackson, R. E. and Pope, G. A., "Development of Partitioning Tracer Tests for Characterization of Nonaqueous-Phase Liquid-Contaminated Aquifers," paper SPE 39293, presented at the SPE 72nd Annual Technical Conference & Exhibition, San Antonio, Texas, 1997.
11. Reinsel, M. A., Borkowski, J. J. and Sears J. T., "Partition Coefficients for Acetic, Propionic, and Butyric Acids in a Crude Oil/Water System," Journal of Chemical Engineering Data, 39, 513-516, 1994.
12. Sinha, R., "Simulation of Natural and Partitioning Interwell Tracers to Calculate Saturation and Swept Volumes in Oil Reservoirs," MS thesis, The University of Texas at Austin, December, 2003.
13. Tang, J. S. and Harker, B., "Interwell Tracer Test to Determine Residual Oil Saturation in a Gas Saturated Reservoir. Part I: Theory and Design," The Journal of Canadian Petroleum Technology, 30(4), 34, 1991a.
14. Tang, J. S. and Harker, B., "Interwell Tracer Test to Determine Residual Oil Saturation in a Gas Saturated Reservoir. Part II: Field Applications," The Journal of Canadian Petroleum Technology, 30(3), 76, 1991b.
15. Taylor, P., Larter, S., Jones, M., Dale, J. and Horstad, I., "The effect of oil-water-rock partitioning on the occurrence of alkylphenols in petroleum systems," Geochimica et Cosmochimica Acta, 61(9), 1899-1910, 1997.
16. Nelson, R. A., Geologic Analysis of Naturally Fractured Reservoirs, Gulf Publishing Company, Texas, 1985.
17. Yoon, S., Barman, I., Datta-Gupta, A., and Pope, G. A., "In-Situ Characterization of Residual NAPL Distribution Using Streamline-based Inversion of Partitioning Tracer Tests," paper SPE 52729 presented at the 1999 SPE/EPA Exploration and Production Environmental Conference, Austin, Texas, 28 February-3 March, 1999.
18. Zemel, B., Tracers in the Oil Field, Developments in Petroleum Science, 43, Elsevier Science B. V., Amsterdam, 1995.

LIST OF ACRONYMS AND ABBREVIATIONS

Part-I

$\boldsymbol{d}$ = data vector
C_c = calculated tracer concentration
C_o = observed tracer concentration
D = dispersion coefficient
$\boldsymbol{F}_k$ = tangent vector
$\boldsymbol{F}_{kk}$ = acceleration vector
I = identity matrix
k = permeability
L = spatial difference operator
n_b = number of grid blocks
n_o = number of dynamic data observations
s = slowness
S = sensitivity matrix
t = time
u = Darcy velocity
v = Interstitial velocity
β = weighting factor
κ_{am} = measure of nonlinearity for amplitude inversion
κ_{gt} = measure of nonlinearity for generalized travel-time inversion
κ_{tt} = measure of nonlinearity for travel-time inversion
τ = time of flight
$\Delta\tau$ = generalized travel-time or travel-time shift

Part-II

D =Depth from datum, L
f = fractional flow, fraction
F_s = shape factor, L^{-2}
k = permeability, L^2
k_r = relative permeability, dimensionless
l = matrix length, L
P = pressure, $ML^{-1}T^{-2}$
P_c = capillary pressure, $ML^{-1}T^{-2}$
P_{gh} = pressure due to a gravity head in fracture system, $ML^{-1}T^{-2}$
q = source term, L^3T^{-1}
S = saturation, fraction
S_{orm} = matrix residual oil saturation, dimensionless

$S_{wn\ m}$ = normalized water saturation in matrix, dimensionless
t = time, T
u = velocity, LT^{-1}

Subscripts

f = fracture
i = grid-block or node index
m = matrix
n = time-step index
o = oil
w = water
x = x-direction
y = y-direction
z = z-direction

Part-III

D =Depth from datum, L
f = fractional flow, fraction
F_s = shape factor, L^{-2}
k = permeability, L^2
k_r = relative permeability, dimensionless
l = matrix length, L
P = pressure, $ML^{-1}T^{-2}$
P_c = capillary pressure, $ML^{-1}T^{-2}$
P_{gh} = pressure due to a gravity head in fracture system, $ML^{-1}T^{-2}$
q = source term, L^3T^{-1}
S = saturation, fraction
S_{orm} = matrix residual oil saturation, dimensionless
$S_{wn\ m}$ = normalized water saturation in matrix, dimensionless
t = time, T
u = velocity, LT^{-1}

Subscripts

f = fracture
i = grid-block or node index
m = matrix
n = time-step index
o = oil
w = water
x = x-direction

y = y-direction
z = z-direction

Part-IV

C_i = *Concentration of tracer i*
C_{ij} = *Concentration of tracer i in phase j*
C_{iJ} = *Concentration of the injected tracer slug*
C_{niw} = *Normalized water phase tracer*
C_{io} = *Concentration of tracer i in oil*
C_{it} = *Total tracer concentration of tracer i*
C_{iw} = *Concentration of tracer i in water*
C_{iwI} = *Initial concentration of tracer i in water*
C_{iwJ} = *Injected concentration of tracer i in*
f_o = *Fractional flow of oil*
f_w = *Fractional flow of water*
K_i = *Partition coefficient of tracer i*
$\vec{\bar{K}}_{ij}$ = *Dispersion coefficient of tracer i in phase*
m_n = *Mass of tracer produced at producer n*
M = *Total mass of the tracer injected*
m_{0iw} = *Zeroth temporal moment of concentration of tracer i in water*
m_{0i} = *Zeroth temporal moment of tracer i*
m_{1i} = *First temporal moment of tracer i*
n_p = *Total number of phases*
$\vec{N}_i$ = *Flux of tracer i*
q = *Liquid flow rate*
Q = *Injection rate*
Q_o = *Total oil production rate*
R_{fi} = *Retardation factor of tracer i*
S_j = *Saturation of phase j*
$\hat{S}_j$ = *Average saturation of phase j in reservoir*
S_o = *Oil saturation*

$\hat{S}_o$ = *Average oil saturation in reservoir*

$\overline{\hat{S}}_o$ = *Average oil saturation in swept pore*

S_{or} = *Residual oil saturation*

S_w = *Water saturation*

$\hat{S}_w$ = *Average water saturation in reservoir*

t = *Time*

t_{slug} = *Tracer slug time*

$\vec{u}_j$ = *Flux of phase j*

$\overline{V}_i$ = *Mean residence volume of tracer i*

V_s = *Swept pore volume*

V_{slug} = *Volume of tracer slug*

ϕ = *Porosity*